Experiments with Ultracold Fermi Gases : quantum Degeneracy of Potassium-40 and All-solid-state Laser Sources for Lithium

Norman Kretzschmar

Département de physique
École Normale Supérieure

Laboratoire Kastler Brossel

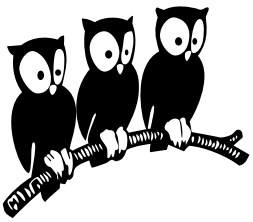

THÉSE de DOCTORAT de l'ÉCOLE NORMALE SUPÉRIEURE

Spécialité : Physique Quantique

présentée par

Norman KRETZSCHMAR

pour obtenir le grade de Docteur de l'École Normale Supérieure

---

Experiments with Ultracold Fermi Gases: Quantum Degeneracy of Potassium-40 and All-solid-state Laser Sources for Lithium

---

Soutenue le 26 Juin 2015

devant le jury composé de :

Robin Kaiser	Rapporteur
Kai Bongs	Rapporteur
Denis Boiron	Examinateur
Jérôme Tignon	Examinateur
Christophe Salomon	Directeur de thèse
Frédéric Chevy	Membre invité

À mon épouse, Nadja.

Contents

Abstract

This thesis presents novel techniques for the experimental study of ultracold quantum gases of fermionic lithium and potassium atoms.

In the first part of this thesis, we describe the design and characterization of the new components of our experimental apparatus capable of trapping and cooling simultaneously ^{6}Li and ^{40}K atoms to ultracold temperatures. We report on a novel sub-Doppler cooling mechanism, operating on the D_1 line transition of alkali atoms, for laser cooling of lithium and potassium. The measured phase space densities after this molasses phase are on the order of 10^{-4} for both ^{6}Li and ^{40}K. We present the forced evaporative cooling of ^{40}K atoms, starting in an optically plugged magnetic quadrupole trap and continuing in an optical dipole trap. In this context, we report on the production of a quantum degenerate Fermi gas of 1.5×10^5 atoms ^{40}K in a crossed dipole trap with $T/T_F = 0.17$, paving the way for the study of strongly interacting superfluids of ^{40}K.

In the second part of this thesis, we present a narrow-linewidth, all-solid-state laser source, emitting 5.2 W in the vicinity of the lithium D-line transitions at 671 nm. The source is based on a diode-end-pumped unidirectional ring laser operating on the 1342 nm transition of Nd:YVO_4, capable of producing 6.5 W of single-mode light delivered in a diffraction-limited beam. We report on three different approaches for second-haromonic generation of its output beam, namely by employing an enhancement cavity containing a ppKTP crystal, intracavity frequency doubling and a ppZnO:LN waveguide structure.

Résumé

Cette thèse présente de nouvelles techniques pour l'étude expérimentale des gaz quantique ultrafroids d'atomes fermioniques de lithium et de potassium.

Dans la première partie de cette thèse, nous décrivons la conception et la caractérisation des nouveaux composants de notre dispositif expérimental capable de piéger et refroidir simultanément des atomes de ^{6}Li et de ^{40}K à des températures ultrabasses. Nous rendons compte d'une nouvelle technique de refroidissement sub-Doppler, reposant sur la transition de la raie D_1 des atomes alcalins, pour refroidir des atomes de lithium et de potassium par laser. Après cette étape de mélasse, nous avons mesuré une densité dans l'espace des phases de l'ordre de 10^{-4} à la fois pour le ^{6}Li et le ^{40}K. Nous présentons le refroidissement par évaporation forcée d'atomes de ^{40}K qui commence dans un piège magnétique quadripolaire pluggé et continue dans un piège optique dipolaire. Dans ce contexte, nous rendons compte de la production d'un gaz quantique de Fermi dégénéré de 1.5×10^5 atomes de ^{40}K dans un piège dipolaire croisé avec $T/T_F = 0.17$, ce qui ouvre la voie à l'étude des superfluides de ^{40}K en interaction forte.

Dans la deuxième partie de cette thèse, nous présentons une source laser à état solide, de faible largeur spectrale et capable d'émettre 5.2 W de puissance autour de 671 nm, dans la gamme des longueurs d'onde des transitions de la raie D du lithium. La source repose sur un laser en anneau pompé par diode, émettant sur la transition à 1342 nm de Nd:YVO_4, capable de produire 6.5 W de lumière dans un faisceau monomode limité par la diffraction. Nous rendons compte de trois différentes approches pour la génération de seconde harmonique du faisceau de sortie, à savoir en utilisant une cavité amplificatrice comprenant un cristal ppKTP, par doublage de fréquence intracavité et par un structure de guide d'onde de ppZnO:LN.

Acknowledgments

The work presented in this thesis would not have been possible without the support of many people. In the following I would like to express my thanks to all of those who were involved in the realization of this project.

In the beginning, I would like to thank Robin Kaiser, Kai Bongs, Denis Boiron and Jérôme Tignon, for having accepted to assist in my thesis committee, for their useful remarks about the present dissertation and the inspiring discussion during my defense.

I am deeply indebted to my thesis supervisor, Christophe Salomon, for having given me the opportunity to work in his research group and for his support of my thesis project. Throughout my thesis I have been impressed by his profound knowledge of experimental physics, his scientific intuition and his talent in leading our team with engaging optimism. The discussions with Christophe about physics were always extraordinarily fruitful and his approach to science had a major influence on my understanding of physical research. I will always remember the moments he spontaneously came by the lab to work with us on the experiment, each time making the crucial suggestions for overcoming any experimental problem.

Equivalently, I am deeply indebted to my co-supervisor, Frédéric Chevy. I very much appreciated his exceptional theoretical understanding, his critical mind and his original teaching of physics. His constant availability, his founded advice as well as his patience gave us a strong support in mastering the daily challenges of laboratory work.

In particular, I would like to thank my fellow lab-mates Diogo Fernandes, Franz Sievers, Daniel Suchet, Mihail Rabinovic and Thomas Reimann for the time we spent together in the lab. Diogo amazed me with his great enthusiasm in planning and realizing new projects, thus pushing the experiment always one step further. I was impressed by Franz tenacity as well as his technical skills and experimental rigor, especially in the context of our joined ^{6}Li cooling and laser project. I thank Daniel for his support of my teaching activities at the UPMC and for sharing his extraordinary motivation for presenting modern physics to a broad public. I also enjoyed to work with Mihail whose patience, critical mind and systematic approach helped me a lot during the last year of my thesis, and who is sharing with me the interest in developing electronics. In addition, I thank Daniel, Mihail and Thomas for having taken over the experiment and for the future I wish them many new technical ideas and scientific

results with our apparatus.

I am grateful that I could take over the laser project of Ulrich Eismann and Andrea Bergschneider, and I thank them both for their support and for sharing their experience with me. In particular, I admire Ulrich's exceptional knowledge about laser physics and nonlinear optics. I also wish to thank my former colleagues Arimin Ridinger, Saptarishi Chaudhuri and Thomas Salez. Although they have always been very busy, they found the time to give me my first lessons in operating the Li-K machine and to discuss physics and lab problems. I am grateful for the fruitful collaboration with Saijun Wu, who suggested cooling on the D_1 line transition of ^{6}Li, thus initiating the gray molasses project and supporting it from a theoretical point of view. I would like to express my gratitude to Lev Khaykovich who joined our group as a visiting professor for several months. His extraordinary capability of putting a physical idea in simple equations was as impressive as his determination to achieve valuable experimental results. Moreover, I had the pleasure to work with Colin Parker, who joined our group as a visitor for a couple of months. All of us were astonished by his outstanding intellectual and experimental skills. His persistent and systematic approach allowed us to solve some of the long-standing technical problems of our setup.

I would like to thank the Lithium team, Sylvain Nascimbène, Nir Navon, Igor Ferrier-Barbut, Benno Rem, Andrew Grier, Marion Delehaye and Sébastien Laurent. They all were of great help during my thesis and I was impressed by the exceptional technical expertise of all members of this research group. Additionally, I thank my colleagues from the other cold atoms groups at the LKB: Alexandre, Christof, Claire, Daniel, David, Dominik, Fabrice, Felix, Florian, Francesco, Hadrien, Jakob, Jean, Jérôme, Katharina, Kenneth, Konstantin, Laura, Lauriane, Leander, Matthias, Ramon, Rémi, Sanjukta, Sebastian, Sebastien, Shao, Sylvain, Tilman, Tim and Vincent. In particular, I appreciated their kind support, for example concerning our frequent request of laboratory material, and I thank them for creating such a stimulating research atmosphere inside our institute.

It is a pleasure to express my gratitude to the LKB administrative services, namely to Christophe Bernard, Thierry Tardieu, Dominique Giafferi, Audrey Gohlke and Monique Granon. I am particularly indebted to the electronics technicians and engineers, namely Toufik El Atmani, Lionel Pérenes and Bernard Trégon, for their indispensable work. Furthermore I thank the informatics service and the workshop staff, namely Saysavanh Sourasing, Thierry Bastien and Jean-Michel Isac.

Apart from my colleagues, I would like to thank my family and friends, in particular my parents who have always provided me with invaluable support and encouragement.

Finally, I wish to thank my wonderful wife, Nadja, for her unconditional support and for the happiness she brings in my life. I dedicate this thesis to her.

1 Introduction

1.1. Ultracold quantum gases

The experimental and theoretical investigation of ultracold quantum gases has become one of the most active research fields in contemporary quantum physics, an evolution that has still been accelerated since the first observation of Bose-Einstein condensation (BEC) in 1995 [1,2]. The motivation to study dilute atomic gases at very low temperatures, typically on the order of 100 nK, is given by the possibility to observe quantum phenomena in this regime. At ultracold temperatures, the description of atoms as distinguishable, point-like particles looses its validity, as a consequence of the emerging fundamental wave nature of the particles. In particular, when the de Broglie wavelength of atoms reaches a size comparable to the interparticle distance inside the atomic ensemble, atoms have to be treated as indistinguishable objects whose physical behavior is governed by the rules of quantum statistics.

There are two distinct classes of particles corresponding to their intrinsic angular moment, the spin. On the one hand, bosons have a spin that is an integer multiple of $\hbar$ and are subject to Bose–Einstein statistics urging them to occupy the same lowest energy quantum state. At ultracold temperatures this results in a phase-transition to a Bose-Einstein condensate [1–5], in which all atoms occupy the motional ground state of the system and can be described by a single macroscopic wave function. One consequence of the coherence of atoms in a BEC is superfluidity, the frictionless motion of particles that can be directly observed by the creation of vortices [6, 7]. On the other hand, fermions have a half-integer spin and are governed by Fermi-Dirac statistics. In particular, they underlie the Pauli exclusion principle which forbids two identical fermions to occupy the same motional and internal quantum state. At zero temperature they behave therefore fundamentally different from bosons, filling up the lowest-lying motional quantum states of the confining potential to the Fermi energy, and forming thus the so-called Fermi sea. The transition from the classical to the quantum degenerate Fermi gas occurs gradually and is, in contrast to bosons, not accompanied by a phase transition. The onset of quantum degeneracy in a trapped gas of fermionic atoms was first observed in 1999 [8].

Bose-Einstein condensation does not rely on interaction effects, since it is a purely statistical phenomenon [3, 4]. As mentioned above, the first BEC was experimentally realized with weakly-interacting alkali atoms in 1995 [1,5,9]. A review of experiments on BEC can be found in [10–13]. These experiments include, besides the mentioned creation of vortices [6, 7], the observation of macroscopic matter wave interference [14], the realization of two-dimensional

gases [15–18], the creation of dark and bright solitons [19–22], and the observation of the superfluid-to-Mott insulator transition in an optical lattice [23].

In the low-energy regime, also the physics of atomic collisions are modified by the wave nature of particles and quantum statistics [24]. In particular, Feshbach resonances [25, 26] allow to tune the collision cross section of a quantum gas and were first observed for bosonic atoms [27]. These resonances occur when two scattering atoms in the open channel resonantly couple to a molecular bound state belonging to a different molecular potential. Tuning the energy spacing between the open and closed channels allows to control their coupling and, as a result, the elastic scattering cross section. Typically, this tuning is achieved by addressing molecular potentials with different magnetic moments, such that their energy spacing can be modified by simply varying the magnetic field [28].

In consequence, Feshbach resonances offer the possibility to enter the regime of strong interactions, which is defined as $n|a|^3 \gtrsim 1$, where n is the atomic density and a the scattering length, characterizing the two-body interaction and the scattering cross section at low temperatures. The regime of strong interactions is an extremely active research field, since the investigation of strongly interacting quantum matter is at the basis of a better understanding of a large spectrum of systems like high-temperature superconductors, quark-gluon plasmas, neutron stars or white dwarfs. As the theoretical models are too complex to be solved numerically, or even analytically, experimental model systems with highly controllable parameters are required, serving ultimately as analogue simulators [29–32]. Moreover, the obtained knowledge might in future lead to new technological developments.

Ultracold Fermi gases are an ideal model system to investigate quantum many body phenomena, also in the strongly interacting regime, since they feature a remarkable degree of control over many system parameters. This can be illustrated by the example of an experiment with a two components mixture. The different components could be represented by two different atomic species or two distinct internal states of a single atomic species. The various controllable parameters of the two component system, range from the species and states of the components, the populations of the components, the temperature, the sign and strength of the interatomic interaction, the species-specific confinement over the mass ratio, to the species-specific dimensionality of the system.

An advantage of ultracold atom experiments is that most of these parameters can be varied between two subsequent experimental cycles. As the cycling time for an ultracold atom experiment usually ranges from some seconds to some tens of seconds, it becomes possible to examine the thermodynamic equation of state of a system and to investigate full phase diagrams.

Another convenience of ultracold atom experiments is the large spectrum of available tools to probe the state of the gas, ranging from time of flight (TOF) measurements [33], where the initial momentum distribution of the gas is obtained after it has been released from the trap and expanded freely, over Bragg spectroscopy [34], radio-frequency (RF) spectroscopy [35], Ramsey interference [36], quantum noise correlations [37–40], to single side imaging in optical lattices [41–43]. Most often absorption and fluorescence imaging of the atoms is performed,

yielding the essential information about each component, namely the overall atom number and the sample's distribution functions in real- and momentum space. Most of the data points presented in the first part of this thesis are obtained by a series of runs, each run consisting in parameter setting, experimental sequence, gas probing and absorption image analysis.

1.2. Quantum degenerate Fermi gases

Quantum degeneracy of a Fermi gas is reached as soon as its temperature becomes lower than the Fermi temperature $T_\mathrm{F} = E_\mathrm{F}/k_\mathrm{B}$, where E_F is the Fermi energy and k_B the Boltzmann constant. The first degenerate Fermi gas of atoms was realized in 1999 with ^{40}K [8], by adapting the cooling methods developed to reach BEC with bosonic atoms to a two-component fermionic system. At ultracold temperatures, it was possible to observe significant deviations of the Fermi gas from the classical behaviour, thus substantiating the Fermi-Dirac distribution of the fermions over the low-lying trap states. Fermionic quantum degeneracy has, as of this writing, also been reached for ^{6}Li [44, 45], metastable ^{3}He* [46], the alkaline earth element ^{87}Sr [47, 48], the rare earth elements ^{173}Yb [49], ^{161}Dy [50] and recently ^{167}Er [51]. Early experiments cooled the atoms to temperatures of about $T = 0.2 - 0.3\,T/T_\mathrm{F}$. Current state-of-the-art experiments reach even temperatures below one tenth the Fermi temperature [52, 53]. Reaching quantum degeneracy requires in general an evaporative process as last cooling stage. The evaporative cooling techniques rely fundamentally on the fast rethermalization of the gas by elastic collisions. The cooling of Fermi gases is challenging in this context, since in the ultracold temperature limit gases can only collide via s-wave collisions, whereas the Pauli exclusion principle forbids these collisions for indistinguishable fermions. A gas of single-state fermionic particles thus becomes collisionless at low temperatures. Therefore, the gas has either to be cooled sympathetically or prepared in two different internal states. Furthermore, the collision rate of fermions decreases in the degenerate regime due to Pauli blocking, meaning that it becomes less likely that scattering into empty low-lying momentum states can occur [8, 54]. Moreover, inelastic collisions can additionally reduce the cooling efficiency and create hole excitations located deep inside the Fermi sea [55, 56].
Several experimental approaches have been applied in order to attain the quantum degenerate regime. The single-species evaporation scheme using two different internal states has been employed for ^{40}K [8], ^{6}Li [57, 58] and ^{173}Yb [49]. Sympathetic cooling with bosonic isotopes has been applied for ^{6}Li-^{7}Li [44, 45], ^{6}Li-^{23}Na [52], ^{6}Li-^{87}Rb [59], ^{6}Li-^{40}K-^{87}Rb [60], ^{6}Li-^{40}K-^{41}K [61], ^{3}He*-^{4}He* [46] and ^{40}K-^{87}Rb [62–66]. Also for the Fermi-Fermi mixture ^{6}Li-^{40}K several approaches have been validated. In Amsterdam, a ^{40}K spin-mixture was evaporated in a magnetic trap, sympathetically cooling ^{6}Li [67]. The Innsbruck group prepared ^{6}Li in two spin states, evaporatively cooled it in an optical trap, while sympathetically cooling ^{40}K [68]. Historically, the first experiments investigated nearly ideal, non-interacting, one-component Fermi gases and their related thermodynamics [8, 44, 69]. Interacting Fermi gases could be realized by tuning the interactions between atoms belonging to different internal states by means of Feshbach resonances. The first investigations on strongly interacting Fermi gases

dealt with the characterization of Feshbach resonances in fermionic systems, for instance for ^{40}K [70–72] and ^{6}Li [73–75]. Contrary to bosonic atoms, fermions are surprisingly stable in the vicinity of a Feshbach resonance, which is due to the fact that the Pauli exclusion principle prohibits three-body relaxation [76] thus increasing the lifetime of the fermion dimers considerably. It was therefore possible to observe Bose-Einstein condensates of weakly bound Feshbach molecules [77–79]. Shortly afterwards also the Bardeen-Cooper-Schriefer (BCS)-regime could be probed and the corresponding superfluid was realized [80–82], proving that in the case of weakly attractive interactions the pairing mechanism is based on Cooper pairing and not on formation of molecules. Moreover, the crossover from the BEC- to the BCS-regime could be investigated [82–84], this crossover smoothly connecting the two limiting cases of superfluid states across the strongly interacting regime.
The superfluid character of strongly interacting Fermi gases was demonstrated by the creation of vortices [85], the phase separation between paired and unpaired fermions in fermionic mixtures with population imbalance [86,87], the determination of the speed of sound [88] and the critical velocities [89] related to a fermionic superfluid. Moreover, a Mott insulator state was realized with fermions [90,91] and the equation of state of a strongly interacting Fermi gas could be measured directly [53, 92, 93]. Interestingly, the transition to a superfluid of paired fermions occurs at a relatively high critical temperature for a strongly interacting Fermi gas, namely at $T_C \simeq 0.17\,T_F$ [94,95]. In this context, future experiments with strongly interacting Fermi gases might play an important role for the understanding of high-T_C superconductivity and give new insights into the underlying physics [96].
The preceding list is only a selection of examples and far from exhaustive, but illustrates the research activity in the field of quantum degenerate Fermi gases.

1.3. Fermi-Fermi mixtures

The investigation of mixtures of different fermionic species promises interesting prospects for the future, since these systems offer a large number of controllable parameters, such as the dimensionality of the system and the mass-imbalance of its components.
Systems in mixed dimensions, where the particles of one species evolve in three dimensions whereas the second species evolves in two, one or zero dimensions [97], can be created by the application of species-selective potentials [98, 99]. The two-body interaction being altered by the mixed dimensionality, this can result in confinement induced resonances [100–104]. Few-body effects, for instance the Efimov-effect in mixed dimensions [105] or p-wave resonances between interspecies dimers and single atoms [106] that are tuned by the lattice depth, can be investigated. The particularly appealing case of 3D-0D confinement is equivalent to the Anderson impurity model and allows the study of Kondo correlated states [107–109]. in addition, Anderson localization can be observed in such a dilute gas of trapped impurity scatterers [110–112]. Moreover, new many-body quantum phases are predicted for the case in which one freely evolving species mediates interactions between a second atomic species confined in different layers, which might lead to interlayer superfluidity [113].

Furthermore, the mass imbalance of the two fermionic species results in unmatched Fermi surfaces, which means that symmetric BCS pairing is not possible any more. Different pairing mechanisms leading to new quantum phases are predicted for this case [114]. Examples of these exotic phases are the Fulde-Ferrell-Larkin-Ovchinnikov (FFLO) state [115–117] and the breached pair state [118,119]. The formation of long-lived trimers [106] and a crystalline phase transition [120] are also in the scope of new phenomena that might arise. Another important motivation for the use of different fermionic species is certainly the possibility to form bosonic polar molecules providing long-range, anisotropic dipole-dipole interaction [121, 122], which may lead to qualitatively new quantum regimes.
The ^{6}Li-^{40}K mixture is an evident candidate for realizing these studies, since lithium and potassium are widely used and experimentally well mastered atoms possessing the only stable, fermionic isotopes among the alkali metals. Both elements have been used in a large spectrum of applications ranging from Bose-Einstein condensation and atom interferometry to fermionic pairing. They possess fermionic and bosonic isotopes which can be conveniently trapped and cooled with laser light delivered by affordable laser sources. Furthermore, the bosonic and fermionic isotopes can also be mixed in order to study Bose-Fermi mixtures, for example in optical lattices [123,124] or in order to study the dynamics of two interacting superfluids [125]. As of this writing, all research groups intending to study Fermi-Fermi mixtures with different atomic species have employed the ^{6}Li-^{40}K mixture [61,67,68,126,127]. To date, three groups in Munich, Innsbruck and at MIT have reported on double quantum degeneracy of this mixture [60, 61, 68]. Characterizations of the interspecies Feshbach resonances have been performed [128–132] and weakly bound Feshbach molecules could be observed [68, 133]. In particular, the Innsbruck group investigated the hydrodynamic expansion of ^{6}Li and ^{40}K in the strong interaction regime [134], measured the excitation spectrum of ^{40}K impurities interacting with a Fermi sea of ^{6}Li[135] and observed a strong attraction between atoms and dimers in the mass-imbalanced two-component fermionic gas [136]. By now, the unitary regime has only been reached for the single species ^{6}Li [137] and ^{40}K [138]. However, it might be possible to attain this regime also for the ^{6}Li-^{40}K-mixture, by using the 1.5 Gauss-wide Feshbach resonance at $B_0 \sim 115$ G [130].

1.4. Thesis outline

This thesis reports on novel techniques for the experimental investigation of ultracold fermionic quantum gas mixtures of lithium and potassium, the further design, construction and characterization of our ^{6}Li- ^{40}K experimental setup and the development of powerful laser sources for laser cooling of lithium.
At the beginning of my thesis, a partially functional experiment including an operational dual-species MOT had already been constructed. It could produce large atomic gas samples of ^{6}Li and ^{40}K, with atom numbers on the order of 10^9 for both species, and temperatures of several hundreds of microkelvins. Furthermore, we were able to perform the first magnetic transport sequences in order to transfer the atomic samples to a high vacuum region. During

my thesis work, all subsequent stages for achieving quantum degeneracy had to be developed, technically implemented and characterized. This comprised the D_1 cooling technique, the development of appropriate laser sources for this cooling scheme, the optimization of the magnetic transport, the revision of the vacuum assembly and the complete setup for forced evaporative cooling in a plugged optical quadrupole magnetic trap as well as in different optical dipole trap configurations.
This manuscript is divided into two parts. In Part I, we present first the experimental setup (Chapter 2), then introduce the simultaneous D_1 sub-Doppler laser cooling of ^{6}Li and ^{40}K (Chapter 3) and conclude with a description of the evaporative cooling of ^{40}K to quantum degeneracy (Chapter 4). In Part II, we present an all solid-state laser source emitting up to 5.2 W output power of 671-nm single-mode light frequency-locked to the Lithium D-line transitions. We detail the design of the fundamental infrared laser source at 1342 nm (Chapter 5) and report on three different technical approaches for second-harmonic generation via an enhancement cavity, intracavity doubling, and a nonlinear waveguide module (Chapter 6).

Chapter 2 – Experimental setup

In this chapter we present the central components of the experimental apparatus, while concentrating on the new subsystems that were implemented in the setup. This includes the laser systems and optical arrangements for the D_1 sub-Doppler cooling, the improved 2D-MOT for ^{40}K, a revision of the vacuum assembly, comprising new coated parts for the transport region and the ultra-high vacuum chamber, new magnetic trap coils, the components required to perform forced evaporative cooling in an optically plugged magnetic quadrupole trap and in a single-beam, and subsequently crossed, optical dipole trap as well as the implementation of an experimental control.

Chapter 3 – Sub-Doppler laser cooling of alkalines on the D_1-transition

This chapter reports on a central scientific result during my thesis work, namely a novel optical molasses scheme for simultaneous sub-Doppler laser cooling of fermionic ^{6}Li and ^{40}K implemented on the D_1 line transition. This cooling strategy is in principle suitable for all alkali atoms, relies on gray optical molasses and yields phase-space densities on the order of 10^{-4} for both ^{6}Li and ^{40}K. First of all, we will motivate the necessity of implementing a sub-Doppler cooling stage in our setup and introduce the main performance numbers of the D_1 molasses scheme. Subsequently, we will present the published articles concerning our experimental and theoretical findings [139, 140] for ^{40}K and ^{6}Li in single species and dual-species operation.

Chapter 4 – Evaporative cooling to quantum degeneracy in magnetic and optical traps

In this chapter we present our current forced evaporative cooling approach. After briefly summarizing the main ideas behind evaporative cooling, we will describe the evaporative

cooling sequence employed for ^{40}K in a plugged magnetic quadrupole trap, the transfer into an optical dipole trap and the optical evaporation to quantum degeneracy inside a crossed dipole trap. As of this writing, we achieved a degenerate spin mixture of ^{40}K in the spin-states $|F = 9/2, m_{\mathrm{F}} = -9/2\rangle$ and $|F = 9/2, m_{\mathrm{F}} = -7/2\rangle$, counting $\sim 1.5 \times 10^5$ atoms in each of both states, with a temperature of 64 nK and $T/T_{\mathrm{F}} \simeq 0.17$.

Chapter 5 – Fundamental laser source at 1342 nm

This chapter describes in detail the design of the fundamental near-infrared laser emitting up to 6.5 W at 1342 nm. We present the thermo-optical properties of the gain medium and the available pumping schemes, and show that considering these parameters is essential for the power scaling of the laser system. The laser is based on a diode end-pumped neodymium-doped yttrium orthovanadate (Nd:YVO_4) gain medium pumped at a wavelength of 888 nm, thus reducing detrimental thermal effects. The bow-tie cavity is formed by four mirrors providing a stable, Gaussian cavity eigenmode. One convex mirror is used to pass the pumping light to the laser crystal and to compensate for the thermal lens that is induced in the laser crystal during operation. Unidirectionality of the traveling-wave ring resonator is achieved by introducing a Faraday rotator and a $\lambda/2$ wave plate. Single-longitudinal-mode operation and wavelength tuning are provided using two intra-cavity etalons.

Chapter 6 – Second harmonic generation

This chapter will present three different frequency-doubling approaches that we realized for second-harmonic generation of the available laser radiation at 1342 nm in order to obtain light at the lithium D-line transition wavelengths next to 671 nm. The first approach consists in employing a resonant enhancement cavity containing a periodically-poled potassium titanyl phosphate (ppKTP) crystal as the nonlinear medium. This technique yielded our record output power of 5.2 W at 671 nm. Furthermore, we used this all-solid-state laser source for our measurements on the D_1 sub-Doppler laser cooling of ^{6}Li. As second doubling method, we investigated intracavity-frequency doubling and achieved output powers of up to 2.1 W. The third approach uses a wavelength conversion module including a nonlinear waveguide structure. This device generates up to 2.4 W of second-harmonic light and is technically the simplest solution to be implemented.

Part I.

^{6}Li-^{40}K Experiment

2 Experimental setup

In this chapter we will present the different technical parts of the experimental apperatus associated with the Fermix experiment, while concentrating on the further developments and technical upgrades of the experimental setup that has already been described at an earlier stage in [127, 141, 142]. The main objective of this experiment is to produce mixtures of ultracold fermions containing two different atomic species, namely ^{6}Li and ^{40}K, that are simultaneously cooled down to degeneracy. Important performance goals for the experimental design are in this context the production of large atom numbers and achieving short experimental cycling times for high experiment repetition rates. Dual-species experiments have in general a higher level of complexity than the simple combination of two single-species setups. Subtle strategies need to be realized in order to meet the prerequisites of implementing certain techniques for both atomic species and to circumvent the constraints imposed by the dual-species operation. With our chosen approach we finally obtained large atom numbers for both species while reducing the complexity of the experimental setup to a minimum.

2.1. General design approach

Quantum degeneracy is reached as soon as the thermal deBroglie wavelength of the atomic wavepackages is on the same order of magnitude as the inter-particle distances. An equivalent criterion states that the phase space density (PSD) has to reach the order of unity. This means that the atoms need to be cooled down as low as possible while remaining confined in a trap that should be as tight as possible. In order to meet these goals we follow the common pathway to quantum degeneracy, which consists in a first laser cooling stage followed by a further stage of forced evaporative cooling.

The laser cooling stage is provided by two techniques, a magneto-optical trap (MOT), see Section 2.6, and a gray optical molasses, presented in Chapter 3. The MOT is simultaneously loaded with both atomic species via two distinct and continuous beams of pre-slowed atoms. This loading method is advantageous for several reasons. Firstly, in contrast to loading from a background vapor, the MOT can be operated in an ultra-high vacuum (UHV) environment, see Section 2.2. Secondly, the atomic beam flux and consequently the MOT loading rate are larger than for pulsed loading schemes using alkali getter dispensers [143] or employing ultraviolet light-induced absorption [144, 145]. Finally, we are able to utilize distinct sources for both species employing even different pre-cooling techniques, namely a Zeeman slower for ^{6}Li, presented in Section 2.4, and a 2D-MOT for ^{40}K, see Section 2.5. Subsequent to the MOT

loading phase, a three dimensional gray optical molasses is performed cooling the atoms of both species down to sub-Doppler temperatures.
The cloud is then magnetically transported to an ultra-high vacuum glass cell, see Section 2.9 and [146]. The improved vacuum quality leads to a longer lifetime of the trapped atoms and therefore a higher efficiency of the evaporative cooling process can be achieved. During a first phase, evaporative cooling induced by driving radio-frequency (RF) transitions in an optically plugged magnetic quadrupole trap is performed. The use of a magnetic quadrupole trap has the advantage of offering large optical access in comparison to other magnetic traps designs. It combines a large trapping volume with tight linear confinement and thus offers the conditions for fast evaporation dynamics. The RF evaporation is performed with ^{40}K being prepared in three different spin states, whereas ^{6}Li in its single spin state is cooled sympathetically.
Subsequently, the pre-cooled, dense atomic cloud is loaded into an optical dipole trap, where we continue to increase the phase space density of the atoms by means of optical evaporation and varying trap geometries, as presented in Chapter 4.

2.2. Vacuum chamber

Figure 2.1 shows a 3D-CAD scheme of our vacuum assembly. The design of our vacuum chamber was optimized in order to provide ultra-high vacuum and a large optical access to the region, the so-called science cell, in which the experiments with quantum degenerate atoms ultimately take place. The vacuum assembly includes two branches for the atom sources, namely the ^{6}Li Zeeman slower and the ^{40}K 2D-MOT, the octagonal MOT-chamber containing the ^{6}Li-^{40}K dual-species MOT, a magnetic transport arm with a 90° elbow, and the science cell, where the measurements on ultracold quantum gases are performed.
The MOT-chamber can be separated from the transport and atom source branches by the integrated all-metal vacuum valves, thus permitting independent bake-out procedures and technical interventions. Differential pumping tubes between the vapor regions of the atom sources and the MOT-chamber were installed in order to improve the vacuum quality inside the MOT-chamber considerably. A further differential pumping stage in the first arm of the transport contains a tube with inner diameter of 1 cm, allowing to increase the vacuum quality in the transport and science cell by another order of magnitude. To pump the MOT-chamber we use a 40 l/s ion pump and an active getter tape (SAES, St 707 strips) that both were installed opposite the Zeeman slower branch. The 2D-MOT and Zeeman slower branches are pumped by one and three 20 l/s ion pumps, respectively. We installed a new vacuum assembly for the transport arm consisting of CF16 vacuum parts replacing completely the setup described in [141]. In particular, the transport tubes and the science cell are now pumped by a 40 l/s ion pump, that is situated at the elbow of both magnetic transport arms, as well as by a 20 l/s ion pump and active getter tape next to the science cell. Furthermore, the tubes of the second transport arm are coated with a Titanium-Zirconium-Vanadium alloy, which is thermally activated and serves as a non-evaporable getter with high pumping speed.

The new vacuum assembly improved the vacuum quality, such that the 1/e-lifetime of ^{40}K in the science cell increased from ∼25 s, measured for the old setup, to more than 100 s, and solved thus one of the main drawbacks of the former experimental apparatus.

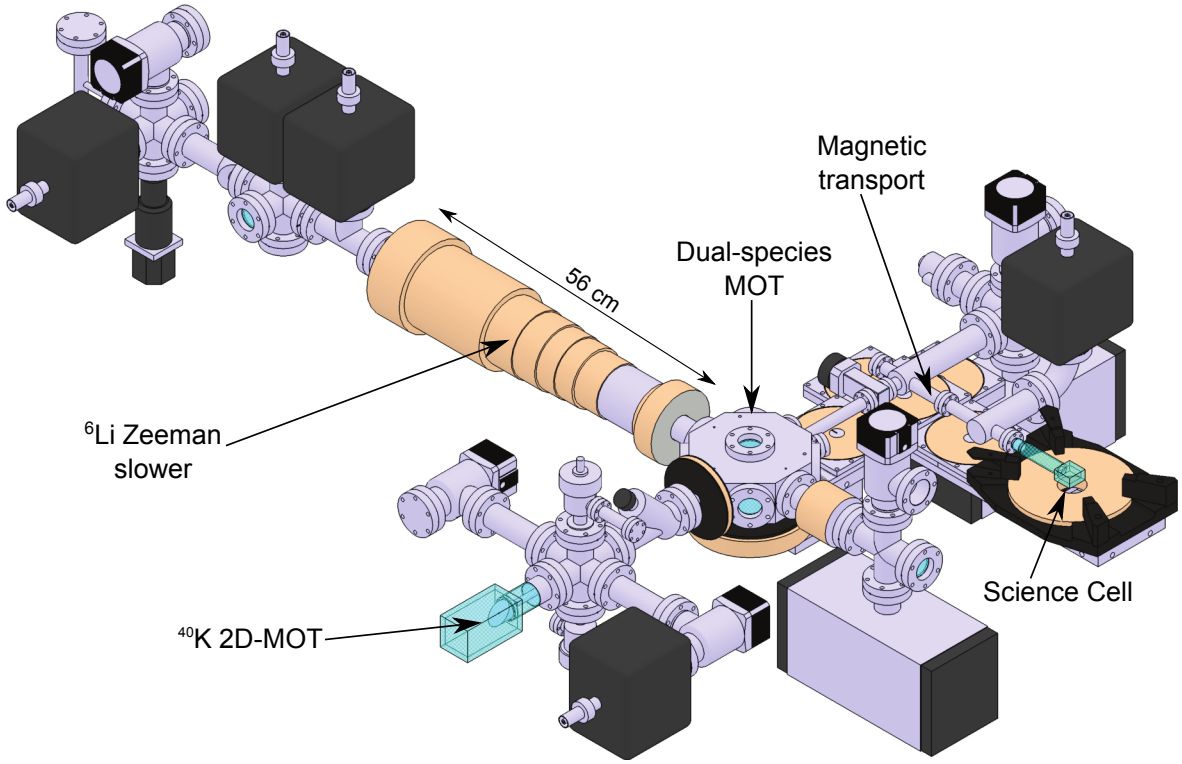

Figure 2.1: 3D-CAD model of the vacuum assembly. A Zeeman slower for ^{6}Li and a 2D-MOT for ^{40}K serve as atom sources for the dual-species MOT contained in the octagonal MOT-chamber. A magnetic transport transfers the cloud to the glass science cell featuring improved vacuum quality and large mechanical and optical access.

The glass science cell was designed to meet the requirements necessary for preparing and investigating samples of ultracold atoms. It was fabricated by Hellma and consists of Vycor, which is a synthetic fused silica. The inner dimensions of the cell are $23 \times 23 \times 10\,\mathrm{mm}^3$ and the glass walls have a diameter of 4 mm. A glass-metal junction connects the glass cell to the magnetic transport vacuum tube. The small size of the cell provides large mechanical and optical access, allowing the magnetic quadrupole coils or a future high-resolution objective to be placed close to the atoms. This permits an increased magnetic trap confinement and hence a better evaporative cooling efficiency. Furthermore, high-resolution imaging relying on an objective with large numerical aperture, becomes possible.

2.3. Laser systems

The laser systems that we realized provide light for manipulating and probing ^{6}Li and ^{40}K atoms. The laser light is applied to slow atoms down and to trap them, but also their internal degrees of freedom like the spin state can be manipulated. In this context, usually the D_2 line

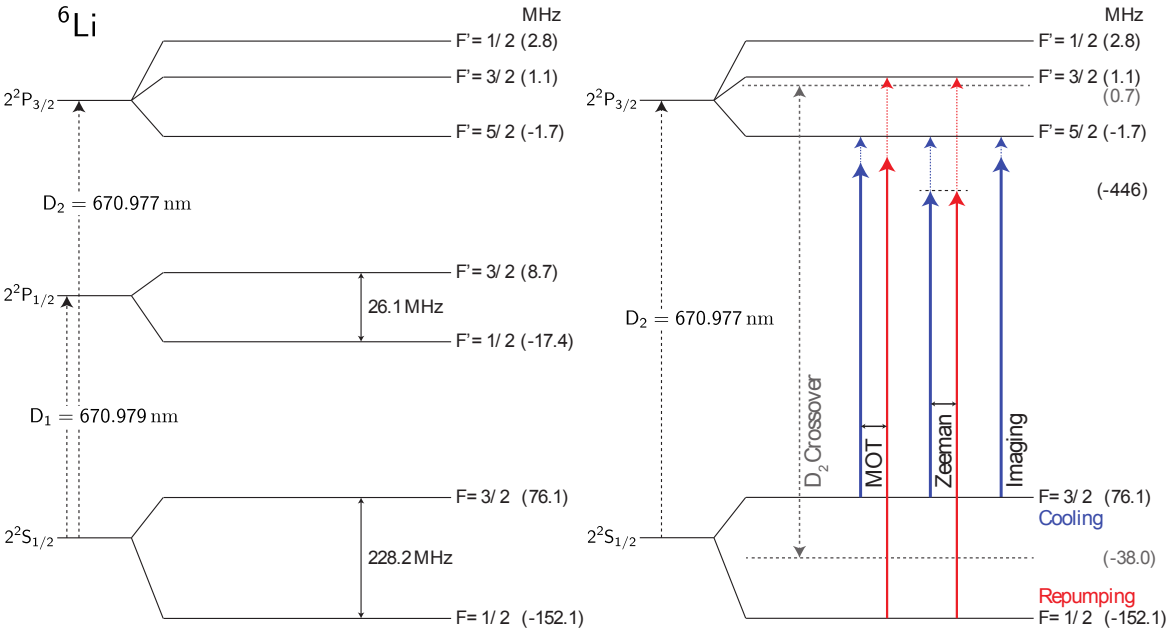

Figure 2.2: (left) Level diagram for the D_2 and D_1 lines of ^{6}Li including the hyperfine structure. The D-lines of lithium lie in the visible red spectral region. Note the small hyperfine splitting of the $2^2P_{3/2}$ manifold of ^{6}Li. (right) D_2 laser transition scheme for ^{6}Li. Solid arrows indicate the frequencies applied for the MOT operation. Dashed arrows illustrate the detunings from the corresponding transitions. The diode laser is locked to the saturated absorption crossover signal $2^2S_{1/2}$ $(|F = 1/2\rangle, |F = 3/2\rangle) \rightarrow 2^2P_{3/2}$ of ^{6}Li.

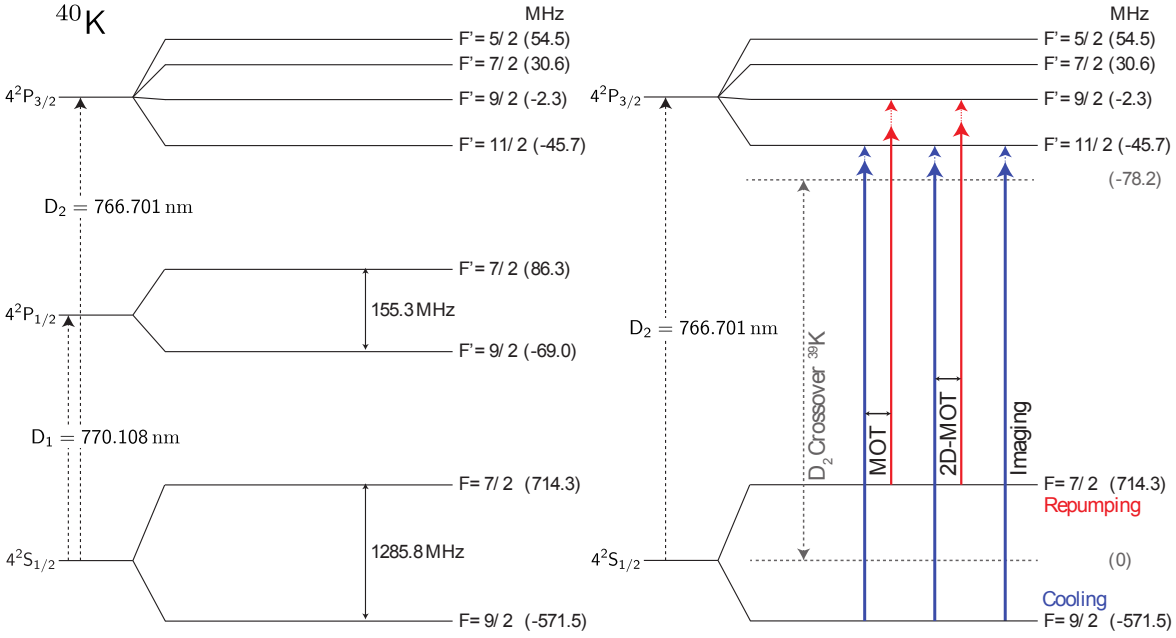

Figure 2.3: (left) Level diagram for the D_2 and D_1 lines of ^{40}K including the hyperfine structure. The D-lines of potassium lie in the visible near-infrared spectral region. Note the inverted hyperfine structure. (right) D_2 laser transition scheme for ^{40}K. Solid arrows indicate the frequencies applied for the MOT operation. Dashed arrows illustrate the detunings from the corresponding transitions. The diode laser is locked to the saturated absorption crossover signal $4^2S_{1/2}$ $(|F = 1\rangle, |F = 2\rangle) \rightarrow 4^2P_{3/2}$ of ^{39}K.

of each alkaline species is addressed. In our experiment we also exploit the D_1 line transition, namely for sub-Doppler cooling, see Chapter 3, and for spin polarization of ^{6}Li, see Section 2.8. Figure 2.2 (left) and Figure 2.3 (left) show the level diagrams corresponding to both D-line transitions of ^{6}Li and ^{40}K, respectively. Since the transition wavelengths of both species differ by $\sim$ 100 nm, distinct laser systems and optical setups are required. Additionally, several beams with different frequency shifts and intensities are required, corresponding to the different applications for each atomic species.

2.3.1. D_2 laser system

Figure 2.2 (right) and Figure 2.3 (right) illustrate the used laser frequency shifts and their application close to the D_2 lines of ^{6}Li and ^{40}K, respectively. The D_2 laser systems for

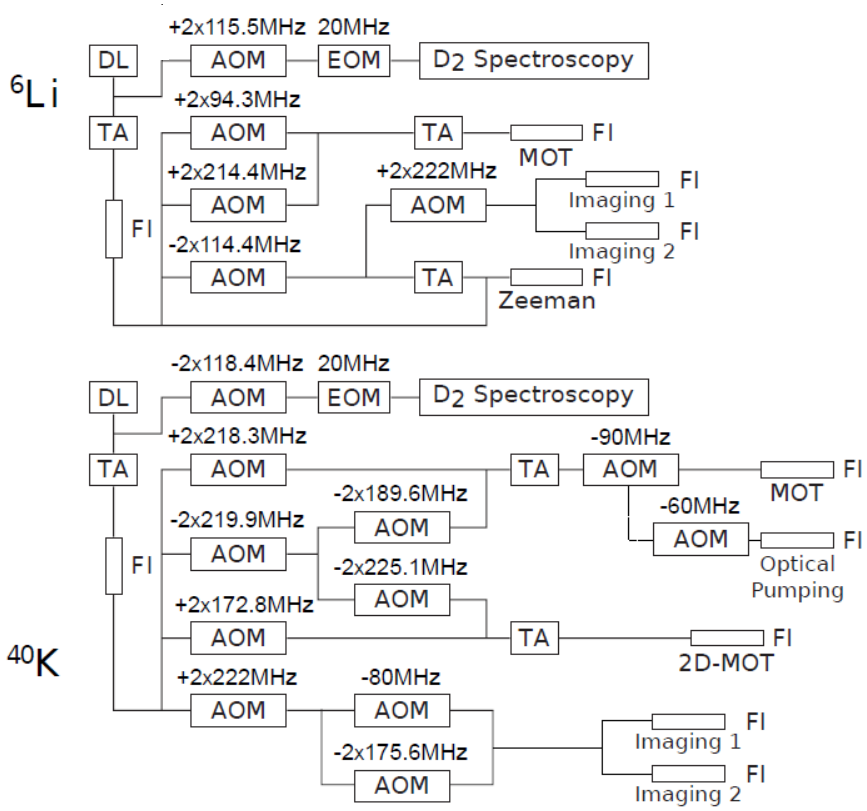

Figure 2.4: Laser systems for addressing the D_2 line tranistions of ^{6}Li and ^{40}K. The frequencies and amplitudes for the different beams are controlled by AOMs in single pass (sp) or double pass (dp) configuration. The EOMs modulate the phase of the spectroscopy beam for frequency stabilization of the diode lasers. Single-mode polarization maintaining fibers (FI) clean the beams spatially. The indicated AOM frequencies correspond to the beam frequencies required for the MOT operation, see Figures 2.2 and 2.3.

^{6}Li and ^{40}K are designed in an analogous manner. Figure 2.4 presents a simplified scheme of the realized laser systems. We constructed them on individual optical tables for each atomic species. Low power diode lasers (DL), namely a DL Pro laser from Toptica for ^{6}Li and a home made diode laser described in [141] for ^{40}K, serve as master light sources.

The laser frequencies are stabilized by means of saturated absorption spectroscopy and lock circuits acting on the tilt angle of the diode gratings. The master laser beams are amplified by tapered amplifier (TA) chips (Toptica TA-0675-0500-1 and Eagleyard EYP-TPA-0765-01500-3006-CMT03-0000) which are installed in home made mounts [141]. Subsequently, they are coupled into single-mode polarization maintaining optical fibers for the purpose of mode cleaning. The fiber output powers are split up by a combination of $\lambda/2$ waveplates and polarizing beam splitters into the different laser beams required for the experiment. Acousto-optical modulators (AOMs) are employed to shift the frequencies and to control the intensities of these beams. The cooling and repumping beams are superimposed and injected into the TAs with orthogonal polarization. As a result the TAs deliver linearly polarized bichromatic output beams, containing both the cooling and repumping frequencies. However, the injection of a TA with two different frequencies creates sidebands due to non-linearities [147]. Fortunately, the power losses are in our case negligible, being on the order of $\sim 5\%$ for ^{6}Li and $\sim 0.2\%$ for ^{40}K. Furthermore, these sidebands do not address undesirable transitions. Yet there is one exception concerning one of the sidebands of the bichromatic Zeeman slower beam. Since this sideband would be near-resonant with the ^{6}Li atoms trapped in the MOT, we solely amplify the Zeeman cooling beam and combine it with the repumping beam only after the Zeeman TA. All generated laser beams are finally injected into single-mode polarization maintaining fibers leading to the main experimental table.

2.3.2. D_1 laser system

Figure 2.5 presents the level schemes corresponding to the D_1 line transitions of ^{6}Li and ^{40}K, together with the molasses beams driving these transitions. The AOMs of the D_2 systems cannot be employed for shifting to the D_1 wavelengths, since they operate only in the range of hundreds of MHz, see Figure 2.4. However, the frequencies of the D_1 and D_2 lines for ^{6}Li and ^{40}K, are separated by $\sim 10\,\mathrm{GHz}$ and $\sim 11\,\mathrm{THz}$, respectively, see Figure 2.2 and 2.3. Therefore two additional laser systems were required for the implementation of the D_1 sub-Doppler cooling scheme in our experimental setup.

The D_1 laser systems for ^{6}Li and ^{40}K are presented in Figure 2.6. For both setups the frequency-lock point can be shifted by tuning the double-pass AOM in the path of the saturated absorption spectroscopy.

For the ^{40}K D_1 system, the repumping frequency is generated by an electro-optic modulator (EOM). In general, a EOM creates two sidebands separated from the original carrier frequency by the modulation frequency of the EOM. In our case the sideband with the lower frequency constitutes the repumping component. The power loss due to the unused second sideband can be neglected, since only low modulation amplitudes are required for the D_1 cooling scheme operating with relatively low repumping power. Furthermore, this second sideband does not address the atoms by exciting unwanted transitions.

The source for the ^{6}Li D_1 molasses light was, at least for for the experimental studies presented in Chapter 3, a home-made all solid-state laser (SSL), whose design and characterization are

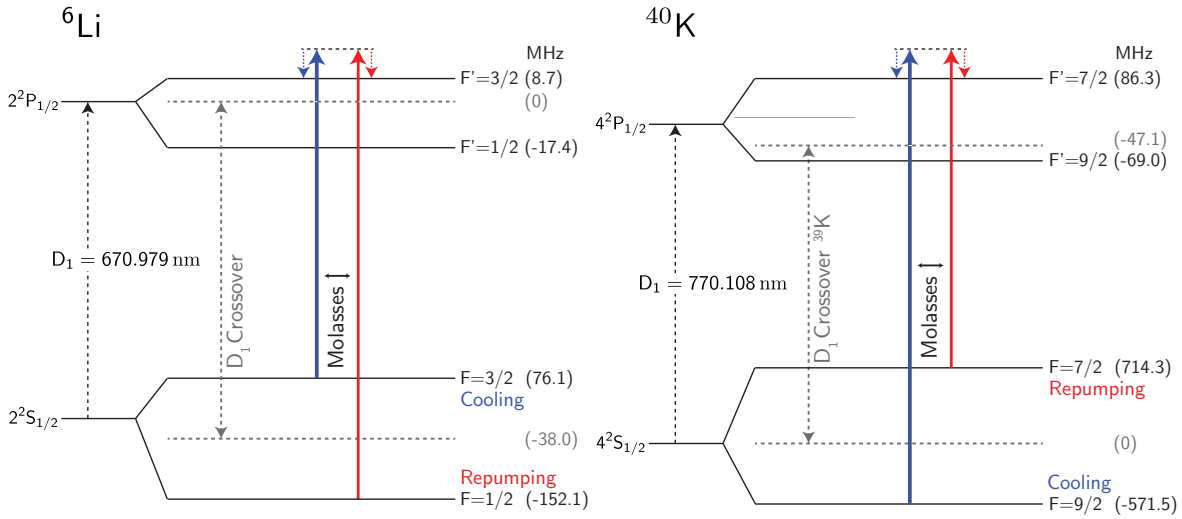

Figure 2.5: Level schemes corresponding to the D_1 line transitions of ^{6}Li and ^{40}K, as presented in [148]. Solid and dashed arrows illustrate the frequencies and detunings required for the sub-Doppler cooling, respectively. The lasers are frequency locked to the saturated absorption crossover signals $2^2S_{1/2}$ ($|F=1/2\rangle, |F=3/2\rangle$) $\rightarrow 2^2P_{1/2}$ of ^{6}Li and $4^2S_{1/2}$ ($|F=1\rangle, |F=2\rangle$) $\rightarrow 4^2P_{1/2}\,|F'=2\rangle$ of ^{39}K. The D_1 sub-Doppler cooling is presented in Chapter 3.

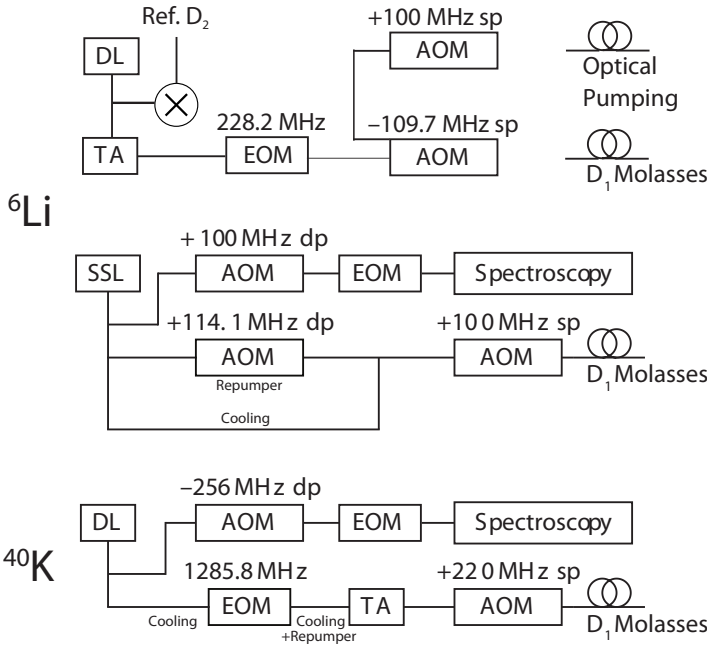

Figure 2.6: Laser systems of the D_1 molasses cooling schemes for ^{6}Li and ^{40}K. The frequencies and amplitudes of the various beams are controlled by AOMs in single pass (sp) or double pass (dp) configuration. EOMs creates the repumping frequency in the ^{40}K setup and in the diode laser (DL) ^{6}Li setup. The EOMs in the spectroscopy phase modulate a sample of the beam for the frequency-lock of the lasers. Single mode polarization maintaining fibers transmit the beams to the main experimental table. The indicated AOM frequencies correspond to the beam frequencies required for the molasses cooling, see Figure 2.5.

presented in Part II. Its high power output of 5.2 W allowed us to employ a flexible setup for the characterization of the D_1 molasses. In particular, we could scan the power and frequency of the repumping component independently from the cooling component.
To operate the ^{6}Li molasses on a daily basis, it is however sufficient to use a 500 mW master oscillator power amplifier (MOPA) setup based on semiconductor laser sources. It consists of a master diode and a tapered amplifier (TA). As for ^{40}K, the repumping frequency component is generated with an EOM. Reasonable atom transfer efficiencies from the compressed MOT (CMOT) to the D_1 molasses are achieved with the available power of $P_{\mathrm{MOPA,fiber}} \sim 150$mW after the optical fiber, as long as an appropriately small beam diameter of the molasses beams is chosen for reaching the required intensities, see Chapter 3.

2.4. ^{6}Li Zeeman slower

The atom source of the ^{6}Li-MOT is a Zeeman slower [149, 150]. It includes an oven, producing a thermal beam of ^{6}Li atoms, an assembly of magnetic field coils and a laser beam counter-propagating the atomic beam. The counter-propagating laser beam need to be kept close to the atomic resonance along the entire length of the slower in order to provide a continuous deceleration. The changing Doppler shift of the decelerating atoms has therefore to be compensated by a corresponding Zeeman shift, which is induced by the spatially varying magnetic field of the coil assembly. A sign-changing field Zeeman slower was implemented

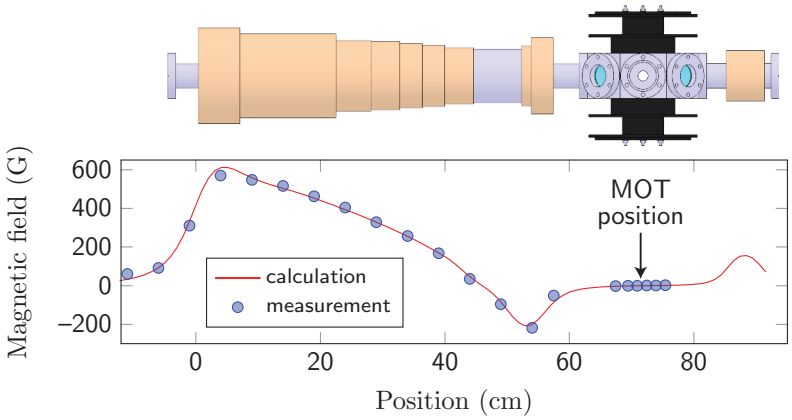

Figure 2.7: Coil assembly of the ^{6}Li Zeeman slower (top) and generated axial magnetic field profile (bottom), as presented in [141] and illustrated in [148]. The thermal atom beam produced by the ^{6}Li-oven enters the coil assembly at position 0, and a fraction of the atoms is decelerated and finally captured in the ^{6}Li-MOT, which is located at position 71.4 cm. A compensation coil, called anti-Zeeman coil, is located on the opposite side of the MOT chamber (at position 84.1 cm) ensuring that the magnetic field at the position of the MOT is cancelled. The whole coil assembly extends over 55 cm.

because of certain advantages in comparison to a positive-field Zeeman slower. In particular, the applied laser beam is non-resonant with the ^{6}Li-MOT atoms, the magnetic field maximum is reduced, and it needs less coil windings close to the MOT, improving thus the optical

access. However, a small amount of repumping light is then needed due to the region with changing magnetic field sign.
At this point we only review the most crucial parameters and performance values of our ^{6}Li Zeeman slower. A detailed characterization was presented in [141]. Figure 2.7 illustrates the coil assembly and the generated axial magnetic field profile of the Zeeman slower. The ^{6}Li-MOT is situated 71.4 cm away from the entry point of the slower. The compensation coil placed at 84.1 cm is supposed to cancel the magnetic field at the MOT position. The optimal parameters of the Zeeman slower are summarized in Table 2.1. With the oven heated to ~ 500°C, we obtain a ^{6}Li-MOT capture rate of $\sim 1.2 \times 10^9$atoms/s.

^{6}Li Zeeman slower	
P_{fiber} [mW]	50
$\Delta\omega_{\text{slow}}$ [Γ]	-75
$\Delta\omega_{\text{rep}}$ [Γ]	-75
$I_{\text{rep}}/I_{\text{slow}}$	1/8
B_{max} [G]	570

Table 2.1. – Optimal values for the ^{6}Li Zeeman slower parameters. $\Delta\omega_{\text{slow}}$ and $\Delta\omega_{\text{rep}}$ correspond to the detunings of the slowing and repumping beams, respectively. The natural linewidth of ^{6}Li is $\Gamma/(2\pi) = 5.87$ MHz. An oven temperature of ~ 500 °C leads to a ^{6}Li-MOT capture rate of $\sim 1.2 \times 10^9$ atoms/s.

2.5. ^{40}K 2D-MOT

A two-dimensional magneto-optical trap (2D-MOT) serves as atom source for our ^{40}K 3D-MOT. A 2D-MOT is a high flux cold atom source, that was realized for rubidium [151–153], potassium [154], cesium [155] and lithium [156]. Even though the atom fluxes generated by Zeeman slowers are generally higher, they are also sources of magnetic fields and hot atom jets in the MOT region. In comparison, 2D-MOTs have a more compact design and can be operated at lower temperatures, being thus more economic with regard to sample consumption. This is an important point for fermionic potassium, since the 4% enriched ^{40}K samples that we use are quite expensive. In addition, the 2D-MOT separates the ^{40}K isotope from the more abundant ^{39}K, since only the ^{40}K atoms are cooled and form the atomic beam, thus reducing the thermal background considerably.

2.5.1. Principle of a 2D-MOT

A 2D-MOT captures atoms from a background vapor, confines and cools them in the transversal directions, and out-couples a pre-cooled atomic beam in the axial direction passing through a differential pumping tube. At the same time this tube serves as a velocity filter, resulting in a transversally and longitudinally cold atomic beam arriving in the 3D-MOT chamber. Additional axial molasses cooling significantly increases the output flux of a 2D-MOT [151], since the atoms are hold in the transverse cooling region for a longer time. In our old setup we

employed two independent, counter propagating, axial molasses beams, labelled axial+ and axial- in Figure 2.8, injected by means of a 45°-angled mirror inside the vacuum chamber. For the upgraded setup we added an independent pushing beam, out-coupling the atomic beam more efficiently through the small hole in the center of the 45°-angled mirror.

2.5.2. Experimental setup

The central part of the 2D-MOT vacuum assembly consists of a glass cell with dimensions $110 \times 55 \times 55\,\mathrm{mm}^3$ illustrated in Figure 2.8. A polished stainless steel 45°-angled mirror is attached to the differential pumping tube inside the vacuum chamber. It has a reflectivity of 50% and is chemically inert to potassium exposure. The distance between the centers of the 2D- and 3D-MOT is 55 cm and the pressure ratio between the corresponding vacuum regions is $\sim 10^3$.

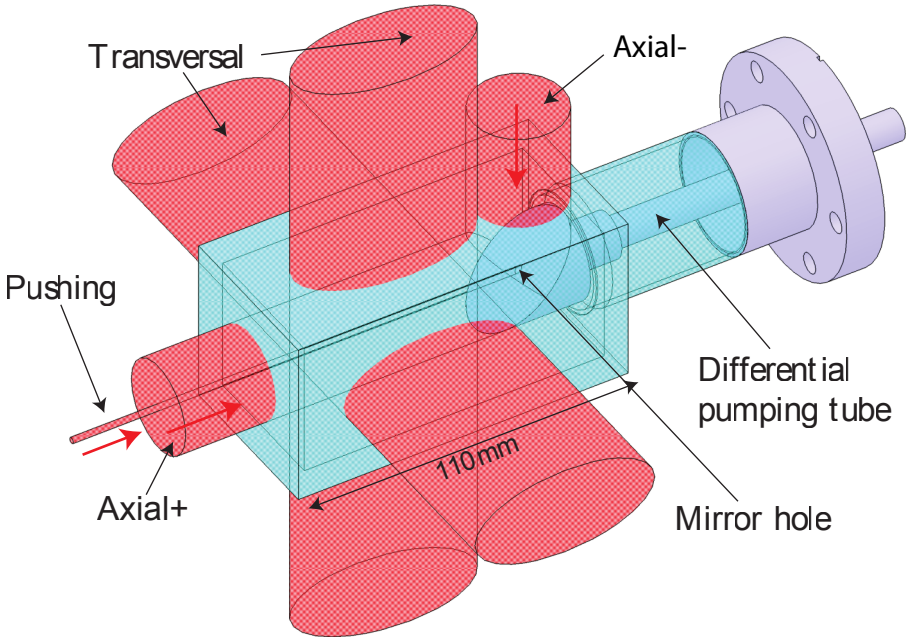

Figure 2.8: Scheme of the ^{40}K 2D-MOT and illustration of the light beams. The elliptic beams transversally cool the atoms. The alignment of the axial molasses beam pair is provided by a 45°-angled mirror placed inside the vacuum chamber. The pushing beam axially out-couples an atomic beam through the mirror hole. The optimal beam parameters are given in Table 2.2.

The potassium sample, which is enriched to 4% of ^{40}K, is situated at a cold point next to the glass-metal junction of the glass cell, see page 21. The cold point is created by a water cooled plastic tube that was winded around this point, see Figure 2.9. The temperature of the cold point is regulated by a water chiller and can be varied in order to set an appropriate potassium pressure in the glass cell. Usually we work at a cold point water temperature of ~ 40°C, corresponding to a total potassium pressure of $\sim 2 \times 10^{-7}$mbar and a partial ^{40}K pressure of $\sim 1 \times 10^{-8}$mbar.

The bichromatic laser beam used for the 2D-MOT has a total power of $P_{\mathrm{fiber}} = 350\,\mathrm{mW}$ at the fiber output. The frequency of the cooling component is red-detuned by $\sim 3.5\Gamma$ from the

$|F = 9/2\rangle \rightarrow |F' = 11/2\rangle$ transition whereas the frequency of the repumper component is red-detuned by $\sim 2.5\Gamma$ from the $|F = 7/2\rangle \rightarrow |F' = 9/2\rangle$ transition, see Figure 2.3. This beam is split up into five beams, two transverse and three axial 2D-MOT beams, see Figure 2.8. The beams are circularly polarized and expanded by spherical and/or cylindrical telescopes. The transverse beams are expanded to an elliptical shape with $1/e^2$-diameters of 27.5 mm and 55 mm. They are retro-reflected by right-angled prisms, such preserving their polarization helicity. The axial cooling beams have a round shape with a $1/e^2$-diameter of 27.5 mm, whereas the $1/e^2$-diameter of the pushing beam is 3.8 mm. 87% of the fiber output power is utilized for the transverse cooling beams, 11% for the axial cooling beams and 2% for the pushing beam. A racetrack coil geometry is employed to create a two dimensional quadrupole magnetic field with cylindrical symmetry around the horizontal 2D-MOT axis where the magnetic field is zero. The optimum for the magnetic field gradients was found to be $\partial_x B = \partial_y B = 11\,\mathrm{G/cm}$. A summary of the optimal values for the essential 2D-MOT parameters is given in Table 2.2. Using these parameters yields a ^{40}K-MOT loading rate of $\sim 3 \times 10^8$ atoms/s.

^{40}K 2D-MOT	
P_{fiber} [mW]	350
$\Delta\omega_{\mathrm{cool}}$ [Γ]	-3.5
$\Delta\omega$rep [Γ]	-2.5
$I_{\mathrm{rep}}/I_{\mathrm{cool}}$	0.5
$I_{\mathrm{trans}+}/I_{\mathrm{trans}-}$	2.4
P_{push} [mW]	8.6
$\partial_x B$, $\partial_y B$ [G/cm]	11
K vapor Pressure [mbar]	2.3×10^{-7}

Table 2.2. – Optimal values for the parameters of the ^{40}K 2D-MOT, resulting in a ^{40}K MOT loading rate of 3×10^8 atoms/s. The definitions of the symbols are given in the text. The natural linewidth of ^{40}K is $\Gamma/(2\pi) = 6.04$ MHz.

2.5.3. Characterization of the 2D-MOT upgrade

The performance of the 2D-MOT can be characterised by measuring the loading rate of the ^{40}K-MOT as a function of the 2D-MOT parameters that are at our disposal. The impact of several parameters, as for example the light intensity ratios, frequency detunings and the vapor pressure in the 2D-MOT cell, have already been studied in [141]. In the following we concentrate on the improvements that have been made on the 2D-MOT setup, namely the new approach to control the pressure in the 2D-MOT glass cell and the implementation of an additional pushing beam whose intensity can be controlled independently.

Cold point

Figure 2.9 illustrates the vacuum assembly of the 2D-MOT. In the old setup the potassium sample was situated in a CF16 bellow 20 cm away from the glass cell. In this bellow a small

ampoule with the isotopically enriched potassium sample had been broken under vacuum. Overheating of this source region caused the potassium sample to migrate to other regions of the vacuum assembly and depleted the old source completely. In order keep the ability to control the potassium vapor pressure, a cold point was created near the glass cell to serve as a new accumulation region for the sample. A water cooled plastic tube is encompassing the glass tube of the 2D-MOT cell, see Figure 2.8. A chiller regulates the water temperature which allows to control the cold point temperature. In the current setup the old source region is heated to $\sim 120°C$, the glass cell to $\sim 80°C$ and all other parts, except for the cold point, to at least 100°C. During operation of the 2D-MOT we set the cold point water temperature to 40°C. Otherwise, it is cooled down to 12°C in order to re-accumulate potassium crystals.

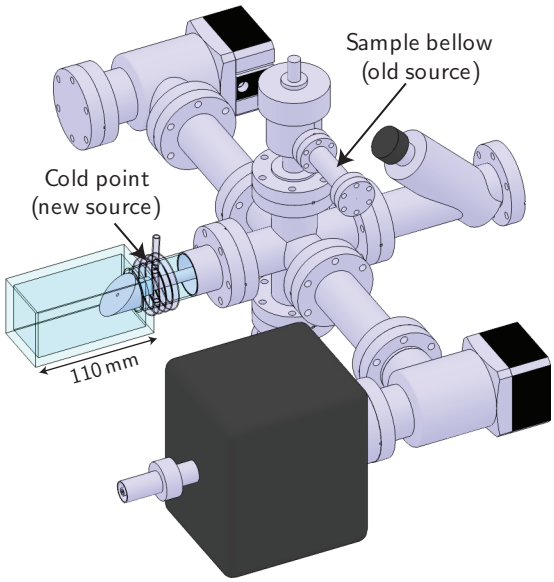

Figure 2.9: The ^{40}K 2D-MOT vacuum assembly. The cold point serves as new potassium source, since the bellow originally containing the sample became depleted. The old source region is heated to $\sim$ 120°C, the glass cell to $\sim$ 80°C and all intermediate parts to at least 100°C to establish a temperature gradient. The cold point water temperature can be regulated by means of a chiller in order to control the 2D-MOT pressure, see Figure 2.10.

The actual vapor pressure of potassium can be determined by a measurement of the resonance absorption profile of a low intensity probe beam that is passed through the 2D-MOT cell over a path length of 10.5 cm, see Appendix A of [141] for a detailed description. Figure 2.10 present the dependence of the 3D-MOT loading rate and the 2D-MOT pressure on the cold point water temperature. A cold point water temperature of 40°C results in to a total potassium pressure of $\sim 2 \times 10^{-7}$mbar, corresponding to a partial pressure of $\sim 1 \times 10^{-8}$ mbar for ^{40}K.

Additional pushing beam

In order to increase the flux of the 2D-MOT an independent pushing beam was added whose $1/e^2$-diameter of 3.8 mm approximately fits the size of the mirror hole, see Figure 2.8. This additional beam offers a further parameter for optimization of the atomic beam out-coupling

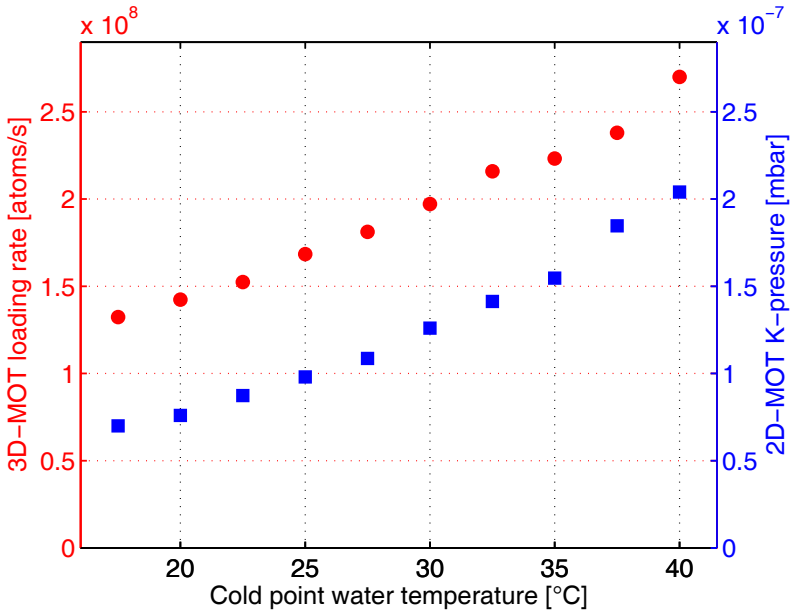

Figure 2.10: ^{40}K 3D-MOT loading rate (red circles) and total potassium 2D-MOT pressure (blue squares) as a functions of the cold point water temperature. The pressure is deduced from the absorption of a weak probe beam which is resonant with the D_2 transition of ^{39}K and passes through the 2D-MOT cell.

and the related axial 2D-MOT molasses. As a consequence, the power of the axial molasses beams could be reduced from 90mW to 40mW, thus allowing for higher transversal beam powers. In comparison to the old setup, meaning the optimized 2D-MOT setup without independent pushing beam, we were able to increase the flux of the 2D-MOT measured via the 3D-MOT loading rate by a factor of two. The best performance was achieved using a circularly polarized pushing beam and a longitudinal molasses in σ^+–σ^- configuration, whereas the old setup employed a lin⊥lin configuration. Figure 2.11 presents the dependence of the 3D-MOT loading rate on the pushing beam power. For this measurement, the powers of the other 2D-MOT beams were kept constant. The maximal loading rate was found to be $\sim 3 \times 10^8$ atoms/s for $P_{\mathrm{push}} = 9\,\mathrm{mW}$.

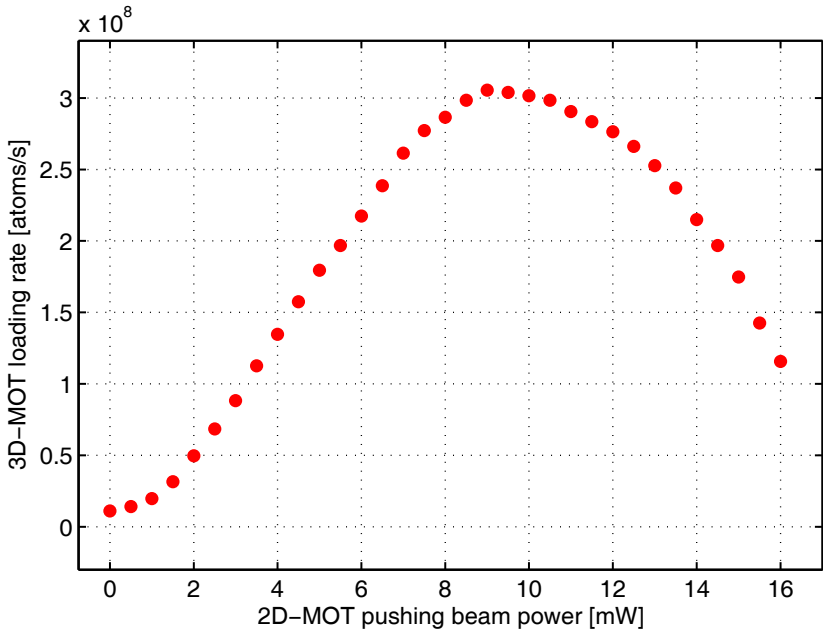

Figure 2.11: 3D-MOT loading rate as a function of the 2D-MOT pushing beam power. The maximal loading rate of $\sim 3 \times 10^8$ atoms/s was found for $P_{\mathrm{push}} = 9\,\mathrm{mW}$.

2.6. ^{6}Li-^{40}K dual-species MOT

This section deals with the technical implementation and performance of the ^{6}Li-^{40}K dual-species MOT. A magneto-optical trap relies on the combination of a magnetic quadrupole field with three orthogonal pairs of counter-propagating red-detuned laser beams leading to cooling and magneto-optical confinement of atoms around the magnetic field zero [150]. For both ^{6}Li and ^{40}K, bichromatic MOT beams with a cooling and repumping frequency component are needed. The repumping component is in general required for all alkali atoms and ensures that the atoms are kept in the nearly cycling cooling transition. In particular ^{6}Li atoms very likely leave the cooling transition due to the very narrow hyperfine structure of the excited-state. Thus the relatively large repumping component even contributes to the cooling of ^{6}Li. For a dual-species MOT it is crucial to minimize light-induced interspecies collisions, since they lead to atom losses. We were able to limit these losses to less than 10%, by employing low magnetic field gradients and relatively low repumping light intensities for both atomic species, as detailed in [127].

2.6.1. Experimental setup

The ^{6}Li-^{40}K dual-species MOT requires a bichromatic laser beams for each species. Both beams are transferred onto the main experimental table via optical fibers. The optical setup, superimposing and expanding the MOT beams, is presented in Section 2.7.2 and Figure 2.12. We note that the MOT beams have a $1/e^2$-diameter of 22 mm.

The fiber output power of the bichromatic beam forming the ^{6}Li-MOT is $P_{\text{fiber,Li}} = 110$mW. The cooling frequency is red-detuned by $\sim 5\Gamma$ from the $2^2S_{1/2}\,|F = 3/2\rangle \rightarrow 2^2P_{3/2}\,|F' = 5/2\rangle$ transition whereas the repumping frequency is red-detuned by $\sim 3\Gamma$ from the $2^2S_{1/2}\,|F = 1/2\rangle \rightarrow 2^2P_{3/2}\,|F' = 3/2\rangle$ transition, see Figure 2.2. The power ratio of the cooling/repumping components is ~ 5.

The fiber output power of the ^{40}K-MOT beam is $P_{\text{fiber,K}} = 220\,\text{mW}$. In this case, the cooling frequency is red-detuned by $\sim 3\Gamma$ from the $4^2S_{1/2}\,|F = 9/2\rangle \rightarrow 4^2P_{3/2}\,|F' = 11/2\rangle$ transition and the repumping frequency is detuned by $\sim 5\Gamma$ from the $4^2S_{1/2}\,|F = 7/2\rangle \rightarrow 4^2P_{3/2}\,|F' = 9/2\rangle$ transition, see 2.3. The power ratio of the cooling/repumping components is with ~ 20 significantly larger than for ^{6}Li.

The MOT magnetic field is a quadrupole field generated by a pair of water cooled coils in anti-Helmholtz configuration. The coils have a distance of ∼6.5 cm to the trap center and generate an magnetic field gradient of 0.94 G/cm A along the symmetry axis. Accordingly, the transverse magnetic field gradient is smaller by a factor 2. The dual-species MOT is operated at $\partial_z B = 8$G/cm, this value optimizing the achievable atom numbers of the ^{40}K-MOT.

In Table 2.3 we summarize the optimal parameter settings for the ^{6}Li-^{40}K dual-species MOT. Dual-species operation of the MOT yields $\sim 2 \times 10^9$ ^{6}Li atoms at $\sim$ 1mK and $\sim 3 \times 10^9$ ^{40}K atoms at $\sim 240\mu$K corresponding to a phase space density on the order of 10^{-7} for both atomic species.

	^{40}K-MOT	^{6}Li-MOT
$\Gamma/(2\pi)$ [MHz]	6.04	5.87
I_{sat} [mW/cm^2]	1.75	2.54
P_{fiber} [mW]	220	110
$\Delta\omega_{\text{cool}}$ [Γ]	-3	-5
$\Delta\omega_{\text{rep}}$ [Γ]	-5	-3
I_{cool} per beam [I_{sat}]	12	4
$I_{\text{cool}}/I_{\text{rep}}$	20	5
$\partial_z B$ [G/cm]	8	8
N_{single} [$\times 10^9$]	3.5	2.1
N_{dual} [$\times 10^9$]	3.2	2
n_0 [$\times 10^{10}$cm^{-3}]	7	2.6
T [μK]	240	1000
ϕ [$\times 10^{-7}$]	2	3

Table 2.3. – Optimal parameter settings for and properties of the ^{6}Li-^{40}K dual-species MOT. T designates the temperature of the atomic ensemble and n_0 the peak atomic density in the center of the trap. $\phi = n_0\lambda_B^3$ corresponds to the peak phase-space density, with the thermal de Broglie wavelength defined as $\lambda_B = \sqrt{2\pi\hbar/mk_BT}$. Here, the given value does not take into account the occupation of different internal states.

2.7. CMOT and gray molasses cooling

The phase-space density of the ^{6}Li-^{40}K mixture is increased after the MOT-phase by applying a compressed MOT phase (CMOT) succeeded by an optical molasses phase. First, the CMOT phase compresses the atomic samples and enhances therefore their densities, then the D_1 molasses phase cools them further down to deep sub-Doppler temperatures. In the following we describe the implementation of the ^{6}Li-^{40}K dual-species molasses beams in the setup of the main experimental table. The comprehensive characterization of this cooling technique is presented in Chapter 3.

2.7.1. Compressed MOT

In order to increase the density of the atomic clouds trapped in the MOT we apply a so-called compressed MOT phase. For this purpose, the magnetic field gradient is linearly ramped from 8 G/cm to 45 G/cm within 5 ms. Simultaneously the MOT beam intensities are reduced, while the frequencies of both the cooling and repumping components are tuned closer to resonance. For ^{6}Li this leads to a density increase from 2.6×10^{10} at./cm^3 to 1.8×10^{11} at./cm^3 and the temperature decreases from 1 mK to 800 μK. For ^{40}K the density increases from 7×10^{10} at./cm^3 to 3.7×10^{11} at./cm^3, while the temperature also increases from 240 μK to 2 mK.

2.7.2. Implementation of the D_1 molasses

The D_1 molasses beams were implemented in the main experimental setup by superimposing the molasses beams with the 3D-MOT beams. The total power of the bichromatic fiber output is $P_{\text{fiber,Li}} = 150$mW for the ^{6}Li molasses and $P_{\text{fiber,K}} = 200$mW for the ^{40}K molasses. In Figure 2.12 we illustrate how the two molasses beams for ^{6}Li and ^{40}K, which are emitted from the optical fiber outputs labeled $D_{1,\text{Li}}$ and $D_{1,\text{K}}$, are nearly superimposed with the 3D-MOT light via the D-shaped mirrors M_D.
The lithium and potassium beams are subsequently combined at a dichroic mirror M_{dichroic}. This beam, that finally includes all MOT- and molasses frequency components, is expanded by a 1:10 lens telescope and distributed by means of polarization optics to the three pairs of σ^+–σ^- counter-propagating beams of the 3D-MOT and the D_1 molasses. The $1/e^2$-diameter of the 3D-MOT beams is $\sim$ 22mm after expansion for both ^{6}Li and ^{40}K. The $1/e^2$-diameters of the molasses beams are $\sim$ 17.1 mm and $\sim$ 17.8 mm for ^{6}Li and ^{40}K, respectively.
The two beams in the horizontal plane are retro-reflected, whereas the vertical axis is driven by two independent beams. Two $\lambda/2$ plates, one of order four for lithium ($\lambda/2^*_{\text{Li}}$), and another one of order four for potassium ($\lambda/2^*_{\text{K}}$), allow to set the ^{6}Li and ^{40}K 3D-MOT power distribution independently. This is due to the fact that each of these wave plates can, to a very good approximation, turn the polarization axis for one wavelength without affecting the polarization axis of the other one since $4.5 \times 671 \approx 4 \times 767$ and $4.5 \times 767 \approx 5 \times 671$. Finally, the 3D-MOT beams are circularly polarized using first order $\lambda/4$ waveplates specified for the

wavelength ^{40}K 767 nm. However, these waveplates perform also sufficiently well for the ^{6}Li wavelength 671 nm.

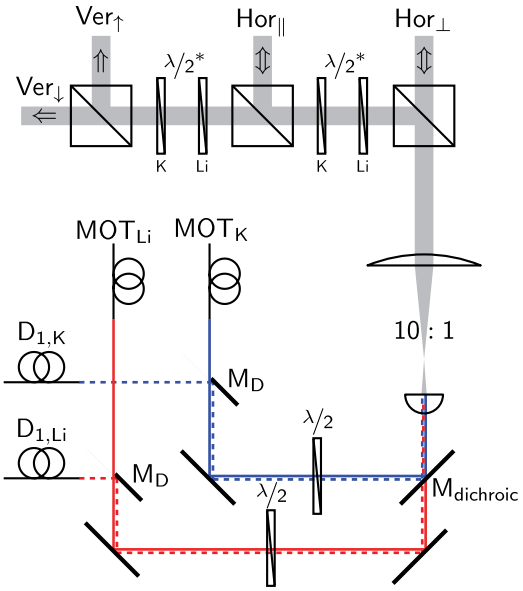

Figure 2.12: Optical scheme for the 3D-MOT and D_1-molasses beams, as presented in [148]. A D-shaped mirror (M_{D}) nearly superposes the 3D-MOT light and the D_1 molasses light for both atomic species. Subsequently, the lithium- and potassium light is combined at dichroic mirror (M_{dichroic}). The resulting beam is finally expanded and distributed to three perpendicular axes forming the 3D-MOT.

2.8. Magnetic trapping

After capturing and cooling the atomic samples by the MOT and the D_1 molasses, their phase space density needs to be further increased by means of evaporative cooling, see Chapter 4. In this context, a transfer of the atoms into a conservative trap is required. Evaporative cooling is commonly performed in magnetic traps and optical dipole traps (ODTs) which act both as non-dissipative traps. ODTs have usually only a poor transfer efficiency of loading atoms directly from a MOT due to their limited trapping volume. As first stage of the evaporation process we therefore decided to perform RF-driven evaporation inside a magnetic trap before ultimately loading the atoms into an ODT, see Chapter 4.
In the following sections we summarize the consecutive steps of magnetic trapping in our experimental sequence and characterize the technical tools, used during these stages.

Loading of the magnetic quadrupole trap

After cooling the atomic samples optically during the D_1 molasses phase, the atoms are loaded into a magnetic quadrupole trap. First, the atoms need to be prepared in magnetically trappable spin states in order to ensure an efficient transfer. Therefore optical pumping is applied, meaning that in the presence of a small bias field, a short spin polarization light

pulse is applied along the magnetic field axis. Subsequently, the magnetic trap is ramped up, the magnetic field being generated by the same coil pair as for the 3D-MOT. Due to technical restrictions, at least ∼3 ms are required to ramp up the magnetic field gradient from zero to 45 G/cm. The gradient is then linearly ramped from 45 G/cm to its final value of 145 G/cm within 500 ms.

2.9. Magnetic transport

The vacuum lifetime of the atomic samples prepared in the 3D-MOT chamber, as well as the optical access have to be increased for an efficient evaporation process and subsequent experiments. This is achieved by transferring the trapped atoms to the UHV science cell. We apply a magnetic transport technique [146] with a 90° elbow, featuring an additional optical access on the transport axis.
The magnetic transport consists of 14 coil pairs which are partly overlapping and one pushing coil. By continuously varying the currents over time, the magnetic trap center is moved over the total distance of 64 cm from the MOT chamber to the science cell.

2.10. Optically plugged magnetic quadrupole trap

After arrival in the science cell, the atomic samples undergo an evaporative cooling step driven by RF transitions in an optically plugged magnetic quadrupole trap. The optical plug repels the atoms from the trap center, where the magnetic field cancels, avoiding thus atom losses due to Majorana spin-flips. The quadrupole trap provides a steep, linear confinement, yielding high elastic collision rates, and allows therefore for efficient evaporation dynamics.

2.10.1. Coils

The magnetic quadrupole trap of the science cell is generated by a custom made coil pair manufactured by Oswald. It includes two pairs of coils, called the inner and the outer coil, see Figure 2.13. Both coil pairs are operated in anti-Helmholtz configuration during the magnetic transport sequence. As soon as the atoms have arrived in the center of the glass cell the current of the outer coil pair is slowly ramped to zero and only the inner coil pair generates the magnetic trapping potential. The entire coil consists of hollow 4 mm thick copper wire with squared cross section impregnated in epoxy. The circular hole with 2.5 mm diameter inside the wire permits permanent water cooling.
Each of the inner coils is composed of 4 layers with 12 turns per layer. The inner coil diameter is 40 mm and the outer diameter is 72 mm. Both coils are placed on the vertical axis of the science cell with a distance of 35 mm, generating an axial magnetic field gradient of 2.5 G/cm A.
The outer coils consist of 4 layers with 4 turns and have inner and outer coil diameter of 73 mm and 90 mm, respectively. In anti-Helmholtz configuration they generate an axial magnetic field gradient of 0.24 G/cm A. Operation in Helmholtz configuration provides a magnetic bias

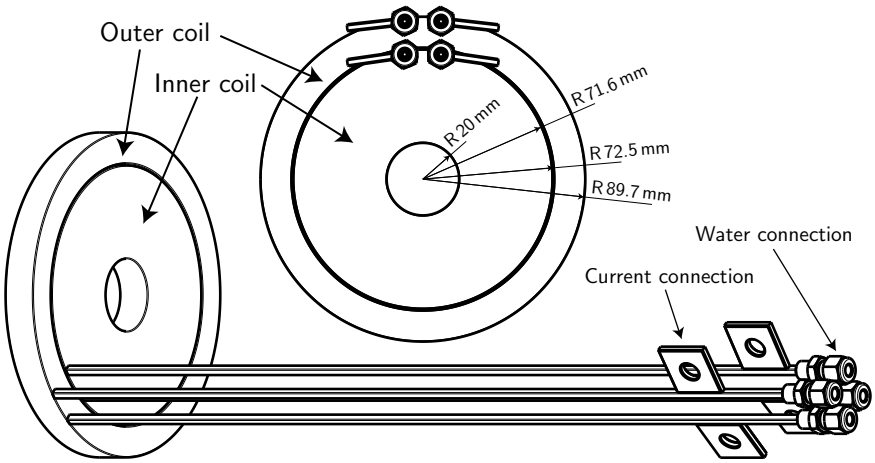

Figure 2.13: Technical drawing of the quadrupole coils which also serve as Feshbach coils (from [148]). They consist of two concentric coil pairs, an inner one and an outer one, both made of hollow copper wire impregnated in epoxy. The inner coils generate in particular the magnetic field for the optically plugged magnetic trap. They are placed at a distance of 17.5 mm from the trap center and create an axial magnetic field gradient of 2.51 G/cm A.

field of 2.2 G/A at the center of the science cell with a curvature of -0.027 G/cm^2 in the axial direction.

The coils are placed inside a stable mount consisting of a fiber-reinforced plastic material. It is attached to the transport coil assembly and provides high mechanical stability and electrical isolation, thus avoiding Eddy currents.

Fast switching of the coil currents is ensured by the implementation of insulated-gate bipolar transistors (IGBTs) which are connected in series with the coils. Varistors in parallel to their source/drain junction protect them from induction currents. The high current circuits are galvanically isolated from the IGBT computer control channels by digital opto-couplers.

2.10.2. Optical plug

Since atoms in a magnetic quadrupole trap need to be prevented from undergoing Majorana spin-flips, we implemented a far blue-detuned laser beam repelling the atoms from the trap center, where the magnetic field cancels. This suppression of Majorana losses is crucial for an efficient evaporative cooling, especially at low temperature. Historically, the first Bose-Einstein condensate was realized with Sodium in such an optically plugged magnetic trap [2].

The laser source of the plug beam is a commercial intracavity-doubled Nd:YVO_4 single mode laser (Verdi V12, Coherent) emitting up to 12 W at a wavelength of 532 nm, which is far blue detuned from the D-line transitions of both ^{6}Li and ^{40}K. A 110 MHz high-power AOM (MCQ110-A2 VIS, AA optoelectronic) is used to switch the plug beam. This AOM is driven by the signal of a voltage-controlled oscillator (VCO) which is amplified (ZHL-5W-1) to 5 W. The plug beam applied to the atoms has eventually a power of 7 W and is focused on the magnetic trap center, along one of the weak axes (y-direction) of the magnetic trap, see

Figure 2.15. Its focal waist is $\sim 20\,\mu$m, yielding a potential barrier with a height of $\sim 700\mu$K for both ^{6}Li and ^{40}K.
The position of the plug beam focus can be regulated via a motor controlled mirror mount (AG-M100N, Agilis) and a four-quadrant photodiode (2901, Newport), that monitors the position of the leaking light from a dichroic mirror, see Figure 2.15. A realignment algorithm was implemented on our control computer and allows for automatic centering of the beam on the four-quadrant photodiode. The computerized realignment ensures a stable positioning of the beam focus and compensates for pointing drifts caused by temperature fluctuations.

2.11. RF evaporative cooling

Compared to bosons, the evaporative cooling of fermions is much more problematic, since s-wave collisions between identical fermions are forbidden and thermalization can thus not take place. Due to the angular momentum barrier, p-wave collisions are furthermore suppressed in the limit of low temperatures, typically below $T \sim 6\,$mK for ^{6}Li and $T \sim 50\,\mu$K for ^{40}K [10, 157]. At low temperatures, only two different species or two different internal states can therefore provide high elastic collision rates and are able to thermalize.
Collisions between ^{6}Li and ^{40}K have several drawbacks concerning their thermalization efficiency. Firstly, their mass difference increases the thermalization time by a factor of two [67] and secondly, their collision cross section is rather modest. Collisions occur in the triplet channel and have a s-wave scattering length of $a = 64.41\,a_0$ [129], resulting in a collision cross section of $\sigma_{\mathrm{LiK}} = 1.5 \times 10^{-10}\mathrm{m}^2$.
Exclusively the stretched state of ^{6}Li is stable inside a magnetic trap, since spin relaxation takes place between different trappable spin states [158]. In the case of ^{40}K, however, spin relaxation is suppressed because of the inverted hyperfine structure [8]. The s-wave scattering length between the magnetically trappable spin states $|F, m_{\mathrm{F}}\rangle = |9/2, 9/2\rangle$ and $|9/2, 7/2\rangle$ of ^{40}K is $a \sim 170\,a_0$ [159]. The resulting collision cross section $\sigma_{\mathrm{KK}} = 1 \times 10^{-9}\mathrm{m}^2$ is thus an order of magnitude larger than σ_{LiK}.
In consequence, we apply the approach presented in [67] for the evaporation of a ^{6}Li-^{40}K mixture inside a magnetic trap. It consists in evaporating a spin mixture of ^{40}K, while sympathetically cooling a small cloud of ^{6}Li [158].
In the following we present the technical tools, applied in our experiment in order to perform RF evaporation in the plugged magnetic quadrupole trap.

2.12. RF system

In the context of RF evaporation of the ^{40}K spin mixture, we need to drive the hyperfine transitions $|9/2, 9/2\rangle \rightarrow |7/2, 7/2\rangle$, $|9/2, 7/2\rangle \rightarrow |7/2, 7/2\rangle$ and $|9/2, 5/2\rangle \rightarrow |7/2, 7/2\rangle$ to transfer the atoms in dependence on their energy to untrapped states. In a magnetic quadrupole trap, which has a linear trap potential, the frequency of the RF knife has to increases for addressing decreasing energy cut values for ^{40}K. The RF evaporation is usually performed at a magnetic

field gradient of $B'_z = 280\text{G/cm}$. For the ^{40}K RF evaporation, we require therefore frequencies ranging from $\sim 1.1\,\text{GHz}$, which results in a effective trap depth of some millikelvin, to $1.285\,\text{GHz}$, corresponding the hyperfine splitting of the ^{40}K ground states at zero field, see Figure 2.3.

The radio frequency signal for the RF evaporative cooling of ^{40}K is generated by a digital signal synthesizer (N5161A MXG ATE, Agilent), that is automatically configurated by our experimental control, see Section 2.15. Its RF signal output passes a fast switch device (ZASW-2-50DR+, Minicircuits) and a 30 W high-power amplifier (ZHL-30W-252+, Minicircuits). The output of the amplifier is protected by a circulator (RADC-800-2000M-S23-10-100WR-b, Raditek) that connects the amplifier to the antenna via its input and transmission port. The corresponding reflection port of the circulator leads to a high power -40 dB attenuator (BW-40N100W+, Minicircuits) and a $50\,\Omega$ termination (KARN-50+, Minicircuits).

In general, an antenna converts signals in the form of varying currents to electromagnetic radiation. The reflected, as well as the radiated RF power of the antenna strongly depends on the frequency of the signal to be emitted and the impedance ratio of the antenna and the feed line. Therefore, the impedance of the ^{40}K RF antenna should be approximately matched for the frequency range from 1.1 GHz to 1.285 GHz. We installed a $\lambda/2$ single-loop antenna with a diameter of $\sim$2 cm, that was chosen as half the wavelength of the RF output. The antenna is made of a Litz wire, being composed of multiple strands insulated electrically from each other. This reduces the losses caused by two effects that occur for current signals in the microwave range. First, the skin effect forces the electric current to flow mainly within a small outer layer of the conductor whose diameter is called the skin depth. Second, the proximity effect imposes constrains to the regions of current flow in conductors that are closely spaced. To match the impedance of the antenna for the targeted frequency range, we apply the stub technique similarly to [160]. In our case, a BNC cable with a loose end, integrated into the RF circuit via a T-connector, servers as a stub. The length of the BNC cable was adjusted, in order to optimize the impedance match of the antenna for the targeted frequency range. As a result, our impedance matched antenna features a low reflectivity in the entire frequency range from 1.1 GHz to 1.285 GHz.

2.13. Optical dipole trap

In our experimental sequence, the RF evaporative cooling inside an optically plugged magnetic quadrupole trap was chosen as pre-cooling stage that allows for an efficient transfer of the atoms into the optical dipole trap (ODT). Besides its strong confinement, an ODT has the advantage, that the magnetic field becomes a free parameter that can be tuned in order to increase the collision cross section of the gas in the vicinity of Feshbach resonances [27]. An ODT relies on the fact that when an atom interacts with a light field that is red(blue) detuned with respect to an atomic transition, the induced negative(positive) light shift of the atomic ground state varies spatially with the light intensity [161]. A gradient of the light intensity therefore induces a dipole force. In the case of a red-detuned light beam the atoms are thus

attracted to the region of highest intensity. As a consequence, atoms can be trapped at the focus of an optical dipole beam.
Our first ODT beam that is applied for loading the atoms from the magnetic quadrupole trap is a 11 W laser beam at a wavelength of 1064 nm which is focused to a beam waist of 42 μm. The light source of the optical dipole beam is a high power, single-mode laser (Mephisto MOPA 25 W, Coherent) with an output power of 25 W at a wavelength of 1064 nm. A 80 MHz AOM (MCQ80-A2.5-L1064, AA Opto-Electronic) serves as control element of the beam power in the -1st diffraction order, that is used for the first ODT (ODT_1). The non-diffracted, zero order beam is recycled for a second ODT beam (ODT_2), which will be discussed in Subsection 2.13.2. The AOM, which is specified for high power applications, includes a quartz crystal with an active aperture of 2.5×2.5 mm, supporting a power density of up to 500 MW/cm^2. In order to increase the pointing stability and to improve the beam quality, the ODT_1 beam is transferred to the optical table placed around the science cell via a high-power fiber. This single-mode, polarization-maintaining, photonic crystal fiber (LMA-PM-10, NKT Photonics) has a length of two meters and is terminated with two high-power connectors at the fiber input (60FC-SMA-T-4-A11-03, Schafter+Kirchoff) and output (60FC-SMA-0-M30-37, Schafter+Kirchoff). The fiber coupling efficiency drops to $\sim 60\%$ at higher powers, and we eventually obtain up to 11 W at the fiber output. On the optical table, see Figure 2.15, a fused silica lens with a focal length of f=200 mm (BFPL-200-UV, Melles-Griot) focuses the beam onto the atomic sample in the science cell.

2.13.1. Power stabilization

The beam power of the ODT is stabilized by the regulator circuit illustrated in Figure 2.14. The laser beam power is controlled via the power of the 80 MHz RF signal applied to the AOM. The RF signal is generated by a voltage controlled oscillator (VCO) followed by a voltage variable attenuator (ZX73-2500-S+, Mini-Circuits), a switch (ZAS-1, Mini-Circuits) and a 20 W high-power amplifier (ZHL-20W-13+, Mini-Circuits). The laser power of the ODT is regulated and stabilized by means of a feedback loop. The beam power is detected with a photodiode (SM05PD4A, Thorlabs) via a reflection from the glass cell, this signal being used to regulate the RF power applied to the AOM. For this purpose, the signal of the photodiode is treated by a logarithmic converter (AD8304, Analog Devices), which outputs a voltage proportional to the logarithm of the photodiode current. This voltage is transmitted to the input of a PID controller (SIM960, SRS). The PID controller compares this input signal to the setpoint that is specified by our settings in the experimental control software. The PID then outputs a corresponding control voltage to the VVA, modifying the RF signal strength and thus the AOM efficiency and ODT power. Due to the logarithmic converter we are able to regulate the laser power over a range of three orders of magnitude.

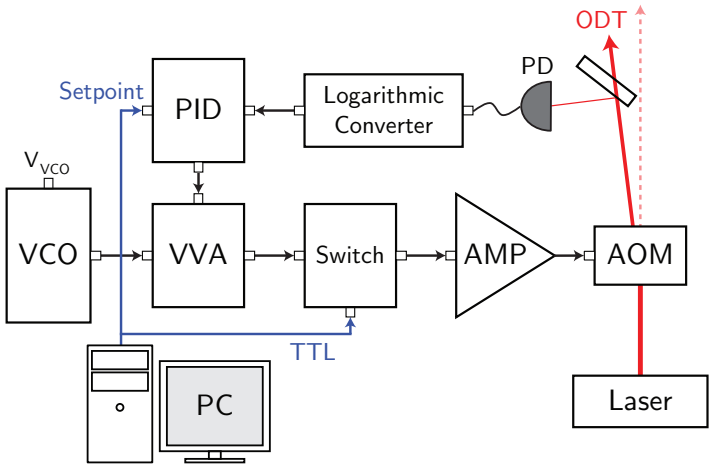

Figure 2.14: Feedback loop for regulating and stabilizing the power of the ODT beam, as illustrated in [148]. The AOM is driven by a RF circuit composed of a voltage controlled oscillator (VCO), a voltage variable attenuator (VVA), a switch and an amplifier (AMP). The power of a reflection of the ODT beam is detected with a photo diode (PD). The photo diode current is converted into a voltage on a logarithmic scale. A PID controller compares this voltage to a setpoint, that is imposed by our settings in the experimental control software, and outputs a control signal to the VVA, modifying the AOM efficiency. Due to the logarithmic converter we are able to regulate the power of the ODT over a range of three orders of magnitude. The switch, which is controlled by a TTL signal from the experimental control, allows to turn the ODT rapidly on or off.

2.13.2. ODT_2

For the second stage of the optical evaporation phase, we transfer the atoms into a crossed ODT. In this context a second ODT beam (ODT_2) had to be implemented. For this purpose, we recycle the zero order beam of the AOM controlling the power of ODT_1. Since the beam power of ODT_1 is considerably decreased during the first optical evaporation stage in the single beam trap, a large fraction of the infra-red power becomes available in the zero order beam of the AOM. This beam is recycled and passes through another 80 MHz AOM whose +1st order-beam is utilized for ODT_2. The circuit for beam power regulation and stabilization is analogous to the one for ODT_1, see Figure 2.14. The components that were employed for this circuit are exactly the same, except for the RF amplifier for which a 2 W model (ZHL-1-2W, Mini-Circuits) was used to drive the AOM of ODT_2. Having one AOM per beam at our disposal, both dipole traps can be regulated independently.

2.14. Optical setup of Science cell

In this section we present the optical setup implemented around the science cell. It is mounted on an U-shaped optical table elevated to the height of the lower transport plate, see Figure 2.15.

The two thick red paths, whose starting points are designated ODT_1 and ODT_2 corresponding to our 1064 nm laser source setup, indicate the beampaths of the crossed dipole trap. Since both beams originate from the same laser source we have to take precautions in order to avoid

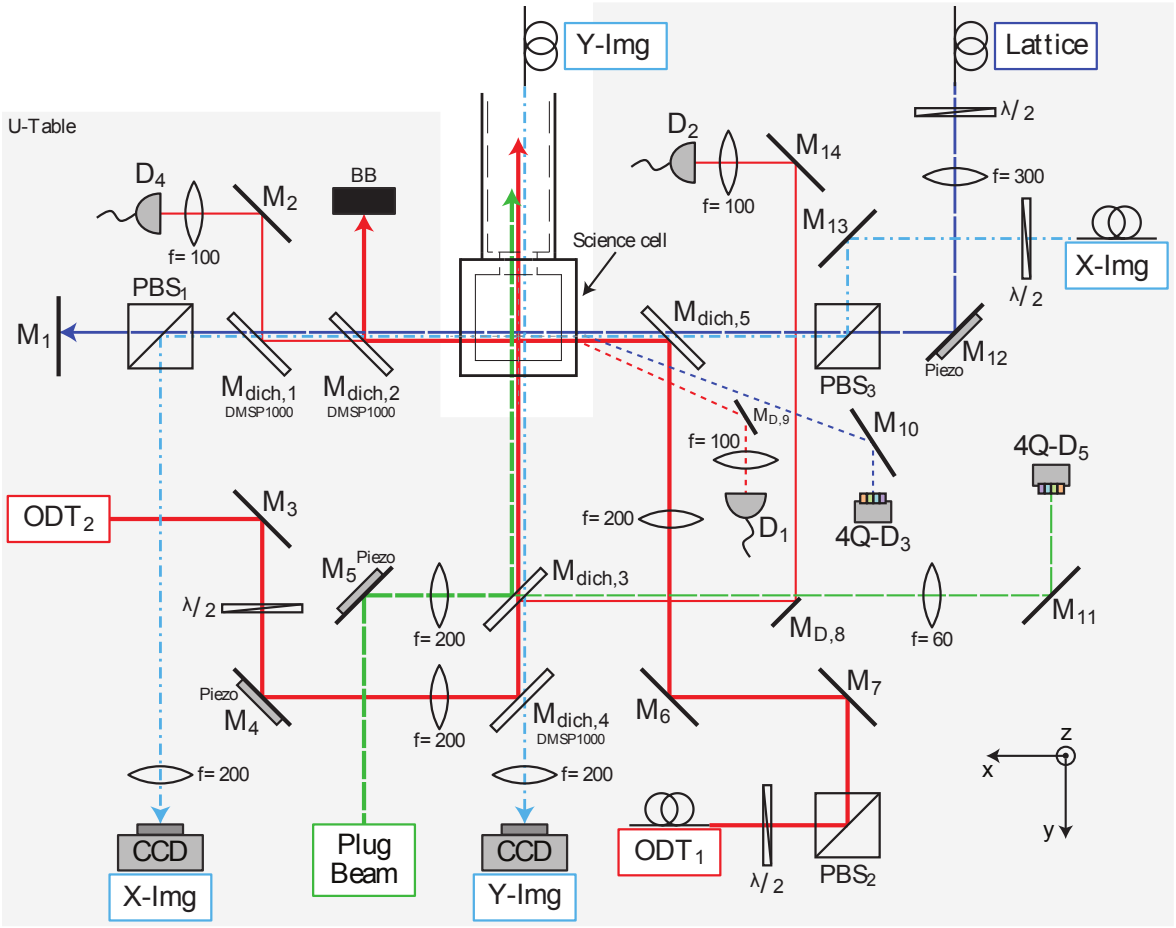

Figure 2.15: Scheme of the optical setup surrounding the science cell. The optics are mounted on a U-shaped table elevated to the height of the lower transport plate. The optical setup includes the crossed optical dipole trap beams ODT_1 and ODT_2 (red) at 1064 nm, the optical plug for the magnetic quadrupole trap (green) at 532 nm, the bichromatic imaging in x- and y-direction (dotted blue) at 671 nm and 767 nm, as well as the beam path of the future optical lattice (dark blue). All beams passing through the glass cell possess an angle of incidence which is non zero in order to avoid direct back reflections and corresponding interference effects. Further details can be found in the text.

interference effects and modulation of the crossed trap potential. First of all, the polarisation axis of ODT_2 is turned orthogonal to the polarization of ODT_1 by a $\lambda/2$ plate. Secondly, both beams are shifted in frequency, since for ODT_1 we utilize the -1st diffraction order of the first AOM, and the +1st diffraction order of the second AOM is used for ODT_2, yielding a frequency difference of 160 MHz. For the purpose of power regulation, see Figure 2.14, reflections or leaking light of both trapping beams are detected on photodiodes (D_1 and D_2) whose current output is converted logarithmically. An additional third photodiode (D_4) in linear operation is employed to monitor ODT_1. The off-resonant blue-detuned plug beam is superimposed with the ODT_2 beam via the dichroic mirror $M_{dich,3}$ (DMLP567, Thorlabs). The position of the plug beam focus is monitored by means of a four-quadrant photodiode (4Q-D_5) connected to the control computer and is regulated by a piezo-driven mirror (M_4). This feedback loop is required as the plug beam focus has to precisely cover the magnetic field zero of the magnetic quadrupole trap. In future, the same technique will be employed in order to regulate the position of the lattice laser which we plan to superimpose with ODT_1 via $M_{dich,5}$ (BSR-15-1025, CVI Melles Griot). For this purpose, a back reflection on the glass cell will be utilized. It is important to note that all beams have a non zero angle of incidence on the glass cell in order to avoid interference effects by back reflections. These beam angles are not illustrated in Figure 2.15 for reasons of clarity.
The two bichromatic imaging beams (X-Img, Y-Img), applied for absorption imaging of ^{6}Li and ^{40}K, are depicted in blue dotted lines, whereas the imaging beam in the vertical z-direction is not shown. We note that the magnetic trap center is shifted in y-direction with respect to the science cell center in order to improve the optical access in y-direction. In this direction, the trap center has a distance of 6.5 mm from the glass windows. Due to this reason, also the laser beam foci are displaced with respect to the cell center. Since the height of the glass cell amounts to only 18 mm, the z-direction has the best optical access. Therefore, we intend to install a future high resolution objective on this axis.

2.15. Computer control system

We implemented three personal computers for controlling the experiment and acquiring the resulting data. The first PC controls the experiment by means of an installed control software and connected National Instruments cards. The second PC receives the raw image data from the CCD cameras and calculates the normalized absorption profile, see Figure 2.16. The measured sample properties, like for example the width of the distribution or the integrated atom number, are extracted and automatically saved to an output file. The third PC accesses these data files and is exploited for data analysis.
As software driving our experimental control electronics we implemented a modified version of Cicero Word Generator [1], an open source control software suite particularly programmed for atomic physics experiments. It offers the possibility to create time sequences via a user

[1] http://akeshet.github.io/Cicero-Word-Generator/

inteface and runs them on National Instruments cards which provide the corresponding analog and digital outputs.
Cicero Word Generator consists of two main applications, Cicero and Atticus [162], thus splitting the task of designing and running output sequences by a client-server architecture. Cicero is the graphical user interface for editing sequences, whereas Atticus translates these sequences to output buffers and sends them to the output hardware. Cicero features also list runs, meaning that parameters can be changed from run to run, while scanning over a set of values. We extended and customized the source code in order to integrate the control of special hardware components (like cameras, RF synthesizers, etc.), to add the ability to drive magnetic transport sequences and to improve the usability of the control software.
The relevant time step durations range from seconds to microseconds during one experimental sequence. For example, the MOT loading step lasts several seconds, during which none of the digital or analog channel values is modified, whereas the duration of an imaging pulse is only $\sim 100\,\mu$s. To avoid long redundant buffers which would be generated for a constant time clock, we synchronize the output cards with a programmable variable clock generator (XEM 3001, Opal Kelly). This FPGA-card generates the clock pulses only when an output channel needs to change, while the output cards use this variable timebase as their sample clock. This reduces the size and generation time of the buffers considerably, and improves the achievable time resolution to $0.2\,\mu$s.
For our experiment we employ currently six analog output cards (NI PXI-6713, National Instruments) and three digital output cards (NI PXI-6533 and NI PXI-6536, National Instruments). Each of the analog cards has 8 BNC outputs delivering 0 to 10 Volts and up to 250 mA. The digital cards have 24 outputs, outputting either 0 V or 5 V (only 3.3V for NI PXI-6536). Most of the digital outputs are opto-coupled in order to galvanically isolate the control electronics from the high current sources in the experiment. Isolation is an important requirement since fast switching of magnetic coils that are driven by high currents induces high voltage peaks which can damage the output cards easily.

2.16. Imaging and data acquisition

Several probing techniques were implemented in our experimental system which allow to perform measurements on the properties of the atomic samples that are prepared by our experimental sequences. In the following we present the absorption imaging technique, the fluorescence monitoring and the data acquisition.

2.16.1. Absorption imaging

The atomic density distribution can be probed by measuring the transmission profile $I_{\mathrm{abs}}(x, y)$ of a near-resonant laser beam that is passing through the atomic sample. This imaging beam features low intensity and is only shined in during a short duration of $100\,\mu$s, resulting in a relative transmission that remains intensity independent under these conditions. The transmission profile $I_{\mathrm{abs}}(x, y)$ is recorded with a charge-coupled device (CCD) camera featuring a

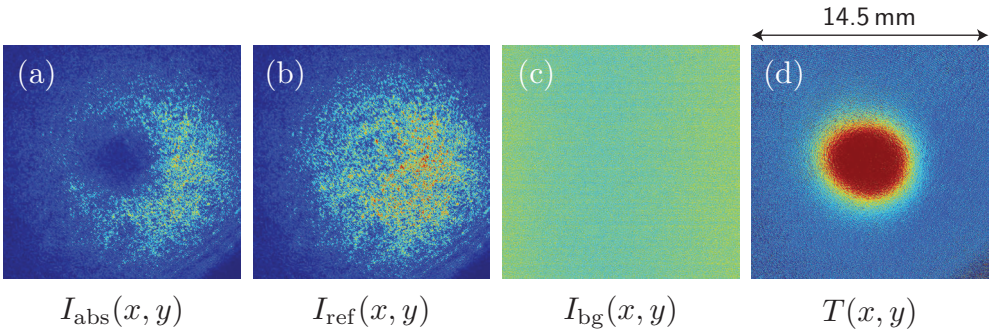

Figure 2.16: Sample data for absorption imaging, from [148]. The normalized transmission profile $T(x,y)$ is calculated by relating three camera pictures: (a) a picture of the near-resonant probe beam after absorption by the atomic sample, (b) a picture of the same probe beam in absence of atoms and (c) a background picture without probe beam. The normalized transmission image (d) is then calculated by Equation (2.1). The image shows a ^{40}K cloud after cooling by the D_1 molasses phase, see Chapter 3, and a time of flight of 13 ms. The sample is probed with an imaging beam that is detuned by 1Γ. According to the resulting image, it consists of $\sim 1.3 \times 10^9$ ^{40}K atoms featuring a temperature of 11μK.

fast double shutter mode. It needs to be normalized in order to accommodate for the intensity profile of the imaging beam and for ambient stray light reaching the camera. Therefore two more pictures need to be recorded. First, a reference picture of the unabsorbed imaging beam giving the intensity profile $I_{\mathrm{ref}}(x,y)$. This picture can be taken by either waiting for the atoms to fall off the field of view or by detuning the imaging beam. Second, a background picture in the absence of the imaging beam, yielding the background signal $I_{\mathrm{bg}}(x,y)$. Figure 2.16 shows the three recorded pictures and the calculated, normalized transmission profile

$$T(x,y) = \frac{I_{\mathrm{abs}}(x,y) - I_{\mathrm{bg}}(x,y)}{I_{\mathrm{ref}}(x,y) - I_{\mathrm{bg}}(x,y)}\,. \tag{2.1}$$

The transmission profile is directly related to the atomic density distribution $n(x,y,z)$ of the probed sample by

$$T(x,y) = \exp\left(-\mathrm{OD}(x,y)\right) = \exp\left(-\sigma \int n(x,y,z)dz\right)\,, \tag{2.2}$$

where $\mathrm{OD}(x,y)$ is the optical density of the atomic sample for the specific imaging beam and σ is the absorption cross section of the atoms. For low beam intensity ($I \ll I_{\mathrm{sat}}$), the absorption cross section is approximately given by

$$\sigma = C^2 \frac{3\lambda^2}{2\pi} \frac{1}{1 + (2\Delta\omega_{\mathrm{img}}/\Gamma)^2}\,, \tag{2.3}$$

where C is the Clebsch Gordan coefficient depending on the image beam polarization and the populations of the magnetic sublevels. λ and $\Delta\omega_{\mathrm{img}}$ are the wavelength of the atomic transition and the detuning of the imaging beam from resonance, respectively. In general we do not spin-polarize the atoms before imaging them in the 3D-MOT chamber. In consequence,

C can be expressed as the mean of the squared Clebsch-Gordan coefficients for all possible transitions. Since we image on the transition $|F = 3/2\rangle \rightarrow |F' = 5/2\rangle$ of ^{6}Li and $|F = 9/2\rangle \rightarrow |F' = 11/2\rangle$ of ^{40}K, the means of the squared Clebsch-Gordan coefficients are given by $C^2_{\mathrm{Li}} = 0.5$ and $C^2_{\mathrm{K}} = 0.4$.

Optical setup

The two beams dedicated for imaging ^{6}Li and ^{40}K in the MOT chamber are superimposed via a dichroic mirror and subsequently expanded to a $1/e^2$-diameter of 27.5 mm. The bichromatic beam is then circularly polarized by a $\lambda/4$ plate, thus driving the $2^2S_{1/2}\,|F = 3/2\rangle \rightarrow 2^2P_{3/2}\,|F' = 5/2\rangle$ cycling transitions of ^{6}Li and the $4^2S_{1/2}\,|F = 9/2\rangle \rightarrow 4^2P_{3/2}\,|F' = 11/2\rangle$ cycling transition of ^{40}K, see Figure 2.2 and 2.3.
The CCD image sensor of our camera (Pixelfly qe (double shutter version), PCO imaging) contains 1392×1024 pixels with a pixel size of $6.45 \times 6.45\,\mu\mathrm{m}^2$. The atoms are imaged on the CCD sensor via a 2-inch lens with a focal length of 6 cm. This lens is placed at a distance of 21 cm from the MOT center and provides thus a numerical aperture of $NA = 0.12$. The magnification of the MOT-imaging system is $1/2.28 \simeq 0.4$.

Time-of-flight temperature measurement

In a time-of-flight (TOF) measurement the atoms are released from the trap and expand freely during a duration t_{TOF} before they are imaged. Under the assumption of a classical Maxwell-Boltzmann momentum distribution and a collisionless expansion, the 1/e radius of the atomic cloud evolves as

$$\sigma_{\mathrm{i}}(t_{\mathrm{TOF}}) = \sqrt{\sigma_{\mathrm{i}}^2(t_{\mathrm{TOF}} = 0) + \frac{k_{\mathrm{B}}T}{m} t_{\mathrm{TOF}}^2}\,, \tag{2.4}$$

where $i \in \{x, y, z\}$ indicates the coordinate axes and T is the cloud temperature. The temperature is determined by taking absorption images for different time-of-flight durations t_{TOF} and fitting Equation (2.4) to the measured cloud radii.

Data acquisition

The raw images recorded by the CCD camera are processed and saved by a program written in Python whose initial version was described in detail in [163]. Besides displaying the normalized transmission profile and the density distribution of each camera shot, it integrates several fit functions. Another program written in Octave is used to automatically calculate the interesting parameters, like total atom number, cloud size and central optical density. It analyses all incoming images and saves the results to an output file that is subsequently accessed by other applications for further data analysis.

2.16.2. Auxiliary fluorescence monitoring

We continuously monitor the emitted MOT fluorescence light for both species with two large area photo diodes in order to estimate the corresponding atom numbers. The fluorescence is proportional to the atom number but depends in general also on the number of excited atoms which is related to the effective MOT beam intensities, detunings and component ratios. However, the fluorescence signal delivers good estimates, when calibrated to the more accurate atom number counting by absorption imaging, see Subsection 2.16.1. Moreover, we monitor the MOT fluorescence also with a video camera that is connected to a TV-screen to obtain a live image of the atomic sample in the MOT showing its position, size and shape. Both auxiliary detection systems are convenient tools for optimizing the MOT-beam alignment and other system parameters as well as for technical error debugging.

2.17. Conclusion

In this chapter we presented the technical components of our experimental setup. We described and specified the vacuum system, the optical systems, the atomic sources, optical and magnetic traps, the magnetic transport, the optical setup around the science cell, the computer control system and the imaging devices.

3 Sub-Doppler laser cooling of alkalines on the D_1-transition

In the previous chapter we stated that the measured phase-space density (PSD), after trapping and cooling of ^{6}Li and ^{40}K atoms in a double magneto-optical trap, is of the order of 10^{-7}. Further cooling stages are therefore required in order to achieve the quantum regime with a PSD $\simeq 1$. Our intended procedure was to perform evaporative cooling in a plugged magnetic quadrupole trap after magnetically transporting the atoms to the science cell. However, our first experimental attempts proved that the initial temperature of the atomic sample was too high, and thus its density too low, in order to achieve a sufficiently large elastic collision rate for rendering the evaporation process efficient. Therefore, we sought for implementing an intermediate cooling step, like for instance sub-Doppler cooling, that could enhance the initial collision rate. Due to the lack of ordinary sub-Doppler cooling schemes for ^{6}Li and ^{40}K, we were in search of alternatives and discovered eventually a novel mechanism based on a gray molasses scheme [164, 165]. We showed that by adopting this cooling technique the PSD was increased by almost three orders of magnitude compared to the MOT, which provided significantly better conditions for performing efficient evaporative cooling of ^{6}Li and ^{40}K.
Consequently, this chapter presents our new, three-dimensional optical molasses scheme for simultaneous sub-Doppler cooling of fermionic ^{6}Li and ^{40}K [139, 140]. This cooling scheme operates on the D_1 line, relies on gray optical molasses cooling and applies in principle to all alkali atoms. It is a simple and robust technique, resulting in a phase space density on the order of 10^{-4} for both atomic species, if it is combined with a preceding CMOT phase for enhancing the atomic density, see Subsection 2.7.1. In particular, we will show that the two molasses do not affect each other. This cooling scheme therefore allows for efficient direct loading of magnetic and optical dipole traps. Especially experiments working with alkali atoms which feature a narrow hyperfine structure of the $P_{3/2}$ excited level, hindering efficient sub-Doppler cooling on the D_2 line, can profit from the D_1 molasses technique, as the large gain in temperature offers a promising route for fast evaporation to quantum degeneracy.
Besides this introductory summary, this chapter includes the printed paper manuscripts of the following articles, which present our experimental and theoretical investigations in detail:

Sub-Doppler laser cooling of fermionic ^{40}K atoms in three-dimensional gray optical molasses, see page 47 for print version
D. R. Fernandes, F. Sievers, N. Kretzschmar, S. Wu, C. Salomon and F. Chevy
EPL (Europhysics Letters) **100**, 63001 (2012)

Simultaneous sub-Doppler laser cooling of fermionic ^{6}Li and ^{40}K on the D_1 line: Theory and experiment, see page 53 for print version
F. Sievers, N. Kretzschmar, D. R. Fernandes, D. Suchet, M. Rabinovic, S. Wu, C. V. Parker, L. Khaykovich, C. Salomon and F. Chevy
Phys. Rev. A **91**, 023426 (2015)

In these publications we detail in particular our investigation of the dependence of both the final temperature of the atomic cloud and the photon scattering rate on the Raman-detuning, thus revealing the importance of the Raman-resonance condition.
For zero Raman-detuning, long lived coherences between hyperfine states are established, generating a new class of dark states. This Λ-enhancement leads to additional cooling forces and reduced photon scattering, yielding an improved cooling efficiency and a lower temperature limit. We compare the experimental data to numerical results of a semiclassical MonteCarlo wavefunction simulation. This simulation accounts for all relevant Zeeman sublevels and the three dimensional σ^+–σ^- counter-propagating beam configuration. As a result, we can state a good qualitative agreement between the experimental outcomes and the simulation.
In addition to the published cooling procedures for ^{6}Li and ^{40}K, we used the D_1 molasses scheme to cool bosonic ^{41}K. We cooled all 5×10^9 ^{41}K atoms from a CMOT to a final temperature of 40 μK leading to a phase-space density of 0.4×10^{-4}. We note, that the final temperature could probably be lower for ^{41}K, since at the time when this measurement was performed, the ambient magnetic bias fields were not perfectly compensated.
To date, several other research groups implemented our D_1 cooling scheme to improve the performance of their experiments working with ^{6}Li [166], ^{7}Li [167] [1] and ^{39}K [168–170]. In addition, this scheme might allow for the implementation of single-atom resolved imaging of fermions in a pinning lattice, as was shown by the group of Stefan Kuhr in Glasgow working with ^{40}K ([171] and private communication).
In dual-species operation, the presence of the other species reduces the number of atoms in the MOT by 4 % for ^{6}Li and by 10 % for ^{40}K. During the CMOT and the D_1 molasses phase, however, no detrimental mutual influence is observed. Neither the relative atom numbers nor the temperatures are altered in dual-species operation when compared to single-species operation. This might be explained by the short duration of the CMOT and the molasses phase, which both last only some milliseconds.
Table 3.1 outlines the resulting performance parameters for the consecutive sequence steps in dual species-operation. The D_1 molasses phase largely reduces the temperature of both the

[1] The D_1 molasses scheme is also applied for ^{7}Li by Ketterle at MIT, Cambridge, United States (private communication).

^{6}Li and the ^{40}K sample, while the compressed cloud-size resulting from the CMOT phase is preserved. A phase-space density of almost 10^{-4} is thus obtained for both species permitting efficient, direct loading of an optical dipole trap [169].

	T (μK)	N ($\times 10^9$)	n ($\times 10^{10}\,\mathrm{cm}^{-3}$)	ϕ ($\times 10^{-5}$)
Potassium (^{40}K)				
MOT	240	3.2	7	0.02
CMOT	2000	3.2	37	0.06
Molasses	11	3.2	30	10.7
Lithium (^{6}Li)				
MOT	1000	2.0	2.6	0.03
CMOT	800	2.0	18	0.29
Molasses	48	1.2	7.6	8.2

Table 3.1. – Main performance parameters of ^{6}Li and ^{40}K for the consecutive sequence steps in dual species operation. The listed parameters are the optimum temperature T, the atom number N, the density n and the phase-space density ϕ. We note that the indicated phase-space density does not account for the different magnetic sublevels and is calculated as $\phi = n\lambda_\mathrm{B}^3$, with the thermal de Broglie wavelength λ_B.

Appendix 3.A Publications

Sub-Doppler laser cooling of fermionic ^{40}K atoms in three-dimensional gray optical molasses, see page 47 for print version
D. R. Fernandes, F. Sievers [1], N. Kretzschmar, S. Wu, C. Salomon and F. Chevy
EPL (Europhysics Letters) **100**, 63001 (2012)

Simultaneous sub-Doppler laser cooling of fermionic ^{6}Li and ^{40}K on the D_1 line: Theory and experiment, see page 53 for print version
F. Sievers, N. Kretzschmar, D. R. Fernandes, D. Suchet, M. Rabinovic, S. Wu, C. V. Parker, L. Khaykovich, C. Salomon and F. Chevy
Phys. Rev. A **91**, 023426 (2015)

A Letters Journal Exploring the Frontiers of Physics

December 2012

EPL, **100** (2012) 63001
doi: 10.1209/0295-5075/100/63001

www.epljournal.org

Sub-Doppler laser cooling of fermionic ^{40}K atoms in three-dimensional gray optical molasses

D. Rio Fernandes[1(a),(b)], F. Sievers[1(a),(c)], N. Kretzschmar[1], S. Wu[2], C. Salomon[1] and F. Chevy[1]

[1] *Laboratoire Kastler-Brossel, École Normale Supérieure, CNRS and UPMC - 24 rue Lhomond 75005 Paris, France, EU*
[2] *Department of Physics, College of Science, Swansea University - Swansea, SA2 8PP UK, EU*

received 4 October 2012; accepted in final form 23 November 2012
published online 20 December 2012

PACS 37.10.De – Atom cooling methods
PACS 37.10.Gh – Atom traps and guides
PACS 67.85.-d – Ultracold gases, trapped gases

Abstract – We demonstrate sub-Doppler cooling of ^{40}K on the D_1 atomic transition. Using a gray-molasses scheme, we efficiently cool a compressed cloud of 6.5×10^8 atoms from ~ 4 mK to $20\,\mu$K in 8 ms. After transfer to a quadrupole magnetic trap, we measure a phase space density of $\sim 10^{-5}$. This technique offers a promising route for fast evaporation of fermionic ^{40}K.

Introduction. – Cooling of fermionic atomic species has played a fundamental role in the study of strongly correlated Fermi gases, notably through the experimental exploration of the BCS-BEC crossover, the observation of the Clogston-Chandrasekhar limit to superfluidity, the observation of the Mott-insulator transition in optical lattices, and the study of low-dimensional systems (see for instance [1,2] for a review). When the temperature is further decreased, new exotic phases are predicted (*p-wave* superfluids for spin imbalanced gases, antiferromagnetic order... [1,3,4]) and, as a consequence, intense experimental effort is currently under way to push the temperature limit achieved in ultracold fermionic samples in order to enter these novel regimes.

Most experiments on quantum degenerate gases begin with a laser cooling phase that is followed by evaporative cooling in a non-dissipative trap. Achieving quantum degeneracy depends critically on the collision rate at the end of the laser cooling phase and sub-Doppler cooling [5] is often a key ingredient for initiating efficient evaporation. In the case of fermionic lithium-6 and potassium-40, the narrow hyperfine structure of the $P_{3/2}$ excited level does not allow for efficient Sisyphus sub-Doppler cooling to the red of a $F \to F' = F + 1$ atomic transition [6,7].

Experiments for producing quantum degenerate gases of ^{40}K typically start with $\sim 10^8$ atoms laser-cooled to the Doppler limit ($145\,\mu$K) [8]. More refined laser-cooling schemes have produced ^{40}K temperatures of $\sim 15\,\mu$K, but with only reduced atom numbers ($\sim 10^7$) [7,9,10]. This relatively poor efficiency is due to the combination of the fairly narrow and inverted hyperfine level structure of the $P_{3/2}$ excited state which results in the washing out of the capture velocity of the molasses when the laser detuning is increased [11]. To overcome these limitations, two groups recently realized Magneto-Optical Traps (MOT) in the near-UV and blue regions of the spectrum to cool ^{6}Li [12] and ^{40}K [13], respectively. The associated transitions, being narrower than their D_2 counterparts, lead to a smaller Doppler temperature and were used to improve the final phase space density typically by one order of magnitude.

In this letter, we report efficient sub-Doppler cooling of ^{40}K atoms using gray molasses on the D_1 atomic transition at 770 nm. Thanks to the much reduced fluorescence rate compared to standard bright sub-Doppler molasses, we could produce cold and dense atomic samples. The temperature of a tightly compressed cloud of 6.5×10^8 atoms was decreased from ~ 4 mK to $20\,\mu$K in 8 ms without significant change of the density in the process. After transfer to a quadrupole magnetic trap, we achieved a phase space density of $\sim 2 \times 10^{-5}$.

Gray molasses. – Sub-Doppler cooling using gray molasses was proposed in ref. [14] and realized in the mid 1990s on the D_2 atomic transition of cesium and rubidium, allowing one to cool atomic samples close to 6 times the

(a) These authors contributed equally to this work.
(b) E-mail: diogo.fernandes@lkb.ens.fr
(c) E-mail: franz.sievers@lkb.ens.fr

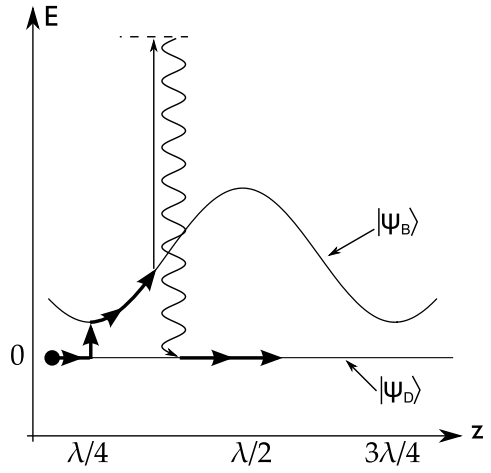

Fig. 1: Gray-molasses scheme. On a $F \to F' = F$ or $F \to F' = F-1$ optical transition with positive detuning, the ground state splits into a dark and a bright manifold with positive energy, shown as $|\psi_D\rangle$ and $|\psi_B\rangle$, respectively. In the presence of a polarization gradient, the bright-state energy is spatially modulated. Like in Sisyphus cooling, energy is lost when an atom in $|\psi_B\rangle$ climbs a potential hill before being pumped back into the dark state $|\psi_D\rangle$. Motional coupling between $|\psi_D\rangle$ and $|\psi_B\rangle$ occurs preferentially at the potential minima.

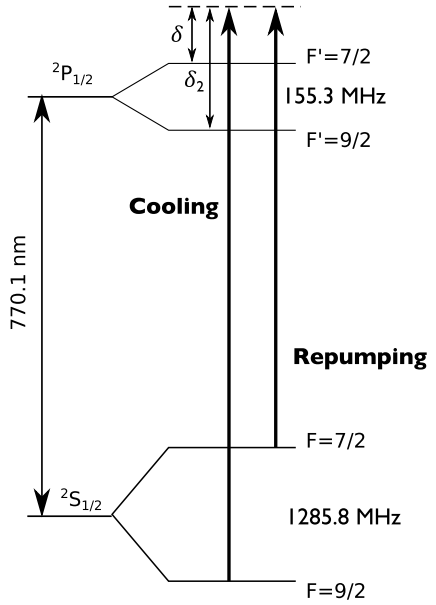

Fig. 2: Level scheme for the D_1 transition of ^{40}K and transitions used for gray-molasses cooling. The laser detuning from the cooling/repumping transitions is δ and the detuning from the off-resonant excited hyperfine state $F' = 9/2$ is δ_2 (see text).

single-photon recoil energy [15–17]. For an atomic ground state with angular momentum F, gray molasses operate on the $F \to F' = F$ $(F \to F' = F-1)$ optical transition. For any polarization of the local electromagnetic field, the ground-state manifold possesses one (two) dark states which are not optically coupled to the excited state by the incident light [14,18]. When the laser is detuned to the blue side of the resonance, the ground-state manifold splits into dark states which are not affected by light and bright states which are light-shifted to positive energy by an amount which depends on the actual polarization and intensity of the laser field (see fig. 1).

When the atom is in a bright state, it climbs up the hill of the optical potential before being pumped back to the dark state near the top of the hill. The kinetic energy of the atom is thus reduced by an amount of the order of the height of the optical potential barrier. The cooling cycle is completed near the potential minima by a combination of motional coupling and optical excitation to off-resonant hyperfine states.

We implement 3D gray-molasses cooling in ^{40}K on the D_1 transition (see fig. 2). In alkali atoms, the $P_{1/2}$ excited level manifold has only two hyperfine states, which are better resolved than their $P_{3/2}$ counterparts. These facts allow for less off-resonant excitation and a good control of the cooling mechanism. A first laser beam (cooling beam) is tuned to the $|^2S_{1/2}, F = 9/2\rangle \to |^2P_{1/2}, F' = 7/2\rangle$ transition with a detuning $\delta > 0$. A second laser beam (repumping beam) is tuned to the $|^2S_{1/2}, F = 7/2\rangle \to |^2P_{1/2}, F' = 7/2\rangle$ transition with the same detuning δ.

As mentioned above, two mechanisms can lead to the departure from the dark state. The first one is the motional coupling V_{mot} due to the spatial variations of the dark state internal wave function induced by polarization and intensity gradients. The second one is the dipolar coupling V_{off} via off-resonant excited hyperfine states. A rough estimate shows that $V_{\mathrm{mot}} \simeq \hbar k v$, where v is the velocity of the atom and k the wave vector of the cooling light, while $V_{\mathrm{off}} \simeq \hbar\Gamma\,(\Gamma/\delta_2)\,I/I_{\mathrm{sat}}$, where Γ^{-1} is the lifetime of the excited state, I the light intensity, I_{sat} the saturation intensity and δ_2 the detuning to off-resonant excited state. Comparing the two couplings, we see that the motional coupling is significant in the high velocity regime $v \gtrsim \Gamma/k\,(\Gamma/\delta_2)\,I/I_{\mathrm{sat}}$. In our case, the off-resonant level $F' = 9/2$ (see fig. 2) is detuned by $\delta_2 = 155.3\,\mathrm{MHz} + \delta$ from the cooling transition $|^2S_{1/2}, F = 9/2\rangle \to |^2P_{1/2}, F' = 7/2\rangle$. For $I \simeq I_{\mathrm{sat}}$, motional coupling dominates for $T \gtrsim 50\,\mu\mathrm{K}$, meaning that both processes are expected to be present in our experiments. In general, the transition rate between $|\psi_{\mathrm{D}}\rangle$ and $|\psi_{\mathrm{B}}\rangle$ induced by motional coupling V_{mot} and the off-resonant coupling V_{off} are both maximal when the distance between the dark and bright manifolds is smallest, which favors transitions near the bottom of the wells of the optical lattice.

In ^{40}K, the simplified discussion presented so far must be generalized to the case involving many hyperfine states $(10+8)$. However, the essential picture remains valid.

Indeed, by numerically solving the optical Bloch equations for the ^{40}K system in the presence of the cooling and repumping laser fields, we obtain the light shifts ϵ and the total optical pumping rates γ of all the dressed states for an atom at rest (see fig. 3). This is done for the particular case of a one-dimensional optical lattice in the lin⊥lin configuration and with a low repumping intensity (1/8 of the cooling beam intensity, typical for our experiments). In fig. 3a) we see 8 bright states, 2 weakly coupled states and 8 dark states combining both hyperfine manifolds. In fig. 3b) we plot the optical pumping rates of the corresponding dressed states. We find that the optical pumping rate is low for the weakly coupled states and it practically vanishes for the dark states. In fig. 3c) the optical pumping rates display a good correlation with the light shift magnitude, which favors efficient sub-Doppler cooling. Note also the long-lived dark states. This correlation shows that the gray-molasses picture remains valid for this more complex level scheme.

We now turn to the question of the capture velocity of the gray-molasses scheme. Let Γ' be the optical pumping rate from bright to dark states. The atom is pumped efficiently towards dark states if it stays a time $\tau \gtrsim \Gamma'^{-1}$ near the top of the hill. If the atom moves at a velocity v in the lattice, then $\tau \simeq 1/kv$ and the optical pumping to dark states is efficient when $kv \lesssim \Gamma'$. $v_c \simeq \Gamma'/k$ thus defines the capture velocity of the gray molasses. For a beam with detuning δ to the main cooling transition, $\Gamma' \propto I/\delta^2$ and thus v_c increases with laser intensity. On the other hand, the cooling efficiency is reduced when the atom cannot climb the potential hill anymore, which leads to an equilibrium temperature that scales as $k_B T \propto I/\delta$, when $T \gg T_{\mathrm{Recoil}} = \hbar^2 k^2/2mk_{\mathrm{B}}$ [5,19].

Experimental results. – Our setup is based on the apparatus presented in [20]. In the experiments presented here, 6.5×10^8 ^{40}K atoms are loaded from a two-dimensional magneto-optical trap (2D-MOT) into a three-dimensional magneto-optical trap (MOT) operating on the D_2 line. The initial temperature of the cloud is 200 μK, not far from the Doppler temperature $T_D = \hbar\Gamma/2k_{\mathrm{B}} = 145\,\mu$K, with $\Gamma/2\pi \approx 6.035$ MHz. In the MOT, the cooling and repumping laser intensities are $I_{\mathrm{cool}} = 13 I_{\mathrm{sat}}$ and $I_{\mathrm{repump}} = I_{\mathrm{cool}}/20$ per beam, with $I_{\mathrm{sat}} = 1.75$ mW/cm^2. After the loading phase, we ramp the magnetic field gradient from 9 G·cm^{-1} to 60 G·cm^{-1} in 5 ms without changing the laser detunings in order to compress the cloud. This process yields a cloud with high density, but with a much higher temperature of ~ 4 mK. At this point the magnetic field is switched off in $\simeq 100\,\mu$s and the D_1 molasses beams are switched on for a time τ_{m}.

The D_1 cooling and repumping beams are detuned by the same amount δ in the range of 2Γ–5Γ as shown in fig. 2. The repumping beam is detuned from the main cooling beam by 1285.8 MHz using an electro-optical modulator. Its intensity is typically 1/8 of the cooling beam intensity. After propagation through an optical fiber, the total D_1 optical power is 240 mW and the beam is magnified to a waist of 1.1 cm. We then split the beam into two vertical beams and two retro-reflected horizontal beams in a three-dimensional σ^+/σ^- configuration. The maximum D_1 cooling intensity per beam attained in our experiments is 25 mW/cm^2 or $I = 14 I_{\mathrm{sat}}$.

We first measure the atom number and temperature of the D_1 molasses as a function of the cooling beam

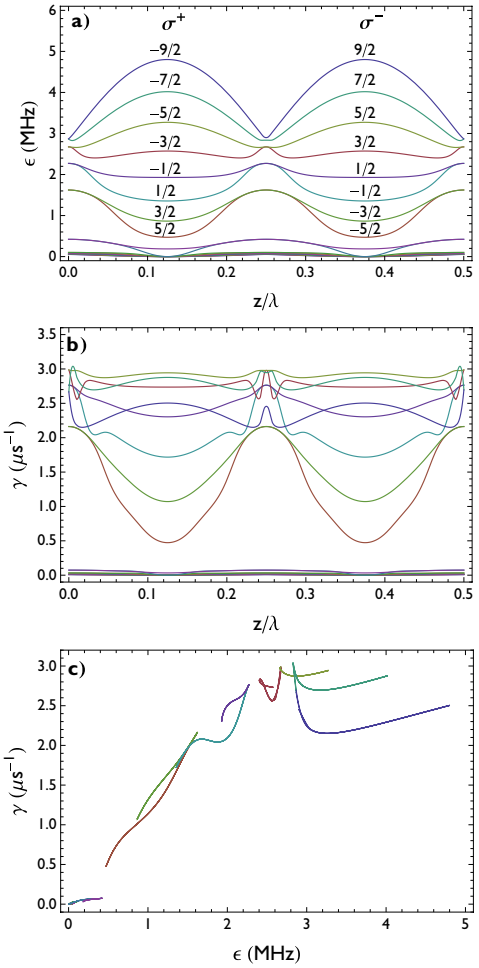

Fig. 3: (Color online) Semi-classical calculation of the effect of dual frequency counterpropagating laser beams in a 1D lin⊥lin configuration on a ^{40}K atom at rest. a) Light shifts ϵ *vs.* position; b) optical pumping rates γ; c) optical pumping rates *vs.* light shifts. The laser intensities are $I_{\mathrm{cool}} = 20 I_{\mathrm{sat}}$ and $I_{\mathrm{repump}} = I_{\mathrm{cool}}/8$ per beam, with $\delta = +3\Gamma$. The different lines correspond to the 18 dressed states of the $^2S_{1/2}$ ground state. At $z = \lambda/8$ the local polarization is σ^+ and here each curve corresponds to a pure m_F state. At this position the light shift increases with $-m_F$. The $|^2S_{1/2}, F = 7/2\rangle$ manifold interacts only weakly with light since the repumping beam is kept at low intensity. Consequently, the light shifts and optical pumping rates are small.

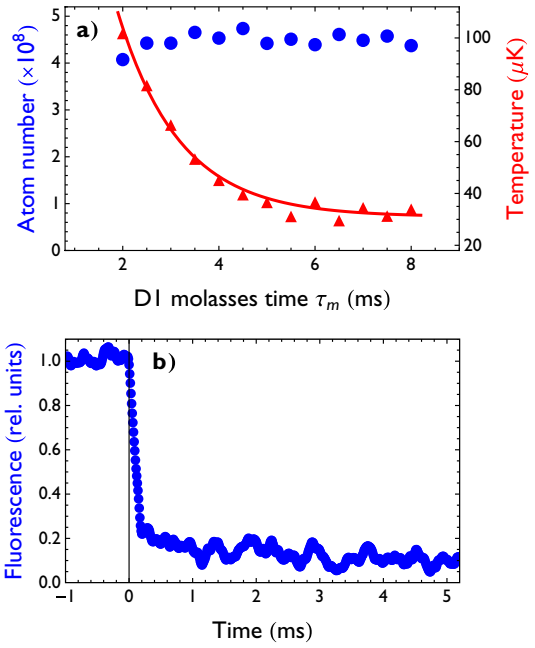

Fig. 4: (Color online) a) Number of atoms captured in the D_1 molasses (circles) and their temperature (triangles) as a function of molasses duration. The number of atoms in the compressed MOT was 4.5×10^8. b) Measured fluorescence during the MOT and the D_1 molasses phase. Both experiments were performed with $I_{\rm cool} = 14 I_{\rm sat}$, $\delta = 2.3\Gamma$ and $I_{\rm repump} = I_{\rm cool}/8$.

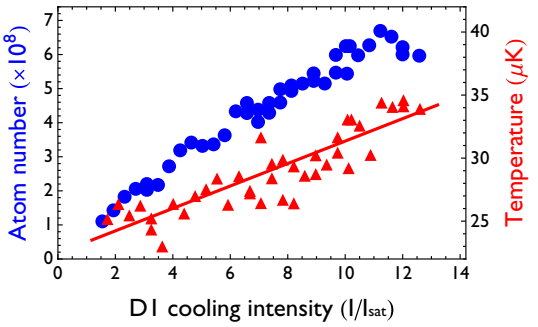

Fig. 5: (Color online) Number of atoms captured in the D_1 molasses (circles) and their temperature (triangles) as a function of the D_1 cooling beam intensity for $\delta = 2.3\Gamma$ and $I_{\rm repump} = I_{\rm cool}/8$. The number of atoms in the compressed MOT was 6.5×10^8 and the capture efficiency reaches $\sim$ 100% for $I \geqslant 11 I_{\rm sat}$.

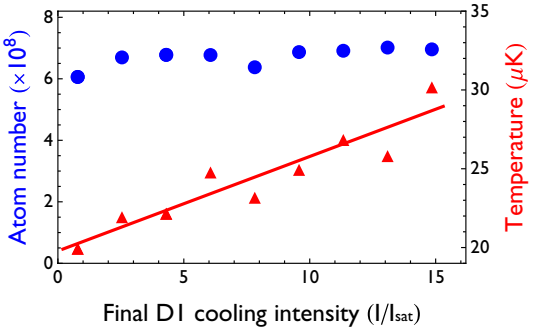

Fig. 6: (Color online) Number of atoms captured in the D_1 molasses (circles) and their temperature (triangles) after a 6 ms capture phase at high intensity $I_{\rm cool} = 14 I_{\rm sat}$ followed by a 2 ms linear intensity ramp to adjustable value. The detuning is fixed to $\delta = 2.3\Gamma$. The number of atoms in the compressed MOT was 7×10^8.

duration $\tau_{\rm m}$ (fig. 4). The temperature is determined by time of flight. At high intensity $I_{\rm cool} = 14 I_{\rm sat}$ and detuning $\delta = 2.3\Gamma$, all 4.5×10^8 compressed MOT atoms are cooled to a temperature of 30 μK in 6 to 8 ms. Although the initial temperature of the compressed MOT is rather high, D_1 cooling occurs rapidly. As shown in fig. 4a), the temperature drops from $\sim$ 4 mK to 100 μK in 2 ms, and reaches its asymptotic value in about 6 ms. These dynamics are confirmed by direct measurement of the fluorescence light emitted during the D_1 molasses phase, as displayed in fig. 4b). The fluorescence exhibits a fast decay in $\sim$ 200 μs to about 20% of the MOT light followed by a slower decay in $\sim$ 3 ms to 10%, which indicates the accumulation of atoms in weakly coupled states.

When repeating the experiment for lower D_1 laser intensities for a fixed time of 6 ms, we observe both a decrease of the number of atoms cooled by gray molasses and a further lowering of the temperature down to 24 μK (fig. 5). The number of atoms is measured after a time of flight of 20 ms, after which we would not detect any atoms in the absence of D_1 molasses. The capture efficiency increases with the cooling intensity indicating a higher capture velocity at higher laser intensity and it reaches $\sim$ 100% for $I \geqslant 11 I_{\rm sat}$. Similarly, the equilibrium temperature increases with laser intensity in the explored range in agreement with Sisyphus-type cooling mechanisms.

The results of fig. 4 and fig. 5 suggest implementing a cooling sequence with two successive phases. A first phase lasting 6 ms at high D_1 cooling intensity takes advantage of the high capture velocity. This phase is followed by a 2 ms stage in which the intensity is linearly reduced by an adjustable amount to further lower the temperature. As illustrated in fig. 6, this supplementary cooling phase allows the sample to reach a temperature of 20 μK by reducing the intensity by one order of magnitude and without any atom loss. No significant change of the atomic cloud volume was observed during this 8 ms sequence.

In fig. 7, we show the number of atoms captured in the D_1 molasses and their temperature as a function of the laser detuning δ for the complete 8 ms sequence. For $\delta \in [0.5\Gamma, 2\Gamma]$, we observe a steep decrease of the temperature from 100 μK to 30 μK, as expected from Sisyphus cooling,

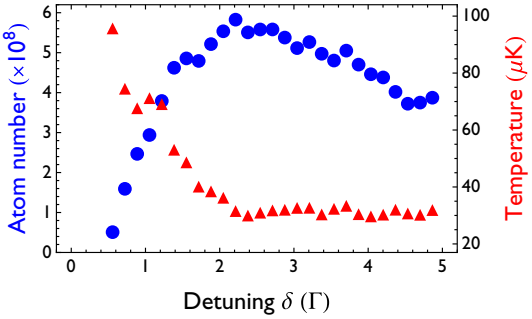

Fig. 7: (Color online) Number of atoms captured in the D_1 molasses (circles) and their temperature (triangles) for the dynamic 8 ms cooling sequence as a function of the detuning δ. The number of atoms in the compressed MOT was 6×10^8.

followed by a plateau near $30\,\mu$K for detunings above 2Γ. The capture efficiency raises sharply to $\sim 100\%$ at $\delta \sim 2.3\Gamma$, displays a broad maximum and slowly decreases above 4Γ, indicating a decrease of the capture velocity.

We have also scanned the intensity and the detuning of the repumping laser. We observe a very weak dependence of the molasses temperature and capture fraction upon repumping intensity. On the other hand, when scanning the repumper detuning, we observe that cooling is optimal within 300 kHz from the exact Raman condition. This points to the existence of long-lived coherences between the two hyperfine manifolds $|^2S_{1/2}, F = 9/2\rangle$ and $|^2S_{1/2}, F = 7/2\rangle$, resulting in the formation of new inter-manifold dark states. Finally, optimal parameters for ^{40}K gray molasses are summarized in table 1.

We checked that the minimum temperature of $20\,\mu$K is not limited by residual magnetic fields nor by atomic density. We found that the residual magnetic field during the D_1 molasses should be minimized. Indeed, introducing a small tunable bias magnetic field B in the vertical direction, the D_1 molasses temperature increased quadratically as $\Delta T \approx 80 B^2 \mu\mathrm{K/G}^2$. For this reason, the stray magnetic field was cancelled to less than 100 mG in three directions using compensation coils. We also searched for a density dependent temperature limitation and observed no significant temperature change when the density was reduced by a factor of 4 from $n_0 \sim 2 \times 10^{10}\mathrm{cm}^{-3}$. Modeling gray-molasses cooling in three dimensions in order to understand the temperature limit remains today an open problem.

Magnetic trapping. – After the D_1 molasses phase, the atoms are optically pumped to the $|^2S_{1/2}, F = 9/2, m_F = 9/2\rangle$ stretched state and then transferred into a quadrupole magnetic trap. The σ^+ polarized optical pumping laser beams are pulsed for $120\,\mu$s in the presence of a bias magnetic field. After this phase, the trap axial magnetic field gradient is raised from 0 to $37\,\mathrm{G \cdot cm}^{-1}$ in 3 ms, followed by a compression

Table 1: Optimized parameters for ^{40}K D_1 gray molasses. Using these parameters, all the 6.5×10^8 atoms from a compressed MOT are cooled to $20\,\mu$K in D_1 gray molasses.

	Duration (ms)	$I_{\mathrm{cool}}(I_{\mathrm{sat}})$	$\delta(\Gamma)$
Capture phase	6	14	+2.3
Cooling phase	2	14→1	+2.3

to 76 $\mathrm{G \cdot cm}^{-1}$ in 147 ms and a thermalization stage lasting 350 ms during which the field gradient remains constant. At this point we detect 2.5×10^8 atoms at a temperature of $80\,\mu$K. Assuming that all atoms are in the $|F = 9/2, m_F = 9/2\rangle$ stretched state, the central phase-space density is $\mathrm{PSD} = n_0 \lambda_{\mathrm{dB}}^3 \approx 2 \times 10^{-5}$. In the absence of gray-molasses phase, the central phase-space density is about 100 times lower. From the *p-wave* cross-section $\sigma \approx 2 \times 10^{-11}\,\mathrm{cm}^2$ at a temperature of $80\,\mu$K measured in [21], we estimate the trap averaged initial collision rate to be $\gamma_{\mathrm{coll}} = n_0 \sigma \bar{v}/8\sqrt{2} \approx 23\,\mathrm{s}^{-1}$. This rate is quite favorable for initiating evaporative cooling.

Conclusion. – We have shown that gray molasses operating on the D_1 optical transition is a very simple and powerful method to increase the phase space density of laser-cooled ^{40}K alkali gases to $\sim 10^{-5}$. This phase space density leads to excellent starting conditions for evaporative cooling in magnetic or optical dipole traps. For ^{40}K, this is particularly useful as the low temperature allows direct transfer into an optical trap and magnetic tuning to a Feshbach resonance for efficient evaporation. Moreover, our results open the way for sub-Doppler cooling of other atoms with narrow $P_{3/2}$ excited states, such as ^{6}Li and ^{7}Li. We already have experimental evidence for sub-Doppler D_1 cooling of ^{6}Li and ^{7}Li and this will be the subject of a future publication.

* * *

We acknowledge useful discussions with J. V. Porto, J. Dalibard, L. Khaykovich and D. Suchet. We acknowledge support from Région Ile de France (IFRAF), EU (ERC advanced grant Ferlodim) and Institut Universitaire de France. DRF acknowledges the support of Fundação para a Ciência e Tecnologia (FCT-Portugal), through the grant number SFRH/BD/68488/2010.

REFERENCES

[1] Inguscio M., Ketterle W. and Salomon C. (Editors), *Ultracold Fermi gases*, in *Proceedings of the International School of Physics "Enrico Fermi"*, Course CLXIV (IOS Press, Società Italiana di Fisica) 2006.

[2] Bloch I., Dalibard J. and Zwerger W., *Rev. Mod. Phys.*, **80** (2008) 885.

[3] Bulgac A., Forbes M. M. and Schwenk A., *Phys. Rev. Lett.*, **97** (2006) 020402.
[4] Werner F., Parcollet O., Georges A. and Hassan S. R., *Phys. Rev. Lett.*, **95** (2005) 056401.
[5] Dalibard J. and Cohen-Tannoudji C., *J. Opt. Soc. Am. B*, **6** (1989) 2023.
[6] Lin Z., Shimizu K., Zhan M., Shimizu F. and Takuma H., *Jpn. J. Appl. Phys.*, **30** (1991) L1324.
[7] Modugno G., Benkö C., Hannaford P., Roati G. and Inguscio M., *Phys. Rev. A*, **60** (1999) R3373.
[8] DeMarco B. and Jin D. S., *Science*, **285** (1999) 1703.
[9] Taglieber M., Voigt A.-C., Aoki T., Hänsch T. W. and Dieckmann K., *Phys. Rev. Lett.*, **100** (2008) 010401.
[10] Gokhroo V., Rajalakshmi G., Easwaran R. K. and Unnikrishnan C. S., *J. Phys. B: At. Mol. Opt. Phys.*, **44** (2011) 115307.
[11] Landini M., Roy S., Carcagn L., Trypogeorgos D., Fattori M., Inguscio M. and Modugno G., *Phys. Rev. A*, **84** (2011) 043432.
[12] Duarte P., Hart R., Hitchcock J., Corcovilos T., Yang T.-L., Reed A. and Hulet R., *Phys. Rev. A*, **84** (2011) 063420.
[13] McKay D., Jervis D., Fine D., Simpson-Porco J., Edge G. and Thywissen J., *Phys. Rev. A*, **84** (2011) 063420.
[14] Grynberg G. and Courtois J.-Y., *Europhys. Lett.*, **27** (1994) 41.
[15] Boiron D., Meacher D. and Verkerk P., *Phys. Rev. A*, **52** (1995) 3425.
[16] Esslinger T., Sander F., Hemmerich A., Hänsch T. W., Ritsch H. and Weidemüller M., *Opt. Lett.*, **21** (1996) 991.
[17] Boiron D., Michaud A., Lemonde P., Castin Y., Salomon C., Weyers S., Szymaniec K., Cognet L. and Clairon A., *Phys. Rev. A*, **53** (1996) R3734.
[18] Ol'shani M. and Minogin V., *Opt. Commun.*, **89** (1992) 393.
[19] Castin Y. and Dalibard J., *Europhys. Lett.*, **14** (1991) 761.
[20] Ridinger A., Chaudhuri S., Salez T., Eismann U. Fernandes D., Magalhaes K., Wilkowski D., Salomon C. and Chevy F., *Eur. Phys. J. D*, **242** (2011) 223.
[21] DeMarco B., Bohn J. L., Burke J. P., Holland M. and Jin D. S., *Phys. Rev. Lett.*, **82** (1999) 4208.

Simultaneous sub-Doppler laser cooling of fermionic ^{6}Li and ^{40}K on the D_1 line: Theory and experiment

Franz Sievers,[1,*] Norman Kretzschmar,[1] Diogo Rio Fernandes,[1] Daniel Suchet,[1] Michael Rabinovic,[1] Saijun Wu,[2,†] Colin V. Parker,[3] Lev Khaykovich,[4] Christophe Salomon,[1] and Frédéric Chevy[1]

[1]*Laboratoire Kastler Brossel, École Normale Supérieure, CNRS, UPMC, 24 rue Lhomond, 75005 Paris, France*

[2]*State Key Laboratory of Surface Physics and Department of Physics, Fudan University, 200433 Shanghai, People's Republic of China*

[3]*James Franck Institute, Enrico Fermi Institute and Department of Physics, University of Chicago, Chicago, Illinois 60637, USA*

[4]*Department of Physics, Bar-Ilan University, Ramat-Gan 52900, Israel*

(Received 30 October 2014; revised manuscript received 30 January 2015; published 23 February 2015)

We report on simultaneous sub-Doppler laser cooling of fermionic ^{6}Li and ^{40}K using the D_1 optical transitions. We compare experimental results to a numerical simulation of the cooling process applying a semiclassical Monte Carlo wave-function method. The simulation takes into account the three-dimensional optical molasses setup and the dipole interaction between atoms and the bichromatic light field driving the D_1 transitions. We discuss the physical mechanisms at play, identify the important role of coherences between the ground-state hyperfine levels, and compare D_1 and D_2 sub-Doppler cooling. In 5 ms, the D_1 molasses phase greatly reduces the temperature for both ^{6}Li and ^{40}K at the same time, with final temperatures of 44 and 11 μK, respectively. For both species this leads to a phase-space density close to 10^{-4}. These conditions are well suited to direct loading of an optical or magnetic trap for efficient evaporative cooling to quantum degeneracy.

DOI: 10.1103/PhysRevA.91.023426 PACS number(s): 37.10.De, 32.80.Wr, 67.85.−d

I. INTRODUCTION

The road towards quantum degeneracy in atomic gases usually starts with a laser cooling and trapping phase. The resulting initial phase-space density of the atomic ensemble and the initial collision rate should be as high as possible for initiating efficient evaporative cooling to quantum degeneracy. Sub-Doppler cooling has proven to be a powerful technique to increase the phase-space density of most alkali atoms and other atoms with multiple-level structure [1–3]. However, in the case of lithium and potassium, the narrow excited-state structure of the D_2 transition compromises the efficiency of this cooling scheme [4,5]. Both species possess stable fermionic and bosonic isotopes, and they play an important role in recent experimental studies of strongly correlated quantum gases. Thus, important efforts have been devoted to searching for alternative laser cooling schemes.

For instance, it has recently been shown that three-dimensional (3D) Sisyphus cooling for ^{7}Li, some gigahertz red detuned from the D_2 line, can lead to temperatures as low as 100 μK, with up to 45% of the atoms in the cooled fraction [6]. A second option is to operate the magneto-optical trap (MOT) on a transition with a smaller linewidth to reduce the Doppler temperature [7–9]. Such transitions exist for ^{6}Li and ^{40}K in the near-UV and blue regions of the spectrum, respectively, leading to temperatures of 33 μK for ^{6}Li and 63 μK for ^{40}K. Yet, special optics and a coherent source at 323 nm for ^{6}Li and at 405 nm for ^{40}K are needed for this approach. Additionally, at these wavelengthes the available power is still a limiting factor.

More recently a simpler sub-Doppler cooling scheme using blue-detuned molasses operating on the D_1 line was proposed and demonstrated on ^{40}K [10] and has been extended to other atomic species such as ^{7}Li [11], ^{39}K [12,13], and ^{6}Li [14]. Using this technique, temperatures as low as 20 μK (^{40}K), 50 μK (^{7}Li), 6 μK (^{39}K), and 40 μK (^{6}Li) were reached.

Even though the main ingredients of the D_1 cooling scheme are now understood at a qualitative level, in particular, the role of the coherences between hyperfine ground-state levels [11], a complete picture, taking into account the full level structure of the atoms, is still missing. In this paper, we present a 3D semiclassical solution of the optical Bloch equations that takes into account the full set of relevant energy levels of alkali atoms and we apply it to the case of ^{6}Li and ^{40}K. The model fully confirms the experimentally observed cooling behavior and its robustness with respect to changes in experimental parameters. The model is validated by a good match between the simulation and the experimentally measured temperature and fluorescence rate. We recover the important role of the Raman detuning between the main cooling laser and the repumping laser on the achievable temperature. We show here, for both ^{6}Li and ^{40}K, that the gain in temperature of a factor of $\sim$3 at the exact Raman resonance is well reproduced by the theoretical model and that the amount of coherence between both hyperfine states shows a pronounced resonance behavior. Beyond individual studies of the two species, we also show experimentally that simultaneous cooling of ^{6}Li and ^{40}K does not lead to any severe trade-off and is technically easy to implement. We are able to capture more than 1×10^9 atoms of each species, with a capture efficiency exceeding 60% from a compressed magneto-optical trap (CMOT), and reach temperatures as low as 44 μK for ^{6}Li and 11 μK for ^{40}K within 5 ms.

II. D_1 COOLING MECHANISM

In a typical D_1 cooling setup (Fig. 1), all the D_1 hyperfine levels are involved in the interaction. The sub-Doppler cooling effects include a mix of Sisyphus cooling, motion-induced and off-resonant light coupling from gray to bright levels, and

*franz.sievers@lkb.ens.fr
†saijunwu@fudan.edu.cn

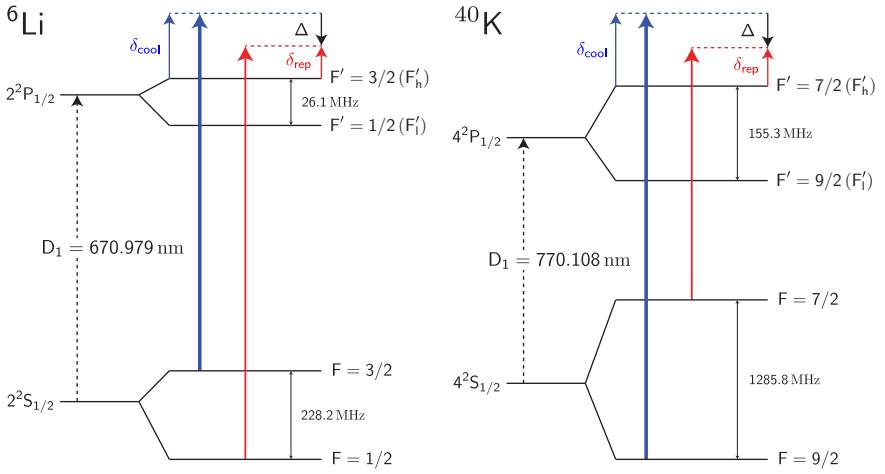

FIG. 1. (Color online) Cooling scheme on the ^{6}Li and ^{40}K D_1 lines. The cooling beam (blue) is blue detuned by $\delta_{\rm cool}$ from the $|F = 3/2\rangle \rightarrow |F'_h = 3/2\rangle$ ($|F = 9/2\rangle \rightarrow |F'_h = 7/2\rangle$) transition, where F'_h (F'_l) is the upper (lower) excited-state level. The repumping beam (red) is blue detuned by $\delta_{\rm rep}$ from the $|F = 1/2\rangle \rightarrow |F'_h = 3/2\rangle$ ($|F = 7/2\rangle \rightarrow |F'_h = 7/2\rangle$) transition. Detuning from the Raman condition is denoted $\Delta = \delta_{\rm rep} - \delta_{\rm cool}$.

coherent population trapping of slow atoms in nearly decoupled states. In this section we first introduce our semiclassical laser cooling model. We then present and compare the results from experimental observations and numerical simulations and, finally, discuss the physical mechanism of D_1 cooling.

A. Semiclassical Monte Carlo simulation

The level diagrams of our bichromatic cooling scheme for both ^{6}Li and ^{40}K are depicted in Fig. 1. The D_1 molasses is composed of a 3D lattice whose polarization configuration is the same as that of a six-beam standard MOT, but with two sidebands to address the $|F = 3/2\rangle$ and $|F = 1/2\rangle$ hyperfine ground states of ^{6}Li (respectively, $|F = 9/2\rangle$ and $|F = 7/2\rangle$ for ^{40}K) in the D_1 Λ system at positive detunings.

Here, by convention, we refer to the $|F = 3/2\rangle \rightarrow |F'_h\rangle$ and $|F = 1/2\rangle \rightarrow |F'_h\rangle$ transitions as cooling and repumping transitions. It is, however, important to note that neither the cooling nor the repumping D_1 transitions are actually closed.

Our numerical simulation of the cooling process is based on a semiclassical Monte Carlo wave-function method. The simulation takes into account the 3D optical molasses setup and the dipole interaction between the single atoms and the polarized light driving the transitions of the D_1 manifold, which is spanned by the $4(2I + 1)$ hyperfine Zeeman sublevels ($I > 0$ is the nuclear spin). We treat the external states of the atom classically and update its position $\mathbf{r}(t)$ and velocity $\mathbf{v}(t)$ according to the calculated expectation value of the light force:

$$\mathbf{f}(t) = \frac{\langle\psi(t)| - \nabla H_{\rm eff}(\mathbf{r}(t))|\psi(t)\rangle}{\langle\psi(t)|\psi(t)\rangle}. \quad (1)$$

The atomic internal states $|\psi(t)\rangle$ evolve in a dressed basis with respect to the cooling laser (Fig. 1), according to the Monte Carlo wave-function method [15,16] with the effective rotating-wave Hamiltonian

$$H_{\rm eff} = H_0 + H_{F=I-1/2} + H_{F=I+1/2} - i\hat{\Gamma}/2, \quad (2)$$

where

$$H_0 = \sum_m |F = I - 1/2, m\rangle\hbar\Delta\langle F = I - 1/2, m| - \sum_{F'm'} |F', m'\rangle\hbar(\delta_{\rm cool} + \delta_{{\rm hfs},F'})\langle F', m'|. \quad (3)$$

Here H_0 operates over the whole D_1 manifold and $\delta_{\rm cool}$ is the detuning of the cooling laser with respect to the $F = I + 1/2 \rightarrow F'_h$ transition, where F'_h (Fig. 1) corresponds to the excited hyperfine level that is higher in energy, e.g., $F'_h = 3/2$ for ^{6}Li and $F'_h = 7/2$ for ^{40}K. $\Delta = \delta_{\rm rep} - \delta_{\rm cool}$ is the two-photon detuning for the $F = I - 1/2 \rightarrow F = I + 1/2$ Raman transition, $\delta_{{\rm hfs},F'}$ the hyperfine splitting of the excited state for F'_l, and 0 for F'_h. The 0 of energy is chosen as that of the bare $F = I + 1/2$ ground state.

The light-atom coupling Hamiltonian

$$H_{F=I\pm1/2} = \hbar \sum_{m,\sigma,F',m'} \Omega_{F,\sigma} c_{F,m,\sigma,F',m'} \times |F, m\rangle\langle F', m'| + {\rm H.c.} \quad (4)$$

describes the cooling ($F = I + 1/2$) and repumping ($F = I - 1/2$) interactions [17]. Here $\Omega_{F,\sigma}$ are the Rabi frequencies of the repumping and cooling laser beams for $F = I - 1/2$ $F = I + 1/2$, respectively. $c_{F,m,\sigma,F'm'}$ represent the Clebsch-Gordan coefficients associated with the transitions coupled by σ polarized light. To take into account the radiation damping we include the spontaneous emission rate $\hat{\Gamma} = \Gamma\hat{P}_{ee}$ where Γ is the excited-state linewidth and $\hat{P}_{ee} = \sum_{F',m'} |F'm'\rangle\langle F'm'|$. This leads to a decay of the internal-state wave-function norm $\langle\psi(t)|\psi(t)\rangle$. The speed of this decay probabilistically dictates the collapse of the internal quantum states in the numerical simulation, which corresponds to spontaneous emission. We take into account the polarization of the spontaneous scattering photon and follow the standard quantum jump procedure to project the atomic states to ground states, with the norm

reset to unity [15]. To effectively account for heating due to both absorption and spontaneous emission, we assign a recoil momentum shift to $\mathbf{v}(t)$ twice before continuing to evolve $|\psi(t)\rangle$ via $H_{\rm eff}(\mathbf{r}(t))$.

The simulations are performed with parameters matching the experimental setup by properly introducing the spatially dependent $\Omega_{F,\sigma}(\mathbf{r})$, the detunings Δ, $\delta_{\rm cool}$, and atomic initial conditions. To reproduce experimental conditions, we fix the relative phases for all 12 cooling and repumping laser beams at values randomized for each simulation trial. We record the evolution of the 3D atomic velocity, the time-stamped fluorescence events corresponding to quantum jumps, and internal-state properties such as state population and coherence. The observables are averaged over multiple simulation trials for comparison with the experiment.

B. Raman-detuning dependence for ^{6}Li

A critical parameter in the D_1 molasses scheme is the Raman detuning Δ (Fig. 1). In the following we investigate the Raman-detuning dependence of the ^{6}Li molasses temperature and fluorescence rate both theoretically and experimentally, for various cooling and repumping laser intensities.

Our ^{6}Li-^{40}K machine is described in [18]. We first load a lithium MOT using a laser-slowed atomic beam (Zeeman slower). After a compressed MOT phase the magnetic field and the D_2 light are switched off and the D_1 molasses is applied (a more detailed description of the sequence is presented in the Appendix). To probe the Raman-detuning dependence we apply a 100-μs D_1 molasses pulse with variable Δ to an atomic cloud precooled to 100 μK. Figures 2(a) and 2(b) show the fluorescence rate and the temperature after the pulse as functions of the Raman detuning Δ for the intensities used in the simulations. We observe a temperature dip at zero Raman detuning and a heating and fluorescence peak at positive Δ whose position and amplitude are correlated with the molasses intensity.

In the simulations we set the initial velocity of lithium to 0.2 m/s ($T \sim 30\ \mu$K). The simulation time is set to 200 μs. In the first 100 μs we allow the cooling dynamics to equilibrate, and during the second 100 μs we record the velocity $\mathbf{v}(t)$ as well as the time-stamped quantum jump events to calculate the equilibrium temperature and fluorescence rate. At each Raman detuning we average over 25 trajectories. The simulation results for two intensities, $I_{\rm cool} = 2.7\, I_{\rm sat}$, $I_{\rm rep} = 0.13\, I_{\rm sat}$ and $I_{\rm cool} = 9\, I_{\rm sat}$, $I_{\rm rep} = 0.46\, I_{\rm sat}$, are shown in Figs. 2(c) and 2(d), respectively (here $I_{\rm sat}$ refers to the saturation intensity of the D_2 line).

The simulated heating and fluorescence peak positions for low and high intensities (Fig. 2) agree well with the experimental findings. Also, the shift between the heating and the fluorescence peak, which increases with the molasses intensity, is numerically reproduced without any freely adjustable parameters.

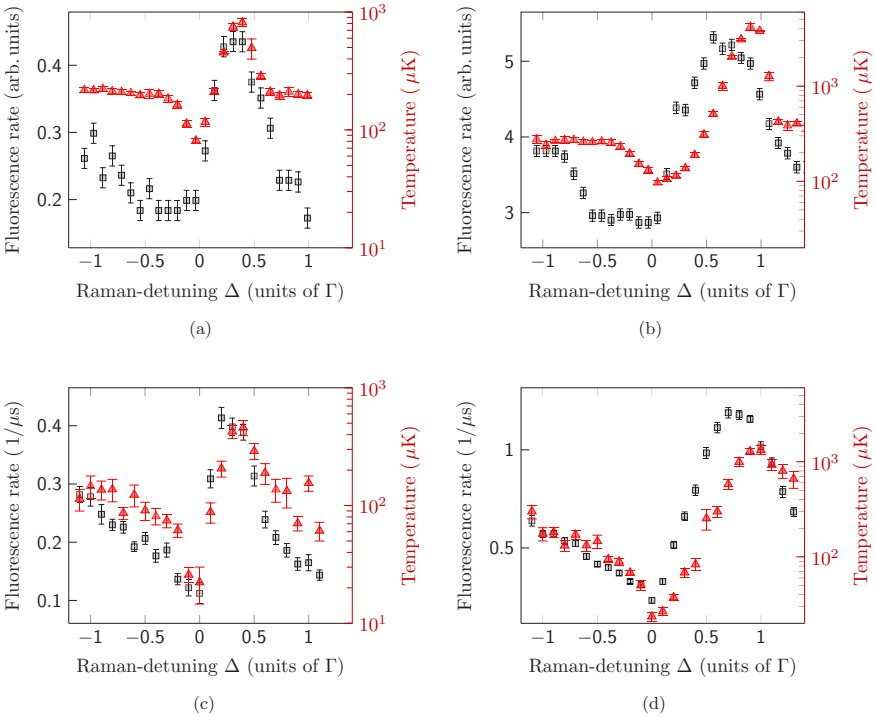

FIG. 2. (Color online) Fluorescence (squares) and temperature (triangles; logarithmic scale) of the ^{6}Li atomic cloud after a 100-μs pulse of D_1 light with variable Raman detuning Δ. Experiment: (a) low intensity; (b) high intensity. Simulation: (c) low intensity; (d) high intensity. Experimental and simulation results (a, c) for $I_{\rm cool} = 2.7 I_{\rm sat}$, $I_{\rm rep} = 0.13 I_{\rm sat}$ and (b, d) for $I_{\rm cool} = 9\, I_{\rm sat}$, $I_{\rm rep} = 0.46\, I_{\rm sat}$ per beam.

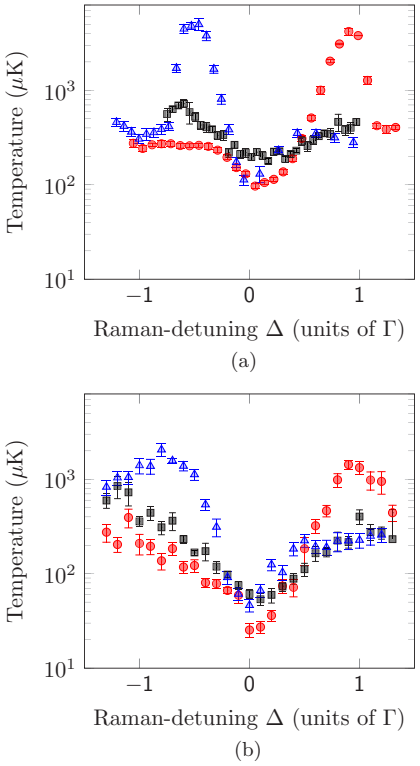

FIG. 3. (Color online) Temperature of the ^{6}Li D_1 molasses after a 100-μs pulse with variable Raman detuning Δ for different cooling and repumping intensities. (a) Experiment; (b) simulation. Standard intensities [(red) circles]: $I_{\rm cool} = 9\, I_{\rm sat}$, $I_{\rm rep} = 0.46\, I_{\rm sat}$. Equal cooling/repumping ratio (black squares): $I_{\rm cool} = I_{\rm rep} = 9\, I_{\rm sat}$. Inverted cooling/repumping ratio [(blue) triangles]: $I_{\rm cool} = 0.6\, I_{\rm sat}$, $I_{\rm rep} = 4.6\, I_{\rm sat}$.

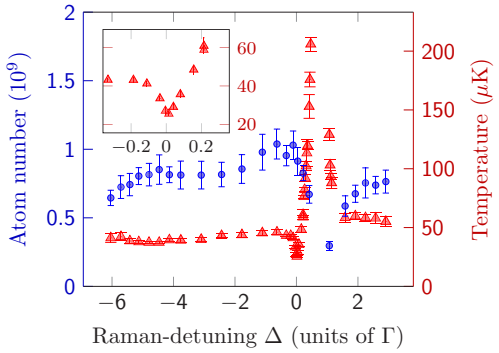

FIG. 4. (Color online) Experiment: Atom number and equilibrium temperature of the ^{40}K D_1 molasses as functions of the Raman detuning Δ. $\delta_{\rm cool} = 3\ \Gamma$, $I_{\rm cool} = 6\, I_{\rm sat}$, $I_{\rm rep}/I_{\rm cool} = 7.6\%$, $t_{\rm m} = 5$ ms. In the constant-temperature regions below $-0.1\ \Gamma$ and above $2\ \Gamma$ gray molasses cooling involves coherences between Zeeman states in a given hyperfine state but not between hyperfine states. At the exact Raman condition $\Delta = 0$, long-lived coherences between hyperfine states are established, as shown in the simulation in Fig. 5. In a narrow detuning range, the temperature [(red) triangles] drops to 20 μK. Inset: Expanded scale.

Despite the nice match between simulations and experiments in Figs. 2 and 3, we observe that the semiclassical simulations provide temperatures that are systematically lower by a factor of 2 to 4 than the measured ones, particularly near the Raman-resonance condition $\Delta = 0$. Here the simulation predicts a temperature of 20 μK, whereas the lowest measured temperature is 50 μK. The reason for this is not fully understood and may come from both theory and experimental limitations. First, the simulation is semiclassical and neglects the wave-function extent of the cold atoms. The predicted temperature of 20 μK corresponds to only six times the recoil energy $E_R = \frac{1}{2} m v_{\rm recoil}^2 = k_B \times 3.5\ \mu$K. Therefore, only a quantum treatment of the atoms' external motion can be expected to give a quantitative equilibrium temperature prediction in the low-intensity limit. In the simulation we observe that slow atoms are likely trapped within subwavelength regions, where the light shift is minimal and the atom is nearly decoupled from light over a long time without quantum jump. This coherent population trapping effect enhances the cooling at both large and small Δ, although it is most pronounced at the Raman resonance ($\Delta = 0$) since more choices of decoupled states emerge. The semiclassical picture clearly exaggerates the cooling effect since the wave nature of the atoms' external motion is not included in the model. In fact, the wave function of the slow atoms will sample a larger volume of the subwavelength traps and will shorten the lifetime of the dark periods.

On the experimental side the residual magnetic field cancellation has only been coarsely tuned for the data set presented in Fig. 2 (as well as in Figs. 3 and 4). With careful tuning of the magnetic field zeroing we were able to lower the ^{40}K temperature to 11 μK (Sec. II C, on ^{40}K) for lower-density samples. Interestingly, other groups have indeed found on ^{39}K lower temperatures (6 μK) than ours under the Raman condition [12]. Note also that in Fig. 2 for positive Raman detunings ($\Delta \sim 0.5\Gamma$ at low intensity and $\Delta \sim \Gamma$ at high intensity) the "temperature" corresponds to out-of-equilibrium situations as the atoms are quickly heated away and lost from the molasses. The notion of temperature should thus be taken with care in this region, unlike for negative Raman detunings, where a steady-state temperature is reached.

Another reason for shortening the lifetime of dark periods of the slow atoms is reabsorption of photons emitted by other atoms. We have indeed seen a density-dependent excess temperature, which we measured to be 4.6 μK $\times\ 10^{11}$ at/cm^3 for ^{40}K. A careful simulation of cooling including photon reabsorption processes is far more complex and is beyond the scope of this work.

We also study the same Raman-detuning-dependent effects, but for different cooling/repumping ratios. Typical experimental and simulation results are presented in Fig. 3. Here again, the simulation parameters are chosen according to the experimental values. The simulation and experiments match fairly well. In particular, for the usual configuration with $I_{\rm cool}/I_{\rm rep} > 1$ ($I_{\rm cool} = 9 I_{\rm sat}$ and $I_{\rm rep} = 0.45 I_{\rm sat}$), we observe a

heating peak at $\Delta > 0$. When inverting the roles of the cooling and repumping light, i.e., $I_{\rm cool}/I_{\rm rep} < 1$ ($I_{\rm cool} = 0.6 I_{\rm sat}$ and $I_{\rm rep} = 4.6 I_{\rm sat}$), the heating peak appears for $\Delta < 0$ instead. In all cases, cooling is most efficient at the Raman resonance ($\Delta = 0$). Finally, for $I_{\rm cool}$ equal to $I_{\rm rep}$, both as large as $9 I_{\rm sat}$, we observe less efficient cooling at $\Delta = 0$, with moderate heating at blue and red detunings.

C. Raman-detuning dependence for ^{40}K

Typical simulation results for ^{40}K are shown in Fig. 5(a). Compared to ^{6}Li, simulations for ^{40}K require a significantly higher computational power due to the larger internal-state dimensions as well as the larger atomic mass and therefore slower cooling dynamics. To save computation time, we start at a velocity of 0.2 m/s ($T \sim 50\ \mu$K) and set the simulation time to 2 ms. We record the velocity $\mathbf{v}(t)$ as well as the time-stamped quantum jump events for $t > 1$ ms to calculate the fluorescence rate. For each Raman detuning Δ, 13 trajectories are simulated.

Experimental results for ^{40}K are presented in Fig. 4, which shows the temperature and atom number of the D_1 molasses as functions of the Raman detuning Δ. The total molasses

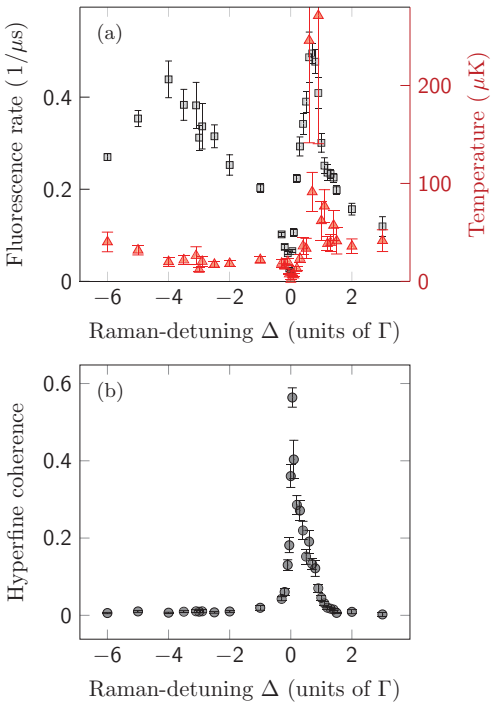

FIG. 5. (Color online) Simulation: Hyperfine coherence and Λ-enhanced cooling for the ^{40}K D_1 molasses. Simulation time, 2 ms; $\delta_{\rm cool} = 3\ \Gamma$; $I_{\rm cool} = 6 I_{\rm sat}$; $I_{\rm rep}/I_{\rm cool} = 7.6\%$. (a) Fluorescence (squares) and temperature (triangles) as functions of the Raman detuning Δ. (b) Coherence $4 \cdot \langle \rho^2_{F=7/2,F=9/2} \rangle$ between the two hyperfine ground states, $F = 7/2$ and $F = 9/2$ (see Sec. II E). The coherence is peaked under the Raman-resonance condition, with a width matching the temperature dip.

duration $t_{\rm m} = 5$ ms. In the last 2 ms a linear intensity ramp to $I_{\rm cool} = 6 I_{\rm sat}$ is performed. Just like ^{6}Li, we observe a sharp temperature drop under the Raman condition, a heating resonance at $\sim 0.7\ \Gamma$, and constant-temperature regions below $-0.1\ \Gamma$ and above $2\ \Gamma$. For the constant-temperature regions the temperature $T \sim 45\ \mu$K is low compared to the Doppler temperature $T_{\rm Doppler,K} = 145\ \mu$K. Under the Raman condition the temperature decreases to $23\ \mu$K. Under carefully optimized conditions we measured temperatures as low as $11\ \mu$K.

As for ^{6}Li, the comparison between Fig. 4 and Fig. 5(a) again demonstrates the qualitative agreement between simulations and experimental results and that the heating peak position is reproduced by the simulation without adjustable parameters. Interestingly, the inverted hyperfine structure in the ground and excited states of ^{40}K and the different $F \to F' = F - 1$ transition for the cooling laser and $F \to F' = F$ repumping transition does not significantly modify the D_1 cooling scheme compared to ^{6}Li.

D. The D_1 cooling mechanism

The agreement between simulation and experiment suggests that the semiclassical picture is able to catch the essential physics behind the D_1 molasses cooling. In particular, the mechanisms behind the cooling dips and heating peaks in Figs. 2 to 4, previously interpreted using the dressed atom picture with a simplified three-level model [11], survive in the full level scheme of the D_1 transition.

It is well known that efficient D_2 sub-Doppler cooling requires isolated excited hyperfine levels for alkaline atoms [4,5]. In contrast, D_1 gray molasses operates well even when all D_1 levels are excited (as in the case of ^{6}Li) and even at zero excited-state hyperfine splitting as confirmed numerically. The robustness of D_1 molasses is also seen in its insensitivity to the relative phase between the "cooling" and the "repumping" lattices, a critical parameter for D_2 bichromatic cooling where no polarization gradient was introduced [19].

In the following we discuss the physics behind the robustness of the D_1 sub-Doppler cooling. We then revisit the cooling dips and heating peaks in Figs. 2 to 4.

We note that all the dipole-allowed D_1 transitions (Fig. 1) are "open": when addressed with weak off-resonant light, the probability of inelastic (m_F- or F-changing) photon scattering is comparable to or higher than that of elastic scattering. When blue detuned from the D_1 transitions, an off-resonant bichromatic lattice can establish a correlation between the spatially varying light shift (due to virtual elastic scattering) and decay (due to real inelastic scattering) for the dressed ground states, since a larger light shift is accompanied by a stronger light-atom coupling and typically a larger inelastic scattering cross section.

We verify this idea with the full D_1 model for ^{6}Li atoms subjected to a 1D lattice with orthogonal linear polarizations (lin $\perp$ lin configuration) with typical cooling parameters. The spatially varying light shifts ϵ of the six dressed ground states of ^{6}Li are plotted in Fig. 6(a). The decay of the dressed states, due to inelastic light scattering, is characterized by the decay rate γ, which is plotted versus ϵ in Fig. 6(d). We see a correlation between ϵ and γ for $\epsilon < 1.5$ MHz. This correlation is robustly established for the D_1 transitions, as

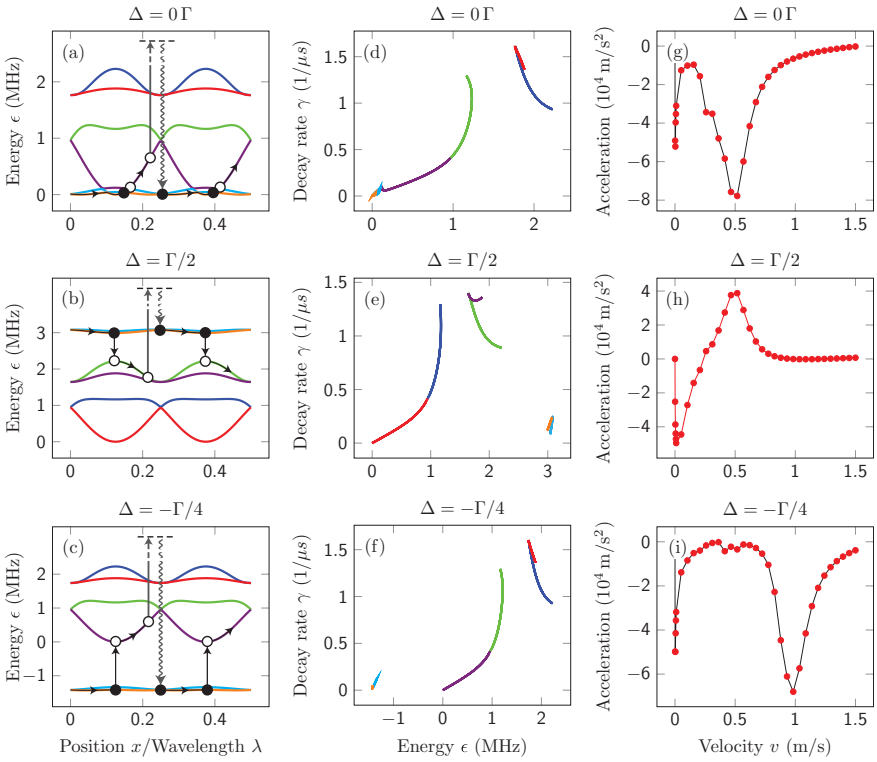

FIG. 6. (Color online) Cooling mechanism around the Raman condition in a simplified model. Optical Bloch equation simulation for ^{6}Li subjected to a 1D bichromatic lattice with linear orthogonal polarizations near D_1 resonance. The cooling lattice and repumping lattice are displaced by π ($\lambda/4$). $I_{\text{cool}} = 15I_{\text{sat}}$, $I_{\text{rep}} = 0.75I_{\text{sat}}$, $\delta_{\text{cool}} = 4\,\Gamma$. (a–c) Dressed states as functions of the position, in units of the D_1 optical wavelength. The two dressed $F = 1/2$ levels (light blue and orange) are nearly flat in all the graphs due to the small I_{rep}. (d–f) Decay rate of dressed states as a function of their energy shifts. Here the two dressed $F = 1/2$ levels span a very small energy range and have a low decay rate. (g–i) Velocity-dependent optical force for an atom dragged at velocity v. (a, d, g) $\Delta = 0$; (b, e, h) $\Delta = \Gamma/2$; (c, f, i) $\Delta = -\Gamma/4$. Note the negative sign of the force in (g) and (i), implying cooling, and the anticooling force for velocities near 0.5 m/s in (h).

verified numerically in the more complicated 3D lattices and for other atomic species. The correlation even persists for a fictitious atom with vanishing D_1 hyperfine splitting and reduced m_F-changing light scattering [20].

Such a correlation between the spatially dependent light shift ϵ and decay rate γ has two consequences: First, atoms with $kv < \gamma$ tend to accumulate in dressed states with low light shifts, which facilitates cooling through motion-induced coupling to higher energy dressed states [21]. This coupling is nonadiabatic as in the famous σ^+–σ^- 1D velocity selective coherent population trapping subrecoil cooling mechanism (VSCPT), where the spatial gradient of the atomic wave function induces a coupling to a bright state. Second, for a slowly moving atom that adiabatically follows a particular dressed state, the atom tends to leave the dressed state when the light shift is high, leading to Sisyphus cooling. In addition, at locations where $\epsilon, \gamma \sim 0$, slow atoms can be confined near the local dark states such as those in Fig. 6(a) near $x = 0, \lambda/8, \lambda/4, 3\lambda/8$ [22]. The resulting optical cooling force is plotted in Fig. 6(g) and is negative (cooling effect) over a broad range. We emphasize that this simplified 1D analysis remains valid in the more complex 3D beam geometry and is not restricted to ^{6}Li atoms. The D_1 laser cooling mechanism applies to all alkalis, even those amenable to efficient D_2 sub-Doppler cooling such as cesium and rubidium. As D_1 laser cooling involves dark states, it is less affected by density-dependent photon multiple scattering and heating than D_2 sub-Doppler cooling. Therefore it would be interesting to quantify the gain in phase-space density by applying D_1 sub-Doppler cooling for these atoms.

In comparison, sub-Doppler cooling on the D_2 lines is significantly different. While the $F = I \pm 1/2 \rightarrow F' = I \pm 1/2$ transitions are as "open" as in D_1, the $F = I + 1/2 \rightarrow F' = I + 3/2$ and $F = I - 1/2 \rightarrow F' = I - 3/2$ transitions have both "closed" and open transitions. Here the closed transitions are characterized by a greater-than-unity elastic-to-inelastic scattering ratio. If the $F = I + 1/2 \rightarrow F' = I + 3/2$ transitions can be isolated, then by taking advantage of the nearly closed $m_F - m_{F'}$ transitions, a correlation between the light shift and the decay rate can be established with (instead) a red-detuned lattice, as in standard sub-Doppler cooling [1–3]. However, in the case of small hyperfine splitting the open hyperfine transitions are as well addressed at red detuning, leading to short-lived potential minima and

degraded correlations, contributing to the inefficiency of the sub-Doppler cooling [23].

E. Physical picture of the Raman-detuning effect

We now extend the three-level picture in Ref. [11] to understand the details of the experiment. The cooling dips observed both experimentally and numerically under the Raman-resonance condition are also fairly easy to understand in the full model: At $\Delta = 0$ the resonant Raman-coupling splits the $F = I \pm 1/2$ hyperfine ground states into a bright and a dark manifold. The dark manifold is weakly coupled to the molasses. More precisely, the coupling strength of the Raman dark manifold is even weaker than those due to individual cooling-repumping couplings. Therefore the emergence of the Raman dark manifold enhances all sub-Doppler cooling effects.

Since the dark manifold is a coherent superposition of the two hyperfine states $F_1 = I - 1/2$ and $F_2 = I + 1/2$, we expect that laser-cooled atoms mostly occupy the dark manifold and therefore display a hyperfine coherence ρ_{F_1,F_2} with significant amplitude. To test this picture, we record the time-dependent off-diagonal density matrix quantity $4 \cdot \langle \rho^2_{F_1,F_2}(t) \rangle$ for all the quantum trajectories of the numerical simulations. The factor 4 ensures the normalization to one for the maximally coherent situation. To compute the two-photon detuning Δ-dependent quantity $4 \cdot \langle \rho^2_{F_1,F_2} \rangle$, we average over both the equilibrium time and many quantum trajectories at fixed Δ. Typical results for ^{40}K are given in Fig. 5, with the cooling parameters corresponding to Fig. 4. We see that the coherence $4 \cdot \langle \rho^2_{F_1=7/2,F_2=9/2} \rangle$ is peaked under the Raman-resonance condition and becomes significant, with a width matching the temperature dip.

As in Figs. 2 to 4 and [11] we now explain the heating peaks with the full D_1 model. We first focus on the case of $I_{\rm cool} \gg I_{\rm rep}$ so that at large $|\Delta|$ the dressed $F = I - 1/2$ hyperfine level is relatively long-lived and populated. As shown in Figs. 6(b) and 6(c), the Raman detuning Δ determines the energy level of the dressed $F = I - 1/2$ hyperfine level, and it is clear that when $\Delta < 0$, the motion-induced coupling to the dressed $F = I + 1/2$ level should still contribute to cooling [as in Figs. 6(c), 6(f), and 6(i)] [21], apart from Sisyphus cooling. On the contrary, for $\Delta > \max[\epsilon_{F=I+1/2}]$, e.g., a Raman detuning beyond the maximum light shift of the dressed $F = I + 1/2$ manifold [as in Figs. 6(b), 6(e), and 6(h)], motion-induced coupling to the lower energy dressed $F = I + 1/2$ manifold would lead to heating. In addition, the Sisyphus effect at the $F = I + 1/2$ manifold also contributes to heating, since atoms coupled from $F = I - 1/2$ are more likely to start at the antitrap positions. The corresponding heating peak is located at $\Delta \sim \max[\epsilon_{F=I+1/2}] > 0$.

When $I_{\rm cool} \ll I_{\rm rep}$, the heating peak is shifted to $\Delta \sim -\max[\epsilon_{F=I-1/2}] < 0$, as in Fig. 3. This is straightforward to understand, as the roles of the two hyperfine ground states are now inverted with respect to the previous case. Finally, for $I_{\rm cool} \sim I_{\rm rep}$, the two hyperfine ground states have similar lifetimes and therefore similar steady-state populations. As the heating effects are balanced by cooling effects, the corresponding heating peaks in Fig. 3 (black squares) at $\Delta \sim \max[\epsilon_{F=I+1/2}]$, $\Delta \sim -\max[\epsilon_{F=I-1/2}]$ are substantially suppressed.

TABLE I. Parameters of the simultaneous ^{6}Li and ^{40}K D_1 cooling phase.

Parameter	Potassium	Lithium
P (mW)	230	300
$\delta_{\rm cool}$ (Γ)	2.3	4
$\delta_{\rm rep}$ (Γ)	2.3	4
$I_{\rm cool}$ per beam ($I_{\rm sat}$)	14	14
$I_{\rm cool}/I_{\rm rep}$	8	20
D-line property	^{40}K	^{6}Li
$\Gamma/(2\pi)$ (MHz)	6.04	5.87
$I_{\rm sat}$ (mW/cm^2)	1.75	2.54

III. SIMULTANEOUS ^{6}Li AND ^{40}K D_1 COOLING

Finally, we discuss the simultaneous operation of the ^{6}Li and ^{40}K D_1 molasses. We found that this simultaneous operation is required for subsequent efficient thermalization between both species in a quadrupole magnetic trap. The timing sequence and parameters are the same as for single-species operation. Experimental details are given in the Appendix and in [10]. The D_1 molasses phase is composed of a 3-ms capture phase and a 2-ms cooling phase. Table I summarizes the optimal parameters of the dual-species molasses. The presence of the other species reduces the atom numbers in the MOTs by 4% for ^{6}Li and by 10% for ^{40}K. However, we observe no mutual influence during the CMOT and the D_1 molasses phase. The temperatures and relative atom numbers in dual-species operation do not differ from those in single-species operation. There are several reasons for this. First, the D_1 resonances and lasers are $\sim$100 nm apart in wavelength. Second, the CMOT and molasses phases are short in duration (5 ms) and the light-induced interspecies collision losses or heating are minimized as atoms are accumulated in dark states. Table II summarizes the performance of the different experimental

TABLE II. Performance of the different experimental phases for ^{6}Li and ^{40}K, in dual-species operation. We list the optimum temperature T, the atom number N, the density n, and the phase-space density ϕ.

	T (μK)	N (10^9)	n (10^{10} cm^{-3})	ϕ[a] (10^{-5})
		Lithium		
MOT	1000	2	2.6	0.03
CMOT	800	2	18	0.29
Molasses	48	1.2	7.6	8.2
		Potassium		
MOT	240	3.2	7	0.02
CMOT	2000	3.2	37	0.06
Molasses	11	3.2	30	10.7

[a]The given phase-density does not take into account the different internal states and is calculated as $\phi = n\lambda_{\rm B}^3$, where $\lambda_{\rm B}$ is the thermal de Broglie wavelength.

phases in dual-species operation. For both ^{6}Li and ^{40}K the D_1 molasses phase largely reduces the temperature, while the cloud size after the CMOT phase is conserved. For both species this leads to a phase-space density close to 10^{-4}.

IV. CONCLUSION

In this study we have investigated the properties of D_1 laser cooling both experimentally and with numerical simulations. The simulations take into account all relevant Zeeman and hyperfine levels as well as the 3D bichromatic lattice geometry. Simulations and experimental results match fairly well for both lithium and potassium. Various sub-Doppler cooling effects [10] are recovered in the full model. We have outlined the importance of coherences between the ground-state hyperfine levels [11] and interpreted the cooling mechanisms as resulting from a combination of VSCPT-like nonadiabatic transitions between dark and coupled states and Sisyphus-type cooling. The discrepancy (factor of 2 to 4) between the temperature predicted by the semiclassical model and the experimentally observed ones calls for further investigations and the development of a full quantum treatment of the external atomic motion using a Monte Carlo wave-function approach [15,29].

We have discussed the physics behind the robustness of the D_1 cooling scheme, in particular, its insensitivity to the excited-state hyperfine splitting and to the relative phase between the cooling and the repumping lattices, which is in sharp contrast to its D_2 counterpart [4,5,19]. We first suggest and numerically verify that, due to the predominance of the "open transitions" at D_1, the bichromatically dressed ground states exhibit a robust correlation between light shift and decay. We clarify that such a correlation leads to the accumulation of an atomic population in the lowest energy dressed states at Raman resonance for both nonadiabatic and Sisyphus cooling. The picture also helps to explain the enhanced cooling at Raman resonance, as well as the reduced cooling or even heating at large Raman detunings. Because of the smaller absorption cross section for atoms cooled in weakly coupled states, D_1 gray molasses should also be less affected by the density-dependent heating than its D_2 counterpart [24].

Experimentally, using commercial semiconductor laser sources delivering $\sim$200 mW of CW power, we achieve efficient, simultaneous cooling of ^{6}Li and ^{40}K, resulting in a phase-space density close to 10^{-4} for both species. This D_1 cooling scheme enables efficient direct loading of a dipole or magnetic trap because of the large gain in temperature. As recently shown in [12] and [14], these conditions are well suited to direct loading of an optical dipole trap and to the performance of all-optical evaporation to quantum degeneracy. In our own experiments, we load a magnetic trap, transport the atoms to a separate science cell, and perform evaporative cooling of ^{40}K in two Zeeman states with a combined magnetic-optical trap scheme introduced in [25]. Deep quantum degeneracy ($T/T_F = 0.14$) in the dipole trap has been achieved and will be the subject of a future publication.

Finally, we have also used the D_1 gray molasses scheme to cool the bosonic ^{41}K isotope. All of 5×10^9 ^{41}K atoms from a CMOT were cooled to a final temperature of 20 μK, leading to a phase-space density of 1.1×10^{-4}. This confirms the generality of this D_1 sub-Doppler cooling method.

ACKNOWLEDGMENTS

We acknowledge useful discussions with A. T. Grier, I. Ferrier-Barbut, B. S. Rem, M. Delehaye, S. Laurent, and J. V. Porto and support from Région Ile de France (DIM Nano-K and IFRAF), the European Union (ERC grants Ferlodim and Thermodynamix), Institut de France (Louis D. Award), and Institut Universitaire de France. D.R.F. acknowledges the support of Fundação para a Ciência e Tecnologia (FCT-Portugal) through Grant No. SFRH/BD/68488/2010. S.W. acknowledges the support of the Physics Department at Swansea University, where part of this research was carried out.

APPENDIX: EXPERIMENTAL DETAILS

In this section we describe the experimental details, as well as the results of additional measurements on the D_1 molasses scheme, in particular, the single-species operation of ^{6}Li. Our experimental setup has been described previously [18]. A Zeeman slower for ^{6}Li and a 2D$^+$ MOT for ^{40}K load the 3D dual-species MOT in the MOT chamber. The D_2 laser systems for ^{6}Li and ^{40}K comprise master oscillator power amplifiers (MOPAs) to produce light at 671 and 767 nm, respectively. Beamsplitters and acousto-optic modulators generate the cooling and repumping beams, which are combined before injecting tapered amplifiers for the Zeeman slower and 3D MOT for ^{6}Li and, accordingly, the 2D$^+$ MOT and 3D MOT for ^{40}K.

The D_1 laser system for ^{40}K operates at 770 nm and is composed of a MOPA and an electro-optic modulator to produce the repumping frequency. The total power used for the ^{40}K cooling is 240 mW, with an intensity per molasses beam of $14 I_{\mathrm{sat}}$.

The source for the ^{6}Li D_1 light at 671 nm used in this work is a homemade solid-state laser, the next generation of [26] and [27], with up to 5 W output power. Acousto-optic modulators allow us to independently tune the frequencies and powers of the cooling and repumping beams, before recombination and injection into an optical fiber. We typically use 300 mW total power for the ^{6}Li D_1 cooling. The waist of the ^{6}Li D_1 beam after the telescope (Fig. 7) is 8.6 mm. We have also used a commercial 671-nm tapered amplifier system (MOPA) with 130 mW available power impinging on the atoms and obtained similar performances for the capture efficiency and sub-Doppler temperatures.

Our optical scheme superimposes the D_1 and D_2 light for both ^{6}Li and ^{40}K and produces the molasses and 3D MOT beams (Fig. 7). D-shaped mirrors (M_{D}) superimpose the D_1 cooling light and the 3D MOT light of each species before a dichroic mirror (M_{dichroic}) combines the lithium and potassium light. The beam containing all eight frequencies is expanded and distributed to the three pairs of σ^+-σ^- counter-propagating beams of the 3D MOT and the D_1 molasses. The two horizontal axes are retroreflected, and the vertical axis consists of two independent beams. The $\lambda/2$ plates of order 4 for lithium ($\lambda/2^*_{\mathrm{Li}}$) and potassium ($\lambda/2^*_{\mathrm{K}}$)

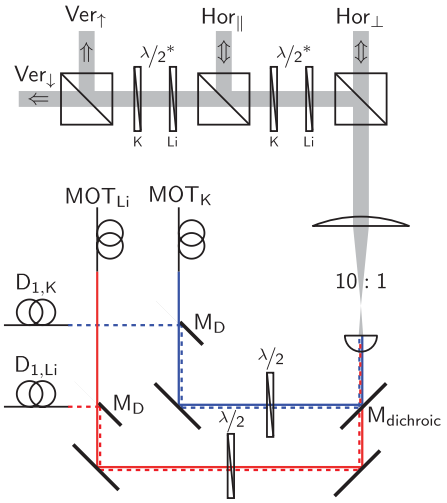

FIG. 7. (Color online) Optical scheme of the D_1 molasses. The 3D MOT light and the D_1 cooling light are superposed using a D-shaped mirror (M_D). Afterwards a dichroic mirror ($M_{dichroic}$) combines the lithium and potassium light, which is subsequently expanded and distributed to the three perpendicular axes of the 3D MOT.

allow for independent control of the ^{6}Li and ^{40}K MOT power distribution.

The experiment starts with the loading of the dual-species MOT. In 10 s we typically load 8×10^8 ^{6}Li atoms with an initial temperature of 1 mK and 3×10^9 ^{40}K atoms at 200 μK. Then a CMOT phase [28] increases the density of the atom cloud. The magnetic gradient is linearly ramped from 9 to 60 G/cm in 5 ms. Meanwhile the frequencies of the cooling and the repumping beams are tuned closer to resonance and their intensities are linearly decreased. The CMOT phase results in an increase in the peak density by a factor of 7 (5.3) and a temperature of 800 μK (2 mK) for ^{6}Li (^{40}K). At the end of the CMOT phase the current of the MOT coils is switched off within ~100 μs. We start the D_1 molasses phase for ^{6}Li with a delay of 200 μs in order to wait for transient magnetic fields to decay. We found that this delay is not needed for ^{40}K.

1. ^{6}Li D_1 molasses

Here we study the cooling dynamics of ^{6}Li alone. We set the peak intensity of the molasses to $14.6 I_{sat}$ per beam, set the cooling/repumping ratio to $I_{cool}/I_{rep} = 20$, and fix the global detuning to $\delta = \delta_{cool} = \delta_{rep} = 4\ \Gamma$. Here $I_{sat} = 2.54$ mW/cm^2 is the saturation intensity of the D_2 cycling transition, and $\Gamma = 2\pi \times 5.87$ MHz the D_1 line natural linewidth for ^{6}Li. Figure 8 shows the atom number and temperature of the D_1 molasses as functions of the molasses duration t_m. The temperature is determined through time-of-flight measurements. We capture 60% of the 8×10^8 CMOT atoms. Within 3 ms the atoms are cooled from 800 μK to the asymptotic temperature of 120 μK with a $1/e$ cooling time constant $\tau_{cool} = 0.6$ ms. The direct

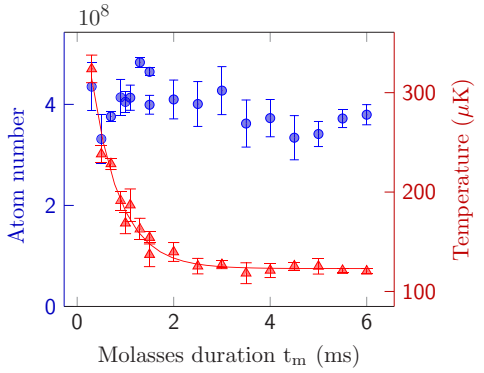

FIG. 8. (Color online) Number of atoms captured in the ^{6}Li D_1 molasses (circles) and their temperature (triangles) as functions of the molasses duration, with a $1/e$ cooling time constant $\tau_{cool} = 0.6$ ms. The number of atoms in the compressed MOT is 8×10^8.

measurement of the fluorescence shows a very fast decay at the beginning ($\tau_{fast} < 1$ μs), followed by a further decrease by another factor of 2 within 2 ms. This indicates that the atoms are accumulated in dark states during the cooling process. We find the $1/e$ lifetime of the D_1 molasses atom number for these parameters to be $\tau_{D1} = 90$ ms.

The molasses atom number and temperature as functions of the global detuning δ are shown in Fig. 9. We observe a decrease in the temperature from 188 to 100 μK for $\delta_{cool} = 2 \ldots 7$. The capture efficiency increases sharply until 4 Γ and stays constant until 7 Γ.

We now study the influence of the D_1 light intensity. When increasing the cooling intensity, while keeping the molasses time fixed to 3 ms, we observe an increase in both the capture efficiency and the temperature (Fig. 10). To take advantage of the intensity-dependent temperature, we use two successive phases in the cooling sequence. During the first

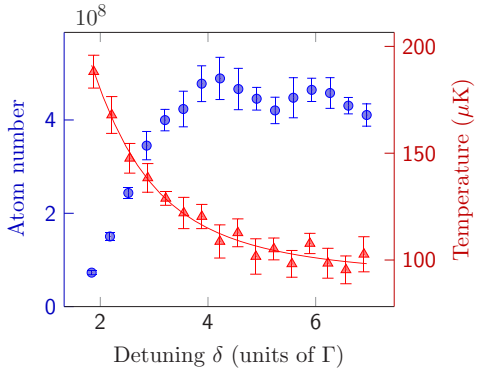

FIG. 9. (Color online) Number of atoms captured in the ^{6}Li D_1 molasses (circles) and their temperature (triangles) after a 3-ms capture phase at a high intensity, $I_{cool} = 14.6 I_{sat}$, as functions of the global detuning $\delta = \delta_{cool} = \delta_{rep}$. The number of atoms in the compressed MOT is 8×10^8.

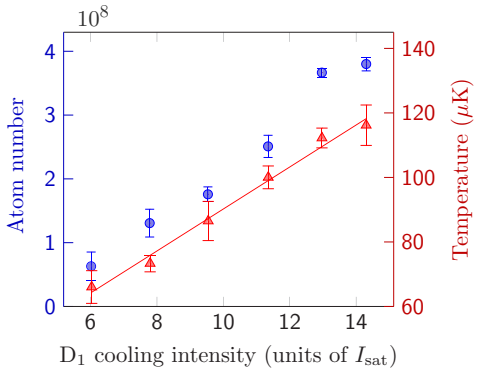

FIG. 10. (Color online) Number of atoms captured in the ^{6}Li D_1 molasses (circles) and their temperature (triangles) as functions of the D_1 cooling beam intensity for $\delta_{cool} = 4\,\Gamma$ and $I_{rep} = I_{cool}/20$. The number of atoms in the compressed MOT is 8×10^8. The atom number (temperature) increases linearly with a slope of 4×10^7 atoms/I_{sat} (6.5 μK/I_{sat}).

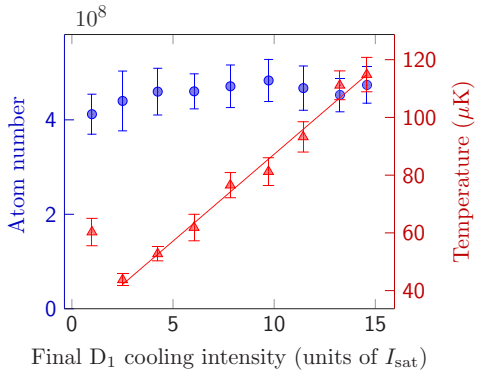

FIG. 11. (Color online) Number of atoms captured in the ^{6}Li D_1 molasses (circles) and their temperature (triangles) after a 3-ms capture phase at a high intensity, $I_{cool} = 14.6 I_{sat}$, followed by a 2-ms linear intensity ramp to an adjustable value. The temperature increases linearly for a higher intensity, with a slope of $\sim$6 μK/I_{sat}. The detuning is fixed to $\delta_{cool} = 4\,\Gamma$. The number of atoms in the compressed MOT is 8×10^8.

3 ms we capture the atoms at a high intensity, yielding the highest capture efficiency. Then the intensity is linearly ramped within 2 ms to an adjustable final intensity to further lower the temperature. Figure 11 shows that the intensity ramp reduces the final temperature from 115 to 44 μK without a significant atom loss, for a final intensity $I_{cool,final} = 2.5 I_{sat}$. For lower intensities we observe heating and atom loss. The cooling/repumping intensity ratio influences the atom number and the temperature. We find an optimal temperature for $I_{cool}/I_{rep} = 20$. For a lower ratio the temperature increases slightly and the atom number starts to drop at around $I_{cool}/I_{rep} = 7$. For $I_{cool}/I_{rep} > 33$ the cooling mechanism becomes inefficient, leading to atom loss and heating.

Measuring the atom cloud size at the end of the CMOT and molasses phases, we see no significant change, proving that diffusion during the molasses phase is small. In terms of the phase-space density the atom loss is largely overcompensated by the 14 times reduction in temperature.

[1] J. Dalibard and C. Cohen-Tannoudji, J. Opt. Soc. Am. B **6**, 2023 (1989).
[2] P. D. Lett, W. D. Phillips, S. L. Rolston, C. E. Tanner, R. N. Watts, and C. I. Westbrook, J. Opt. Soc. Am. B **6**, 2084 (1989).
[3] D. S. Weiss, E. Riis, Y. Shevy, P. J. Ungar, and S. Chu, J. Opt. Soc. Am. B **6**, 2072 (1989).
[4] A. Bambini and A. Agresti, Phys. Rev. A **56**, 3040 (1997).
[5] X. Xu, T. H. Loftus, J. W. Dunn, C. H. Greene, J. L. Hall, A. Gallagher, and J. Ye, Phys. Rev. Lett. **90**, 193002 (2003).
[6] P. Hamilton, G. Kim, T. Joshi, B. Mukherjee, D. Tiarks, and H. Müller, Phys. Rev. A **89**, 023409 (2014).
[7] P. M. Duarte, R. A. Hart, J. M. Hitchcock, T. A. Corcovilos, T.-L. Yang, A. Reed, and R. G. Hulet, Phys. Rev. A **84**, 061406 (2011).
[8] D. C. McKay, D. Jervis, D. J. Fine, J. W. Simpson-Porco, G. J. A. Edge, and J. H. Thywissen, Phys. Rev. A **84**, 063420 (2011).
[9] J. Sebastian, C. Gross, K. Li, H. C. J. Gan, W. Li, and K. Dieckmann, Phys. Rev. A **90**, 033417 (2014).
[10] D. R. Fernandes, F. Sievers, N. Kretzschmar, S. Wu, C. Salomon, and F. Chevy, EPL (Europhys. Lett.) **100**, 63001 (2012).
[11] A. T. Grier, I. Ferrier-Barbut, B. S. Rem, M. Delehaye, L. Khaykovich, F. Chevy, and C. Salomon, Phys. Rev. A **87**, 063411 (2013).
[12] G. Salomon, L. Fouché, P. Wang, A. Aspect, P. Bouyer, and T. Bourdel, EPL (Europhys. Lett.) **104**, 63002 (2013).
[13] D. Nath, R. K. Easwaran, G. Rajalakshmi, and C. S. Unnikrishnan, Phys. Rev. A **88**, 053407 (2013).
[14] A. Burchianti, G. Valtolina, J. A. Seman, E. Pace, M. De Pas, M. Inguscio, M. Zaccanti, and G. Roati, Phys. Rev. A **90**, 043408 (2014).
[15] J. Dalibard, Y. Castin, and K. Mølmer, Phys. Rev. Lett. **68**, 580 (1992).
[16] H. Carmichael, *An Open Systems Approach to Quantum Optics*, *Lecture Notes in Physics Monographs*, Vol. 18 (Springer-Verlag, Berlin, 1993).
[17] By assuming the ground-state hyperfine splitting to be large enough, the $F = I + 1/2$ ($F = I - 1/2$) is dark to the repumping (cooling) laser and the associated couplings are ignored in the Hamiltonian. This approximation allows us to write down the Hamiltonian in the time-independent form.
[18] A. Ridinger, S. Chaudhuri, T. Salez, U. Eismann, D. R. Fernandes, K. Magalhães, D. Wilkowski, C. Salomon, and F. Chevy, Eur. Phys. J. D **65**, 223 (2011).
[19] R. Gupta, C. Xie, S. Padua, H. Batelaan, and H. Metcalf, Phys. Rev. Lett. **71**, 3087 (1993).
[20] W. Happer, Rev. Modern Phys. **44**, 169 (1972).

[21] C. Cohen-Tannoudji, *Atomic Motion in Laser Light*, edited by J. Dalibard, J. Raimond, and J. Zinn Justin (Les Houches, Session LIII, 1990), pp. 1–164.

[22] Exact locations of the dark states depend on the relative phase between the cooling and the repumping lattices.

[23] For D_2 transitions the complication is also Δ dependent. A complete comparison of D_1 and D_2 cooling will be the subject of a future publication.

[24] M. Drewsen, P. Laurent, A. Nadir, G. Santarelli, A. Clairon, Y. Castin, D. Grison, and C. Salomon, Appl. Phys. B **59**, 283 (1994).

[25] Y.-J. Lin, A. R. Perry, R. L. Compton, I. B.Spielman, and J. V. Porto, Phys. Rev. A **79**, 063631 (2009).

[26] U. Eismann, F. Gerbier, C. Canalias, A. Zukauskas, G. Trénec, J. Vigué, F. Chevy, and C. Salomon, Appl. Phys. B **106**, 25 (2011).

[27] U. Eismann, A. Bergschneider, F. Sievers, N. Kretzschmar, C. Salomon, and F. Chevy, Opt. Express **21**, 9091 (2013).

[28] M.-O. Mewes, G. Ferrari, F. Schreck, A. Sinatra, and C. Salomon, Phys. Rev. A **61**, 011403 (1999).

[29] Y. Castin and K. Mølmer, Phys. Rev. Lett. **74**, 3772, (1995).

4 Evaporative cooling to quantum degeneracy in magnetic and optical traps

4.1. Introduction

After magnetically transporting the atom samples to the science cell, another stage of cooling has to be applied in order to reach the quantum degenerate regime. We employ a technique called forced evaporative cooling, which relies on the selective removal of atoms with high kinetic energy. In order to achieve a maximal phase space density, while maintaining a large final atom number, our approach is to first evaporatively cool the atoms in a plugged magnetic quadrupole trap by driving energy selective RF transitions. Subsequent to this intermediate stage, we transfer the atoms into an optical dipole trap, where we continue the optical evaporation by lowering the trap potential gradually until the atomic ensemble reaches the quantum degenerate regime.

4.2. Principle of evaporative cooling

The basic principle of forced evaporative cooling is to remove constantly the high-energy tail of a thermally distributed atomic ensemble, while the ensemble rethermalizes due to elastic collisions [172–175]. In consequence, the reduction of the mean energy per particle results in a lower temperature of the remaining atomic ensemble. Progressive application of this process with gradually decreasing removal energy further decreases the temperature. Even if there is in principle no fundamental lowest temperature limit, the decreasing atom number as well as heating and loss mechanisms are limiting the achievable phase space density. We stress the fact that evaporative cooling requires high atomic densities to be efficient, in contrast to laser cooling where density effects like multiphoton scattering play a detrimental role regarding the lowest temperature limit.
One possible definition of the evaporation efficiency is given by the relation

$$T \propto N^{\alpha}\,, \tag{4.1}$$

where T is the sample temperature, N is the total atom number and α is the corresponding efficiency parameter depending on a large set of other parameters, like for instance the elastic collision rate, the evaporation trajectory, the efficiency of energy removal, as well as losses due to background collisions and other loss mechanisms. A large elastic collision rate is crucial

for fast rethermalization dynamics. The elastic collision rate

$$\gamma = n\sigma v_T \tag{4.2}$$

depends on the density of atoms n, the elastic collision cross-section σ and the mean relative speed of particles v_T. For a classical gas, the mean relative speed is given by

$$v_T = \sqrt{\frac{16 k_\mathrm{B} T}{\pi m}}\,, \tag{4.3}$$

where m is the mass of a particles and k_B is the Boltzmann constant. Since the size of the trapped cloud decreases with T, an efficient evaporation in a trap with constant confinement (like it is the case for magnetic traps) can increase the density and thus the collision rate during the evaporation process. This holds if the increase in density is faster than the decrease of v_T. If the efficiency parameter α is sufficiently large this can lead to runaway evaporation in the case of bosonic gases as well as for fermionic gases in the classical regime. However, as soon as a Fermi gas attains the degenerate regime, the collisional properties of the gas become subject to Fermi-Dirac statistics. Pauli blocking and Fermi pressure then lead to a reduced collision rate, eventually cancelling at zero temperature.

4.3. Experimental approach and results

For our experiment we have decided to follow the approach of evaporatively cooling a spin mixture of ^{40}K, while ^{6}Li is sympathetically cooled. As of this writing, our group is still optimizing the evaporative cooling stage. We are already able to sympathetically cool lithium with potassium in the optically plugged magnetic quadrupole trap and to load $\sim 3 \times 10^5$ atoms of each atomic species at a temperature of $\sim 35\mu$K into the optical dipole trap. Before continuing to optimize the dual-species evaporation in the near future, we first have characterized the single-species evaporation of ^{40}K.
In the following, we present our results concerning the single species evaporation of ^{40}K to quantum degeneracy.

4.3.1. RF evaporation

Since in a magnetic trap the potential energy of the atoms is proportional to the magnetic field strength, atoms with a higher total energy can probe larger magnetic fields. A RF field, at a given frequency, couples trapped low-field-seeking states ($g_\mathrm{F} m_\mathrm{F} > 0$) to untrapped high-field-seeking states ($g_{\mathrm{F}'} m_{\mathrm{F}'} < 0$) at a specific magnetic field. The resonance frequencies vary with the magnetic field due to the Zeeman shift of the magnetic sublevels. This allows to specifically remove highly energetic atoms from the trap by setting the RF frequency such that only these atoms reach sufficiently large magnetic fields to become resonant with the RF radiation. The effective trap depth is changed with the RF frequency, thus enabling forced evaporation.

For ^{40}K we drive the magnetic field dependent transitions $|F = 9/2, m_F = 9/2\rangle \rightarrow |7/2, 7/2\rangle$, $|9/2, 7/2\rangle \rightarrow |7/2, 7/2\rangle$ and $|9/2, 5/2\rangle \rightarrow |7/2, 7/2\rangle$ with a single microwave frequency to remove highly energetic atoms [157].
The quadrupole trap in the science cell consists of a coil pair with inner and outer coils, see the description in Subsection 2.10.1. As soon as the ^{40}K atoms have arrived in the science cell, the current in the outer coils is slowly ramped to zero. The power supply, driving the inner coils, is at this stage operated in current control mode in order to keep the current of the inner coils constantly at 100 A during the RF evaporation. This yields a magnetic field gradient of $B'_z = 280\,\mathrm{G/cm}$ on the strong vertical axis. We typically start the evaporation process with 8×10^8 ^{40}K atoms at 650 μK, and sweep the RF field linearly from 1150 MHz to 1260 MHz in 5 s, regularly producing an atomic sample of 6×10^7 potassium atoms at a temperature of 110 μK for the mentioned trap confinement.
These numbers were obtained without applying a plug beam to the center of the magnetic trap, as described in Subsection 2.10.2. For the single species evaporation of ^{40}K, the utilization of the plug beam is not mandatory, since this yields at best a factor of two in the final atom number.

4.3.2. Optical dipole trap

The first optical dipole trap beam at 1064 nm (ODT_1) is already switched on at the beginning of the RF evaporation. A 11 W beam, oriented horizontally (x-axis), perpendicular to the transport direction in the second arm, is focused to a waist of $w_0 = 42\,\mu$m and displaced by $z_0 = 100\,\mu$m below the magnetic trap center. We thus use a combination of a magnetic quadrupole potential and an optical potential during the RF evaporation, an approach that was presented in [176] and leads to a reduction of Majorana losses. The cold and dense cloud at the end of the RF evaporation is loaded into the optical dipole trap by linearly ramping the magnetic field gradient from 250 G/cm down to 5 G/cm in 800 ms. We note that the ambient magnetic bias fields are compensated by the outer coils and auxiliary coils placed around the science chamber in order to prevent the magnetic trap center from displacing during opening of the trap. We are able to transfer 3×10^7 ^{40}K atoms with a temperature of 55 μK into the ODT. After loading of the ODT, approximately 60% of these atoms are in the $|9/2, 9/2\rangle$ state and 40% are in the $|9/2, 7/2\rangle$ state.

Optical evaporation

In the dipole trap forced evaporation is continued by lowering gradually the beam power. The exact expression of the potential for atoms in the combined magnetic quadrupole and optical dipole trap is presented in [176]. By neglecting the contribution of the magnetic confinement, the dipole potential for an atom with an optical transition frequency ω_0 can be simplified, to

$$U_{\mathrm{dip}}(\mathbf{r}) = \frac{3\pi c^2}{2\omega_0^3}\frac{\Gamma}{\Delta} I(\mathbf{r})\,, \tag{4.4}$$

assuming a detuning $|\Delta| \ll \omega_0$. Here, Γ is the natural linewidth of the transition, $\Delta = \omega - \omega_0$ is the detuning of the driving frequency ω from the transition frequency ω_0, and $I(\mathbf{r})$ is the intensity profile of the ODT [161]. Lowering the beam power forces evaporation, because atoms with an energy higher than the gradually decreasing trap depth can escape. During the optical evaporation, the inner coil current is set to 2.75 A, such that the magnetic gradient compensates the gravitational force for atoms in the $|9/2, 9/2\rangle$ state and provides confinement in the axial direction of the ODT. We exponentially decrease the ODT beam power from 11 W to 170 mW in 5.5 s, to obtain $\sim 8 \times 10^6$ ^{40}K atoms at a temperature of $\sim 1.5\,\mu$K.

Landau-Zener sweep

For future experiments, we intend to benefit from the possibility to tune the interaction strength by means of a Feshbach resonance. Therefore we have to prepare the atoms in the appropriate Zeeman states, before further continuing the evaporative cooling process. In the case of the resonance at $B = 202.1$ G the relevant states are $|m_F = -9/2\rangle$ and $|m_F = -7/2\rangle$ of the $F = 9/2$ manifold [177, 178]. Since at this point of the cooling sequence almost all of the atoms are in the positive states $|m_F = +9/2\rangle$ and $|m_F = +7/2\rangle$, a spin-preparation step needs to be performed. This is realized by inducing consecutive adiabatic passages between the subsequent Zeeman states by means of a RF field. The adiabatic passage, also called Landau-Zener sweep, is a well known technique in atomic physics for transferring atoms from one state to another by slowly sweeping the frequency of an electromagnetic signal over the resonance frequency coupling both states [10, 94].
We chose to perform the Landau-Zener sweep for a magnetic field of $B = 19.2$ G. In this regime, the transitions between the Zeeman states are situated around 6MHz and are not degenerate, since the difference in frequency of two adjacent Zeeman transitions is 62 kHz. Since the estimated Rabi frequency is on the order of $\Omega_R \sim 10$ kHz we can actually choose the target Zeeman state by tuning the final frequency of the sweep. In our experimental sequence we perform a linear RF sweep from 6.5MHz to 5.5MHz in 10ms.

Crossed dipole trap

In order to increase the elastic scattering rate, we add an additional optical confinement in the axial direction (x-direction). For this purpose we shine in a second laser beam at 1064 nm, propagation along the transport direction (y-axis). Its focus crosses ODT_1 perpendicularly, thus creating a crossed dipole trap. This second dipole trap beam (ODT_2) is linearly ramped up from zero to 4.8 W in 1.5 s, and has a waist of 330 μm. A wait step of 200 ms lets the atoms gather in the dimple potential created by ODT_2. Subsequently, we ramp the magnetic bias slowly below the Feshbach resonance at 202.1 G and sweep as fast as possible to the high-field imaging value of 243.5 G. Alternatively, for performing a Stern-Gerlach experiment, we ramp the bias down to a value of a few Gauss. We note that a small bias field in z-direction needs always to be applied during the complete evaporation. This ensures that the atomic spins remain quantified along the same axis and do not change their spin state. The

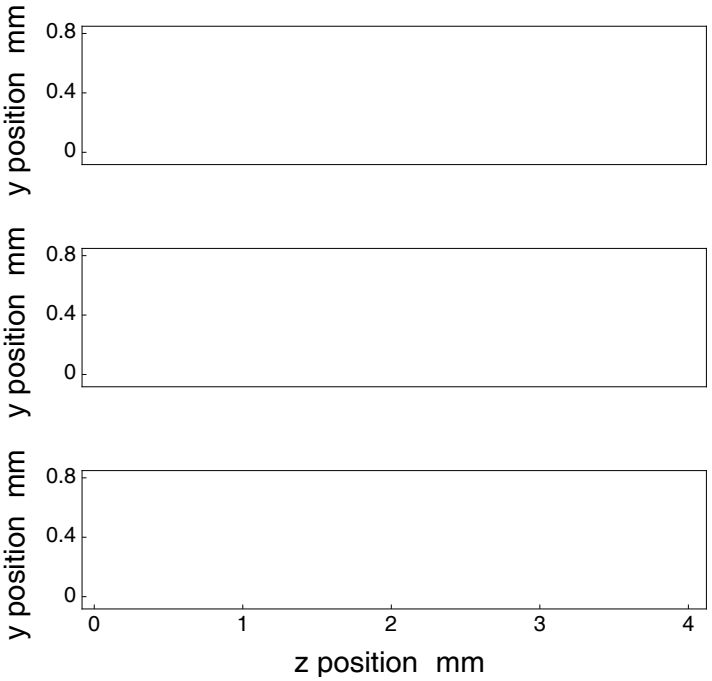

Figure 4.1: Landau-Zener sweep performed at constant magnetic field 19.2G, as presented in [179]. The RF field is swept from 6.5MHz to 5.5MHz in 10ms. The images are absorption pictures taken in the direction of the optical dipole trap after a Stern-Gerlach experiment. (Top) Initial state. (Middle) After one RF sweep. (Bottom) 10 back-and-forth frequency sweeps in 10ms. All of the 10 states in the $F = 9/2$ manifold became populated.

evaporation is continued by exponentially ramping the ODT_1 power from 170 mW to 57 mW in 8 s. Depending on the aimed final temperature we add another evaporation step of 6 s with a variable, slightly reduced final power value of ODT_1.
The trap frequencies at the end of a typical evaporation ramp ($P_{\mathrm{ODT},1} \simeq 40\,mW$ and $P_{\mathrm{ODT},2} = 4.8\,W$), are measured to be $\omega_\mathrm{x} = 2\pi \times 25$ Hz, $\omega_\mathrm{y} = 2\pi \times 154$ Hz and $\omega_\mathrm{z} = 2\pi \times 160$ Hz. We use two different techniques in order to measure the number of atoms in the different spin states and the corresponding temperatures, namely the Stern-Gerlach experiment and high-field imaging.

Stern-Gerlach experiment

We can perform a Stern-Gerlach experiment to spatially separate the spin states [180, 181]. For this purpose, we apply a magnetic field gradient of $\sim$25 G/cm in z-direction and switch off the crossed optical dipole trap, thus letting the atomic sample expand under the influence of magnetic and gravitational forces. The magnetic field gradient exerts a force on the atoms, hence accelerating them. Since the force experienced by the atoms depends on their magnetic moment and therefore on their spin state, this leads to a spatial separation of the different spin states, under the condition that the width of the atomic spin samples due to thermal expansion is smaller than the accumulated separation. In practice, the gradient is switched off after 15 ms, when the spatial separation of the spin states is sufficiently large.

An additional wait step of 10 ms ensures that the magnetic field due to eddy currents reached zero. Subsequently, we perform absorption imaging.

High-field imaging

When an external magnetic field is applied, the energy of the atomic states is shifted due to the Zeeman effect. Consequently, also the imaging transitions will shift in frequency. We can benefit from the fact that these frequency shifts depend on the internal spin state of the atoms in order to image our samples spin-selectively. Details on the calculation of the imaging frequency shifts can be found in the thesis of Diogo Fernandes [179]. In our experiment, we installed an additional AOM in order to shift the imaging beam frequency for ^{40}K to suitable values. This setup is flexible enough to image the three states of interest ($|9/2, \mathrm{m_F} = -9/2, -7/2, -5/2\rangle$) in the desired field range of $B = 150 - 250\,\mathrm{G}$ with σ^- or π polarization.

Final result: Degenerate Fermi gas

Figure 4.2(a) illustrates an image section of an high-field absorption image, showing ^{40}K atoms in the $|m_\mathrm{F} = -9/2\rangle$ state after a time-of-flight of 20 ms. A polylog fit [160] is applied to the integrated 1D cloud profile, taking into account the measured trap frequencies. [1] It yields an atom number of $\sim 1.5 \times 10^5$, a temperature of 64 nK and $T/T_\mathrm{F} \sim 0.17$, see Figure 4.2(b). In the $|m_\mathrm{F} = -7/2\rangle$ state we have about the same number of atoms at the same temperature. This result is a main achievement of this thesis. It prove that we are able to produce a deeply degenerate spin-mixture of ^{40}K atoms with relatively large atom numbers in the $|m_\mathrm{F} = -9/2\rangle$ and the $|m_\mathrm{F} = -7/2\rangle$ states. In order to investigate a degenerate gas in the strongly interacting regime we have simply to decrease the magnetic field to the Feshbach resonance at $B = 202.1\,\mathrm{G}$. For a unitary Fermi gas, the transition to a superfluid of paired fermions should then occur below $0.17\,T/T_\mathrm{F}$ [94, 95].

[1] We use the following fit model for the integrated 1D profile of the atomic density: $n_\mathrm{1D}(x) = -A_\mathrm{F}\mathrm{Li}_{5/2}\left(-\mathrm{Z_F}\exp\left(\frac{(\mathrm{x}-\mathrm{x_F})^2}{2\mathrm{s_F^2}}\right)\right) + \mathrm{B_F} + \mathrm{m_F x}$, with A_F and s_F being related by the trap parameters and the time of flight. T/T_F can be directly inferred from the fugacity Z_F.

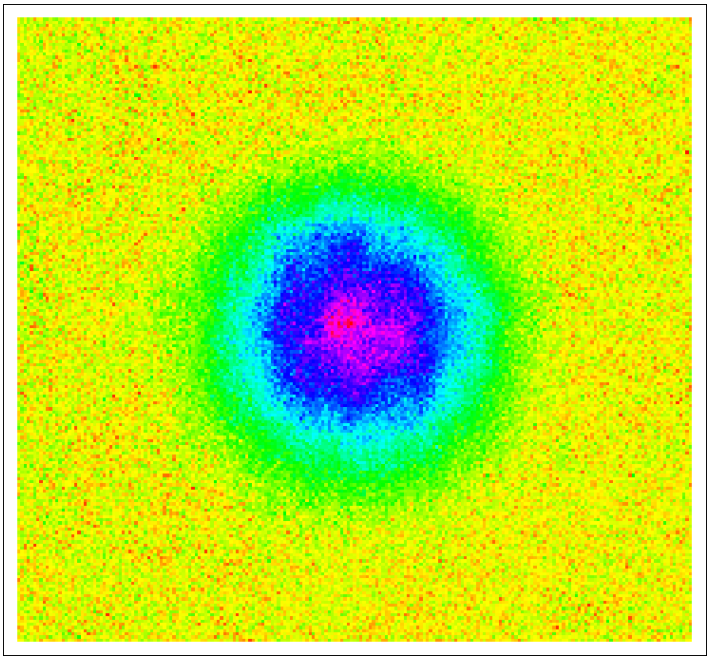

(a) Absorption imaging

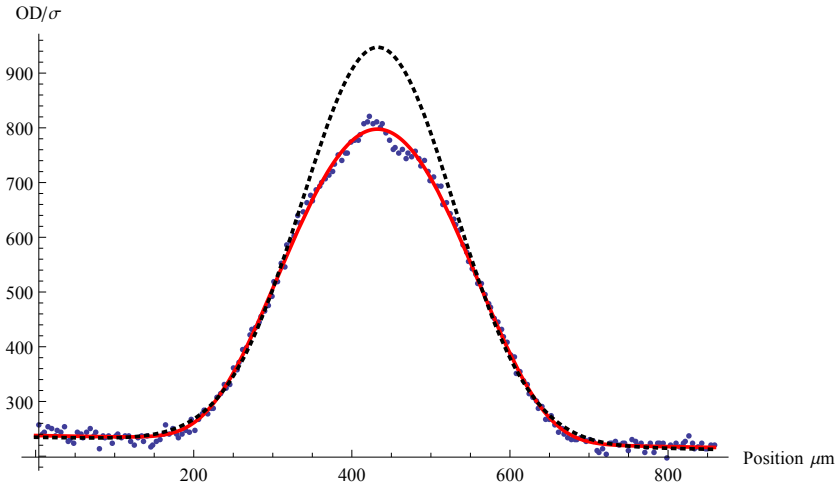

(b) Thomas-Fermi fit

Figure 4.2: (a) High-field absorption image of a degenerate Fermi gas of ^{40}K atoms in the $|9/2, -9/2\rangle$ state at $T/T_F \sim 0.17$ after a time-of-flight of 20 ms. (b) Density distribution integrated along y-direction. The observed profile (circles) is well described by fitting a polylogarithmic function to the data (red, solid line). A classical Gaussian distribution, fitted to the wings of the cloud (gray, dashed line), features a significant deviation from the data. The absorption image is averaged over four individual picture shots.

Part II.

Multi-watt level 671-nm laser source

Introduction

Lithium is one of the most popular elements for research on quantum gases. For producing a degenerate quantum gas of lithium, the implementation of different laser cooling schemes is required, which can only be realized by generating near-resonant single-frequency light with powers typically in the watt range. In this context, all-solid-state lasers must be seen as advantageous light sources whose design offers a broad range of benefits, such as large output power, high reliability, low maintenance effort and high intrinsic stability.

In this part we will present an all-solid-state laser emitting multi-watt single-frequency radiation near 671 nm. The fundamental infrared laser is based on a diode-end-pumped ring-cavity design employing neodymium-doped yttrium orthovanadate (Nd:YVO_4) as the gain medium, since it features a laser transition at the wavelength of 1342 nm. Second harmonic generation (SHG) of the fundamental wavelength is realized using three different approaches, namely frequency-doubling via an enhancement cavity, intracavity doubling, and wavelength conversion in a nonlinear waveguide. The designs of related laser sources that have been published recently [182, 183], as well as a previous version of our laser system [184], reached only output powers of a few hundreds of milliwatts. The main limitations for power-scaling the single-frequency Nd:YVO_4 laser, as well as for the employed doubling devices, to the multi-watt range are the losses introduced by detrimental thermal lensing in the active medium, and the break down of the conversion efficiency in the nonlinear medium for high intensities. In consequence, the most important feature of our novel high-power laser design is an improved heat management in the Nd:YVO_4 crystal and the nonlinear media.

Apart from laser cooling, other applications in the fields of atomic phyics, nonlinear optics and technology require enhanced single-frequency powers around 671 nm. The small mass of lithium is advantageous for atom interferometers, as it yields a large spatial splitting of the atomic wavepackets [185]. By employing laser beams with higher power the signal-to-noise ratio can be improved and even the spatial splitting can be increased by means of multi-photon Bragg scattering [186]. In addition, a narrow-linewidth laser source is an option for optical techniques of lithium isotope separation [187], since the isotope splitting of the lithium D-line is sufficiently large to allow for selective addressing of the isotopes in hot vapor. Furthermore, a scheme for the creation and long-distance transmission of entangled photons has recently been proposed, this technique utilizing the output of a sub-threshold optical parametric oscillator in the degenerate regime pumped by a single-frequency 671-nm laser [182]. Finally, Cr:LiSAF laser setups could employ our laser as a pump source featuring low intensity-noise [188].

5 Fundamental laser source at 1342 nm

In the preceding introduction, we have mentioned our new approach for an improved version of an all all-solid-state 671-nm laser source. In the following sections, we will discuss the fundamental near-infrared laser source at 1342 nm in more detail.
In Section 5.1 the most important physical properties of the Nd:YVO_4 gain medium will be presented. We will illustrate its crystal structure as well as its absorption and emission spectra. Furthermore we detail on the thermo-optical properties of the gain medium and the available pumping schemes, and show that considering these parameters was essential for the power scaling of the laser system. In Section 5.2 we will indicate the basic theoretical concepts that we employed for designing the laser cavity. We will include our measurements with respect to thermal lensing effects and present the final design following these observations. In Section 5.3 we will discuss our technical approach for achieving unidirectional, single-longitudinal-mode operation of the laser by means of a Faraday rotator and two intra-cavity etalons. In Sections 5.4 we will present our measurements of the characteristic parameters of the fundamental laser source, in particular of the output power, the output spectrum and the spatial mode quality. Finally, we will summarize this chapter in Section 5.5.
A three-dimensional view of the opto-mechanical parts of our cavity setup is given in Figure 5.1.

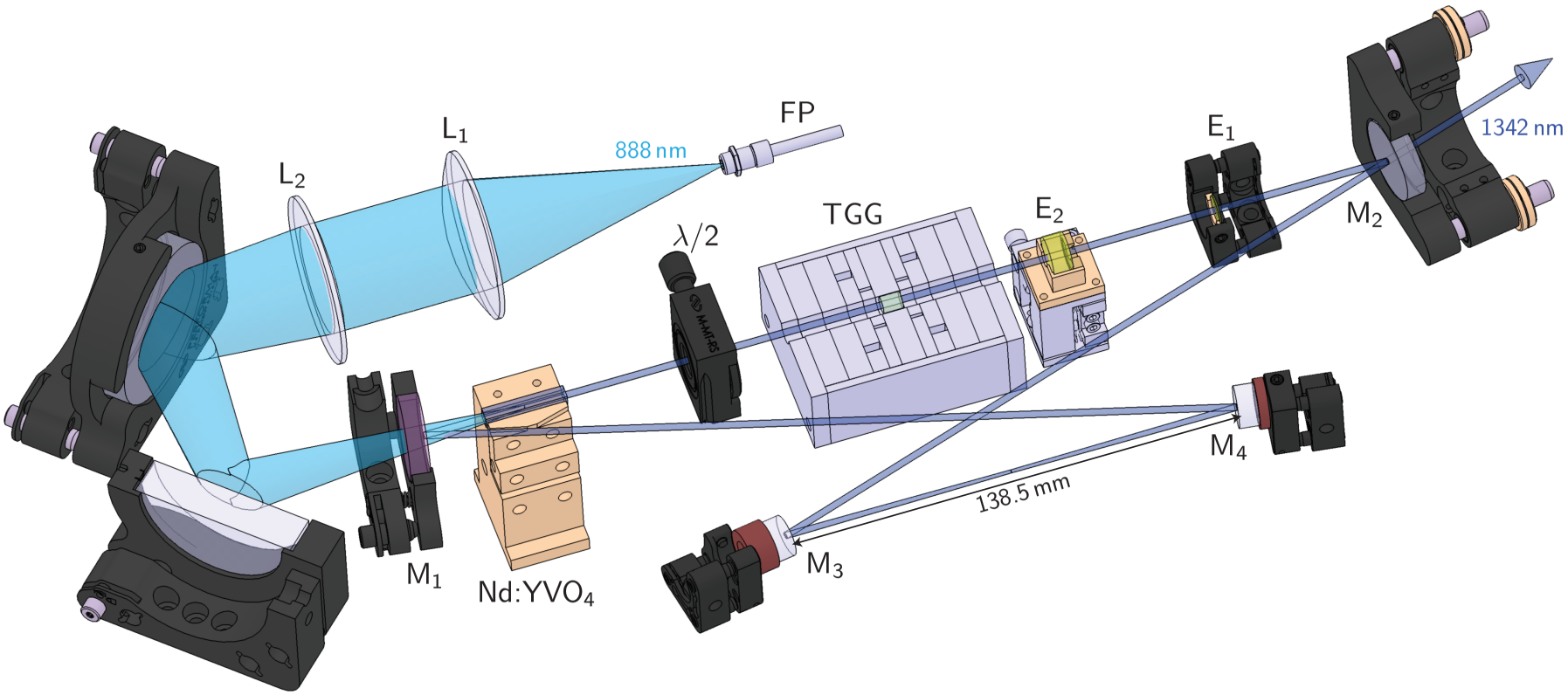

Figure 5.1. – Setup of the 1342 nm laser source from [140]. Two lenses, L_1 and L_2, image the output of the pump source, a fiber-coupled diode laser bar (FP) emitting at 888 nm, into the Nd:YVO_4 gain medium. The ring resonator consists of four mirrors M_{1-4} in bow-tie configuration, which are all highly reflective at 1342 nm except M_2 serving as partly transmitting output coupling mirror. A Faraday rotator (TGG) in combination with a half-wave plate ($\lambda/2$) enforces unidirectional operation. Insertion of two etalons E_{1-2} allows for single-longitudinal-mode behavior and wavelength tunability. For a technical drawing of the cavity setup see Figure 5.10.

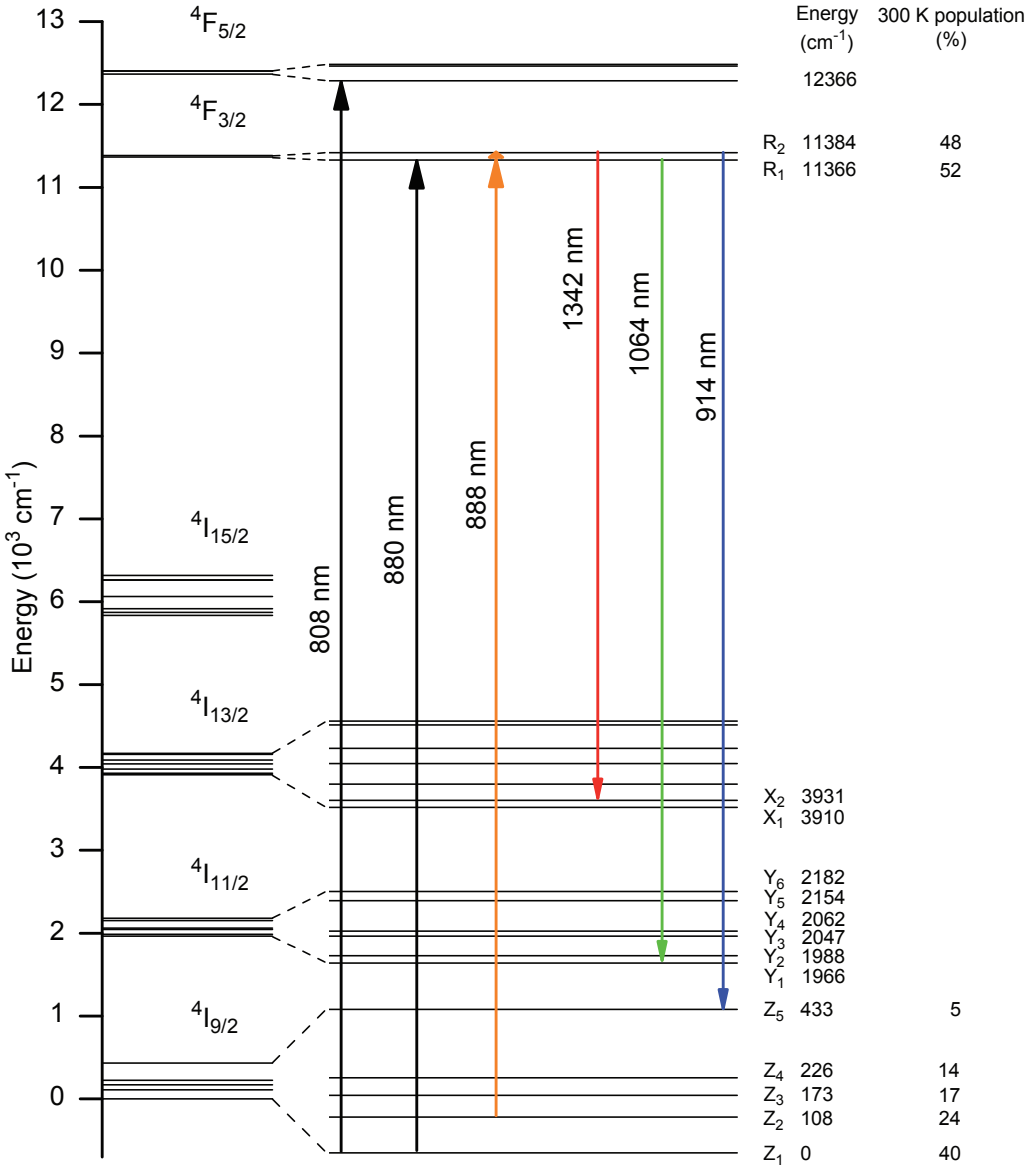

Figure 5.2: Energy level scheme of the neodymium ion (Nd^{3+}) in an YVO_4 host material, its main optical transitions for pumping and lasing, and the partial sublevel populations at room temperature [189]. We operate the laser source on the ${}^4F_{3/2} \rightarrow {}^4 I_{13/2}$ transition, corresponding to an output wavelength of 1342 nm. Three pumping schemes to the metastable ${}^4F_{3/2}$ level are indicated, where the 808 nm transition pumps via the short-living ${}^4F_{5/2}$ level. The 888 nm transition shows significantly less absorption but also a lower contribution to heating per cycle.

5.1. Nd:YVO_4 as laser gain medium

Neodymium-doped yttrium (ortho-) vanadate (Nd:YVO_4) has become one of the gain mediums of choice for lasers delivering average output powers from hundreds of milliwatts to a few tens of watts, in cw, Q-switched, or mode-locked regime. Being employed in many commercial medium-power solid-state lasers, it is an inexpensive material available from numerous suppliers. It benefits from many desirable optical and spectroscopic properties. Most importantly for our purpose, it features a laser transition at 1342 nm with a large emission cross-section. Unfortunately the YVO_4 host material suffers unfavorable thermo-optical and mechanical characteristics as a major drawback, limiting the accessible output power. Figure 5.2 shows an energy level scheme and the main optical transitions of the neodymium ion (Nd^{3+}) in an YVO_4 host crystal. We exploit the ${}^4F_{3/2} \rightarrow {}^4I_{13/2}$ transition, which corresponds to the emission line at 1342 nm. In this section, the physical structure and parameters of Nd:YVO_4 will be presented, most of all its optical characteristics.

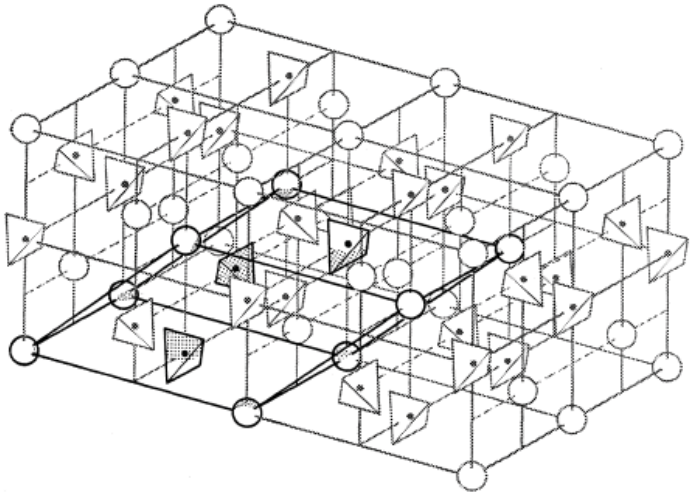

Figure 5.3: Crystal structure of YVO_4, which is of the tetragonal zircon type, from [190]. The tetrahedra represent the VO_4^{3-} ions, balls are Y^{3+} ions. The unit cell is marked in bold lines.

5.1.1. Crystal structure

The crystal structure of yttrium orthovanadate (YVO_4) is of zircon tetragonal type (space group D_{4h}) with $a = b$, see Figure 5.3. It is a (positive) uniaxial crystal grown with the Czochralski method. As a birefringent material, rods made of it are usually rectangular. There are two equivalent ordinary a-axes and one extraordinary c-axis, all mutually orthogonal. We use a-cut crystals, meaning that the optical surface normal vector is parallel to one of the a-directions. By rotating the polarization direction of a linearly polarized beam passing the crystal, we can therefore make use of the optical properties of both the a- and c-axis.

The yttrium atoms can be replaced by impurities or dopants of similar size. The value for a neodymium doping is commonly given in at. %, meaning that the corresponding percentage of Yttrium ions is replaced by neodymium ions. Since the trivalent neodymium substitutes for trivalent yttrium, no charge compensation is required. However the radius of Nd^{3+} is approximately 5% larger than that of Y^{3+}, so that high doping values will lead to strained crystals. Fortunately the high pump absorption coefficients of Nd:YVO4 limit the typical doping values to 0.1–3 at. % for most applications. In practice the doping is chosen in such a way that the requirements regarding pump absorption per unit length and heat density are satisfied, see Section 5.1.3 and Section 5.2.2.

The major shortcoming of YVO_4 arises from its relatively poor thermal properties, as the material exhibits for example a lower thermal conductivity than YAG, see Table 5.1. This limits the amount of pump light that can be absorbed before excessive thermal lensing and aberrations occur, ultimately leading to crystal fracture.

In Table 5.1 we list important material parameters of Nd:YVO_4.

Property	**Value**	**Ref.**
Typical doping	0.1–3 at.%	[191]
Atomic Density Nd^{3+}	$1.26 \cdot 10^{20} cm^{-3}$	[191]
Refractive index @ 1342 nm	1.9587(a), 2.1659(c)	[192]
Absorption coefficient α_{abs} @ 808 nm	18 cm^{-1}(a), 35 cm^{-1}(c)	[193]
Absorption coefficient α_{abs} @ 888 nm	1.7 cm^{-1}(a), 1.6 cm^{-1}(c)	[193]
Intrinsic Loss	0.16% cm^{-1}	[194]
Peak stimulated emission cross section $\sigma_{em,max}$	$18 \times 10^{-20}\,cm^2$	[195]
Peak excited-state absorption cross section $\sigma_{ESA,max}$	$18 \times 10^{-20}\,cm^2$	[195]
Stimulated emission cross section $\sigma_{em}(2\lambda_{Li})$	$15 \times 10^{-20}\,cm^2$	[195]
Excited-state absorption cross section $\sigma_{ESA}(2\lambda_{Li})$	$3 \times 10^{-20}\,cm^2$	[195]
Upper-state fluorescence lifetime τ_{fl} (doping-dependent)	$50 - 110\,\mu s$	[196]
Upper-state fluorescence lifetime τ_{fl} (for 0.5 at.%)	$100 - 110\,\mu s$	[196]
Upper-state radiative lifetime τ_{rad}	120 μs	[196]
Gain bandwidth	1.7 nm $\widehat{=}$ 280 GHz	[195]
Breakage stress	51-53 MPa	[197, 198]
Thermo-optical coefficient dn/dT (a/c)	$(2.9/8.5) \times 10^{-6}\,K^{-1}$	[191]
Thermal conductivity κ (a/c)	$(5.10/5.23)\,W.K^{-1}.m^{-1}$	[197]

Table 5.1. – Important material parameters of Nd:YVO_4. All values are for typical doping of 1 at.%, if not stated otherwise.

5.1.2. Emission

The full emission spectrum was measured by [199] and is presented in Figure 5.4. The quantity presented in the figure is the difference $\sigma_{em} - \sigma_{ESA}$, which is the direct observable of the standard measurement methods. σ_{em} denotes the stimulated-emission cross section and σ_{ESA}

is the so-called excited-state absorption (ESA) cross section for absorption of light by excited ions.

As can be noticed on this graph, the neodymium ion exhibits two features at around 1 μm and 1.3 μm. Moreover the impact of ESA becomes clear by the fact that it causes dips in the emission spectrum in Figure 5.4 and has detrimental effects on laser emission. Since the spectral resolution of the data from [199] is only 2.5 nm, our collaboration partners from Toulouse contacted the group of R. Moncorgé CIMAP, Université de Caen, France and asked them to perform a more precise measurement of the stimulated-emission cross section around the feature at 1342 nm. The result with a notably higher spectral resolution of 0.5 nm is shown in Figure 5.5. The value for the stimulated-emission cross section at twice the vacuum wavelength of the lithium D-transitions,

$$2\lambda_{\mathrm{LiD-Lines}} = 2 \times 671.0\,\mathrm{nm} = 1342.0\,\mathrm{nm}\,, \tag{5.1}$$

is close to the peak value and can be determined to be

$$\sigma = 15 \times 10^{-20}\,\mathrm{cm}^2\,. \tag{5.2}$$

Since the emission cross section is always higher for c-polarization in the interesting wavelength range, we usually chose this axis as the polarization axis of the operating laser.

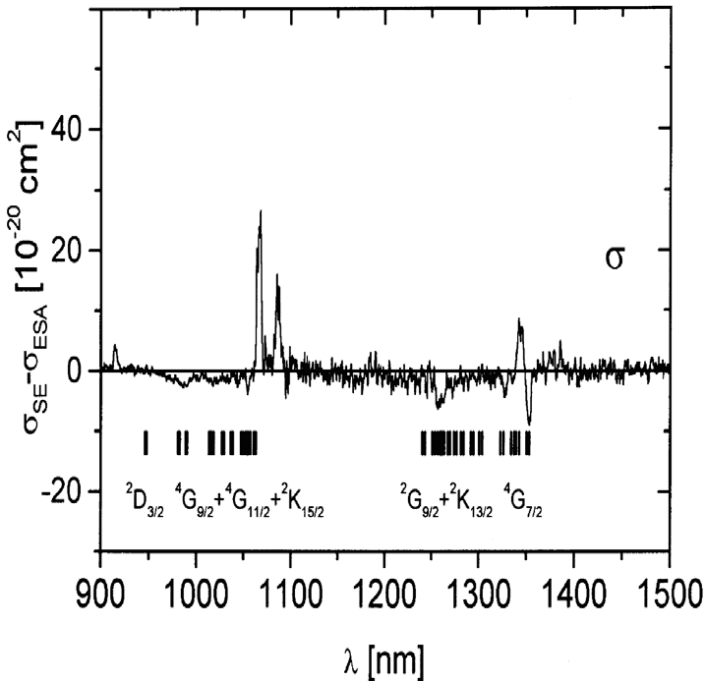

Figure 5.4: Emission spectrum of Nd:YVO_4 measured for the c-axis with a spectral resolution of 2.5 nm (from [199]). It exhibits two noticeable features around 1064 nm and at 1342 nm.

The metastable state lifetime τ is another spectroscopic quantity that is important for the performance of a laser medium. A long lifetime is advantageous, since the gain in the small-

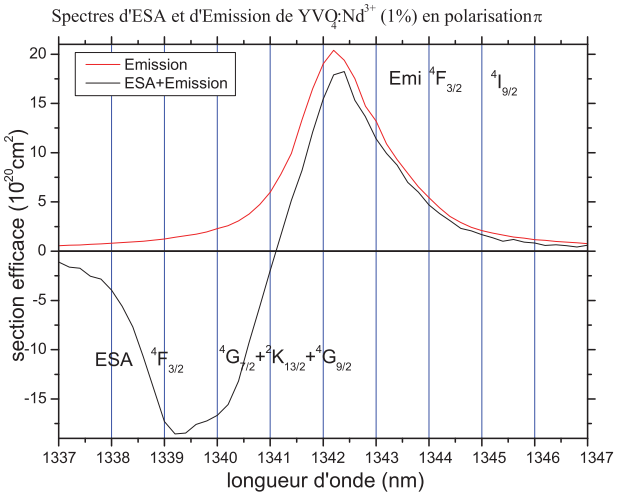

Figure 5.5: High-resolution emission spectrum around the 1342 nm transition, measured on the c-axis by the group of R. Moncorgé [195] and first published in [184]. For the wavelength $2\lambda_{\mathrm{LiD-Lines}}$ we are interested in, one can deduce an emission cross-section of $\sigma_{\mathrm{em}}(2\lambda_{\mathrm{LiD-Lines}}) = 12 \times 10^{-20}\,\mathrm{cm}^2$ and an excited-state absorption (ESA) cross-section of $\sigma_{\mathrm{ESA}}(2\lambda_{\mathrm{LiD-Lines}}) = 3 \times 10^{-20}\,\mathrm{cm}^2$

.

signal limit is proportional to the product $\sigma_{\mathrm{em}}\tau$. It depends, however, strongly on the density of the dopant atoms, see [196]. For crystals with doping values around $0.5\,at.\,\%$ the upper-state fluorescence lifetime is $\tau = 100-110\,\mu$s, whereas the radiative lifetime caused exclusively by radiative decay, is given by $\tau_{\mathrm{rad}} = 120\,\mu$s.

5.1.3. Absorption

A convenient optical pumping of the gain medium is a requirement for laser action. We decided for end pumping, where the pump light is injected along the laser beam, meaning that the pump beam propagates collinear to the cavity mode in the active medium and provides high power efficiency.
In the next subsections we will first describe the advantages and disadvantages of the common optical pumping at 808 nm, and subsequently present a novel pump concept employing a pumping wavelength of 888 nm.

Pumping at 808 nm

Nd:YVO_4 is most commonly pumped at its peak absorption wavelength around 808 nm, which is a consequence of the strong absorption cross section of the $^4I_{9/2} \rightarrow ^4F_{5/2}$ transition and the availability of pump diodes at this wavelength. The absorption spectrum is shown in Figure 5.6, as published in [193]. It was measured for a Nd-doping of 1 at.% and for both linear polarizations parallel to the a- and c-axis, covering a wavelength range from 800 nm to 900 nm. The absorption coefficient scales linearly with doping if the mutual influence of the neodymium ions is negligible, which holds in the limit of small doping. The absorption line at 808 nm corresponds to the transition from the $^4I_{9/2}$ ground state to the $^4F_{5/2}$ upper

pump level. The maximal absorption coefficient of $\alpha = 34\,\mathrm{cm}^{-1}$ is achieved for light polarized parallel to the c-axis. The absorption is reduced by a factor of 2 if the light is polarized parallel to the a-axis. In the case of pumping at 808 nm the absorption is thus strongly polarization dependent. Another large absorption line can be found at 880 nm and corresponds to the transition from the ground state directly to the ${}^4F_{3/2}$ laser level. For this wavelength the absorption of light polarized parallel to the c-axis is a factor 2 lower compared to the transition at 808 nm and is even more polarization dependent. In addition a weak absorption feature can be noticed around 888 nm. We will detail this transition in the next subsection. We notice that all three absorption bands are conveniently addressable by commercially available laser diode stacks. However, when pumping at 808 nm, the pump diode stacks typically need to be temperature stabilized in order to tune the emission wavelength to match the relatively narrow absorption feature at its maximum.

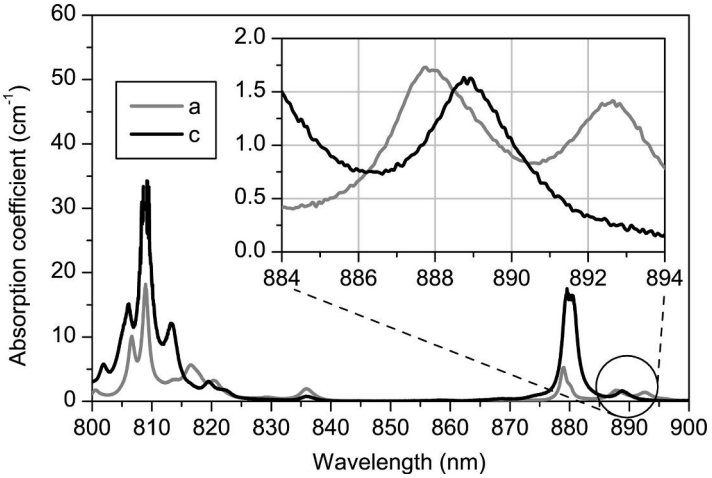

Figure 5.6: Absorption spectrum of Nd:YVO_4 (1 at. % doping) for light polarized parallel to the a- and c-axis in the wavelength range from 800 nm to 900 nm (from [193]). The material features several absorption bands at 808 nm, 880 nm and 888 nm, the latter being almost polarization-independent.

The advantage of pumping at 808 nm consists in the possibility to achieve high absorption of the incident pump beam on relatively short distances inside a laser crystal of only some millimeters length. By focusing the pump beam on small waists, this allows the realization of efficient laser sources even with low pump powers. Moreover light sources, like semiconductor laser stacks, at 808 nm are readily available and inexpensive industry products.
However the possibilities of realizing high power lasers at a pumping wavelength of 808 nm are quite restricted. At higher pump powers, due to the strong absorption on short distances, strong thermal lensing with aspherical components occurs, that cannot be compensated any more by a suitable cavity design. The ultimate limit for the pump power is set by the fracture threshold which is readily reached for strong absorption in a small volume, since a large part of the absorbed power is deposited as heat load close to the input facet of the crystal. An additional drawback is the polarization dependence of absorption at 808 nm. If the pump light is partially polarized, as it is most often the case for fiber-coupled diodes, a modification

of the polarization state by for instance mechanical stress on the fiber, will result in a varying distribution of the heat load along the crystal length, unstable output powers and mode jumps. A possible solution is to use fully polarized pump light with free-space propagation, but this has the disadvantage of not allowing for the physical separation of the pump diodes and the laser resonator.

Pumping at 888 nm

The inset in Figure 5.6 shows an enlarged view of the absorption spectrum of Nd:YVO_4 in the vicinity of 888 nm. In this wavelength range the absorption coefficient is by more than one order of magnitude smaller than at a wavelength of 808 nm for the same doping value of 1 at.%. In addition, the absorption is almost the same for both polarization directions. The quasi-equality is still enhanced by the fact that common pump diodes have a spectral width that is not negligible. Figure 5.7 depicts the convolution of the absorption spectrum with a gaussian diode laser spectrum of 3.5 nm width (FWHM) as well as experimental values for the effective absorption coefficient measured for a real 3.5 nm wide diode as a function of the center wavelength [193]. It shows that the relatively large width of several nanometers of such a pump diode results in a broad wavelength range in which the absorption is practically constant and polarization independent. The 888 nm absorption line being quasi-polarization-insensitive, it is favorable to use laser diode stacks that are coupled to non-polarization-maintaining multi-mode optical fibers, since the radiation emitted from these fibers is typically randomly polarized. Furthermore this facilitates the handling and improves the robustness of the whole optical setup.

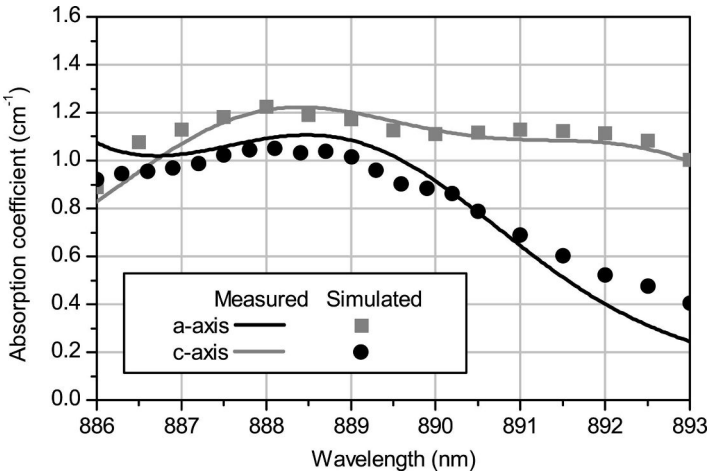

Figure 5.7: Theoretical curve for the convolution of the absorption spectrum with a 3.5 nm wide (FWHM) gaussian diode laser spectrum as well as experimental values for the effective absorption coefficient measured for a real 3.5 nm wide diode as a function of the center wavelength (from [193]).

As a consequence of the reduced absorption coefficient at 888 nm it becomes possible to deposit a considerably higher pump power in the laser crystal. The left side of Figure 5.8

illustrates the usual principle of end-pumping of a solid-state laser at 808 nm. The pump beam is strongly focused onto the entrance facet of the crystal and absorbed over a short distance due to the high absorption. Therefore only relatively weak pump powers can be applied without risking the destruction of the crystal by thermal fracture. The right side of the same figure depicts the principle of pumping at 888 nm. The pump beam is less tightly focused onto a larger diameter inside the long low-doped crystal. Because of the weak absorption and the large waist of the pump beam, the power is distributed over a large volume of the crystal, thus allowing the application of considerably higher powers without any disadvantages due to the thermal load.

A further advantage of optical pumping at 888 nm is the reduced quantum defect, which means that a larger relative part of the pump photon energy is converted to laser photon energy instead of heat, reducing thus detrimental thermal effects, see Section 5.2.2. At a lasing wavelength of 1342 nm the value of the quantum defect for pumping at 808 nm is $\eta_{\mathrm{qd},808} = 0.4$, whereas for a pumping wavelength of 888 nm it is reduced by 15% to $\eta_{\mathrm{qd},888} = 0.34$.

The presented pumping concept should therefore allow for the application of higher pump powers and power scaling of solid-state lasers at 1342 nm. In order to confirm the realizability of a laser cavity that operates in the stability range, it is necessary to have information about the thermo-optical and thermo-mechanical properties of the laser crystal when it is exposed to the injected pump beam and under the condition of cavity lasing. Most importantly we are interested in the focal length of the induced thermal lens, which will be subject of Section 5.2.2.

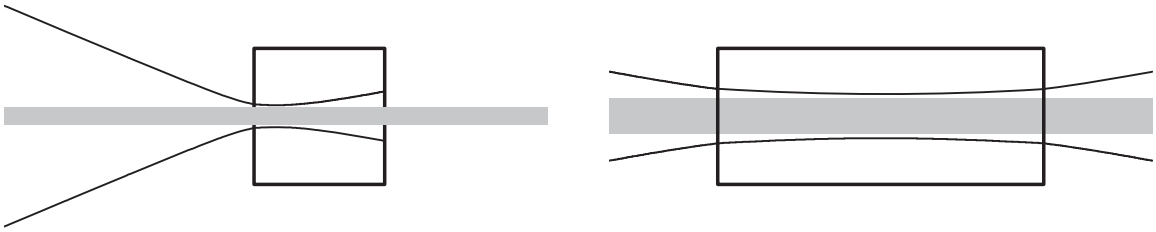

Figure 5.8: Tight pump beam focusing in a short crystal that is end-pumped at 808 nm (left) and less tight focusing in a longer crystal that is end-pumped at 888 nm (right), as published in [189]. The laser mode is illustrated in gray.

5.2. Laser cavity design: Theory and realization

In this section, we will give a short outline of the theoretical concepts needed for the design and optimization of the laser cavity. The discussion starts with the properties of Hermite-Gaussian beams which describe the cavity eigenmodes. The thermal effects occurring in the gain material are investigated both theoretically and experimentally, and we will indicate analytic expressions for the output power of a solid-state laser. In the last subsection, the final technical design of the near-infrared laser cavity is presented.

5.2.1. Hermite-Gaussian beam modes and resonators

Laser beams are in general sufficiently collimated along their propagation axis to be described by the Helmholtz equation in paraxial approximation [200], see Equation (5.3). They can therefore be decomposed into Hermite-Gaussian modes which form a complete set of solutions of the paraxial Helmholtz equation, indicated here for a beam propagating in the z-direction,

$$\left(\frac{\partial^2}{\partial x^2} + \frac{\partial^2}{\partial y^2} - 2\mathrm{i}k\frac{\partial}{\partial z}\right)\mathbf{E}(\mathbf{r},t) = 0 \tag{5.3}$$

where $k = 2\pi/\lambda$ is the wave number for the wavelength λ. Any solution to this equation can be written as a linear superposition of orthogonal solutions

$$\mathbf{E}(\mathbf{r},t) = E_0\,\mathbf{n}\,u_m(x,z)\,u_n(y,z)\,\mathrm{e}^{-\mathrm{i}(kz-\omega t)}\,, \tag{5.4}$$

with the field amplitude E_0, the normalized polarization vector $\mathbf{n}$ and the phase term $\mathrm{e}^{-i(kz-\omega t)}$. We will restrict our description to the x-coordinate, since the eigenfunctions $u_m(x,z)$ and $u_m(y,z)$ are identical for both transversal directions. The basis functions are given by

$$u_m(x,z) = \left(\frac{2}{\pi}\right)^{\frac{1}{4}}\sqrt{\frac{\exp\left(\mathrm{i}(2m+1)\varphi_x(z)\right)}{2^m m! w_x(z)}}\,H_m\left(\frac{\sqrt{2}x}{w_x(z)}\right)\exp\left(-\mathrm{i}\frac{kx^2}{2R_x(z)} - \frac{x^2}{w_x^2(z)}\right). \tag{5.5}$$

where H_m is the Hermite polynomial of order m, $w_x(z)$ is the characteristic radius of the beam along direction x at position z and $R_x(z)$ is the radius of curvature of the wavefront. The characteristic radius reads

$$w_x(z) = w_{0,x}\sqrt{1 + \left(\frac{z}{z_{\mathrm{R},x}}\right)^2}\,, \tag{5.6}$$

where $z_{\mathrm{R},x}$ is the Rayleigh length. The smallest value at $z = 0$ is called the waist of the beam

$$w_{0,x} = \sqrt{\frac{\lambda z_{\mathrm{R},x}}{\pi}}. \tag{5.7}$$

The additional phase factor $\varphi_x(z)$ denotes the so-called Gouy phase shift and is expressed by

$$\varphi_x(z) = \arctan\left(\frac{z}{z_{\mathrm{R},x}}\right). \tag{5.8}$$

which describes the acquired phase shift which differs from that for a plane wave with the same frequency ω.

Ray transfer matrix analysis and cavity resonance condition

The description of the evolution of a beam propagating in z-direction can be simplified by introducing the complex parameter

$$q_x(z) = z + \mathrm{i} z_{\mathrm{R},x} \,, \tag{5.9}$$

with z being the distance from the beam focus position and the Rayleigh length $z_{\mathrm{R},x}$. The evolution of a Hermite-Gaussian beam mode passing through linear optical elements can then be calculated by applying the $ABCD$-matrices formalism known from ray transfer matrix analysis, according to the following transformation:

$$q'_x = M_x * q_x \equiv \frac{A_x q_x + B_x}{C_x q_x + D_x} \,, \tag{5.10}$$

The transfer matrices

$$M_x = \begin{pmatrix} A_x & B_x \\ C_x & D_x \end{pmatrix} \tag{5.11}$$

are tabulated for standard optical components, see for instance [200, 201]. An optical system consisting of several optical elements is also represented by a matrix M_x, that can be derived by simple matrix multiplication to the left for successive components.
The eigenmodes of an optical cavity can de determined by first calculating the cavity matrix M_x independently for the two transverse axes. An eigenmode is defined as an eigenvector of the cavity matrix, meaning that the eigenmode reproduces itself after one complete resonator round-trip:

$$q_x \equiv q'_x = M_x * q_x \,, \tag{5.12}$$

Defining the stability parameter

$$p_{\mathrm{stab},x} = \frac{A_x + D_x}{2} \,, \tag{5.13}$$

one can show that a stable cavity eigenmode only exists if the following stability criterion is fulfilled:

$$-1 < p_{\mathrm{stab},x} < 1 \,. \tag{5.14}$$

The operation of an laser resonator also requires that the laser mode reproduces itself after one resonator round-trip in terms of the acquired phase. This yields a resonance condition for the total phase φ_{tot} acquired during one resonator round-trip

$$\varphi_{\mathrm{tot}} \equiv 2\pi p \,, \tag{5.15}$$

where $p \in \mathbb{N}$ is the longitudinal mode index. Apart from the fundamental Gaussian beam mode, also higher cavity TEM_{mn} eigenmodes, with $m, n > 0$, may occur. As already men-

tioned, a Hermite-Gaussian beam accumulates the so-called Gouy phase shift $\varphi_{m;x}$ that expresses the phase difference with respect to a plane wave of the same frequency during one round-trip, see [200] and Equation (5.5):

$$\begin{aligned}\varphi_{m,x}(z) &= \left(m + \frac{1}{2}\right)\varphi_x(z) \\ &= \left(m + \frac{1}{2}\right)\arctan\left(\frac{z}{z_{\mathrm{R},x}}\right) .\end{aligned} \tag{5.16}$$

The y-direction has to be treated in the same way, resulting in a $\varphi_{n,y}$ as in Equation (5.16). Thus the total phase shift is

$$\varphi_{mn}(z) = \varphi_{m,x}(z) + \varphi_{n,y}(z) . \tag{5.17}$$

The total optical length of a cavity is defined as sum over all optical path lengths

$$L_{\mathrm{opt}} = \sum_k n_k t_k , \tag{5.18}$$

with the geometrical path lengths t_i between optical surfaces and the refractive indices n_i of the corresponding media i. The resonance condition therefore reads

$$k_{mn} L_{\mathrm{opt}} + \varphi_{mn}(L_{\mathrm{opt}}) + \varphi_{\mathrm{res}} \equiv 2\pi p , \tag{5.19}$$

with the residual phase term φ_{res}, due to, for example, optical surfaces with dielectric coatings, which is assumed to be constant for all eigenmodes. The wavenumber k_{mn} is

$$k_{mn} = \frac{2\pi}{\lambda_{mn}} = \frac{2\pi\nu_{mn}}{c} , \tag{5.20}$$

with the vacuum speed of light c. The resonance condition for the longitudinal mode thus reads

$$k_{mn} = \frac{1}{L_{\mathrm{opt}}}\left(2\pi p - \varphi_{mn}(L_{\mathrm{opt}}) - \varphi_{\mathrm{res}}\right) . \tag{5.21}$$

This yields the eigenfrequencies

$$\nu_p = p\nu_{\mathrm{FSR}} + \nu_{\mathrm{res}} . \tag{5.22}$$

where the free spectral range ν_{FSR} is defined as the frequency spacing between neighboring longitudinal modes of identical transversal mode numbers m, n,

$$\nu_{\mathrm{FSR}} = \frac{c}{L_{\mathrm{opt}}} . \tag{5.23}$$

Finally we consider the frequency distance $\Delta\nu_{\Delta m \Delta n}$ between different Hermite-Gaussian modes at fixed longitudinal mode number p:

$$\begin{aligned}\Delta\nu_{\Delta m\Delta n} &= \frac{c}{2\pi L_{\mathrm{opt}}}\varphi_{\Delta m\Delta n}(L_{\mathrm{opt}}) \\ &= \frac{c}{2\pi L_{\mathrm{opt}}}\left(\Delta m\varphi_x(L_{\mathrm{opt}}) + \Delta n\varphi_y(L_{\mathrm{opt}})\right) ,\end{aligned} \tag{5.24}$$

where $\Delta m = m - m'$ and $\Delta n = n - n'$ for two transversal modes with indices m, n and m', n', respectively. This result shows that in general, Hermite-Gaussian cavity eigenmodes of different order are not degenerate in resonance frequency. We can benefit from this property for coupling exclusively to the TEM_{00} mode of an enhancement cavity used for frequency doubling, as we will describe in Section 6.2.

5.2.2. Thermal effects and power scaling

The power scaling of diode-end-pumped solid-state lasers to higher output powers is in general limited by thermal effects induced in the gain medium at high pump powers. The absorption of pump photons and the subsequent emission of laser photons lead to local heating inside the laser crystal due to phononic transitions. In a four-level laser medium, the first phononic relaxation process that take place after a pump excitation is from the highest excited state to the metastable intermediate state creating the necessary population inversion. Subsequently the Nd^{+3}-ion relaxes optically, namely by stimulated or spontaneous emission of a laser photon, to an intermediate state. From there another phononic de-excitation brings them finally back to the ground state.
The local heating induced by pump light and laser action in an active medium results in several thermo-mechanical and optical effects [202]:

— Since the refractive index of most materials is temperature-dependent, it varies locally according to the temperature profile induced by the pump beam absorption and laser action. The resulting refractive index profile acts like an optical lens and affects the eigenmodes and the stability range of the laser resonator [203].

— In particular for end-pumped solid-state lasers a large amount of the heat load is located close to the input facet causing stress along the optical axis of the pump light and thus bulging of the crystal facets. Hence, the crystal acts as a thick lens.

— The thermally induced stress also causes spatial variations of the refractive index due to stress-dependence of the refractive index of most materials. This represents a third effect that causes thermal lensing. However, this effect is relatively small and can in general be neglected.

— The preceding causes for thermal lensing can also lead to optical birefringence. This effect has only importance for optically isotropic media, since for naturally birefringent materials like Nd:YVO_4 it is negligibly small.

— If the stress inside the crystal becomes to large, it might exceed the breakage stress of the crystal medium, resulting eventually in its fracture. Since most materials possess

a higher resistance under compression than under tension, crystal fracture will usually originate from the crystal edge on the input facet, where tensile stress is maximal [198].

These thermal lensing effects have in general strong non-spherical contributions leading to losses for gaussian laser beams arising from thermal diffraction and aberrations. As a consequence, the expression for the total cavity round-trip loss, that will be used in Section 5.2.3, depends on the absorbed pump power:

$$\alpha_{\mathrm{tot}}\left(P_{\mathrm{abs}}\right) = \alpha_{\mathrm{T}} + \alpha_{\mathrm{res}}\left(P_{\mathrm{abs}}\right) . \tag{5.25}$$

We consider the three-dimensional heat conduction equation, that relates the local temperature $T(x, y, z)$ to the local heat load $Q(x, y, z)$ under steady-state conditions of pumping, optical extraction, and cooling:

$$\nabla^2 T(\mathbf{r}) + \frac{Q(\mathbf{r})}{\kappa} = 0 , \tag{5.26}$$

where κ denotes the thermal conductivity. If the pump beam diameter is significantly smaller than the crystal length, we can apply the thin slice approximation that neglects an axial heat flow within the crystal along z. Thus only the radial heat flow is taken into account. In order to simplify the problem, the thermal conductivity is considered isotropic and the crystal as well as the pump distribution radially symmetric. Instead of considering a square-section crystal with different thermo-optical properties along the a- and c- axes, we therefore simplify to the pumping of a cylindrical rod with isotropic properties. The steady-state heat conduction equation then reduces to a one-dimensional problem in cylindrical coordinates:

$$\frac{1}{\rho}\frac{\partial}{\partial \rho}\left(\rho \frac{\partial T(\rho, z)}{\partial \rho}\right) + \frac{Q(\rho, z)}{\kappa} = 0 . \tag{5.27}$$

The constant heat deposition within the pump spot of a top-hat pump profile of radius ω_{p} is given by:

$$Q(\rho, z) = \frac{\eta_{\mathrm{h}}}{\pi \omega_{\mathrm{p}}^2(z)} \left| \frac{\mathrm{dP_P(z)}}{\mathrm{dz}} \right| \Theta(\omega_{\mathrm{p}}^2(z) - \rho^2) . \tag{5.28}$$

where $\left|\frac{\mathrm{dP_P(z)}}{\mathrm{dz}}\right|$ is the differential absorbed pump power, which, in the case of single end-pumping with isotropic absorption, is given by $\left|\frac{\mathrm{dP_P(z)}}{\mathrm{dz}}\right| = \alpha P_{\mathrm{P}}(0)\mathrm{e}^{-\alpha z}$. Assuming a fixed temperature $T(\rho_{\mathrm{c}}, z) = T_0$ at the crystal edge, Equation (5.27) can be solved analytically to obtain the temperature difference between a position at a radius ρ from the crystal center and the cooled crystal edges at the crystal radius ρ_{c}:

$$T(\rho, z) - T_0 = \frac{\eta_{\mathrm{h}} P_{\mathrm{abs}}}{4\pi\kappa} \frac{\alpha \mathrm{e}^{-\alpha z}}{1 - \mathrm{e}^{-\alpha l_{\mathrm{cry}}}} \times \begin{cases} \ln\left(\frac{\rho_0^2}{w_{\mathrm{p}}^2(z)}\right) + 1 - \frac{\rho^2}{w_{\mathrm{p}}^2(z)}, & \text{if } \rho \le w_{\mathrm{p}}(z) \\ \ln\left(\frac{\rho_0^2}{\rho^2}\right), & \text{if } \rho \ge w_{\mathrm{p}}(z) \end{cases} \tag{5.29}$$

Here, η_{h} denotes the relative amount of the pump photon energy contributing to heating and differs for lasing and non-lasing conditions. This solution shows that the temperature

distribution is parabolic inside the pump spot and logarithmic outside the pump spot towards the outer surface of the crystal. For a given pump spot size, the maximum temperature is directly proportional to the absorbed pump power per length and is located in the center of the crystal. In the case that the side surfaces of the crystal are kept at a constant temperature along its whole length, the temperature difference between the center and a position at radius ρ follows a parabola within the pump spot:

$$\Delta T(\rho, z) = T(\rho, z) - T(0, z) = -\frac{\eta_\mathrm{h} P_\mathrm{abs}}{4\pi\kappa} \frac{\alpha \mathrm{e}^{-\alpha z}}{1 - \mathrm{e}^{-\alpha l_\mathrm{cry}}} \left(\frac{\rho_0^2}{w_\mathrm{p}^2(z)} \right) . \tag{5.30}$$

Once the temperature distribution inside the crystal has been calculated, the thermo-optic contribution to the thermal lens can be directly calculated from the change in refractive index with temperature:

$$\Delta n(\rho, z) = n(\rho, z) - n(0, z) = \frac{\mathrm{dn}}{\mathrm{dT}} \Delta T(\rho, z) = -\frac{\mathrm{dn}}{\mathrm{dT}} \frac{\eta_\mathrm{h} P_\mathrm{abs}}{4\pi\kappa} \frac{\alpha \mathrm{e}^{-\alpha z}}{1 - \mathrm{e}^{-\alpha l_\mathrm{cry}}} \left(\frac{\rho_0^2}{w_\mathrm{p}^2(z)} \right) . \tag{5.31}$$

The refractive index then follows a parabolic evolution from the crystal center,

$$n(\rho, z) = n(0, z) \left(1 - \frac{\rho^2}{b^2} \right) , \tag{5.32}$$

with

$$\frac{1}{b^2} = \frac{\mathrm{dn}}{\mathrm{dT}} \frac{\eta_\mathrm{h} P_\mathrm{abs}}{8\pi n(0, z)\kappa} \frac{\alpha \mathrm{e}^{-\alpha z}}{1 - \mathrm{e}^{-\alpha l_\mathrm{cry}}} \left(\frac{1}{w_\mathrm{p}^2(z)} \right) . \tag{5.33}$$

If we assume that the focal length is long compared to the crystal length, this results in a differential gradient-index lens of power $\mathrm{dD_{th}}$ at a given position z:

$$\mathrm{dD_{th}} = \frac{4\mathrm{n}(0, \mathrm{z})\mathrm{dz}}{\mathrm{b}^2} = \frac{\mathrm{dn}}{\mathrm{dT}} \frac{\eta_\mathrm{h} \mathrm{P_{abs}}}{2\pi\kappa} \frac{\alpha \mathrm{e}^{-\alpha \mathrm{z}}}{1 - \mathrm{e}^{-\alpha \mathrm{l_{cry}}}} \left(\frac{1}{\mathrm{w}_\mathrm{p}^2(\mathrm{z})} \right) \mathrm{dz} . \tag{5.34}$$

Integration of this expression over the entire crystal length, while assuming that the pump beam is collimated along the absorption length, yields

$$D_\mathrm{th} = \frac{\mathrm{dn}}{\mathrm{dT}} \frac{\eta_\mathrm{h} P_\mathrm{abs}}{2\pi\kappa w_\mathrm{p}^2} , \tag{5.35}$$

meaning that the thermal lens power is proportional to the absorbed pump power P_abs divided by the beam cross section πw_p^2.
One has furthermore to distinguish between the non-lasing and lasing case due to the different branching ratios η_h [196]. The fractional thermal loading without laser action $\eta_\mathrm{h,NL}$ is given by

$$\eta_\mathrm{h,NL} = 1 - \eta_\mathrm{q}(1 - \beta) \frac{\lambda_\mathrm{p}}{\lambda_\mathrm{fl}} \tag{5.36}$$

where the parameter β, denoting the fraction of energy stored in the upper laser level that decays non-radiatively, reads

$$\beta = 1 - \frac{\tau_{\mathrm{fl}}}{\tau_{\mathrm{rad}}} \,. \tag{5.37}$$

η_{q} is the pump quantum efficiency, λ_{p} and λ_{fl} are the pump and mean fluorescence wavelength, respectively. τ_{fl} is the fluorescence lifetime and τ_{rad} the purely radiative lifetime of the metastable state in the active gain medium. Under lasing conditions instead of fluorescence, a higher quantity of energy per pump photon is deposited in heat. The fractional heating power changes to

$$\eta_{\mathrm{h,L}} = 1 - \eta_{\mathrm{q}} \left(\frac{\lambda_{\mathrm{p}}}{\lambda_{\mathrm{L}}} \right) \cdot \frac{\sigma_{\mathrm{em}}}{\sigma_{\mathrm{em}} + \sigma_{\mathrm{ESA}}} \,, \tag{5.38}$$

where λ_{L} is the laser wavelength, σ_{em} and σ_{ESA} are the stimulated emission and the ESA (excited-state absorbtion) cross-section, respectively. Equation (5.38) states that excited state absorption not only lowers the available output power, but also detrimentally influences the thermal effects, since the excited-state decay channels can be supposed fully phononic. Since the ratio $\eta_{\mathrm{L}}/\eta_{\mathrm{NL}}$ equals the ratio between the two resulting dioptric powers, one has to consider the corresponding dioptric power range when designing a cavity, as will be shown in the next section.

Another result of the simplified model that we applied is, that the thermal lens is independent of the crystal length and absorption coefficient. Yet, in practice a shorter crystal with higher absorption coefficient will induce higher inversion densities and temperatures, leading to stronger thermal lens aberrations caused by the reduction of the thermal conductivity with increasing temperature. Therefore a longer crystal with low and homogeneous inversion density will favour a lower and less aberrated gradient-index thermal lens.

Experimental determination of the thermal lens

Numerous methods to measure and quantify the thermal lens have been developed in the past. These different approaches measure output beam parameters [204], use degeneration resonator lengths [205], employ transverse mode beat frequencies [206] or are based on interferometric methods [207]. All these methods require, however, an active laser operation. Consequently, these approaches are not appropriate for our purpose, since we intend to determine and compare the thermal lens with and without lasing. Thus we applied a method reported by [203, 208] using a probe beam to determine the focal length of the thermal lens. The setup for measuring the thermal lens by use of a probe beam is presented in Figure 5.9. The probe beam of a Helium-Neon laser emitting at 633 nm is linearly polarized parallel to the vertical c-axis of the laser crystal. This ensures that the probe beam measures the effect of the thermal lens correctly for the laser radiation also polarized along the c-axis. Subsequently, the polarized probe beam is injected into the laser crystal via two mirrors (M6, M7), while optimizing the overlap with the 888 nm pump beam. The beam of the Helium-Neon laser

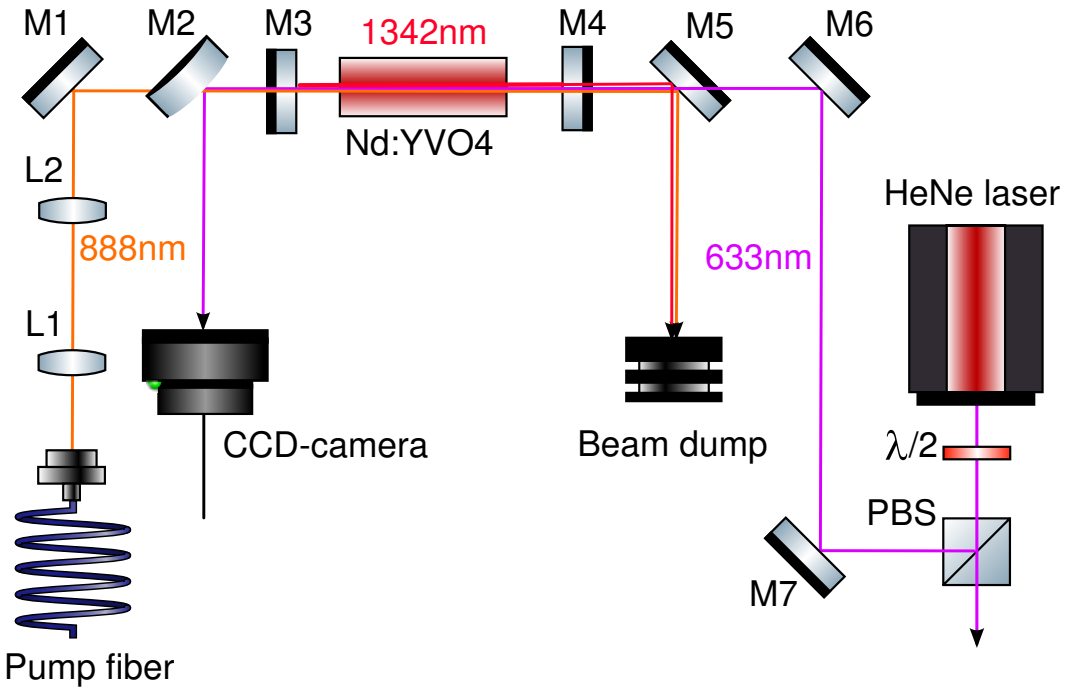

Figure 5.9: Scheme of the measurement setup for determination of the thermal lens with and without laser operation.

is Gaussian and approximately collimated with a beam waist of 350 μm. The beam waist is therefore sufficiently small for not being affected by diffraction effects due to the pump beam profile. The power of the Helium-Neon laser amounts only to several milliwatts.

The experiment is performed under the same pumping conditions as during laser operation with the common cavity setup presented in Section 5.2.4. The pump source is a fiber-coupled QPC BrightLase Ultra-50 diode stack emitting up to 42.6 W at 888 nm (Spectral width (FWHM): 2.2 nm). The fiber output is imaged by two lenses L_1 and L_2 to a top-hat profile of radius $w_{\text{pump}} = 970\,\mu\text{m}$ inside the laser crystal. The laser resonator is formed by mirrors M_3 and M_4, which are both planar. Due to the short resonator length, transversal multi-mode operation of the laser occurs. This ensures a homogeneous overlap of the pump beam and the laser beam in the entire pumped volume of the laser crystal. As a result, the spatial contribution of the ESA to the crystal heating, occurring only in the presence of 1342 nm light, is not altered by a an inhomogeneous mode overlap.

The thermal lens is determined by measuring its impact on the propagation of the probe beam after the Nd:YVO_4 crystal. For this purpose, we measure the beam profile at different distances from the crystal with a CCD camera. Repeating this measurement for all three possible situation (without pumping, pumping without lasing, and pumping with lasing), we can deduce the induced thermal lens from the beam parameters and the geometry of our measurement setup. In this context we approximated the thermal lens as a thin lens situated at the entrance facet of the laser crystal. Without lasing operation we measured a focal

length of 280 mm, whereas for lasing operation at 1342 nm the focal length of the thermal lens amounts to 170 mm.
We decide to compensate for this detrimental thermal lensing effect in the gain medium by installing a curved pump coupling mirror, with a convex radius of curvature of 500 mm, in front of the crystal. The backside of the mirror is also curved correspondingly, such that the pump beam passing through this mirror is not altered by any lensing effect (zero lens mirror). Thus the position and the waist of the pump beam focus remain unchanged. The major purpose of this curved mirror is the compensation for the thermal lens inside the laser crystal, as the defocusing effect of its convex curvature counteracts the focusing effect of the latter.

5.2.3. Characteristic curve and output power

The slope efficiency and the maximum output power are the most crucial parameters of a laser source and depend strongly on its design. In particular for our design considerations of an improved version of the IR-laser, the central goal was to reach an output power in the multi-Watt range.
In general, for diode-end pumped laser emitting at a wavelength $\lambda_\mathrm{L} = c/2\pi\omega_\mathrm{L}$, the output power P_out has a quasi-linear dependence on the absorbed pump power P_abs above a threshold P_th:

$$P_\mathrm{out} = \eta_\mathrm{s}\left(P_\mathrm{abs}\right)\left(P_\mathrm{abs} - P_\mathrm{th}\left(P_\mathrm{abs}\right)\right) \text{ , for } P_\mathrm{abs} > P_\mathrm{th}\,, \tag{5.39}$$

where the slope efficiency η_s varies with P_abs for higher pump powers and is defined as

$$\eta_\mathrm{sl}\left(P_\mathrm{abs}\right) = \frac{\partial P_\mathrm{out}}{\partial P_\mathrm{abs}} = \frac{\alpha_\mathrm{T}}{\alpha_\mathrm{tot}\left(P_\mathrm{abs}\right)}\eta_\mathrm{q}\eta_\mathrm{OI}\left(P_\mathrm{abs}\right)\,. \tag{5.40}$$

α_T denotes the output coupler transmittance and α_tot is the total round-trip loss

$$\alpha_\mathrm{tot}\left(P_\mathrm{abs}\right) = \alpha_\mathrm{T} + \alpha_\mathrm{res}\left(P_\mathrm{abs}\right)\,, \tag{5.41}$$

with α_res summarizing all residual round-trip losses inside the resonator that can in principle depend on P_abs due to losses induced by thermal effects. The quantum efficiency η_q, also often termed quantum yield in literature, describes the energy conversion efficiency between pump and laser photons and is given as

$$\eta_\mathrm{q} = \frac{\omega_\mathrm{L}}{\omega_\mathrm{pump}}\,, \tag{5.42}$$

where $\omega_\mathrm{pump} = c/2\pi\lambda_\mathrm{pump}$ is the pump frequency in radians. The integral

$$\eta_\mathrm{OI}\left(P_\mathrm{abs}\right) = \frac{\left(\int \mathrm{d}V \epsilon_\mathrm{L}(\mathbf{r})\epsilon_\mathrm{P}(\mathbf{r})\right)^2}{\int \mathrm{d}V \epsilon_\mathrm{L}^2(\mathbf{r}) \int \mathrm{d}V \epsilon_\mathrm{P}^2(\mathbf{r})} \tag{5.43}$$

evaluates a normalized overlap of the adimensional mode distribution factor $\epsilon_{\mathrm{L}}(\mathbf{r})$ and the normalized pump distribution $\epsilon_{\mathrm{P}}(\mathbf{r})$ of the laser and pump beams, respectively. We note that the normalizations are chosen such that $\int \mathrm{d}V \epsilon_{\mathrm{L}}(\mathbf{r}) = V$ and $\int \mathrm{d}V \epsilon_{\mathrm{P}}(\mathbf{r}) = 1$. The pump power absorbed in the gain medium of length l_{cry} can be written as

$$P_{\mathrm{abs}} = (1 - \mathrm{e}^{-\alpha_{\mathrm{abs}} l_{\mathrm{cry}}}) P_{\mathrm{pump}} \,, \tag{5.44}$$

where α_{abs} denotes the linear absorption coefficient for the pump radiation and P_{p} the pump power incident on the gain medium. Equation (5.39) includes moreover the absorbed pump power at lasing threshold

$$P_{\mathrm{th}}\left(P_{\mathrm{abs}}\right) = \frac{I_{\mathrm{sat}}}{\eta_{\mathrm{q}} l_{\mathrm{cry}}} \alpha_{\mathrm{tot}}\left(P_{\mathrm{abs}}\right) V_{\mathrm{eff}}\left(P_{\mathrm{abs}}\right) \,, \tag{5.45}$$

the saturation intensity I_{sat} being defined as

$$I_{\mathrm{sat}} = \frac{\hbar \omega_{\mathrm{L}}}{\sigma_{\mathrm{em}} \tau_{\mathrm{rad}}} \,, \tag{5.46}$$

containing the emission cross section σ_{em} and the excited state lifetime τ_{rad}. The values of both material parameters are well known by spectroscopic measurements, as presented in Section 5.1.2. Equation (5.45) furthermore includes the effective volume

$$V_{\mathrm{eff}} = \frac{\int \mathrm{d}V \epsilon_{\mathrm{L}}(\mathbf{r})}{\int \mathrm{d}V \epsilon_{\mathrm{L}}(\mathbf{r}) \epsilon_{\mathrm{P}}(\mathbf{r})} \,. \tag{5.47}$$

It is apparent from Equations (5.39), (5.40) and (5.45) that the maximum output power is achieved in the limit of an on-axis Delta-peak-shaped pump distribution. Apart from being impossible to be realized experimentally, we have seen in section 5.2.2 that in the presence of a real gain medium this would lead to detrimental thermal effects.

5.2.4. Laser cavity design

In the following subsection we will substantiate the chosen cavity design of our improved laser version by taking into account the theoretical assertions presented above and considering the imposed design constraints. Since we had already gained some experience with the first IR-laser version pumped at 808 nm, that was presented in [184, 209], we considered its design principals as a starting point for a sufficiently flexible setup that could be adapted to the modified system parameters due to our thermal lens compensation attempts. In general, the chosen laser design is supposed to account for several important issues.

A first important point is the optimization of the total optical L cavity length that determines the free spectral range $\Delta\nu = c/L$. On the one hand, the cavity length has to be as short as possible, since longitudinal single-mode operation becomes easier to achieve by increasing the spectral mode spacing. On the other hand, we had also to take into account the space requirements imposed by the insertion of additional intra-cavity elements. As we will point

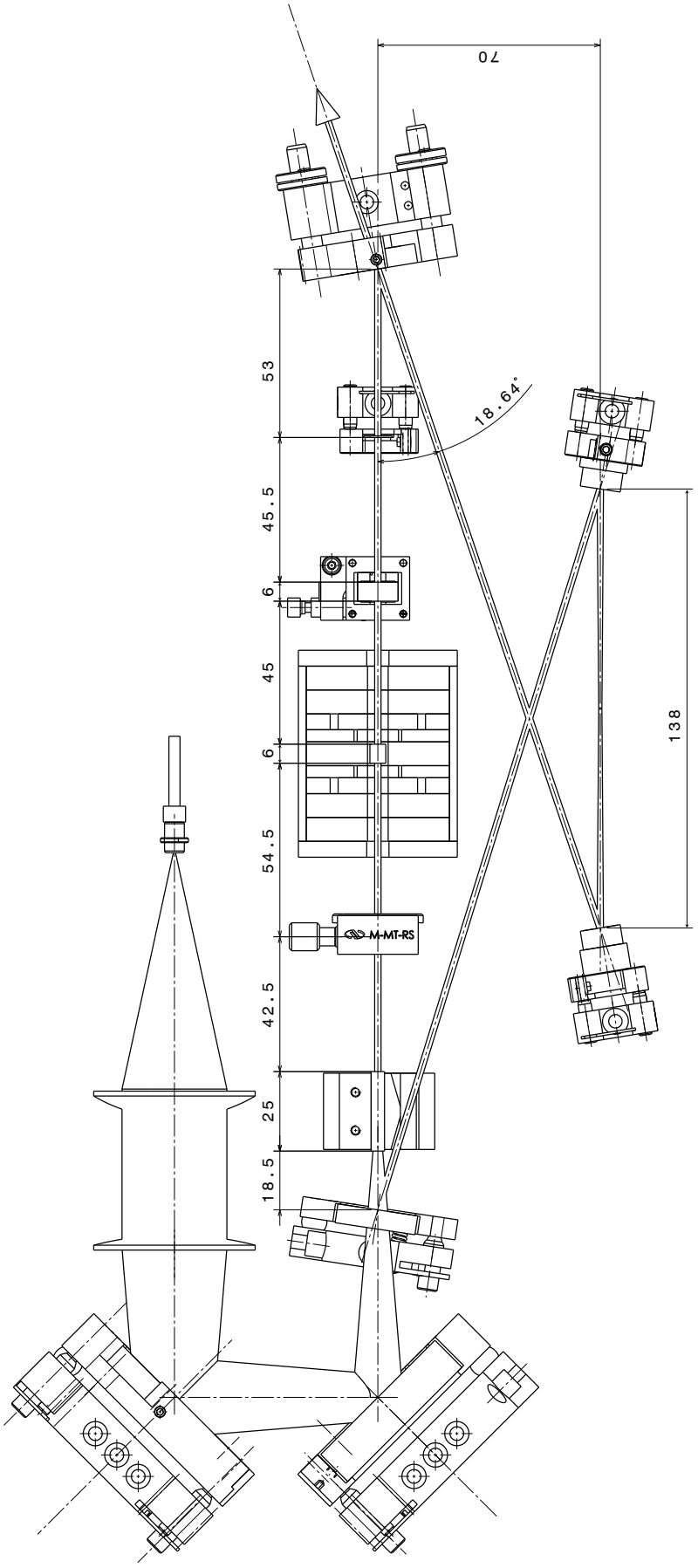

Figure 5.10. – Technical drawing of the final cavity geometry, including all intra-cavity elements. The ring cavity consists of four mirrors M_{1-4}, where M_1 is the zero lens pump coupling mirror, M_2 is the flat output coupling mirror, and M_3 and M_4 are concave. Besides the laser crystal, intra-cavity elements are the half-wave plate $\lambda/2$, a TGG crystal in a large magnet ensemble and two etalons E_{1-2}. The pump spot radius w_p in the Nd:YVO_4 crystal can be varied by using different sets of telescope lenses f_1 and f_2.

out in the following sections, we need to introduce beside the gain medium, a Faraday rotator, a half-wave plate, and two etalons in order to enforce unidirectional single-mode behavior. In order to handle the resulting geometric constraints, which are mainly due to the magnet ensemble of the TGG Faraday rotator with its outer dimensions of $50 \times 50 \times 65\,\mathrm{mm}^3$, the entire laser cavity was designed using the Dassault CATIA CAD-software. The cavity length was further reduced by mounting all optic elements with small-size holders. A schematic 3D-view of the laser setup has already been shown shown in Figure 5.1, and additionally a technical drawing is given in Figure 5.10.

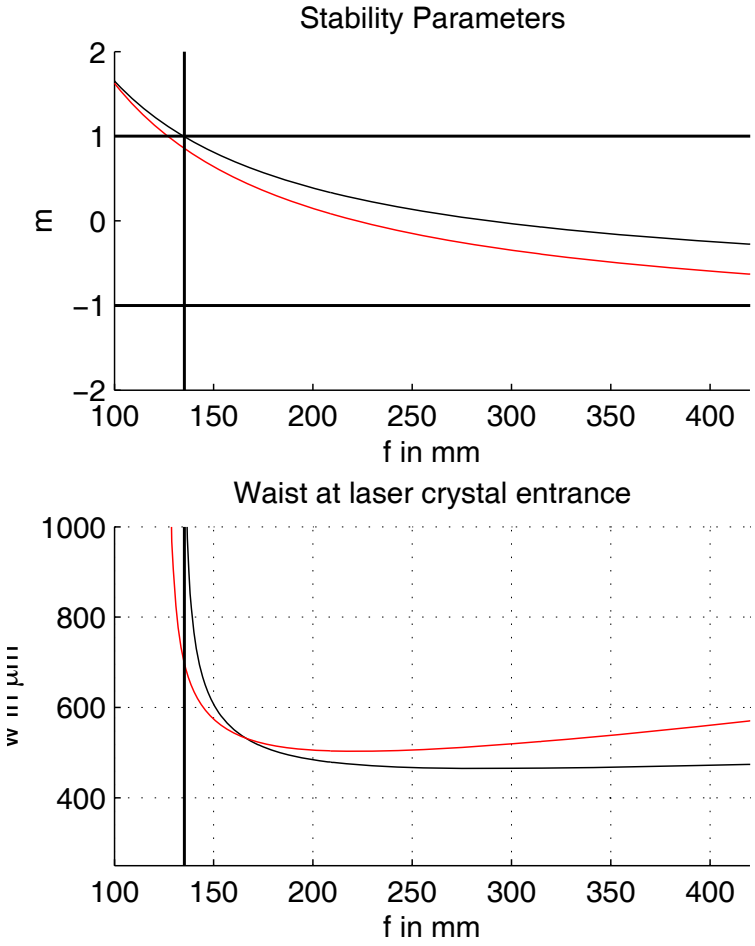

Figure 5.11: The stability diagram (upper panel, see Equation (5.14)) and the mode sizes (lower pannel) in the laser crystal as a function of the thermal lens focal length f_{th}. The black (red) lines denote the horizontal (vertical) direction. The vertical line indicates the limit of cavity stability. The resonator remains stable down to $f_{\mathrm{th,min}} = 135\,\mathrm{mm}$.

We continued to use the bow-tie cavity configuration as it was presented in [184, 209] because it features many advantages. The resonator eigenmode is practically collimated between the convex zero lens mirror M_1 and the plane mirror M_2, and we have in this region enough space at our disposal for the installation of the additional intra-cavity elements, in particular

for the magnet ensemble. The cavity mode is strongly focused between the two concave mirrors M_3 and M_4, and by modifying the distance between these mirrors, the diameter of the cavity mode at the Nd:YVO_4 crystal position can be tuned. Therefore the spatial overlap between the laser and pump mode profiles can be adjusted to optimize output power and mode quality, see Section 5.2.2. The focus between these two mirrors allows the placement of a nonlinear crystal inside the cavity in order to frequency-double the laser directly without the need for an external enhancement cavity or a waveguide. We tested this approach, using periodically poled potassium titanyl phosphate ($KTiOPO_4$, ppKTP), as presented in Section 6.3 and [210].

The small reflection angle of the beam on the four cavity mirrors is a further advantage of our chosen bow-tie design, since we could use the same coatings for all mirrors, except for the output coupler. The zero lens pump coupling mirror M_1 as well as the curved mirrors M_3 and M_4 are highly-reflective coated for 1342 nm at an angle of incidence of 10° for both s- and p-polarization. The same coating efficiently transmits the pump wavelength 888 nm at the same angle of incidence and random polarization. Optionally, we used also another coating design that additionally allows for transmission of the second harmonic output at 671 nm, such that the corresponding (concave) mirrors can be employed inside the enhancement doubling cavity or for intra-cavity doubling. As appropriate, the rear sides were anti-reflective coated at either the pump or the second-harmonic wavelength. The mirror substrates usually consist of fused-silica. However, for the output couplers and the zero lens pump coupler we opted for infrared fused silica as substrate material, since normal fused silica suffers absorption features around for example 1340 nm. Our set of output couplers comprises values for the transmittance between 2% and 17% and the value 10% for the coupler designated for the enhancement doubling cavity. The back sides of the couplers are as well anti-reflective coated at 1342 nm.

An important requirement for the cavity design is that the cavity eigenmode remains stable for a range of focal length values f_{th} of the thermal lens induced in the Nd:YVO_4 crystal, the extreme values of this range corresponding to the lasing and non-lasing state. If this were not the case, intra-cavity power would either not build up starting from fluorescence or the lasing state would suffer unstable behavior and reduced output power. From Equations (5.35), (5.36) and (5.38) we deduce

$$\frac{f_{\mathrm{th,NL}}}{f_{\mathrm{th,L}}} = \frac{\eta_{\mathrm{th,las}}}{\eta_{\mathrm{th,nonlas}}} \,. \tag{5.48}$$

The available spectroscopic data for τ_{fl}, σ_{em} and σ_{ESA}, summarized in Table 5.1, allows an estimation of this ratio. As a result, the stability range needs to cover a focal length range of

$$\frac{f_{\mathrm{th,NL}}}{f_{\mathrm{th,L}}} \simeq 2 \,. \tag{5.49}$$

We can calculate the properties of the cavity eigenmode by solving (5.12) under the condition that (5.14) holds. Figure 5.11 gives a plot of the cavity stability domain and of the mode

radius at the position of the laser crystal as a function of the focal length f_{th} of the thermal lens. It shows that the cavity stability range reaches from infinite focal lengths, corresponding to no thermal effects, down to $f_{\mathrm{th,min}} = 135\,\mathrm{mm}$. The dependence of the mode radius inside the Nd:YVO_4 crystal on f_{th} is also given, reaching from 480 μm to 700 μm.
The optimal ratio of cavity mode size and pump beam size for high-power lasers, namely for $P_{\mathrm{abs}} > 10\mathrm{W}$, is given as [211]

$$\frac{w_{\mathrm{L}}}{w_{\mathrm{p}}} \simeq 0.8\,. \tag{5.50}$$

The mode overlap can be readily optimized for a given value of the thermal lens f_{th} by tuning the distance between the two curved mirrors M_3 and M_4. We realized this in practice by mounting M_4 on a linear translation stage and adjusting its position to optimize the output power and the spatially single-mode quality at the same time, because a too small mode size can lead to the excitation of undesirable higher order modes that artificially increase the output power. The radii-dependence calculated as a function of the mirror distance is plotted in Figure 5.12 for a focal length of $f_{\mathrm{th}} = 170\,\mathrm{mm}$, as measured in Subsection 5.2.2. The accessible waists in the crystal cover thus a range from 520 μm to $\sim$ 1000 μm.
We note, that the distances of the optical elements in our setup can only be determined with a precision on the order of 1 mm. The values for the calculated stability parameters and waists presented in this section depend, however, significantly on these distances. Furthermore, neither the analytic model nor the performed measurement of the thermal lensing effect inside the Nd:YVO_4 crystal, as presented in Section 5.2.2, can give a precise value of the thermal focal length under optimized lasing conditions. We thus refer to Section 5.4.3, where the measured optimized cavity eigenmode is presented permitting another determination of this parameter.
The pump source is a temperature-stabilized fiber-coupled QPC BrightLase Ultra-50 diode stack (NA = 0.22, 400 µm fiber core diameter), emitting up to 42.6 W at 888 nm (Spectral width (FWHM): 2.2 nm). It is cooled down to 4°C to optimize the spectral overlap between pump emission and the gain medium absorption. The fiber output is imaged by two lenses ($f_1 = 75\,\mathrm{mm}$, $f_2 = 175\,\mathrm{mm}$) to a top-hat profile of radius $w_{\mathrm{pump}} = 970\,\mu\mathrm{m}$ inside the laser crystal. The dimensions of the Nd:YVO_4 crystal (a-cut, anti-reflection coated for 1342 nm and 888 nm) were chosen to be $4 \times 4 \times 25\,\mathrm{mm}^3$ and the ion doping was accordingly adjusted to 0.5 at. %. It is wrapped in Indium foil and fixed in a solid water-cooled copper mount to efficiently remove heat. Care needs to be taken to avoid acoustic perturbations of the mount due to turbulent water flow, thus only a small continuous flux of tap water was applied to prevent power and frequency fluctuations of the laser output. The pump coupling mirror M_1 is, as mentioned above, a convex meniscus mirror with a radius of curvature of 500 mm whereas M_3 and M_4 are concave mirrors with a radius of curvature of 100 mm and 150 mm, respectively. The optimal transmittance of the flat output coupler M_2 regarding the maximum output power was found to be 7.5%.

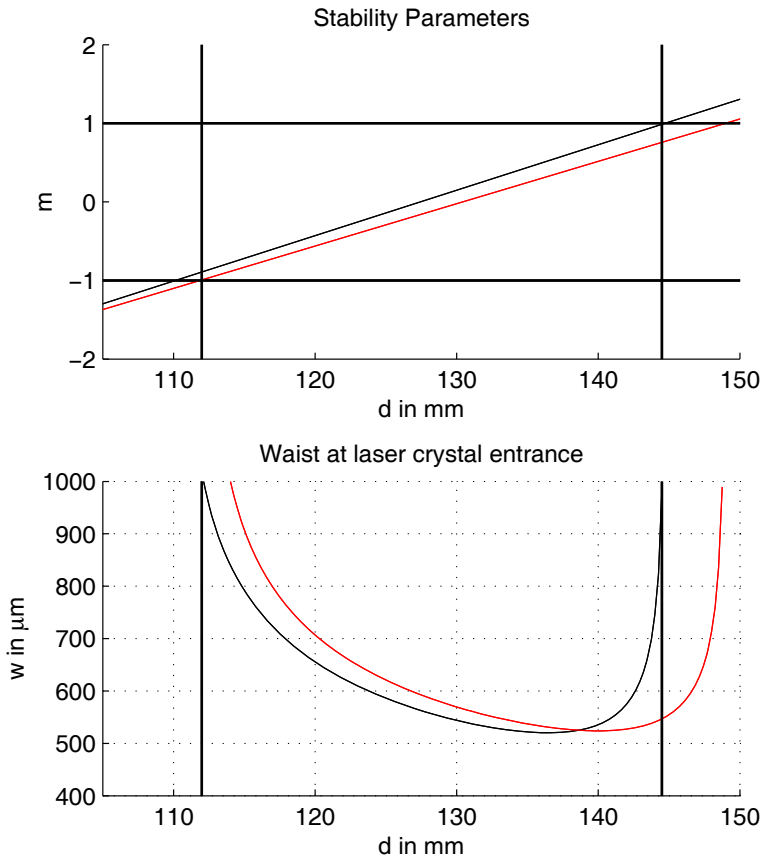

Figure 5.12: (Upper Panel) The stability parameters of the laser cavity as a function of the distance d_{cu} between the curved mirrors M_3 and M_4. The thermal focal length is fixed to 170 mm. (Upper Panel) The mode sizes in the laser crystal $w_{\mathrm{h(v)}}$, the black (red) lines denoting the horizontal (vertical) direction, whereas the vertical lines indicate the range of stability.

The laser cavity elements were mounted on a standard optical table. A temporary housing made of polyvinyl chloride was placed around the cavity in order to keep the setup continuously under a dry-air atmosphere preventing dust and moisture from having detrimental effects on the long-term performance of the system.

5.3. Single-mode operation and frequency tuning

The fundamental IR laser source is supposed to emit single-frequency light, since it is intended to be employed in the context of atom cooling and trapping. In this section we will present the technical methods applied to force unidirectional laser operation in a single longitudinal mode.

5.3.1. Unidirectional operation via Faraday rotator

Running-wave resonators are the preferred choice for realizing a single-longitudinal-mode laser, since standing-wave cavities suffer from the fact that standing waves in the active medium cause spatial hole burning. As a consequence, different longitudinal modes address distinct areas of the gain medium, which partially suppresses mode competition [200].
There exist two approaches for realizing a running-wave laser. A first option is the twisted-mode linear cavity [212], however it cannot be operated together with a birefringent gain medium like Nd:YVO_4. The alternative approach is to force unidirectional operation of a ring cavity. For this purpose, several methods were presented in the past [213–215]. We decided for the insertion of a Faraday rotator and a zero-order half-waveplate inside the cavity that serve together with the birefringent laser crystal as an optical diode.
A linearly polarized light beam experiences a rotation β_{rot} of its polarization axis when propagating through a medium exposed to a magnetic field component B_z in the propagation direction z:

$$\beta_{\mathrm{rot}} = \mathcal{V} \int_0^{l_{\mathrm{F}}} B_z(z)\,\mathrm{d}z\,. \tag{5.51}$$

This expression contains a path integral over the magnetic field in the medium of length l_{F} and the Verdet constant $\mathcal{V}$ which is material- and wavelength dependent. This constant drops significantly for higher wavelengths outside the visible range and the absorption rises in the near-infrared. Therefore the use of a short crystal in a strong magnetic field is more appropriate. Furthermore a transversal variation of the beam polarization has to be avoided by assuring a sufficiently homogeneous field.
In order to meet these requirement Gérard Trénec and coworkers developed an appropriate magnet assembly that consists of a NdFeB ring magnets ensemble [216]. It is designed for Faraday crystals with a length of 6 mm and 5 mm diameter providing a magnetic field of 1.5 T. Accordingly, the measured value for the magnetic field path integral is $\int B_z(z)\,\mathrm{d}z = 9\,\mathrm{T.mm}$. The bulky housing with outer dimensions of $50 \times 50 \times 65\,\mathrm{mm}^3$ is the most limiting constraint for building a compact cavity, as presented in 5.2.4.
We chose Terbium gallium garnet (TGG) as Faraday medium, being the standard material for near-infrared lasers. Our TGG sample was purchased from FEE[1], since their samples have featured relatively large Verdet constants in the past. The measurement of the single-pass rotation angle for the TGG sample placed in the Faraday rotator yields $\beta = 8.9(1)°$ corresponding to a Verdet constant $\mathcal{V} = 17.3(2)\,\mathrm{rad.T^{-1}.m^{-1}}$.
An anti-reflective-coated, zero-order $\lambda/2$-wave plate serves as polarization back-rotating device. We avoided utilizing multi-order wave plates because at high intra-cavity powers instabilities related to thermal effects can occur [217]. Since the Nd:YVO_4 crystal provides a higher gain in the c-direction and is moreover birefringent, it acts as the intra-cavity polar-

[1] Forschungsinstitut für mineralische und metallische Werkstoffe -Edelsteine/Edelmetalle- GmbH

izer. The lasing direction is chosen as indicated in Fig. 5.1, the output beam being spatially separated from the residual pump light.

5.3.2. Frequency-selective filtering via Etalons

Single longitudinal mode operation can be facilitated by the laser design, as it was presented before, for instance by using a running-wave resonator. A compact cavity setup furthermore provides the largest possible free spectral range, meaning the largest longitudinal-mode frequency spacing

$$\nu_{\mathrm{FSR,laser}} = \frac{c}{L_{\mathrm{opt}}} \simeq 320\,\mathrm{MHz}\,, \tag{5.52}$$

where L_{opt} is the optical path length of a cavity round-trip and c is the vacuum speed of light. Since the gain peak of Nd:YVO_4 is $\simeq 280\,\mathrm{GHz}$ broad, and thus three orders of magnitude larger than ν_{FSR}, additional arrangements have to be made to ensure laser operation in only a single longitudinal mode. Therefore two etalons are introduced into the cavity in order to modulate the transmission function of a cavity round-trip.
An etalon is a small frequency-selective Fabry-Pérot resonator whose transfer function, in the limit of plane waves, is given by

$$T_{\mathrm{FP}} = \left(1 + \left[\frac{2F}{\pi}\sin\left(\pi\frac{\nu-\nu_{\mathrm{res}}}{\nu_{\mathrm{FSR,etalon}}}\right)\right]^2\right)^{-1}\,, \tag{5.53}$$

where ν_{res} is a constant offset frequency that summarizes the phase shifts due to the optical coatings. The parameter F, the so-called finesse, is defined as

$$F = \frac{\pi\sqrt{R}}{1-R}\,, \tag{5.54}$$

with the power reflectivity R of both surfaces. The resonance condition $T_{\mathrm{FP}} = 1$ is fulfilled for the corresponding resonance frequencies $\nu_p = p\,\nu_{\mathrm{FSR,etalon}} + \nu_{\mathrm{res}}$, $p \in \mathbb{N}$, similar to Equation (5.22).
By inspecting the product $\mathcal{T}_{\mathrm{cav}}(\nu) \times \sigma_{\mathrm{em}}(\nu)$ we can characterize a condition for single mode operation. $\mathcal{T}_{\mathrm{cav}}(\nu)$ is defined as the total transmission function of one cavity round-trip and is, in good approximation for the amplified frequency range, only determined by the impact of the etalons. The gain accumulated by a light beam passing through the gain medium is furthermore proportional to $\sigma_{\mathrm{em}}(\nu)$. If the product $\mathcal{T}_{\mathrm{cav}}(\nu) \times \sigma_{\mathrm{em}}(\nu)$ is, for small signals, larger for one particular cavity mode p than for all other modes, these cavity modes will be suppressed and prevented from oscillating due to mode competition [200]. Therefore the laser will operate only in the favored mode with mode index p as soon as sufficient mode competition is provided by the optical elements inside the ring cavity.
For the choice of appropriate etalons we have, according to Equations (5.53)–(5.54), two parameters at our disposition. First of all, the free spectral range $\nu_{\mathrm{FSR,etalon}}$, which determines

the frequency spacing of the transmission peaks, is given by the diameter and the refractive index of the etalon material. Secondly, the finesse F, which defines the modulation amplitude and the peak width, is determined by the surface reflectivity of the etalon.
Furthermore the impact of losses has to be taken into account. Some losses depend on material and fabrication quality of the etalon, like for instance residual absorption of the substrate and coatings, scattering, as well as surface nonparallelity and roughness. They can be minimized to negligible values by applying appropriate materials and methods in the etalon fabrication process.
However, there is another loss mechanism called walk-off loss which cannot be avoided because of its fundamental cause. It is due to the fact that the etalon transmission function presented in Equation (5.53) is strictly valid only in the limit of plane waves. For a beam wave propagating through the etalon inside a cavity additional mode losses occur because of the angle-dependent walk-off. It can be explained by the lateral walk-off of subsequent orders of the transmitted waves, when the surface normal vector and the direction of propagation of a Gaussian beam form an angle of incidence. The non-unity overlap integral between the cavity mode and the transmitted beam leads to insertion loss when installing a tilted etalon in a resonator [218].

5.3.3. Etalon parameters

We opted for a combination of two etalons inside the cavity in order to realize a tunable single-frequency laser. Using a first uncoated etalon E_1 with a width of 0.5 mm and $R = 3.3\%$, distant modes are efficiently suppressed. For suppression of closely-spaced modes from oscillating, we employed a thicker uncoated etalon E_2 with a width of 4 mm. The typical frequency scales are summarized in Table 5.2. The substrate material of both etalons is infrared fused silica. With this combination of etalons presented here, reliable single-mode operation and frequency tunability was achieved.

Element	Length L	Typ. freq.	Typ. R	Finesse F	Q-factor
Gain profile width	-	280 GHz	-	-	-
Laser cavity	93 cm	320 MHz	92.5%	40	2.8×10^7
Etalon E_1	0.5 mm	210 GHz	3.3%	0.6	6.4×10^2
Etalon E_2	4 mm	26 GHz	3.3%	2.1	5.1×10^3

Table 5.2. – Frequency scales of the setup. The characteristic frequencies are the free spectral ranges ν_{FSR} and the width (FWHM) of the gain profile taken from [195]. Reflectivities R are given for the output coupling mirror of the laser cavity and for the two etalon surfaces. The finesses F and Q-factors are calculated from the indicated R-values, not taking into account further losses.

In Figure 5.13 we present a possible realization of a transmission-gain function $T_{\mathrm{cav}}(\nu_p) \times \sigma_{\mathrm{em}}(\nu_p)$ calculated by using the data shown in Figure 5.5. The reflectivity of E_1 and E_2 was set to 15% for this plot in order to improve the visibility of their effects. We note that the resolution of the spectroscopic data is 0.5 nm or 80 GHz, meaning that additional

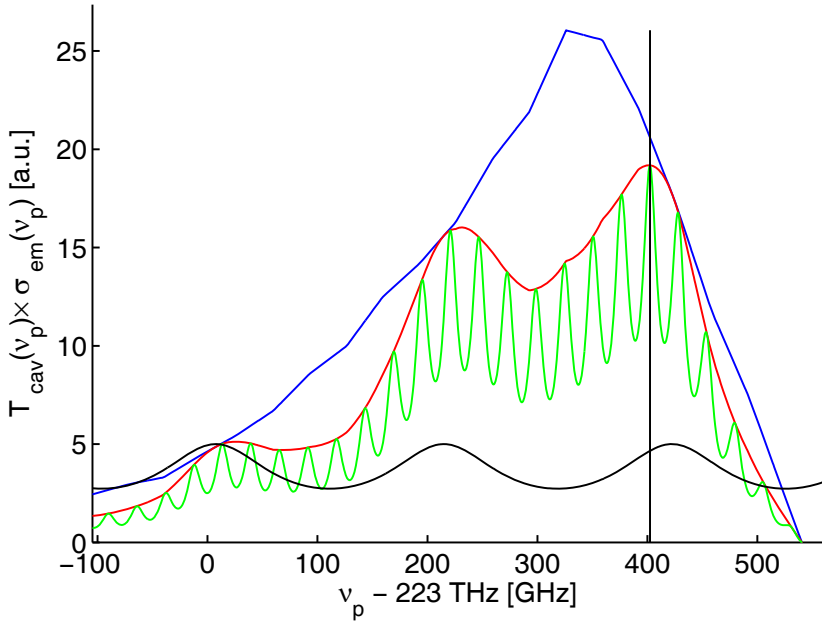

Figure 5.13: Possible realization of a transmission-gain function $T_{\mathrm{cav}}(\nu_p) \times \sigma_{\mathrm{em}}(\nu_p)$ in the non-saturated regime for two etalons as indicated in Table 5.2, except for $R_{\mathrm{E}_1} = R_{\mathrm{E}_2} = 15\%$. The black vertical line represents half the Li D-line transition frequency. The blue line is the spectroscopy data for $\sigma_{\mathrm{em}}(\nu_p)$ from [195], the red line is $\sigma_{\mathrm{em}}(\nu_p)$ modulated by E_1 only. The green line is $\sigma_{\mathrm{em}}(\nu_p)$ modulated by both etalons, and the black line is the transmission of E_1 in a.u. The cavity modes spaced by $\nu_{\mathrm{FSR}} = 320\,\mathrm{MHz}$ are not resolved here.

sub-structures are smoothed out. The actual measurement of the single-frequency output spectrum of the laser is given in Section 5.4.2 .

The installation of an intra-cavity etalon requires a minimum tilt angle ϑ_{min} with respect to the cavity mode propagation direction in order to avoid the creation of additional coupled cavities and a highly unstable behavior of the laser. An estimate of this angle is the cavity-eigenmode beam divergence, which is at most 2.3 mrad in our case. This value corresponds to the Gaussian beam mode inside the cavity with a minimal waist radius of 375 μm, see Section 5.4.3. Any angular etalon tuning will start from this point with a minimum tilt loss towards higher tilt angles and losses.

The offset frequency ν_{res} and the free spectral range $\nu_{\mathrm{FSR,etalon}}$ in the etalon transmission function (5.53) include an arbitrary etalon diameter offset, given the fact that the etalon diameter L_{etalon} can only be fabricated with a precision larger than the laser wavelength. This means that in the worst case one has to tune the etalons by $\nu_{\mathrm{FSR,etalon}} = c/(2nL_{\mathrm{etalon}})$ to reach the lithium resonance. In the case of the thinner etalon E_1, tilt losses are negligible over this range. The walk-off losses of E_2 are, however, significantly higher and reach several percent for angular tuning over one free spectral range [209]. Therefore we decided to adjust this etalon to its minimum angle and to tune its temperature instead, which proposes another mean for acting on the laser frequency.

The mode-hop-free scan range of the laser was measured to be $\simeq 450\,\mathrm{MHz}$, slightly higher than the free spectral range $\nu_{\mathrm{FSR}} = 320\,\mathrm{MHz}$, see (5.52).

We note that single-mode operation is significantly favored when intra-cavity frequency doubling of a laser is applied, as presented in Section 6.3. In this case, mode competition is enhanced due to sum-frequency generation, causing higher losses for the low-power modes [219].

5.3.4. Etalon temperature tuning

As mentioned before, angle tilting of E_2 should be avoided because of the occurring losses inherent to this frequency tuning method. Another mean to shift the resonance comb of an etalon is to tune its temperature, since both its length L and refractive index n are temperature dependent. The variation in frequency is given by

$$\frac{\partial \nu_p(T)}{\partial T} = p\,\frac{\partial \nu_{\mathrm{FSR}}(T)}{\partial T} = -p\,\nu_{\mathrm{FSR}}\left(\frac{1}{n}\frac{\partial n}{\partial T} + \frac{1}{L}\frac{\partial L}{\partial T}\right), \tag{5.55}$$

where n is the refractive index and L the geometric diameter of the etalon. For fused silica the values of the derivatives are $\frac{\partial n}{\partial T} = 12.2 \cdot 10^{-6}\mathrm{K}^{-1}$, with $n = 1.446$, and $\frac{1}{L}\frac{\partial L}{\partial T} = 5.5 \cdot 10^{-7}\mathrm{K}^{-1}$ according to [220, 221]. As a consequence, E_2 requires a temperature variation $\Delta T = 13\,\mathrm{K}$ to tune over a full spectral range.
Furthermore etalon E_2 is temperature-stabilized to avoid frequency and mode-hop drifts during the warm-up process and the operation of the laser setup. For temperature tuning and stabilization, E_2 is enclosed in a temperature-regulated copper mount stabilized to $\simeq 0.1\,\mathrm{K}$.

5.4. Characterization of performance

In this sections we will present our measurements on the output power and the output spectrum of the IR laser source, as well as the spatial mode properties of the output beam providing further information about the thermal lens induced in the gain medium.

5.4.1. Output power

The output power of a laser system is naturally one of its most important features. It determines both the design and the potential applications of a particular laser source. In this subsection we will present the measurements concerning the output power of our fundamental laser.
The optimization of the laser output power was performed in several steps, starting with an empty cavity that was pumped at maximum absorbed pump power. This means that in the beginning all optical elements that are not necessary for lasing had not been inserted in the cavity, including the TGG, the half-waveplate and the two etalons. In this way the spatial overlap between the pump beam and the fundamental cavity mode could be optimized (cf. Equation (5.50)) without being affected by the additional power-modulations due to the frequency selectivity of the etalons. Moreover, in the empty cavity it was possible to put a power meter directly behind the Nd:YVO_4 crystal in order to measure the powers incident

on the laser crystal, P_{tot},as well as the non-absorbed power transmitted through it, P_{trans}. Thus the absorbed pump power, P_{abs}, could be deduced.
As the effective pump absorption coefficient depends on the spectrum of the pump source, see Section 5.1, the central pump wavelength needs to be tuned in order to match the peak at 888 nm in the absorption spectrum of Nd:YVO_4. Our pump source being a semiconductor diode stack, its central emission wavelength can be shifted by changing its temperature. For this purpose, we use a water chiller with variable set temperature inside a closed cooling water circuit. The cooling water temperature is in general set to 4°C.

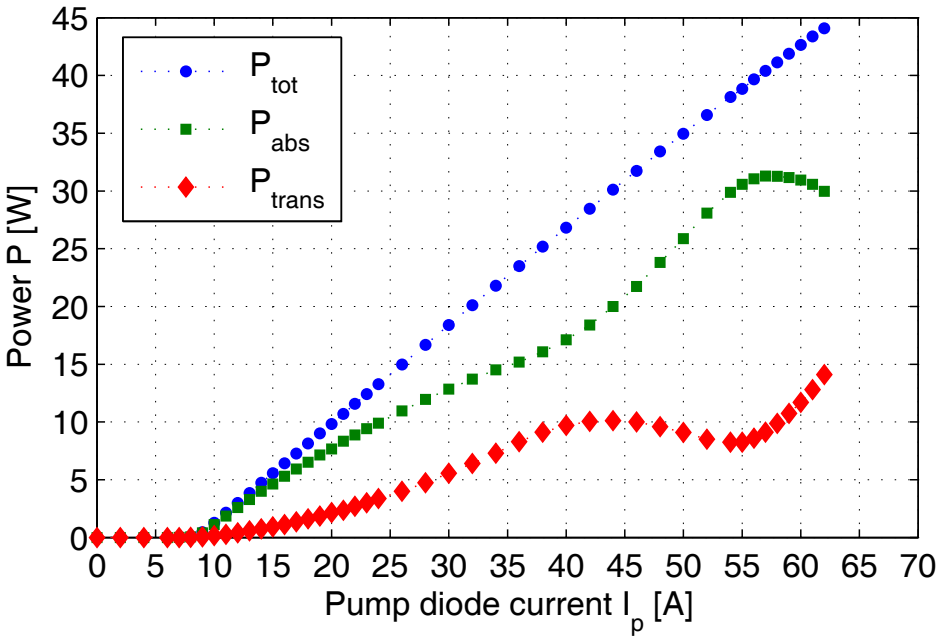

Figure 5.14: Absorption of the pump light ($w_{\mathrm{pump}} = 970\,\mu\mathrm{m}$) by the 25 mm long Nd:$YVO_4$ crystal with 0.5 at. % doping. Shown are the total power incident on the laser crystal P_{tot}, the transmitted power P_{trans} and the absorbed pump power P_{abs} as a function of the current I_{p} passing through the pump diode stack at a cooling water temperature set to 4°C. Saturation of pump light absorption sets in at $I_{\mathrm{p}} = 57\,\mathrm{A}$.

Figure 5.14 presents the absorbed pump power P_{abs} as a function of the current I_{p} applied to the pump diode stack. It was measured as the difference of the total pump power incident on the crystal P_{tot} and the pump power transmitted through the crystal P_{trans}, since reflection on the Nd:YVO_4 crystal facets is negligible due to their AR-coating. The absorbed power rises quasi-linearly with the incident pump power up to $I_{\mathrm{p}} \simeq 57\,\mathrm{A}$, where the pump diode stack emission probably changes its spectral output characteristics. The maximum absorbed pump power is 31.3 W.
All measurements presented in the course of this work were taken at $I_{\mathrm{p}} = 57\,\mathrm{A}$, if not otherwise stated, since it represents the highest pump absorption value and no degradation of the laser parameters was observed even for the maximum power output of the laser source. The current passed through the diode bar is kept constant at this value for I_{p} to stabilize the laser output power.

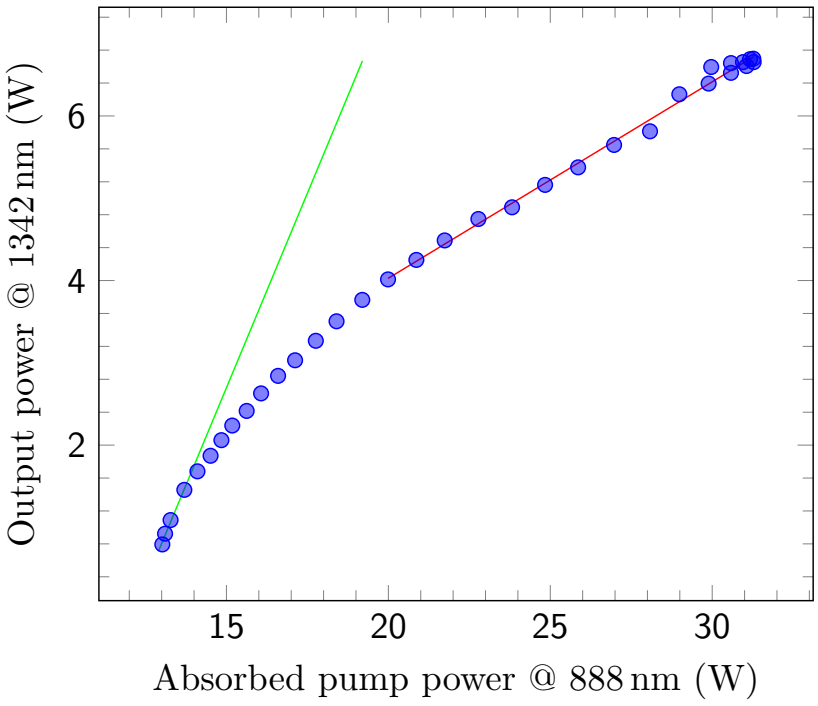

(a)

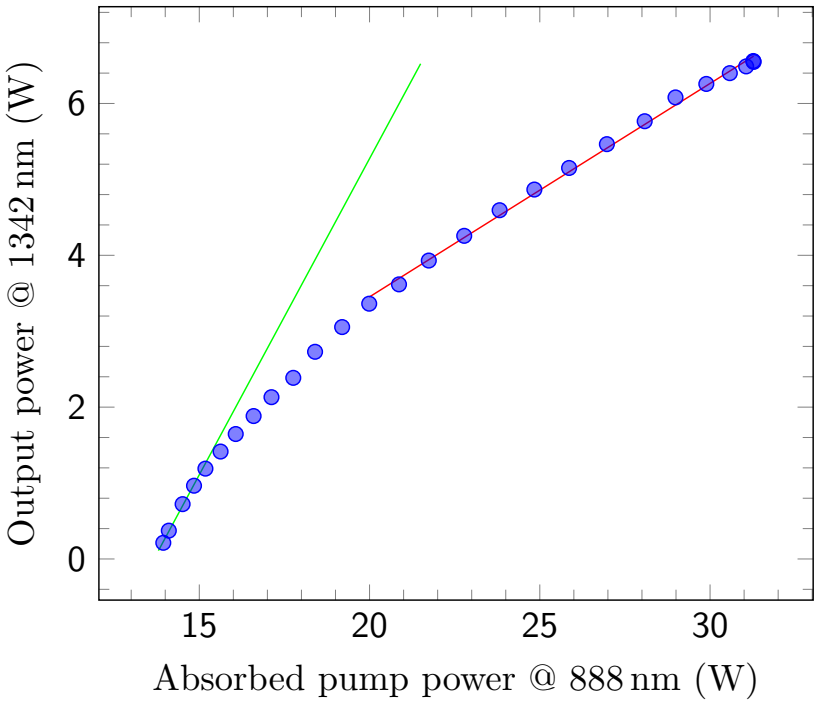

(b)

Figure 5.15: (a) Output power of the laser without additional frequency selective elements (dots) as a function of the absorbed pump power. Linear fits were performed in the low power limit (green line) close to the lasing threshold as well as in the high power regime (red line) for $P_{\mathrm{abs}} > 20\,\mathrm{W}$. (b) Single-frequency laser output power of the complete Nd:YVO_4 laser setup including both etalons as a function of the absorbed pump power.

The cavity power output characteristics in the absence of both etalons are presented in Figure 5.15(a). We inserted the TGG and the waveplate in the cavity in order to enforce unidirectionality for this measurement. Thus the output power is leaving the cavity in only one beam direction via the output coupler M_2. The output coupler mirror was chosen out of the discrete set of available transmission values to be $T = 7.5\%$ to optimize the maximum output power at maximum absorbed pump power in the presence of all additional intra-cavity elements.

The lasing threshold is found at $P_{\mathrm{thr}} = 12.2\,\mathrm{W}$ and the maximum emitted power $P_{\omega,\mathrm{max}} = 6.7\,\mathrm{W}$, whereas the slope efficiency amounts to $\eta_{\mathrm{sl,low}} = 95\%$ in the low power limit next to the lasing threshold and drops to $\eta_{\mathrm{sl,high}} = 23.9\%$ in the high power regime for absorbed pump powers $P_{\mathrm{abs}} > 20\,\mathrm{W}$. The non-linear behavior is in contradiction with (5.39) assuming constant thermal loss L_{th}, which means that the thermal loss L_{th} increases with the absorbed pump power P_{abs}. Another possible explanation is that the overlap integrals (5.43) and (5.47) change accordingly due to the modified cavity parameters in presence of thermal lensing inside the gain medium, yielding the non-linear behavior observed. Yet the laser output power at high pump powers is well fit by a straight line, not showing any signs of thermally induced instabilities.

Figure 5.15(b) shows the output power characteristics of the laser in the presence of all additional intra-cavity elements. The lasing threshold was in this case found at an absorbed pump power $P_{\mathrm{abs}} = 13.7\,\mathrm{W}$. The power rises in this case with a slope efficiency of $\eta_{\mathrm{sl,low}} = 83\%$ in the low power limit and decreases to $\eta_{\mathrm{sl,high}} = 28.1\%$ in the high power regime. As compared to the case of lasing operation without additional frequency selective elements inside the cavity, the maximum output power amounts to about $P_{\omega,\mathrm{max}} = 6.55\,\mathrm{W}$ corresponding to 98% of the maximal value. The lasing threshold is significantly higher, whereas the slope efficiency is lower in the low power limit and similar in the high power limit. These are indications of losses induced by the etalons.

In conclusion, we state that the maximum output power of the IR laser is not limited by detrimental thermal effects but by the maximal output power of the installed pump diode stack. Thus by increasing the pump power, we can expect a further enhancement of the available output power at 1342 nm.

5.4.2. Output spectrum

The emission spectrum of the laser was measured, as shown in Figure 5.16, by changing the temperature of etalon E_2 and optimizing the respective output power. This measurement was based on a slightly modified fundamental laser cavity employing a 1.0 % at.-doped $NdYVO_4$ crystal, as presented in Section 6.3 and [210]. This explains the lower overall power level compared to Section 5.4.1. Nevertheless its results remain valid for the current version of the IR laser source.

The spectrum has a total width of about 1 nm and is smooth except for three narrow dips at 1341.85 nm, 1342.1 nm and 1342.7 nm, where the laser operation is unstable and mode-hops

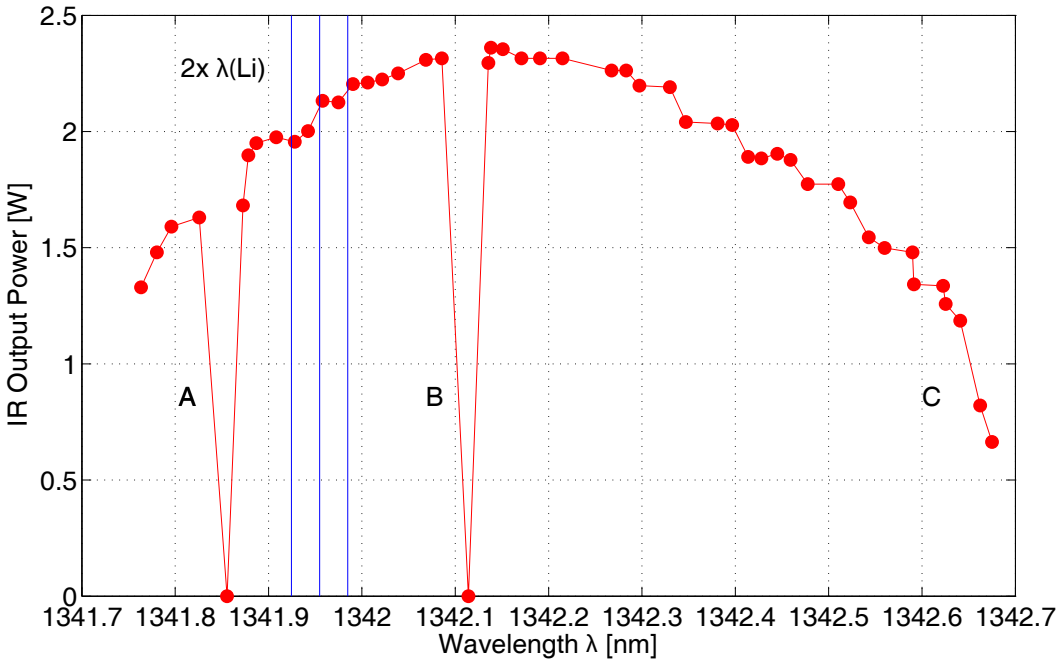

Figure 5.16: Output power of the laser as a function of the emission wavelength (dots, the lines being only guides for the eye). This measurement was based on a slightly modified fundamental laser cavity employing a 1.0 % at.-doped $NdYVO_4$ crystal, as presented in Section 6.3 and [210]. This explains the lower overall power level compared to Section 5.4.1. The values corresponding to twice the lithium D-line wavelengths are indicated by vertical lines. For easy comparison, all wavelengths are given in vacuum values. We note that the wavelength regions marked A,B,C where the output power drops sharply and stable operation of the lasers can not be established coincide with absorption peaks of water molecules.

towards stable regions occur. These power dips can be explained by absorption features of water molecules in the laser cavity, as it can be shown by a water vapor absorption spectrum obtained from the HITRAN database [210, 222]. The wavelength values corresponding to the lithium D-line resonances after frequency doubling are advantageously situated in between the two first dips, and the emitted power is close to the emission maximum. Laser operation on the lithium resonance wavelength, being the essential requirement for its application in the context of lithium laser cooling, is therefore readily accomplished.

5.4.3. Spatial mode

Our laser setup was designed to deliver a spatially single-mode, Gaussian (TEM_{00}) output beam. In order to verify the actual beam quality, we performed a measurement of the beam profile. For this purpose, the laser beam was focused by a lens of $f = 200$-mm focal length and images of the beam profile were taken at different distances using a LuCam LU055M camera which has still a low sensitivity at 1342 nm, even though it is only equipped with a Silicon CCD sensor. Measuring the beam waist as a function of the position of the camera along the beam propagation direction, we can extract the beam quality factor M^2 by fitting Gaussian distributions to the obtained camera images and performing a fit to

$$w^2(z) = w_0^2 + M^4 \left(\frac{\lambda}{\pi w_0}\right)^2 (z - z_0)^2 \,, \tag{5.56}$$

which is a generalization of Equation (5.6). M^2 quantifies the degree of variation of the actual beam from a pure Gaussian (TEM_{00}) beam for which it equals one. As illustrated in Figure 5.17 for the horizontal direction, we obtain $M_x^2 = 0.97(6)$ (horizontal direction) and $M_y^2 = 0.95(8)$ (vertical direction) from the fits, both values being indistinguishable from unity within our experimental resolution. Therefore we state that the output laser beam quality is excellent, which is an important feature for efficient mode matching and frequency doubling, as will be presented in chapter 6.

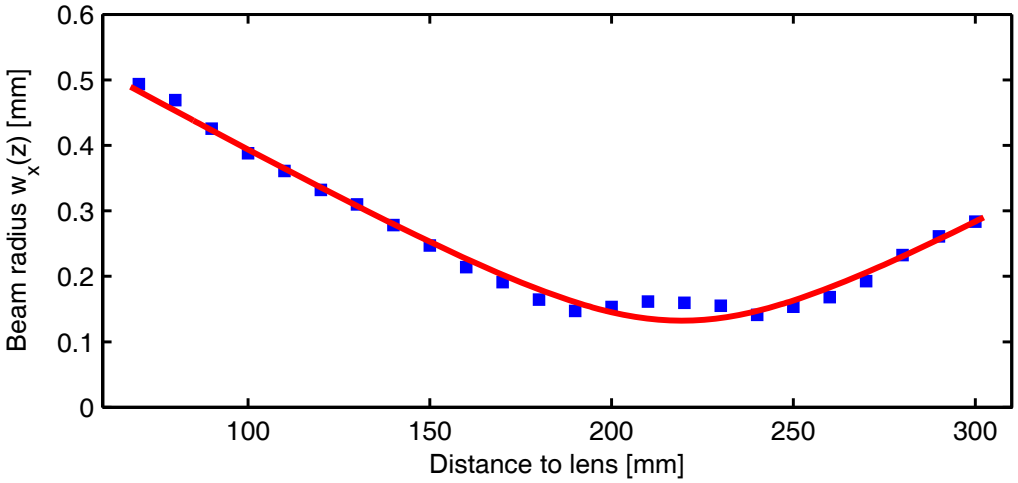

Figure 5.17: Beam quality measurement performed on the horizontal direction of the laser output beam. The M^2 fit yields a value compatible to $M^2 = 1$, or pure Gaussian (TEM_{00}) output.

The laser cavity design presented in Section 5.2 can only give approximate predictions for the mode sizes $w_{x/y}$ of the emitted beam, which is due to the lack of precise values for the material parameters and the simplifications made in the theoretical description of thermal lensing process. However, precise knowledge of the output beam parameters is crucial for the mode-matching that has to be performed between the laser beam and either the doubling cavity or the waveguide coupling fiber, as will be described in chapter 6. The beam parameters of focus position z_0 and Rayleigh length z_R were therefore measured, while assuming $M^2 \equiv 1$, as justified before.

The beam profiling is performed by measuring the radii of the output laser beam at different distances from the output coupler mirror M_2. The comparison of the obtained beam parameters to the cavity calculations yields another method for measuring the focal length of the thermal lens present in the laser crystal under lasing conditions.

Figure 5.18 shows the results yielding $z_{0,x/y} = -98(12)\,\text{mm}/-118(22)\,\text{mm}$ and $w_0 = 374(12)\,\mu\text{m}/436(34)\,\mu\text{m}$ in the horizontal/vertical direction. Backtracing the beam path through the laser resonator indicates a thermal focal length of $f_{th} = 340\,\text{mm}$, as the resulting cavity eigenmode can be deduced from the cavity geometry, see Figure 5.19.

The obtained value for the thermal lens is therefore by a factor two larger than the value $f_{\mathrm{th}} = 170\,\mathrm{mm}$ measured in Section 5.2.2. We attribute this to the onset of thermal lensing in the additional intra-cavity-elements (TGG, waveplate, etalons), which were not included in the linear cavity setup of Figure 5.9. Furthermore the final ring laser is operating spatially single-mode, whereas the test cavity in Section 5.2.2 was oscillating in multiple spatial modes, which tends to increase the ESA contribution to the thermal load.
Comparing the pump mode radius of $w_{\mathrm{P}} = 465\,\mu\mathrm{m}$ to the laser mode radius w_l in the Nd:YVO_4 crystal, we obtain $w_l/w_p = 1.0/1.15$ in the horizontal/vertical direction, these values being significantly greater than the optimal overlap of 0.8 predicted by Equation (5.50). Together with the diminished thermal effect discussed before, this indicates lower aberrations even at mode-size-to-pump-size ratios close to 1.

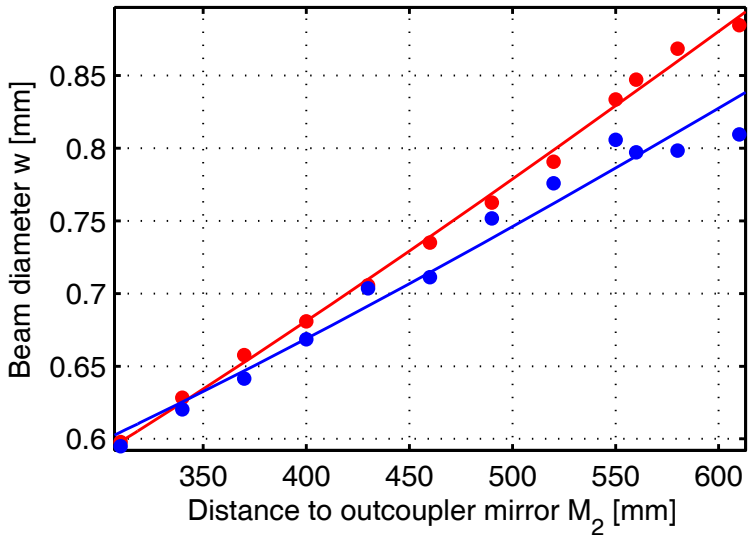

Figure 5.18: Measurement of the beam parameters (red/blue: horizontal$_x$/vertical$_y$ waist) of the laser output beam. The fits assume $M^2 = 1$. This measurement is needed to calculate the necessary coupling optics for mode-matching the enhancement doubling cavity or the waveguide fiber. The ellipticity and astigmatism of the beam can in principle be corrected by cylindrical lenses.

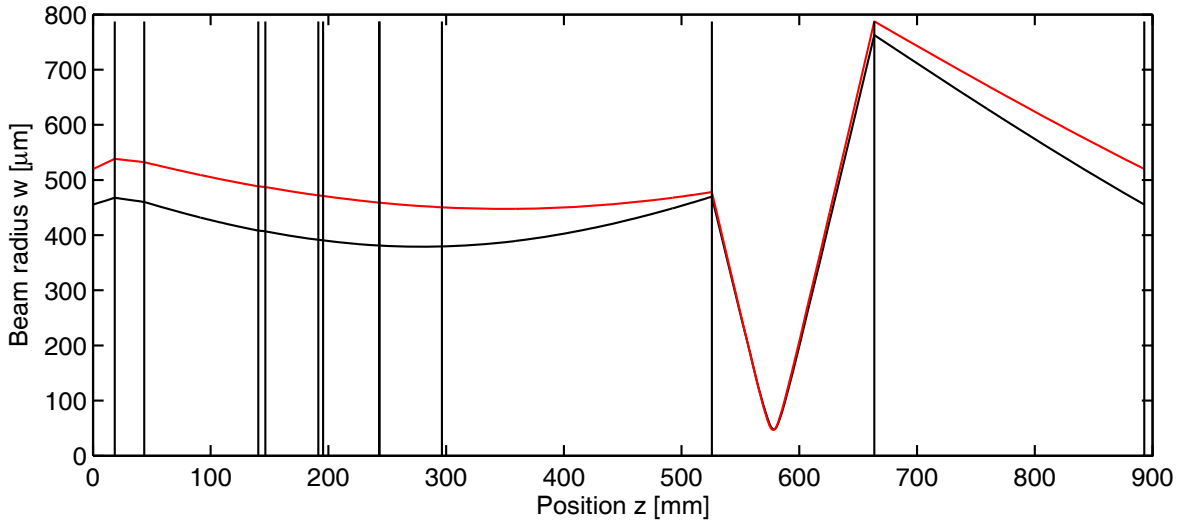

Figure 5.19: The eigenmode of the laser resonator. The horizontal (black) and the vertical (red) widths of the laser beam mode are shown as a function of the position inside the cavity. The vertical lines indicate the position of optical surfaces related to intra-cavity elements. $z = 0$ corresponds to the position of the convex pump coupler (M_1), and the sense of propagation is directed towards the output coupler (M_2), which is located at 297 mm.

5.5. Conclusion

In this chapter we have presented the improved design of a single-mode, diode end-pumped, all-solid-state laser source emitting up to 6.5 W at 1342 nm. It can be readily applied as a fundamental source for second harmonic generation (SHG), the frequency doubled light being usable to address the lithium D-line transitions next to 671 nm. We have justified our choice of pumping the gain medium at a wavelength of 888 nm as a possibility to reduce the detrimental thermal effects inside the Nd:YVO_4 laser crystal. Thereafter, we have given an overview of the theoretical concepts required to design a solid-state laser cavity, and presented eventually the geometry and technical realization of our ring cavity. We then discussed the measures applied to enforce unidirectional and longitudinally single-mode operation. Subsequently, we have characterized the performance of our laser in terms of output power, emission spectrum and spatial mode quality. The laser source is tunable from 1341.7 nm to 1342.7 nm and reaches a maximum single-frequency output power of 6.5 W. We have determined its M^2 beam-quality factor to be approximately 1.0 and measured the output beam parameters. Hence, we have finally been able to efficiently mode-match the powerful Gaussian infrared beam to the doubling enhancement cavity and the SHG waveguide, which will be presented in the next chapter.

6 Second harmonic generation

The output radiation at 1342 nm emitted by the IR laser source presented in the preceding chapter has to be frequency-doubled in order to obtain light at the lithium D-line transition wavelengths next to 671 nm. The applied frequency doubling technique needs to be efficient and at the same time technically simple in order to realize a multi-Watt level second harmonic output that is available for experiments on a daily basis. In this context we have tested three approaches for second-harmonic generation (SHG), namely doubling via a resonant enhancement cavity, intracavity doubling and wavelength conversion by means of a waveguide module.

This chapter will present the different frequency-doubling setups that we have realized. In Section 6.1, we will first give a brief overview of the theoretical concepts explaining second-harmonic generation using periodically-poled nonlinear media. Furthermore we will consider the physical properties of the nonlinear media chosen for our applications, namely of periodically-poled potassium titanyl phosphate (ppKTP) and lithium niobate (ppLN). Subsequently, we will present in Section 6.2 the design of the resonant enhancement cavity and illustrate the results of the nonlinear conversion measurements. In an analogous manner we will detail on the setup and results of the intracavity doubled laser in Section 6.3. The subject of Section 6.4 will be the performance and the theoretical description of our third approach for SHG, a wavelength conversion module employing a waveguide structure. Finally we will summarize the chapter in Section 6.5.

6.1. Theory of second-harmonic generation

In this section, we will consider the theoretical aspects related to the nonlinear interaction of Gaussian beams propagating in free space or guided inside a waveguide structure. The advantageous technique of quasi-phase matching will be described and compared to the alternative method of birefringent phase matching. Finally, we will discuss the physical properties of periodically-poled potassium titanyl phosphate (ppKTP) and lithium niobate (ppLN) and motivate the selection of ppKTP as the nonlinear medium in the resonant doubling cavity.

6.1.1. Nonlinear conversion

An electro-magnetic wave passing through a medium, causes a polarization $\mathbf{P}$ inside this medium induced by the electric field $\mathbf{E}$. The polarization vector $\mathbf{P} = \sum_i P_i \, \mathbf{e}_i$, represented in the orthonormal set $\mathbf{e}_i$, can be decomposed as

$$P_i = \varepsilon_0 \left(\sum_j \chi^{(1)}_{ij} E_j + \sum_{jk} \chi^{(2)}_{ijk} E_j E_k + \sum_{jkl} \chi^{(3)}_{ijkl} E_j E_k E_l + \dots \right) \tag{6.1}$$

where ε_0 is the vacuum permittivity and the susceptibility tensors $\chi^{(k)}$ of rank $k+1$ are material-dependent and responsible for the optical processes of k-th order. Since we are in the following interested in second-harmonic generation, we will focus on quadratic processes only and neglect all higher-order terms, which is a good approximation for the light intensities occurring in the setups presented in the course of this chapter. Several symmetries impose restrictions on the form of the second order susceptibility $\chi^{(2)}$ and reduce the number of independent parameters. For example, $\chi^{(2)}$ is only non-zero for crystals without inversion symmetry and due to the Kleinmann symmetry $\chi^{(2)}$ can in common cases be represented as a 3×6 matrix containing only 10 independent elements d_{jk} [223]. In the context of the theoretical description of second-harmonic generation the nonlinear polarization is represented by two terms [224]

$$\mathbf{P}^{\mathrm{NL}}_{\omega}(\mathbf{r}) = 4\varepsilon_0 d_{\mathrm{eff}} \mathbf{E}_{2\omega}(\mathbf{r}) \mathbf{E}^*_{\omega}(\mathbf{r}) \tag{6.2}$$

$$\mathbf{P}^{\mathrm{NL}}_{2\omega}(\mathbf{r}) = 2\varepsilon_0 d_{\mathrm{eff}} \mathbf{E}^2_{\omega}(\mathbf{r}) \, , \tag{6.3}$$

where d_{eff} is the effective nonlinear coefficient of the material for a specific polarization and the indices ω and 2ω refer to the frequency of the fundamental and second harmonic wave, respectively. The evolution of both waves can be obtained by solving the coupled wave equations

$$(\nabla^2 + k^2)\mathbf{E}_{\omega,j}(\mathbf{r}) = -4\varepsilon_0 \mu_0 \omega^2 d_{jk} \mathbf{E}_{2\omega,k}(\mathbf{r}) \mathbf{E}^*_{\omega,j}(\mathbf{r}) \tag{6.4}$$

$$(\nabla^2 + k^2)\mathbf{E}_{2\omega,k}(\mathbf{r}) = -2\varepsilon_0 \mu_0 (2\omega)^2 d_{jk} \mathbf{E}^2_{\omega,j}(\mathbf{r}) \, , \tag{6.5}$$

which can be solved analytically in the paraxial limit. In the case of weak conversion, or in other words, if the pump is not depleted, the result is in general a second harmonic output power $P_{2\omega}$ obeying a quadratic dependence on the fundamental or pump beam power P_ω,

$$P_{2\omega} = \eta_{\mathrm{SHG}} P_\omega^2 \,, \tag{6.6}$$

where η_{SHG} is the conversion efficiency. For the particular case of second harmonic interaction of a focused Gaussian beam, the following expression for η_{SHG} was derived in [223, 225, 226]:

$$\eta_{\mathrm{SHG}} = \frac{2\omega^3 d_{\mathrm{eff}}^2 L}{\pi \varepsilon_0 c^4 n_\omega n_{2\omega}} h(\alpha, \beta) \,, \tag{6.7}$$

with n_ω and $n_{2\omega}$ being the corresponding refractive indices of the material, L the length of the nonlinear material and c the vacuum speed of light. The function $h(\alpha, \beta)$ can be expressed as

$$h(\alpha, \beta) = \frac{1}{4\alpha} \left| \int_{-\alpha}^{\alpha} \frac{\mathrm{e}^{\mathrm{i}\beta\tau}}{1 + \mathrm{i}\tau} \, \mathrm{d}\tau \right|^2 \,, \tag{6.8}$$

where the focusing parameter $\alpha = L/2z_{\mathrm{R}}$ depends on the Gaussian beam Rayleigh length z_{R} which can be shown to be equal for both waves, resulting in a waist by a factor $\sqrt{2}$ smaller for the second harmonic beam compared to the fundamental beam waist. The phase-matching parameter

$$\beta = \beta(T) = \frac{4\pi z_{\mathrm{R}}}{\lambda} \left(n_\omega(T) - n_{2\omega}(T) \right) \,, \tag{6.9}$$

with λ being the fundamental vacuum wavelength, depends on the temperature and also on the polarizations in the case of a birefringent medium. The derived formulas assume absence of losses and a non-depleted fundamental wave. The integral in Equation (6.8) can be solved analytically for the two limits $\alpha \to 0$ (strong focusing) and $\alpha \to \infty$ (plane wave), whereas in general it has to be calculated numerically. The global maximum of $h(\alpha, \beta)$ is found at $h_{\max}(2.84, 0.57) = 1.068$, the optimal value for β being non-zero which would be unexpected for plane waves. This is due to the fact that we consider here Gaussian beams which feature a wave front curvature and a Gouy phase shift. Entering values for the usual parameters of nonlinear media into these formulas yields doubling efficiencies η_{SHG} on the order of %/W, meaning that for the available continuous laser power of several Watts, single pass doubling cannot be considered as an efficient option. Therefore we need to employ either resonant enhancement inside a cavity or a longer interaction length inside a waveguiding structure.

6.1.2. Quasi-phase matching

An efficient conversion process requires the phase-matching parameter β to be close to zero, such that fundamental and second-harmonic wave remain always in phase. Since all optical materials feature dispersion, this condition is in general not fulfilled. Nevertheless it exist several techniques of phase-matching using angular- and temperature tuning in birefringent

crystals in order to realize $\beta \simeq 0$, as illustrated for example in [223]. Using different polarization axes results, however, only in relatively small conversion efficiencies, as the off-diagonal values of d_{jk} are in general small compared to the diagonal elements d_{jj}. Quasi phase-matching, which was proposed by Armstrong et al. [224] and realized by [227], is a technique that allows to circumvent these restrictions and avoids furthermore the necessity of cumbersome angle tuning. This method is based on the idea to invert the direction of the optical crystal axis as soon as the phase shift between the polarization driven by the fundamental wave and the second harmonic wave becomes destructive for the latter. The polarization then oscillates with an additional phase shift of π and in consequence contributes constructively to the second harmonic wave. The poling period Λ is therefore chosen to be the length of the region over which the phase shift acts constructively. Hence, quasi phase-matching allows for access to the considerably larger diagonal elements d_{jj} of the nonlinear tensor thus offering a higher single-pass efficiency η_{SHG} while keeping the phase matching condition β close to optimum. A widely used approach, which originated from Yamada et al. [228], is the application of a static electric field to invert the orientation of the ferroelectric domains, and consequently of the crystalline c-axis, in bulk ferroelectric materials. Quasi-phase matching is especially favorable in the context of cavity enhancement since an excellent beam quality is achievable without suffering from beam walk-off effects [223, 229]. The equations (6.6)–(6.9) hold also for quasi-phase matched samples with poling period Λ, but the following replacements have to be performed for the phase matching parameter

$$\beta \to \beta - 2\pi z_{\mathrm{R}}/\Lambda \tag{6.10}$$

and the effective conversion coefficient

$$d_{\mathrm{eff}} \to d_{\mathrm{Q}} = 2d_{\mathrm{eff}}/\pi\,. \tag{6.11}$$

From Equations (6.7) and (6.11) we therefore obtain an efficiency improvement of the second-harmonic generation process of

$$\frac{\eta_{\mathrm{SHG,QPM}}}{\eta_{\mathrm{SHG,BPM}}} \approx \left(\frac{2}{\pi}\frac{d_{jj,\max}}{d_{jk,\max}}\frac{n_{j,\omega}}{n_{k,\omega}}\right)^2\,, \tag{6.12}$$

where the index extensions of η_{SHG} indicate quasi phase-matching (QPM) and birefringent phase-matching (BPM). Using the data from [230], this yields in the case of potassium titanyl phosphate (KTP),

$$\frac{\eta_{\mathrm{QPM}}}{\eta_{\mathrm{BPM}}} \approx \left(\frac{2}{\pi}\frac{d_{33}}{d_{32}}\right)^2 \approx 6\,, \tag{6.13}$$

indicating a significantly enhanced single-pass doubling efficiency for QPM in comparison to BPM.

6.1.3. Physical properties of the selected nonlinear media

In this subsection, we will discuss the physical properties of the selected nonlinear media for our frequency-doubling applications: periodically-poled potassium titanyl phosphate (pp-KTP) used in the resonant enhancement cavity and for intracavity doubling, and periodically-poled lithium niobate (ppLN) as the substrate of the doubling waveguide.
As we have shown in Section 6.1.2, periodically poled (pp) materials are advantageous for gaining an enhanced nonlinear conversion efficiency. We are interested in a crystalline material with a high value for one of the diagonal elements d_{jj} of the nonlinear susceptibility tensor, resulting in an efficient conversion process, see Equation (6.7). The material should not be inversion-symmetric, since for crystals possessing this symmetry property, the E^2-term in Equation (6.1) vanishes (as $\chi^{(2)} = 0$), meaning that no second-order conversion would take place. Another material prerequisite, necessary for the quasi phase-matching method treated theoretically in Section 6.1.2, is ferroelectricity, which is the property of a material to feature a spontaneous electric polarization, which can be permanently oriented by temporarily applying an external electric field. These requirements limited our choice to non-inversion-symmetric ferroelectric crystalline materials. The properties of both used materials (KTP = potassium triphosphate, LN = lithium niobate) are given in Table 6.1.

Material	KTP	LN
Nonlinear optical coefficient d_{33}[pm.V^{-1}]	16.9 [230]	20.6 [231]
Refractive index $n_z(\lambda_1 = 1342\,\text{nm})$	1.82 [232, 233]	2.14 [234]
Refractive index $n_z(\lambda_2 = 671\,\text{nm})$	1.86 [232, 233]	2.19 [234]
Material efficiency parameter $\eta_{\text{mat},33}$[pm^2.V^{-2}]	84.4	90.5
Linear absorption coefficient α_{abs}[%.cm^{-1}]	< 0.2 [235]	
transp. window [μm]	0.365-4.3 [236]	0.305-5.5 [236]
Damage treshold I_{dam}[MW.cm^{-2}]	> 37 [237]	0.001-2 [238]
Thermal conductivity κ[10^{-2}W.cm^{-1}.K^{-1}]	(2.0,3.0,3.3) [239]	4.4 [240]/4.6 [241]

Table 6.1. – Comparison of material parameters for the ferroelectric nonlinear media KTP (potassium triphosphate) and LN (lithium niobate). The material efficiency parameter $\eta_{\text{mat},33} \simeq d_{33}^2/n_z(\lambda_1)n_z(\lambda_2)$ appears in Equation (6.7) governing the doubling efficiency. The values for the thermal conductivity κ of KTP from [239] are for the three different axes of the KTP crystal.

All commonly used nonlinear crystals are in general transparent over the entire visible range. The transparency range usually extends in the infrared regions, the actual band edge depending on the material. Linear absorption coefficients are therefore small in our region of interest. A detrimental higher-order absorption effect is the so-called green-induced infra-red absorption (GRIIRA). This effect is due to the enhanced absorption of the fundamental wavelength in the presence of second-harmonic radiation. It is particular deleterious when employing resonant enhancement cavities, thus limiting the application of lithium niobate [242].
Photorefractivity is a further deleterious effect occurring especially in lithium niobate. Due to a field-induced release of charge carriers in the material the refractive index changes rapidly.

As a consequence the optical length of the cavity is shifted abruptly, leading to severe instabilities when trying to keep an enhancement cavity resonant with a pump laser via a frequency-lock.
Additionally, optical media can be irreversibly damaged when they are exposed to high intensities. Depending on the crystal composition (congruent or stoichiometric, doping with MgO, ZnO or Fe), the damage threshold intensity I_{dam} can be dangerously low for lithium niobate, whereas for potassium titanyl phosphate it is much higher. Together with GRIIRA and photorefractivity, this low threshold further restricts the capability of lithium niobate to handle high intensities.
KTP, on the other hand, displays a detrimental effect called gray-tracking. This effect takes its name from the appearence of visible gray tracks in the crystal. This reversible increase of absorption limits frequency-doubling of Nd:YAG lasers at 1064 nm. Since the photon energies involved in our case are a lot lower, we have reason to believe that this effect will not occur for doubling of 1342 nm light.
The material-dependent conversion-efficiency parameter $\eta_{\mathrm{mat},33}$ is highest for LN, but the material suffers from its higher refractive index in comparison to KTP.
In the context of second-harmonic generation inside an enhancement cavity, we considered ppKTP being a good compromise between conversion efficiency and high-power-handling capability. Our crystal sample was manufactured by the group of Carlota Canalias at the Institute of Laser Physics of the Royal Institute of Technology (Kungliga Tekniska Högskolan, KTH). In particular, they performed the electric field poling of our a KTP sample at room temperature [243].

6.2. Enhancement cavity

In Section 6.1 we stated that the single-pass doubling efficiency of a nonlinear medium like ppKTP is to be expected only in the %/W range. One possible solution for achieving a high conversion efficiency is to use a resonant enhancement cavity with the ppKTP crystal placed inside, such that a strong fundamental wave can build up, rendering the conversion more efficient.
The opto-mechanical setup of the doubling cavity is shown in Figure 6.1 and was inspired by the designs presented in [184, 244]. Similar to the laser, a folded-ring cavity consisting of four mirrors is employed. The fundamental light is coupled inside the cavity via the plane mirror M_1' for which a discrete set of reflectivity values R_{c} were tested in order to optimize the impedance matching, see Subsection 6.2.2. Finally the reflectivity $R_{\mathrm{c}} = 90\%$ was selected for this mirror giving the highest SHG output power for the applied fundamental pump power. All other mirrors are highly reflective at 1342 nm and M_4' is additionally transmitting at 671 nm. M_3' and M_4' are concave with a radius of curvature of $\mathrm{R}_{\mathrm{cc,M3}} = 150\,\mathrm{mm}$ and $\mathrm{R}_{\mathrm{cc,M4}} = 100\,\mathrm{mm}$, respectively. M_2' (M_3') is glued on a fast (slow) piezo-electric transducer, allowing to act on the cavity length in the 50 nm (8μm) range. A set of spherical lenses, L_1' and L_2', between the laser output and the cavity provides the necessary mode match-

ing. For temperature stabilization, the crystal is wrapped in indium foil and mounted in a temperature-controlled copper block. The second harmonic light is leaving the cavity through M'_4 and is collimated by a lens of focal length $f'_3 = 200\,\text{mm}$, yielding a Gaussian $1/e^2$ beam diameter of 2.4 mm.

The length of the crystal used in this work is 18 mm, featuring an optical aperture of $1\times6\,\text{mm}^2$. The poling period was chosen to be $\Lambda = 17.61\,\mu\text{m}$, since the phase matching condition $\beta(T) = 0$, see Equation 6.9, is in consequence expected at $T = 23.5°\text{C}$. This temperature is deduced according to the temperature-dependent Sellmeier equations from [232, 233]. Both crystal facets are AR coated for 1342 nm and 671 nm.

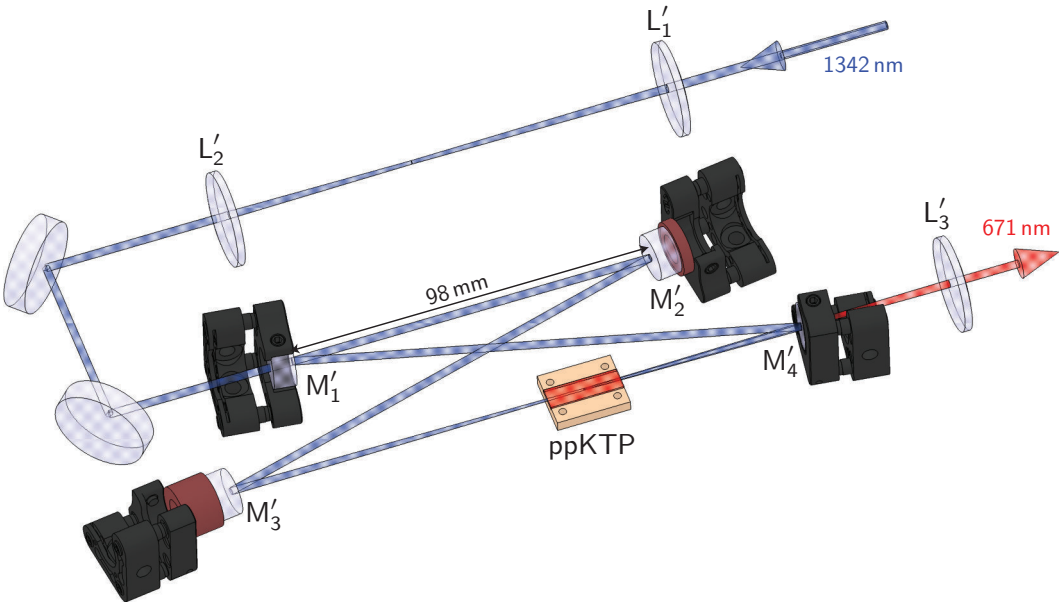

Figure 6.1: Scheme of the doubling cavity setup comprising the four mirrors M'_{1-4} and the ppKTP nonlinear crystal. The light is mainly coupled to the fundamental Gaussian eigenmode (TEM_{00}) by means of mode-matching via the lenses $L'_{1,2}$. L'_3 serves as collimation lens for the second harmonic output. The fundamental laser and second harmonic beam are depicted in blue and red, respectively. The distance between M'_3 and M'_4 is 156 mm. The piezoelectric transducers attached to M'_2 and M'_3, applied for modifying the cavity length, are coloured in dark red.

The dependence of several cavity parameters on the mirror distance d between the two curved mirrors M'_3 and M'_4 is presented in Figure 6.2. The distance $d = 156\,\text{mm}$ that was finally chosen fulfils several requirements: the cavity operates on a position close to the center of the stability range and the waist of $w_0 \simeq 79\,\mu\text{m}$ in the crystal is large enough to avoid detrimental high-intensity effects. The higher-order transverse cavity eigenmodes and the TEM_{00} mode differ significantly in their resonance frequencies, meaning that frequency degeneracy of modes is not occurring. For this particular distance, the beam provides a circular profile in the crystal and accounts thus for a circular SH output. The focusing is considerably weaker than optimal with regard to single-pass efficiency, leading to a clearly reduced $h(\alpha = 0.338, \beta = 0.978) = 0.326$. This value corresponds to a fraction $h/h_{\text{max}} = 30.5\%$ of the optimum value and yields a theoretical single pass efficiency $\eta_{\text{SHG}} = 0.49\,\%/\text{W}$, assuming the literature

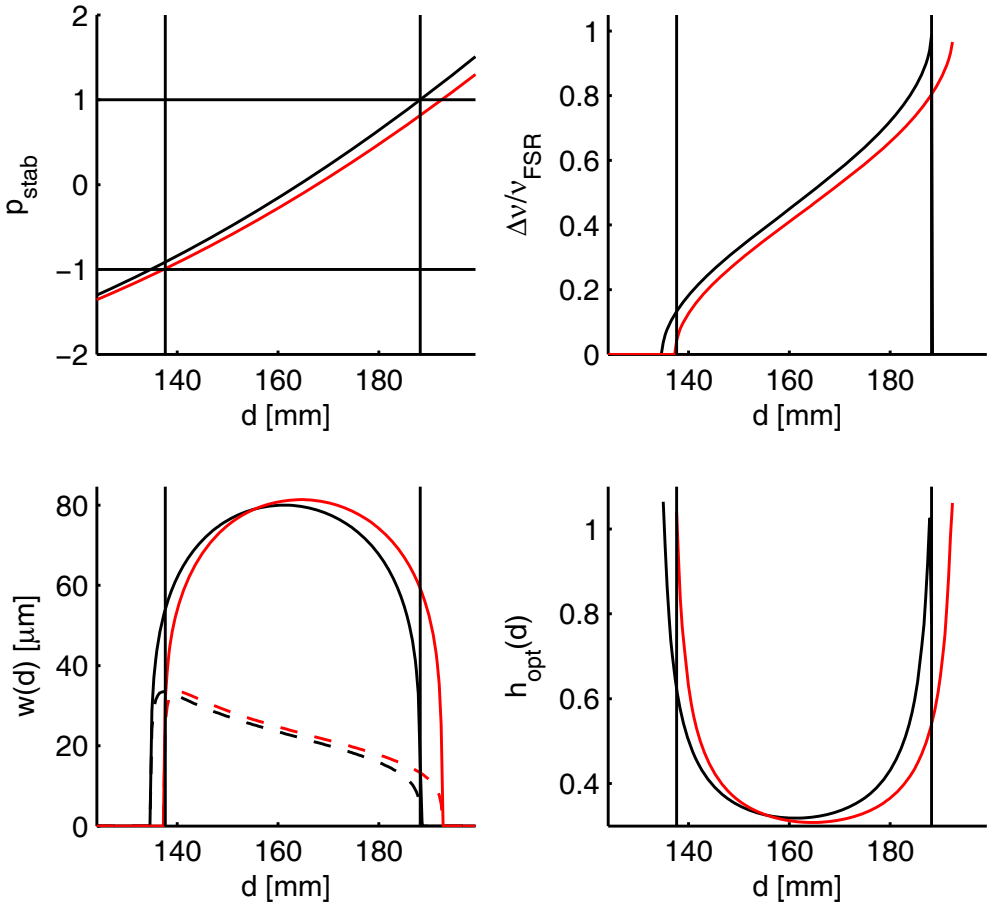

Figure 6.2: Several parameters of the doubling cavity as a function of the distance d between the two curved mirrors M_3' and M_4'. Black (red) lines indicate the horizontal (vertical) direction in the setup.

(Upper left) The stability parameters p_{stab} of the cavity, which is stable between $d_{\mathrm{cu}} = 137.6\,\mathrm{mm}$ and $d_{\mathrm{cu}} = 188.2\,\mathrm{mm}$.

(Upper right) The relative mode spacing $\Delta\nu/\nu_{\mathrm{FSR}}$, defined as relative frequency difference between the TEM_{00} mode and the modes TEM_{10} (horizontal) and TEM_{01} (vertical).

(Lower left) The waist sizes in the doubling crystal (continuous lines). We also indicate the waist radii in the coupling arm (dashed lines) between M_1' and M_2', these values being divided by a factor of ten for the representation.

(Lower right) The optimized Boyd-Kleinman function $h_{\mathrm{opt}}(\alpha(d))$, see Equation (6.8).

We chose the point $d = 156\,\mathrm{mm}$ where both waists in the crystal equal, resulting in a round shaped second harmonic beam. The relative mode spacing is larger than 0.3.

value of $d_{33} = 16.9\,\mathrm{pm/V}$ for the nonlinear optical coefficient [230]. Our choice represents a compromise between a high single-pass doubling efficiency and detrimental intensity-related effects such as two-photon and second-harmonic-induced absorption [245] and possible gray-tracking [246].
It is crucial to keep the doubling cavity under a dry-air atmosphere in an appropriately tight housing to prevent quality deterioration of the optical surfaces due to dust and moisture, and to shield the setup from thermal and acoustic perturbations.

6.2.1. Mode matching and intra-cavity loss

The length of the doubling cavity can be changed by applying a voltage to the piezoelectric transducers mounted below the cavity mirrors M_2' and M_3', see Figure 6.1. In the absence of nonlinear losses the intra-cavity power $P(\delta L)$ reads

$$P(\delta L) = \sum_{mn} \frac{P_{mn}}{1 + F \sin^2\left(\varphi_{mn} + \omega \delta L / c\right)}\,, \tag{6.14}$$

where δL is the induced length variation and P_{mn} are the contributions from the different TEM_{mn} modes. F is a parameter related to the cavity Finesse and thus to linear losses, see Equation (5.53). As mentioned before, by adjusting the cavity geometry the constant round-trip phases φ_{mn} can be chosen such as to not be degenerate. This ensures a good TEM_{00} mode quality of the second-harmonic output, since the simultaneous presence of higher-order modes is suppressed.
The mode-matching efficiency can be defined as

$$\eta_{00} = \frac{P_{00}}{\sum P_{mn}}\,. \tag{6.15}$$

This efficiency could be optimized by means of an cavity scan measurement that was performed for low intra-cavity powers of less than $\approx$ 1 W. Furthermore, the crystal temperature was far detuned from the optimum phase matching value, so that losses of the fundamental wave due to nonlinear conversion can be neglected. As already indicated in Figure 6.1, we are able to act on the cavity length in the 50μm range, by driving the slow piezo-electric transducer (PZT) that is glued below M_3'. We measured an intra-cavity power signal leaking through M_2', while varying the cavity length by δL. The measured signal is proportional to $P(\delta L)$ and allows to determine the mode-matching efficiency.
Adjusting two telescopes that consist of spherical lenses, the mode-matching efficiency could be optimized to $\eta_{00} = 95\%$. One of these two telescopes is illustrated in Figure 6.1. We note that the measured signal scan also provide information about the linear cavity round-trip loss α that can be deduced from the fit parameter F. Inserting the crystal in the cavity increases this loss by $\alpha_{\mathrm{cr}} \simeq 1\%$, as reported by [209]. This can be explained by residual absorption and scattering in the ppKTP crystal, as well as imperfections of its AR coatings.

6.2.2. Impedance matching

The conversion efficiency of an enhancement cavity is optimal if impedance matching is achieved, or in other words, if the input mirror transmission equals all other resonator losses including the nonlinear conversion process. In practice this is realized by optimizing the transmission of the input coupler in presence of nonlinear conversion and passive round-trip loss in order to maximize the second-harmonic output for a given fundamental input power. Taking into account the nonlinear conversion process, the fundamental-mode intra-cavity power $P_\omega = P_{00}$ at cavity resonance of the TEM_{00} mode is a solution of

$$P_\omega = \frac{(1 - R_\mathrm{c} - \alpha_1)\eta_{00} P_\mathrm{in}}{\left(1 - \sqrt{R_\mathrm{c}(1-\alpha_\mathrm{tot})(1-\eta_\mathrm{SHG} P_\omega)}\right)^2}\,, \tag{6.16}$$

where P_in is the fundamental pump power incident on the coupling mirror M_1', α_1 is the transmission loss of M_1' and α_tot is the total passive round-trip loss of the cavity excluding the coupler transmission and nonlinear conversion. The single-pass doubling efficiency η_SHG is calculated according to Equation (6.7) with d_{33} according to [230] and $h(\alpha)$ as given by the cavity design, see Figure 6.2. The solution can be calculated analytically using a computer algebra system, for example *Mathematica*, resulting in an expression of a length of several pages. Hence, it is not explicitly presented in this work. The second-harmonic output power is then simply calculated according to Equation (6.6), and we can define the actual cavity doubling efficiency as

$$\eta_\mathrm{cav} = \frac{P_{2\omega}}{P_\mathrm{in}} = \frac{\eta_\mathrm{SHG} P_\omega^2}{P_\mathrm{in}}\,, \tag{6.17}$$

The computational results are plotted in Figure 6.3. Assuming $\alpha_\mathrm{tot} = \alpha_\mathrm{cr} = 1\%$ and $\alpha_1 = 0$, the solution of Equation (6.16) yields a optimal SH power output of 5.34 W at the maximum available pump power of $P_\mathrm{in} = 5.91\,\mathrm{W}$. This conversion is achieved for an optimal coupling mirror reflectivity of $R_\mathrm{c,opt} = 83\%$, yielding a total conversion efficiency of $\eta_\mathrm{cav} = 90.3\%$. For the chosen $R_\mathrm{c} = 90\%$ coupler we expect satisfying results over a large power range up to the maximum available pump power, where a conversion efficiency of $\eta_\mathrm{cav} = 84\%$ should be achieved.

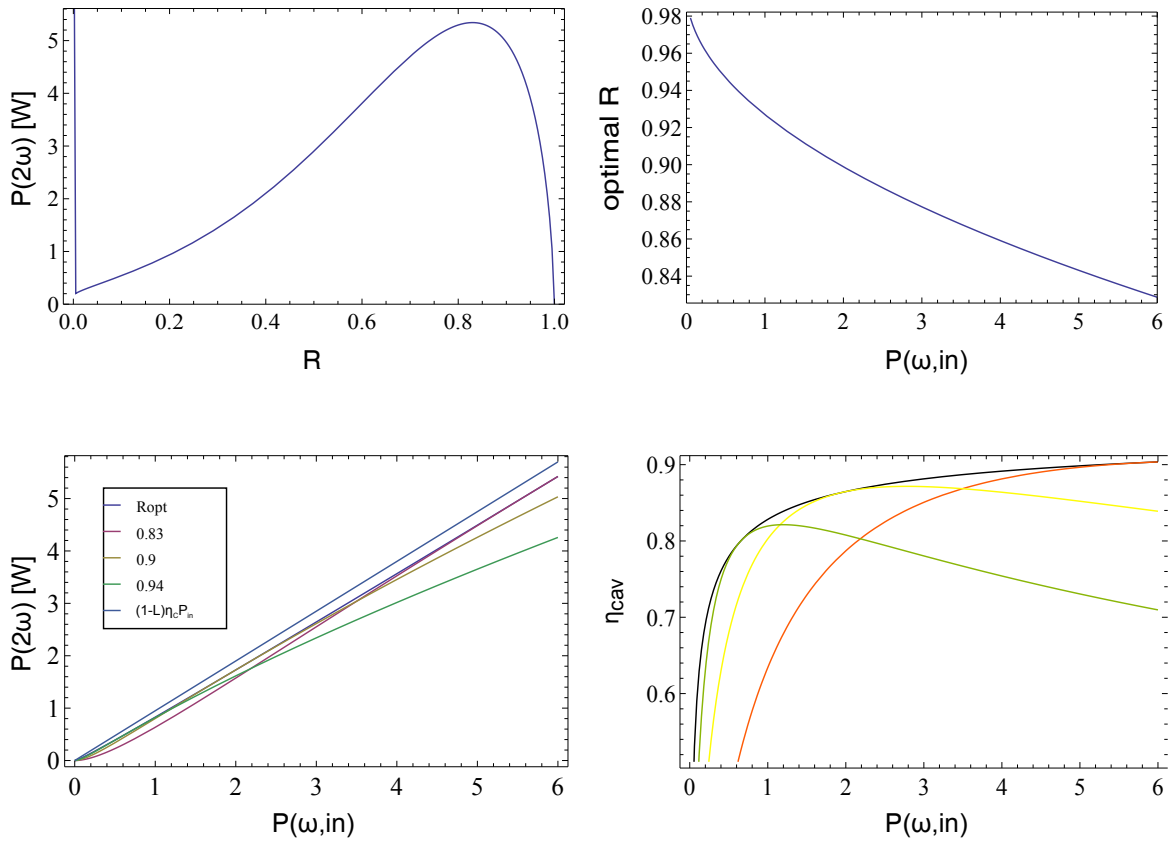

Figure 6.3: Calculations for the cavity conversion efficiency assuming reasonable parameter settings.

(Upper left) The SH power output at maximum available fundamental input power $P_{\mathrm{in}} = 5.91\,\mathrm{W}$ as a function of the coupling mirror (M_1') reflectivity R_{c}.

(Upper right) The optimal input coupler reflectivity $R_{\mathrm{c,opt}}$ as a function of the fundamental input power.

(Lower left) The SH output power as a function of the fundamental input power for different values of the coupler reflectivity. Shown are the three experimentally available couplers, the curve for $R_{\mathrm{c,opt}}$ as before and, as a reference, the power of the fundamental light coupled to the TEM_{00} mode $1-\alpha_1\eta_{00}P_{\mathrm{in}}$.

(Lower right) Cavity doubling efficiencies for the same coupler reflectivity values as before. The $R_{\mathrm{c}} = 90\%$ coupler allows for satisfying conversion for a large range of fundamental input powers up to the maximal value $P_{\mathrm{in}} = 5.91\,\mathrm{W}$, also keeping a good conversion efficiency for lower powers. For still higher fundamental input powers, a lower-reflectivity input coupler should be chosen.

6.2.3. Locking scheme

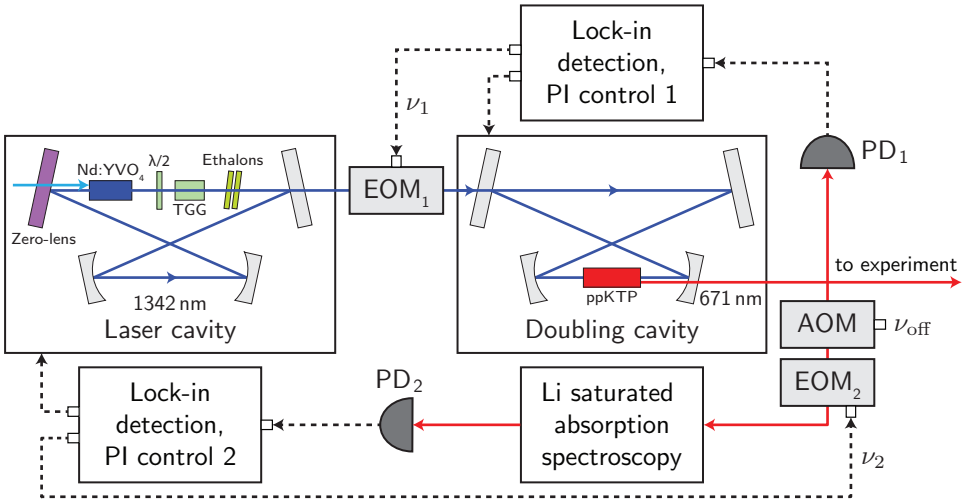

Figure 6.4: Scheme of the lock system, as illustrated in [148]. Light paths and electronic signals are represented by straight- and dashed lines, respectively. First, the doubling cavity is resonantly locked to the free-running Nd:YVO_4 laser using the control circuit components indexed with subscript 1. A small amount of second harmonic light serves as signal for the lithium spectroscopy setup. In a second step the reference signal from the spectroscopy serves to lock the doubled Nd:YVO_4 laser output frequency to one of the Lithium resonance frequencies, using control circuit 2. A double pass AOM with driving frequency ν_{off} allows to control the frequency offset between the atomic resonance and the laser output frequency.

The lock system provides frequency-stabilization of the laser system on the lithium D-lines. Figure 6.4 shows the locking scheme including two feedback loops for the doubling- and the laser cavity. First, the length of the doubling cavity is stabilized such that the cavity remains resonant with the Nd:YVO_4 laser frequency. The generated second harmonic light allows to perform saturated absorption spectroscopy on lithium vapor. Subsequently, the doubled Nd:YVO_4 output frequency is locked to the desired lithium transition by controlling the length of the infrared laser cavity.

The lengths of both cavities are varied by piezo-electric transducers (PZTs) that are mounted below two mirrors per cavity. One of the PZTs features slow actuation and a large range, whereas the other one allows fast actuation but has a limited range.

The doubling cavity is locked resonantly to the laser output by a phase modulation technique. EOM_1 phase-modulates the infrared pump light at $\nu_1 = 0.8\,\text{MHz}$. Consequently, the frequency-doubled light is also phase modulated. A leak of frequency-doubled light is detected by a photodiode, before the signal is demodulated with a home-made lock-in amplifier circuit. It yields an error signal which is fed into a proportional-integral (PI) controller circuit, acting on the two actuator PZTs in different frequency ranges.

The laser cavity is frequency-locked with respect to an atomic transition by means of saturated-absorption frequency modulation spectroscopy [247] of lithium vapor in an oven cell with frequency-doubled light. A double-pass setup with a 200 MHz AOM allows to frequency-shift the spectroscopy light which finally results in a tunable offset of the laser frequency. The

probe beam of the saturated absorption is phase-modulated at $\nu_2 = 1.2\,\mathrm{MHz}$ by EOM_2, before it passes through the spectroscopy cell. An amplified photodiode (Newport, ref. 1801) detects the probe light which is demodulated to the error signal with a lock-in amplifier. A two-way PI acts accordingly on the two actuator PZTs.

6.2.4. Cavity characterization and SH output power

In this section we will present the results of our measurements characterizing the conversion process in the resonant cavity. We will then discuss measures allowing to scale to even higher powers.

Figure 6.5 presents the results of measuring the second harmonic output power $P_{2\omega}$ as a function of the intra-cavity fundamental power P_ω and the input power incident on P_{in}, the cavity being locked to the laser. For this measurement, we used the $\mathcal{R}_c = 90\%$ input coupler. The obtained data allows for a complete characterisation of the cavity. As it could be expected from Equation (6.6), the conversion shows quadratic behavior even for the highest power levels, see Figure 6.5(a). The maximal SH output power $P_{2\omega} = 5.15\,\mathrm{W}$ is reached for a measured intra-cavity fundamental power of $P_\omega = 48.48\,\mathrm{W}$, corresponding to a fundamental input power of $P_{\mathrm{in}} = 5.91\,\mathrm{W}$. This yields a cavity doubling efficiency of $\eta_{\mathrm{conv}} = 87\%$.

A fit to Equation (6.17) is performed including the solution of Equation (6.16), with η_{SHG} and α_{tot} being the fit parameters, see Figure 6.5(b). This fit to the cavity conversion efficiency as a function of the fundamental input power describes the data quite well. The passive intra-cavity losses of $\alpha_{\mathrm{tot}} = 1\%$ fitted with this method confirm those assumed in Subsection 6.2.2, where the theoretical results were calculated supposing $\alpha_{\mathrm{tot}} = 1\%$, see Figure 6.3. Furthermore, the fit yields a single-pass efficiency of $\eta_{\mathrm{SHG}} = 0.16\%/\mathrm{W}$, considerably lower than the theoretical prediction $\eta_{\mathrm{SHG}} \approx 0.49\%/\mathrm{W}$. The direct measurement, inferred from the fit in Figure 6.5(a) gives only a slightly higher values of $\eta_{\mathrm{SHG}} = 0.22\%/\mathrm{W}$. These low values of η_{SHG} could be explained by imperfections of the domain poling, most probably deviations from perfect periodicity. We thus derive an effective nonlinear coefficient of $d_{\mathrm{eff}} = 9.6\,\mathrm{pm/V}$ for our ppKTP crystal, significantly lower than the literature value of $16.9\,\mathrm{pm/V}$ [230].

The maximum measured doubling efficiency of $\eta_{\mathrm{conv}} = 87\%$ is compatible with the theoretical prediction of $\eta_{\mathrm{conv}} = 84\%$ calculated in Subsection 6.2.2. The fact that the measured value is slightly higher than the theory value is a further indication that the intra-cavity loss is most probably not larger than 1.0%.

We could not observe any intensity-related instabilities and the second-harmonic output power follows a variation of the intra-cavity fundamental power without observable hysteresis. Moreover, no long-term degradation was observed, indicating the absence of gray-tracking, even for the highest reachable fundamental pump powers in our setup. We thus state that under the condition of a small passive intra-cavity loss, the lower-than-optimal focusing represents an advantageous choice for the doubling cavity design. Further power-scaling of the doubling enhancement cavity is therefore achievable by enlarging the radius of the Gaussian mode passing through the doubling crystal, even if one would lose in single-pass efficiency

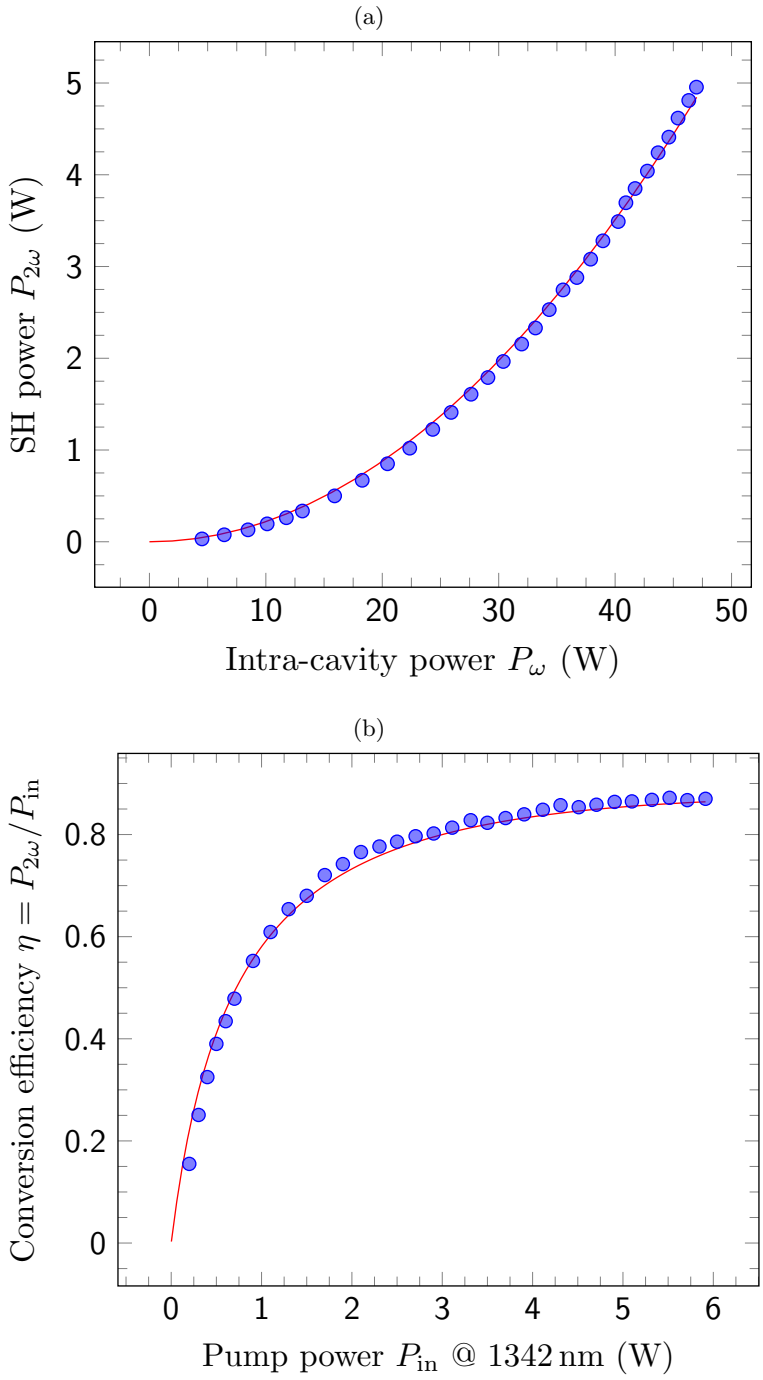

Figure 6.5: Measurement of the cavity doubling efficiency, where blue points are measured data and red lines are fits.

(a) The second harmonic output power as a function of the fundamental intra-cavity power. As expected from Equation (6.6), a quadratic function can be fitted to the conversion.

(b) The cavity conversion efficiency as a function of the fundamental input power. The fit is performed according to Equation (6.17) including the solution of Equation (6.16), with η_{SHG} and α_{tot} being the fit parameters.

η_{SHG}. The resulting compatibility with higher intra-cavity powers should permit even higher second-harmonic output powers at increased fundamental input power values above 6 W.
Power-scaling of the doubling enhancement cavity might also be realized by employing an alternative nonlinear medium. Insertion of a periodically-poled stoichiometric lithium tantalate (ppSLT) crystal of the same length as the ppKTP crystal in use would probably lead to higher power tolerance. Second-harmonic or fundamental-power-induced detrimental effects seem to play a minor role for this material. Furthermore, the value of its nonlinear optical coefficient d_{33} is comparable to the one of ppKTP [248]. Calculations show that the current cavity setup could be kept in the case of a crystal replacement, since the cavity eigenmode would only be slightly modified.

6.3. Intracavity frequency-doubling

This section is based on the following manuscript:

2.1-watts intracavity-frequency-doubled all-solid-state light source at 671 nm for laser cooling of lithium
U. Eismann, A. Bergschneider, F. Sievers, N. Kretzschmar, C. Salomon, and F. Chevy
Opt. Express **21**, 9091 (2013)

In this section, we present the second laser generation based on intracavity second-harmonic generation [210]. In this setup, the nonlinear ppKTP-crystal is directly inserted in the infrared laser cavity (see Fig. 6.6). We develop a simple theory for the efficient implementation of intracavity second harmonic generation. Its application to our system allows us to obtain nonlinear conversion efficiencies of up to 88%. Single-mode operation and tuning is established by adding an etalon to the resonator. The second-harmonic wavelength can be tuned over 0.5 nm. The laser can be mode-hop-free scanned over more than 6 GHz, corresponding to around ten times the laser cavity free spectral range. The output frequency can be locked with respect to the lithium D-line transitions for atomic physics applications. Furthermore, we observe parametric Kerr-lens mode-locking when detuning the phase-matching temperature sufficiently far from the optimum value.
This section is organized as follows: In Section 6.3.1 we present the optimization of the fundamental laser design.[1] In Section 6.3.2, we implement intracavity second harmonic generation. In Section 6.3.3, we report on the course and continuous fine tuning behavior and nonlinear-Kerr-lens mode locking, and we conclude in Section 6.3.4.

6.3.1. The fundamental laser

A first step towards a stable high-power frequency doubled laser source is the availability of an efficient laser system at the fundamental wavelength. To minimize detrimental thermal effects in the gain medium, the following pathway has been chosen: A pump wavelength of

[1] The optimization of the fundamental laser is done without the ppKTP crystal in the cavity

888 nm in contrast to the former 808 nm [184] leads to a lower quantum defect per absorption-emission cycle [193], and thus to lower heating for a given pump rate. In addition, a larger value for the laser crystal length has been chosen in order to spread the heat input over a bigger volume. Therefore, heat transport from the central region to the crystal mount is facilitated. The ND:YVO_4 peak temperature is lower, and thermal issues are less of a concern.

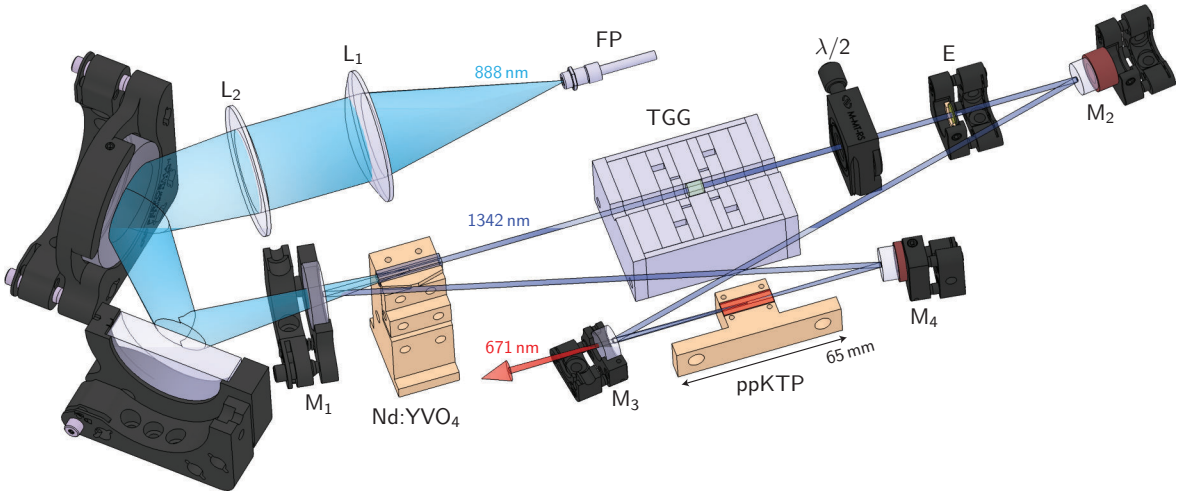

Figure 6.6: Scheme of the second laser generation. The pump source, a fiber-coupled diode laser bar (FP), is imaged into the gain medium by a pair of lenses L_1 and L_2. The Nd:YVO_4 gain medium is placed in a four-mirror bow-tie ring resonator consisting of mirrors M_{1-4}, which are highly reflecting at 1342 nm. Unidirectional operation is forced employing a terbium gallium garnet (TGG)-based Faraday rotator in combination with a half-wave plate ($\lambda/2$). The use of an etalon (E) allows for stable single-longitudinal-mode operation. The nonlinear crystal (ppKTP) is inserted at the tight focus between the curved mirrors M_3 and M_4. The second harmonic output beam (red) is transmitted through M_3. For the measurements presented in Section 6.3.1, the ppKTP was removed and the distance M_3-M_4 adjusted accordingly, and the high-reflectivity mirror M_2 was replaced by a partly transmitting output coupling mirror. The fundamental laser beam (dark blue) is then coupled out through M_2.

A schematic overview of the laser setup is given in Fig. 6.6. The output of an 888-nm fiber-coupled diode laser bar (NA = 0.22, 400 µm fiber core diameter) is imaged by two lenses L_1 and L_2 [2] into the 1.0% at.-doped ND:YVO_4 crystal. The crystal is a-cut, $4 \times 4 \times 25\,\mathrm{mm}^3$ and anti-reflection coated on both sides for 1342 nm and 888 nm. It is wrapped in indium foil and mounted in a water-cooled copper block. The mirrors M_{1-4} constitute a bow-tie cavity. M_1, M_3 and M_4 are highly reflective at 1342 nm, and M_1 is transmitting at 888 nm. M_3 and M_4 are concave mirrors with a radius of curvature of 100 mm. M_2 is the output coupler for which mirrors with different values of transmission are available. The cavity dimensions are $M_1M_2 \sim 300\,\mathrm{mm}$, $M_2M_3 \sim M_1M_4 \sim 210\,\mathrm{mm}$ and $M_3M_4 \sim 97\,\mathrm{mm}$. To force unidirectional operation we use a Faraday rotator consisting of a terbium-gallium-garnet rod-shaped crystal (TGG) of 6 mm length embedded in a strong permanent magnet [216] in combination with a true-zero-order half-wave plate. An uncoated infrared fused silica etalon of 500 μm thickness serves as a wavelength selective element.

[2] $f_1 = 75\,\mathrm{mm}$, $f_2 = 200\,\mathrm{mm}$

For maximum power output, it is crucial to optimize the overlap of the pump beam and the cavity mode [211, 249]. For simplicity, we perform this operation on the empty laser cavity, consisting of M_{1-4} and the ND:YVO_4 only. We use the maximum value of the absorbed pump power $P_{\mathrm{abs,max}} = 32.5\,\mathrm{W}$, and a $\mathcal{T} = 5\%$-transmission output coupler (M_2). By changing the magnification of the pump imaging setup consisting of L_1 and L_2, the top-hat shaped pump spot diameter was altered between 1080 µm and 1400 µm (see Fig. 6.7). The size of the cavity mode in the laser crystal can be changed using the curved mirror distance M_3M_4, and was optimized for each data point. The maximum output power is obtained at a pump diameter of around 1300 µm, where it is kept for the remainder of this section.

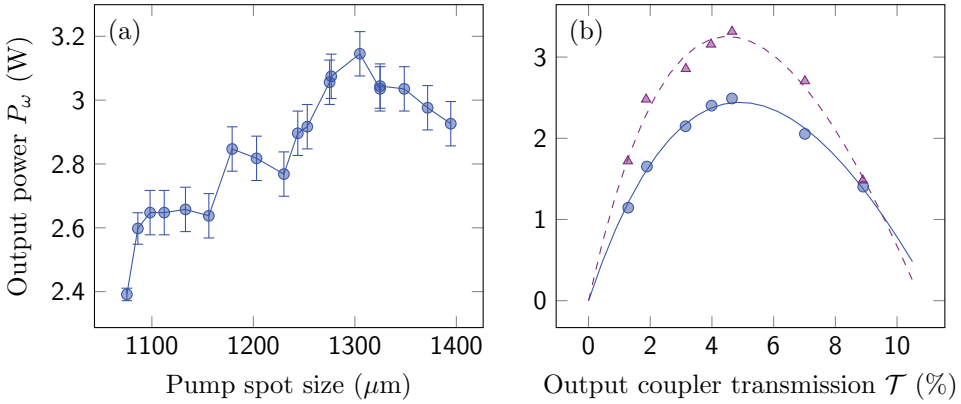

Figure 6.7: (a) Optimization of the output power by changing the pump spot diameter, performed on the laser cavity presented in Fig. 6.6 with all the intracavity elements removed, except for the ND:YVO_4. For a $\mathcal{T} = 5\%$ output coupler (M_2), the mode overlap was optimized for each pump spot diameter by slight adjustments of the curved-mirror distance M_3-M_4. Lines are guides to the eye only. (b) Rigrod analysis. The infrared output power P_ω is measured as a function of the output coupler transmission $\mathcal{T}$ and fitted with the Rigrod model (Eq. (6.18)) for bidirectional (purple triangles, dashed line) and unidirectional (blue circles, solid line) operation at $P_{\mathrm{abs,max}} = 32.5\,\mathrm{W}$ and optimized mode overlap. In both cases the optimum transmission is found at $\mathcal{T} \sim 5\%$. The parasitic roundtrip loss determined from the fits yield 10(4)% for the bidirectional and $\mathcal{L} = 16(6)\%$ for the unidirectional case.

For both the bidirectional (empty cavity only containing ND:YVO_4) and the unidirectional (additional TGG and half-wave plate) operation we measured the maximum output power as a function of the output coupler transmission, see Fig. 6.7b. In both cases a $\mathcal{T} = 5\%$ mirror delivers the maximum fundamental output power P_ω. By equating the single-pass gain with the total round-trip loss $\mathcal{L}_{\mathrm{tot}} = \mathcal{L} + \mathcal{L}_{\mathrm{out}} = \mathcal{L} + \mathcal{T}$ for both the bi- and unidirectional cases, where $\mathcal{L}$ is the sum of the parasitic round-trip losses, we find

$$P_\omega = P_{\mathrm{sat}}\mathcal{T}\left[\frac{G_0}{\mathcal{T}+\mathcal{L}} - 1\right] \tag{6.18}$$

similarly to [250]. Here P_{sat} is the saturation power, G_0 the small-signal gain and $\mathcal{L}$ the sum of the parasitic round-trip losses. Although this analysis essentially relies on plane waves, it can be mapped to the more realistic case of top-hat pump beams and gaussian laser cavity eigenmodes, as present in diode-pumped solid-state lasers, see [184] and references therein.

A least-squares fit to Eq. (6.18) yields $\mathcal{L} = 10(4)\%$ for the parasitic loss in the bidirectional case. In [184] we found the loss in an empty four-mirror bow-tie cavity of mirrors from the same batch to be smaller than 1%. We attribute the remaining 9(4)% mainly to aberrations caused by the thermal lens in the ND:YVO_4.
In the unidirectional case, the fitting procedure yields $\mathcal{L} = 16(6)\%$. Compared to the bidirectional case, the difference of $\mathcal{L}_{\text{Faraday}} = 6(7)\%$ can be attributed to the insertion of the TGG crystal and the waveplate. Indeed, thermal depolarization and the accompanying loss is a well-known effect in TGG. It imposes stringent limits on power scaling of unidirectional ring lasers and Faraday isolators [251]. We observe a dependence of the optimum half-wave plate angle on the circulating intracavity power, which is strong evidence of this effect. From the fit, we furthermore obtain the values $P_{\text{sat}} = 170(50)\,\text{W}$ and $G_0 = 0.27(5)$ for unidirectional operation, which are important for the optimization of intracavity doubling, see Section 6.3.2.
For the now-optimized unidirectional infrared setup, we measure the output power as a function of the absorbed pump power P_{abs} (see Fig. 6.8). As the optimization is performed at the maximum absorbed pump power $P_{\text{abs,max}} \sim 32.5\,\text{W}$, the laser emission only starts at $P_{\text{abs}} \sim 28\,\text{W}$. After reaching threshold, the output power is unstable and displays a hysteresis feature between $P_{\text{abs}} = 29\,\text{W}$ and 30 W. After crossing the hysteresis region, the laser emission is stable and only weakly depends on P_{abs}. This behavior is typical for high-power solid-state laser designs and has been reported in [203]. As discussed before, thermal depolarization in the TGG is significant and can lead to a change of the lasing direction and occasional bistable behavior when increasing the pump power. Thus, the angle of the half-wave plate had to be adjusted for every data point presented here. We keep the pump power constant at $P_{\text{abs,max}} \sim 32.5\,\text{W}$ in the remainder of the section.

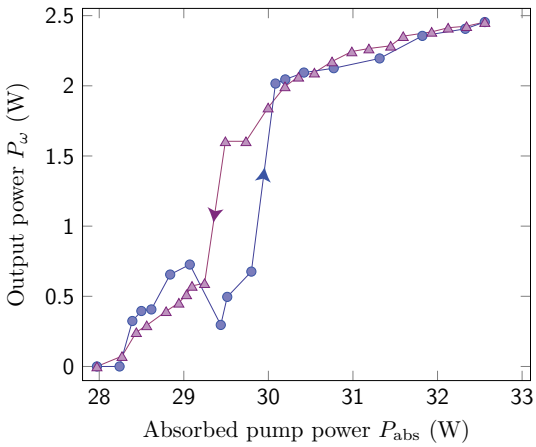

Figure 6.8: Infrared unidirectional output power P_ω as a function of the absorbed pump power P_{abs}. The setup is optimized for the maximal absorbed pump power $P_{\text{abs,max}} = 32.5\,\text{W}$. The oscillation threshold is found at $P_{\text{abs}} \sim 28\,\text{W}$. The data shows hysteresis between $P_{\text{abs}} = 29\,\text{W}$ and 30 W, as indicated by the arrows for increasing or decreasing pump power. This behavior is typical for high-power designs. After a sudden rise the output power increases only slowly until it eventually reaches the maximum of 2.5 W at $P_{\text{abs,max}}$. Lines are guides to the eye only.

6.3.2. Efficient intracavity second-harmonic generation

Efficient frequency doubling of infrared lasers can be established using periodically-poled nonlinear crystals in an external cavity. Using this method at a fundamental wavelength of 1342 nm, a doubling efficiency of $P_{2\omega}/P_{\omega} = 86\%$ has been obtained in our first-generation setup [184], and serves as a benchmark. However, a more direct approach followed here is intra-cavity second harmonic generation (ICSHG), which requires only one cavity and thus represents an important simplification.

For the analysis of the output power of ICSHG lasers, the output coupling loss $\mathcal{L}_{\text{out}} = \mathcal{T}$ discussed in Section 6.3.1 needs to be replaced by ηP, where η is the single-pass doubling efficiency, and P the circulating intracavity power. Similar to the one found in [252, 253], the solution for the SH output power in the unidirectional case reads

$$P_{2\omega} = \frac{P_{\text{sat}} G_0}{\xi} \left[\sqrt{(\xi - \zeta)^2 + \xi} - (\xi + \zeta) \right]^2 , \tag{6.19}$$

where $\xi = \eta P_{\text{sat}} (4G_0)^{-1}$ and $\zeta = \mathcal{L}(4G_0)^{-1}$ are the dimensionless output coupling and loss parameters. As pointed out in [252, 253], it is interesting to note that the value for the optimum output coupling $\mathcal{L}_{\text{out,opt}} = \sqrt{G_0 \mathcal{L}} - \mathcal{L}$ is the same for both linear and non-linear output coupling mechanisms, and delivers the same amount of output power. However, the round-trip parasitic loss $\mathcal{L}$ will contain an additional contribution from the insertion of the nonlinear medium. Hence, $P_{2\omega}/P_{\omega} < 1$ for any realistic system, but efficiencies close to one can be obtained in practice [254]. Using the fit values from Section 6.3.1, we maximize Eq. (6.19) by choosing an optimum single-pass doubling efficiency $\eta_{\text{opt}} = 0.10(5)\%.\text{W}^{-1}$.

To evaluate η, we refer to the Boyd-Kleinman theory for focused gaussian beams [226],

$$\eta(T) = \frac{2\omega^3 d_{ij}^2 L}{\pi \varepsilon_0 c^4 n_{\omega,i}(T) n_{2\omega,j}(T)} \times h[\alpha, \beta(T)] , \tag{6.20}$$

where ε_0 is the vacuum permittivity, c the speed of light in vacuum, d_{ij} is the i,j-th element of the material's nonlinear tensor, $n_{\omega,i}(T)$ the material's refractive index along the i axis at angular frequency ω and temperature T, and L the nonlinear material's length. d_{ij} needs to be replaced by $d_{\text{eff}} = 2d_{ii}\pi^{-1}$ for periodically poled (pp) materials. The function

$$h[\alpha, \alpha_0, \beta(T)] = \frac{1}{4\alpha} \left| \int_{-\alpha-\alpha_0}^{\alpha-\alpha_0} \frac{e^{i\beta(T)\tau}}{1 + i\tau} \, d\tau \right|^2 , \tag{6.21}$$

is the dimensionless Boyd-Kleinman function [226]. $\alpha = L\,(2z_{\text{R}})^{-1}$ and $\alpha_0 = z_0\,(2z_{\text{R}})^{-1}$ are the focusing and offset parameters, respectively. z_{R} is the Rayleigh length, and z_0 is the offset of the beam focus with respect to the nonlinear medium's center. The phase-matching parameter reads $\beta(T) = 4\pi z_{\text{R}} \lambda^{-1} \times \left\{ n_{\omega,i}(T) - n_{2\omega,j}(T) - \lambda[2\Lambda(T)]^{-1} \right\}$, where λ is the vacuum wavelength. The $\Lambda(T)$ term only occurs for periodically poled materials, where $\Lambda(T)$ is the poling period, and the temperature dependence results from thermal expansion.

In the intracavity-doubling setup, we replace the output coupling mirror M_2 by a high-reflectivity mirror, cf. Fig. 6.6. The nonlinear, periodically-poled potassium titanyl phosphate crystal (ppKTP) is inserted between the concave mirrors M_3 and M_4. To account for the ppKTP refractive index, the distance M_3M_4 is increased to ∼106 mm. The nonlinear crystal has outer dimensions of $1 \times 6 \times 18\,\mathrm{mm}^3$ and is antireflection coated at 1342 nm and 671 nm. Its poling period $\Lambda = 17.61\,\mu\mathrm{m}$ is chosen for phase matching at 23.5°C according to the temperature-dependent Sellmeier equations from [232, 233]. However, in a previous study we found the phase-matching temperature at 33.2°C [184]. This deviation can be explained by uncertainties on the reported Sellmeier equations, and the manufacturing tolerance on the ppKTP poling period. The nonlinear coefficient $d_{33} = 14.5\mathrm{pm.V}^{-1}$ found for the crystal in our preliminary study is 14% lower than the highest literature value reported so far [230], probably due to poling imperfections [184]. Using this crystal for nonlinear output coupling, we can easily obtain a single-pass efficiency $\eta > \eta_{\mathrm{opt}}$, such that design considerations are relaxed, and we are able to tune to η_{opt} by changing the phase-matching temperature. For temperature stabilization, the crystal is wrapped in indium foil and mounted in a temperature-controlled copper block. The frequency-doubled light is transmitted through mirror M_3.

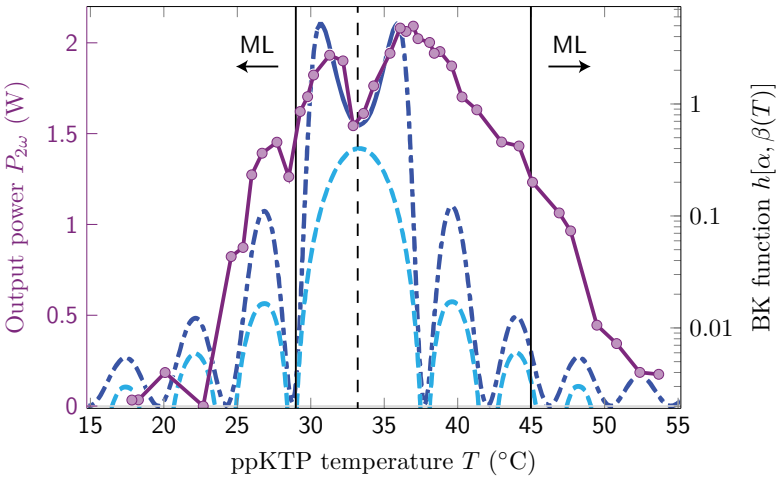

Figure 6.9: Output power as a function of the phase-matching temperature (purple circles, lines are a guide to the eye only). The data shows a double-peak structure of 1.9 W / 2.1 W of output power slightly off of the optimum phase-matching temperature of 33.2°C (central vertical line). A simple theoretical model presented in the text (dash-dotted dark blue line) describes the data well in the central high-conversion region, using the known temperature dependence of the single-pass doubling efficiency, which is proportional to the dimensionless Boyd-Kleinman function $h(T)$ [dashed light blue line, Eq. (6.21)]. The dashed vertical line indicates the perfect phase-matching temperature of $T_{\mathrm{pm}} = 33.2$°C, where $\beta(T_{\mathrm{pm}}) \simeq 0$, and the nonlinear output coupling is too high to reach maximum output power. The vertical lines with arrows indicate the temperature regions where self-mode locking occurs, cf. Section 6.3.3.

In Fig. 6.9 we present the measurement of the second-harmonic output power as a function of the phase-matching temperature of the ppKTP crystal. We find a maximum of 2.1 W of output power at $T_{\mathrm{pm}} = 36$°C, and a second maximum of 1.9 W at $T_{\mathrm{pm}} = 31$°C. As expected from Eq. (6.19), at the perfect phase matching temperature the output power only amounts to 1.6 W because $\eta > \eta_{\mathrm{opt}}$. The FWHM of the temperature-tuning curve is 22 K. As compared to

the maximum infrared power presented in the former section, we obtain a maximum doubling efficiency of 88%. The excellent mode quality of the second-harmonic light is confirmed by a single-mode fiber coupling efficiency larger than 80%.

To gain deeper insight in our data, we employ the ICSHG theory (Eqs. (6.19) to (6.21)). We include the additional parasitic intracavity loss caused by the presence of the etalon and the nonlinear crystal, which amounts to $\mathcal{L}_{\mathrm{add}} = 0.6(1)\%$. Thus, the theory predicts a maximum SH output power of 2.1 W, as is found experimentally. The value of $\mathcal{L}_{\mathrm{add}}$ is compatible to the sum of the ppKTP insertion loss measured independently [184] and the calculated walk-off loss for the etalon [209]. From an ABCD-matrix formalism we obtain the cavity eigenmode, yielding $z_{\mathrm{R}} = 11.5\,\mathrm{mm}$ and $z_0 = 3\,\mathrm{mm}$. At perfect phase matching, we obtain $h = 0.40$, yielding a SH output power of 1.6 W, which is in excellent agreement with our findings. This gives us further confidence in our previously measured value of d_{33} [184]. The temperature-dependent KTP refractive indices and the thermal expansion coefficient of the poling period were presented in [232, 233]. We adjust β by an additive constant in order to account for the measured phase matching condition $\beta(T = 33.2°\mathrm{C}) = 0$, as justified before. The theory (solid purple line in Fig. 6.9) describes the data well in the central high conversion region, and yields the characteristic double-peak structure.

Outside of the central region, the circulating intracavity power rises significantly and the power-dependent thermal depolarization loss would need to be accounted for in our simple model. As compared to the theory, the data displays less evidence of dips. This can be explained by a thermal smearing effect due to residual absorption in the ppKTP at large powers, yielding a spatial dependence of the phase-matching parameter $\beta(T)$. Outside of the region indicated by the solid vertical lines, the laser is in mode-locked (pulsed) operation, and we do not expect our model to be applicable.

6.3.3. Tuning behavior and nonlinear-Kerr-lens mode locking

For course tuning and single-longitudinal-mode (SLM) operation, the laser was equipped with an uncoated etalon of 0.5 mm length, yielding a free spectral range of 210 GHz. We note that this single, weakly-selective etalon is sufficient for this purpose due to the self suppression of axial mode hopping in intracavity-frequency-doubled lasers [255, 256].

The tuning range of the frequency-doubled laser is characterized and compared to the infrared laser in Fig. 6.10. Apart from having the same shape and features, it is striking to note that the output power of the frequency-doubled laser amounts to almost the same value as the non-doubled laser over the entire emission spectrum. As discussed in Section 6.3.2, the nonlinear output coupling is close to the optimum level over the entire emission wavelength range. The gain line center, where the output power is maximal, is found at around 671.1 nm, resulting in 2.2 W of fundamental and 2.1 W of second-harmonic output. At the lithium-D line wavelength the output power amounts to ∼1.8 W. Close to the gain line center, this result compares favorably to the value obtained in [183], where the authors used an etalon for tuning which potentially produces significantly higher tilt loss [209, 218]. Comparing the emitted power of

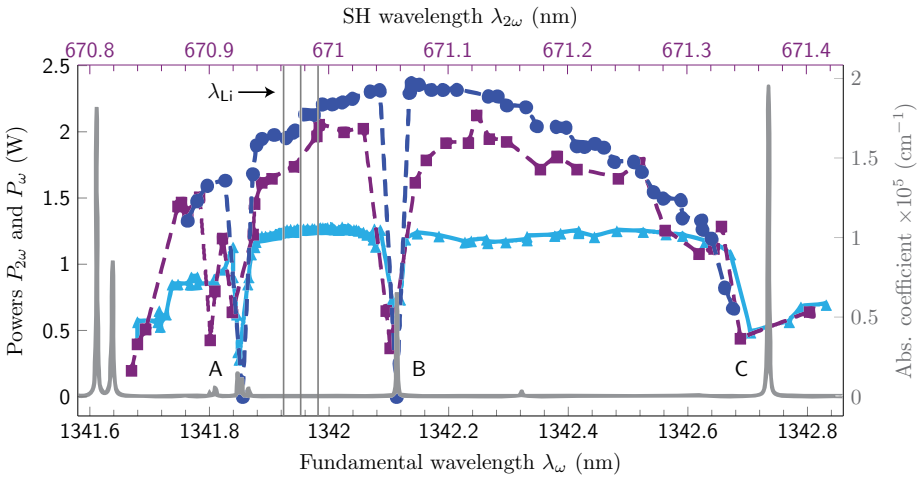

Figure 6.10: (Lines are guides for the eye only) Single-frequency output spectra of the infrared laser presented in Section 6.3.1 (dark blue circles), the intracavity-frequency-doubled laser (purple squares) and the infrared source presented in [184] (light blue triangles). For easy comparison, all wavelengths are given in vacuum values. The vertical lines denote the positions of the lithium-D line resonances. The gray line shows a water vapor absorption spectrum for typical parameters (23 °C, 60% rel. humidity). The wavelength regions marked A,B,C where stable, powerful operation of the lasers can not be established coincide with absorption peaks of water molecules. The level of output power of the infrared laser and the frequency-doubled laser are closely spaced, proving that the nonlinear crystal introduces weak additional passive losses in the laser cavity, whereas the degree of nonlinear output coupling is at its optimum value.

the doubled and non-doubled lasers across the emission spectra, we typically obtain more than 80% of the power at 671 nm, demonstrating a very efficient frequency doubling process. For the absolute maximum values, we obtain $P_{2\omega}/P_\omega = 88\%$. It is even possible to obtain emission further away from resonance, where the non-ICSHG lasers cease to oscillate. Our first-generation source presented in [184] displays an output spectrum that is significantly more plateau-like (light blue triangles in Fig. 6.10), which we attribute to the presence of a second, more selective etalon in the cavity. At the expense of a higher insertion loss baseline, ripples in the emission spectrum have significantly less influence on the tuning behavior of this setup. The identical gaps in all of the emission spectra presented here (A,B,C in Fig. 6.10) can be explained by absorption from water vapor, as we compare the laser spectra to a water vapor absorption spectrum obtained from the HITRAN database [222]. The water absorption peaks coincide with the features A,B and C.

Intracavity-frequency-doubled lasers tend to mode-locked operation when the doubling crystal is mismatched from the optimum phase matching condition [257, 258]. This effect, resulting from an intensity-dependent phase shift of the fundamental beam passing the non-matched crystal, is commonly termed nonlinear-Kerr-lens- or $\chi^{(2)}$:$\chi^{(2)}$ mode locking. Although it has been observed in the 1064-nm-Nd:YVO_4-ppKTP system before [259], we report, to the best of our knowledge, the first observation at 1342 nm. We observe the effect when detuning from the optimum phase-matching temperature to below T_{low} =29°C and above T_{high} =45°C. A scanning Fabry-Perot spectrum analyzer shows no discernible single- or few-mode background once the threshold to mode-locked operation is crossed. We use a fast detector and a spectrum

analyzer to measure the beat frequency between neighboring modes. This simple method to determine the laser cavity free spectral range yields a value of 345(1) MHz.
It is remarkable that the mode locking arises when tuning the phase-matching temperature to colder-than-optimal values. In analogy to standard Kerr-lens mode locking, the $\chi^{(2)}$:$\chi^{(2)}$ process requires an additional intracavity element which modifies the round-trip gain or loss as a function of the power-dependent cavity mode size. This can be realized by the gain medium, cf. Fig. 6.6. As we presented in Section 6.3.1, the pump-to-cavity mode overlap has been carefully optimized in the cw regime. However, an ABCD-matrix-based cavity mode calculation reveals that the beam waist in the Nd:YVO_4 only changes monotonously when crossing over from negative to positive focal powers in the ppKTP. Thus, the induced change in gain or loss should be less favorable whenever the lensing departs from the optimized value. We note that Zondy et al. [254] argue that pulsed operation should occur whenever there exists a power-dependent gain-loss mechanism, whichever is the sign of the focal power in the ppKTP. Furthermore, we also note that in our simple analysis, we do not take into account different Kerr-like and thermal lenses that may occur in the intra-cavity elements other than the laser and nonlinear crystals. Using the temperature-dependent Sellmeier equations of [232,233], we get dephasing parameters of $\beta(T_{\mathrm{low}}) = 8.8(1)$ and $\beta(T_{\mathrm{high}}) = -18.5(1)$, resulting in a single-pass efficiency $\eta(T)$ reduced to less than 5% of the maximum value.

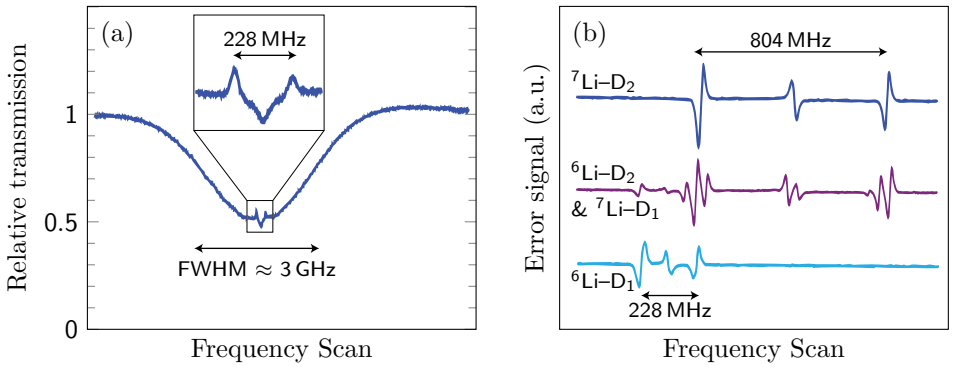

Figure 6.11: Doppler-free saturated absorption spectroscopy of the lithium D-lines. (a) Sample scan over the entire ^{6}Li D_1 Doppler-broadened absorption peak. The inset shows the sub-Doppler features. Similar spectra are obtained for all lithium D lines. (b) Error signals of all lithium D line transitions, generated by phase modulation spectroscopy. These signals provide an excellent reference for frequency-locking of the laser.

The laser can be tuned continuously using a piezoelectric transducer (PZT), upon which mirror M_2 is glued. This allows mode-hope free scans of the 671-nm output frequency over more than 6 GHz. For the resonated fundamental light this amounts to about ten times the laser cavity free spectral range, a typical behavior of ICSHG lasers with self-suppressed mode hopping [255, 256]. We perform Doppler-free saturated absorption spectroscopy on a lithium vapor cell described previously in [184], see Fig. 6.11. In Fig. 6.11a we show a sample scan over the full Doppler-broadened ^{6}Li D_1 line. The ground-state hyperfine structure is clearly resolved. We phase-modulate the probe beam at 20 MHz using an electro-optic modulator, and use a commercial lock-in amplifier to generate a dispersive error signal as presented in

Fig. 6.11b. We can access all D line transitions of both naturally abundant lithium isotopes, and the full ground state hyperfine structure is resolved.
The laser linewidth was estimated by slowly scanning the emission frequency over the D_1 line of ^{6}Li. From the observed peak-to-peak noise in the linear part of the error signal we obtain an upper limit of 1 MHz for the laser linewidth. For frequency-locking the laser, we feed the error signal in a home-made proportional-integral controller. The regulator signal is split internally in a low-frequency part, sent to the slow PZT (M_2) used for scanning the laser, and a high-frequency part, sent directly to a fast PZT glued between M_4 and its mount. The system can easily stay locked for a full day, even in presence of significant acoustic noise coupled to the optical table.

6.3.4. Conclusion

In this section we presented the design and the performance of an all-solid-state, intracavity-frequency-doubled single-mode laser source. The ring laser emits up to 2.5 W of unidirectional multifrequency radiation at the fundamental wavelength, and we determine the parameters necessary for efficient ICSHG. Starting from this well-characterized infrared system, the optimized ICSHG yields up to 2.1 W of single-mode, frequency-stabilized output at 671 nm. We discussed a simple theory describing the output power of an intra-cavity frequency-doubled laser. Within the region of efficient nonlinear conversion, the theory describes our experimental findings well. We furthermore presented a measurement of the emission spectrum of both the fundamental and the ICSHG source, displaying around 1.8 W of output power at the lithium D lines. By comparing both emission spectra, we maximally obtain 88% of the fundamental power at 671 nm, and typically more than 80%. This demonstrates a very efficient ICSHG process across the full emission spectrum. We observe nonlinear-Kerr-lens mode-locked operation when detuning the ppKTP temperature sufficiently far from the phase matching condition. Furthermore, we discussed the fine-tunability of the source by presenting Doppler-free saturated absorption spectra of all lithium D line transitions. The 671-nm output can be mode-hop-free scanned over more than 6 GHz, which corresponds to more than ten times the laser cavity free spectral range. As compared to the most powerful conventional design [184], our laser is an improvement by more than a factor of three in terms of output power. In comparison to commercial semiconductor tapered amplifier designs, we gain a factor of four in terms of output power and keep a beam quality close to the diffraction limit. Compared to vertical external cavity surface emitting laser (VECSELs) designs [260], our laser is five times more powerful together with a linewidth in the 100-kHz range.
The output power of our source is largely sufficient for creating all the laser beams needed for an ultracold atoms experiment. However, for other applications such as atom interferometry, even more power might be helpful and we will briefly discuss how this can possibly be established. An obvious way is to use a different cavity geometry allowing for two-sided pumping of the active medium. Convex pump couplers can compensate the thermal lens close to the laser crystal, which has proved very efficient in high-power resonators, see for instance [203].

A large part of the output power limitations stems from the additional intracavity elements, such as the Faraday rotator. Thus, injection locking of an amplifier consisting of an empty high-power resonator such as presented in [203] could deliver tens of watts of single-frequency fundamental light. At these elevated power levels, efficient single-pass frequency doubling of 1342-nm radiation has been demonstrated [261], the implementation of which considerably relaxes the complexity of multi-cavity designs.
When we started to use the laser for our experiment, we noticed that switching off the laser and turning it on again resulted in a reduced and arbitrary output power. Sometimes the laser would not even start lasing. The re-optimization was often time-consuming and inconvenient for a day-to-day use. We suspect that we operated the laser in a semi-stable regime, probably caused by a too large doping of the laser crystal. The instabilities could be also linked to the self suppression of mode hopping.

6.4. Waveguide

The necessity of frequency doubling increases the complexity of laser systems, for instance they often require additional enhancements cavities that need to be locked to resonance. Therefore, it is of great practical interest to technically simplify the frequency doubling process. In contrast to free-propagation schemes, guiding of optical fields has the intrinsic advantage of small mode field diameters along the guiding structure. Such, high-intensity fields can propagate over long distances in a medium without being limited by diffraction. This allows to increase the effects of interaction between light fields, external fields and fields provided by the medium by a large amount. Therefore, a number of waveguide-based devices has been developed and commercialized, reaching from fiber (Raman) lasers and waveguide EOMs to waveguide-based nonlinear-optics modules, most popular in the form of waveguide frequency doublers.
In this section, we present a SHG approach that yields 2.4 W frequency-doubled light using a custom-made ridge-waveguide PPLN wavelength conversion module. While being largely sufficient for running an atom cooling experiment, the light source features a strongly reduced complexity of the locking scheme.

6.4.1. Setup and characterization

The nonlinear device applied for second harmonic generation (SHG) in this experiment is a wavelength conversion module from NTT Electronics (WH-0671-000-A-B-C) that is described in detail in [262,263]. It contains a periodically poled ZnO-doped $LiNbO_3$ (ppZnO:LN) ridge waveguide with a nearly quadratic cross section of $14.8 \times 14.2\,\mu m^2$ and a length of $L = 10\,mm$. The chosen poling period of 13.2 µm provides quasi-phase-matching (QPM) for SHG at a fundamental wavelength of 1342 nm and at a waveguide temperature of approximately 49°C. It is temperature-stabilized using a built-in NTC thermistor and a thermoelectric cooling element together with a home-made regulator circuit. The entire module is mounted on a

passive heat sink and enclosed in a metal housing. The temperature of the waveguide crystal can therefore be stabilized to within 0.1°C.

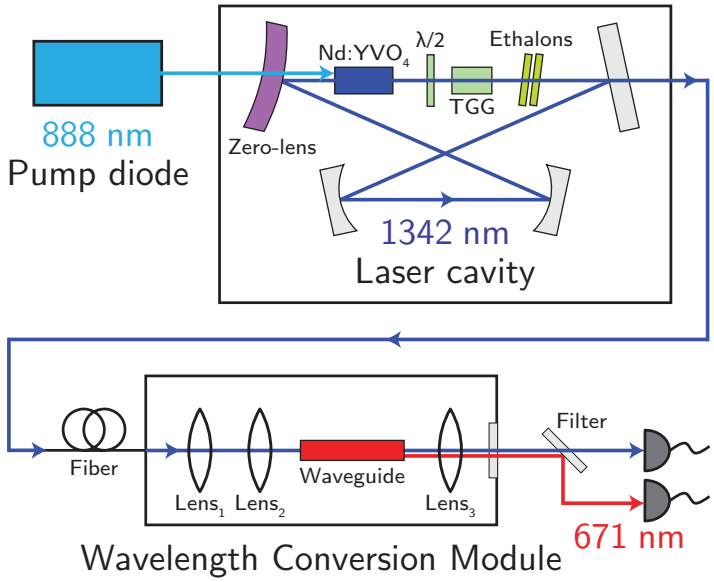

Figure 6.12: Schematic view of the frequency doubling setup. Shown are the IR laser cavity and the wavelength conversion module. The pump diode output is focused in the Nd:YVO4 laser crystal inside the laser cavity, which also contains a Faraday rotator and a $\lambda/2$-waveplate for unidirectional oscillation and two etalons for frequency selection. The wavelength conversion module includes a ppZnO:LN nonlinear waveguide for second-harmonic generation.

The experimental setup for frequency doubling is schematically presented in Figure 6.12. The waveguide module is fiber-pigtailed on the input side and includes collimating and focussing lenses ensuring efficient coupling between the fiber and the waveguide. The output light is collimated by a lens and passes through an AR-coated window (Edmund Optics P/N 47837) before exiting the waveguide module. We separate both second-harmonic and residual fundamental radiation using a dichroic beamsplitter set featuring a total transmission of 98.0% and 93.1% for the SH and IR light, respectively.

The coupling efficiency of the fundamental light to the fiber and through the ppZnO:LN crystal waveguide is measured by comparing the IR light power behind and in front of the module without SHG. For this purpose, the crystal mount temperature is set to 20°C which is sufficiently far detuned from the QPM temperature for the SHG process. Alternatively, the transmission at the extraordinary polarization can be directly determined by measuring the transmission at the ordinary polarization since both equal for our particular waveguide design. Taking into account the optical losses for the fundamental wavelength at the optical elements on the output of the waveguide module, the coupling efficiency could be determined to 78%. This value remains constant over the full available input power range.

Subsequently, the phase-matching curve of the waveguide was investigated by tuning the crystal mount temperature and monitoring the variation in SH power. Two tuning curves for different IR pump powers are presented in Figure 6.13. For a relatively low pump power of 1.07 W, the curve matches the theoretical sinc^2 distribution very well and the maximum SH

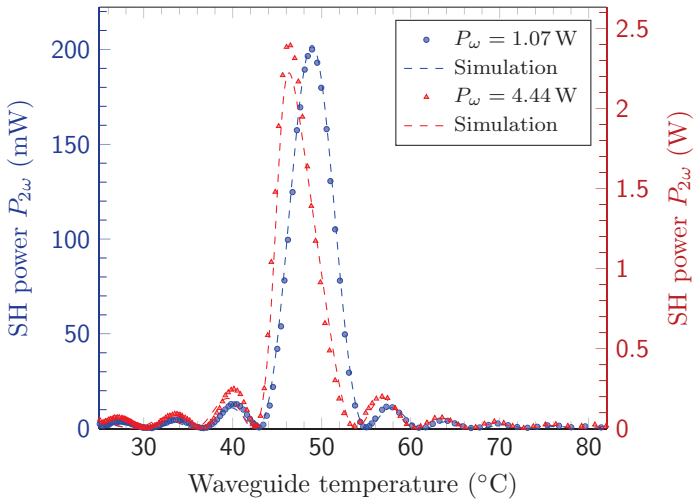

Figure 6.13: SH power as a function of the waveguide mount temperature T_{mount} at the fundamental IR pump power $P_\omega = 1.07\,\mathrm{W}$ and $P_\omega = 4.44\,\mathrm{W}$ coupled to the waveguide. Shown are the measured data points and the simulation results of our fitted model (dashed lines).

power of 200 mW is reached at a crystal mount temperature of 48.9°C. The measured curve is symmetric and has an acceptance width (FWHM) of $\Delta T = 5.4$°C. At elevated fundamental power levels, light absorption effects heat the waveguide and modify the phase-matching curve. This results in a shift of the conversion peak down to 46.4°C for the maximum pump power of 4.44 W and the corresponding SH power of 2.4 W. The shape of the main peak becomes slightly nonsymmetric and its height is lowered with respect to the side-peaks. The acceptance width is in this case only marginally reduced to $\Delta T = 4.8$°C. Since the shape for low conversion efficiency, and especially the zero-efficiency positions do not change, we attribute the observed thermal effects mainly to absorption of either the second-harmonic light, or to second-harmonic induced fundamental absorption.We note that even at the highest power levels present in the course of this section, thermal effects did not cause power instabilities or other types of output power limitations in our setup.

Figure 6.14 presents the adjusted crystal mount temperature maximizing the SH output power for a series of different IR pump power values. As we have already stated, the maximum SH power in the limit of low IR pump powers is reached for 48.9°C. While increasing IR pump power, the crystal mount temperature has to be gradually reduced and reaches its minimum value of 46.4°C at the maximum pump power of 4.44 W.

The SH output power characteristics of the waveguide were measured as a function of the coupled fundamental pump power, as shown in Figure 6.15. At high pump powers, the crystal mount temperature had to be adjusted at each IR pump power value in order to maximize the conversion, as discussed above. For small pump powers up to 400 mW, the experimental results are well fit by a parabola with a conversion efficiency of 18.4 %/W. For elevated fundamental power, pump depletion effects set in and the data points can be very well fit by the coupled waves theory presented in [264]. Fitting the well known lossless solution $\eta_{\mathrm{wg}} = \tanh^2\left[(\eta_0 \mathrm{P}_\omega \mathrm{L}^2)^{1/2}\right]$ to our experimental data yields the normalized efficiency

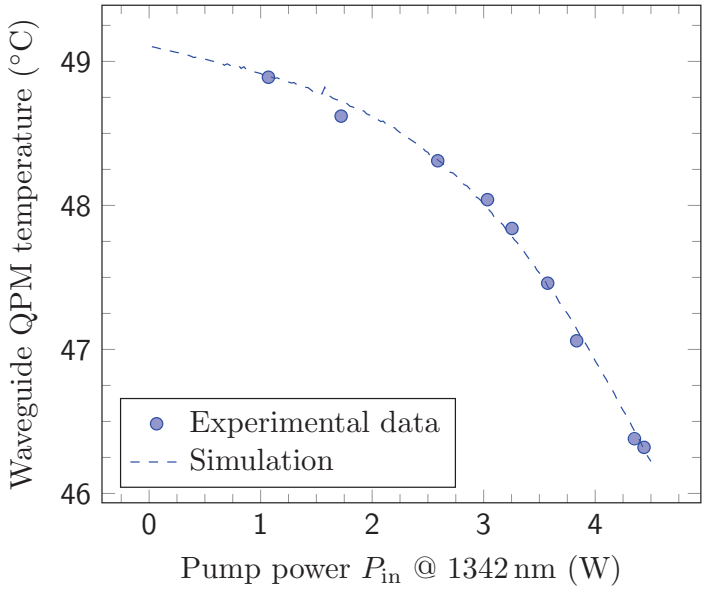

Figure 6.14: Optimal crystal mount temperature $T_{\mathrm{mount,opt}}$ during SHG process in dependence of the fundamental IR pump power P_ω coupled to the waveguide. The crystal mount temperature is adjusted for every pump power value in order to maximize the corresponding SH power.

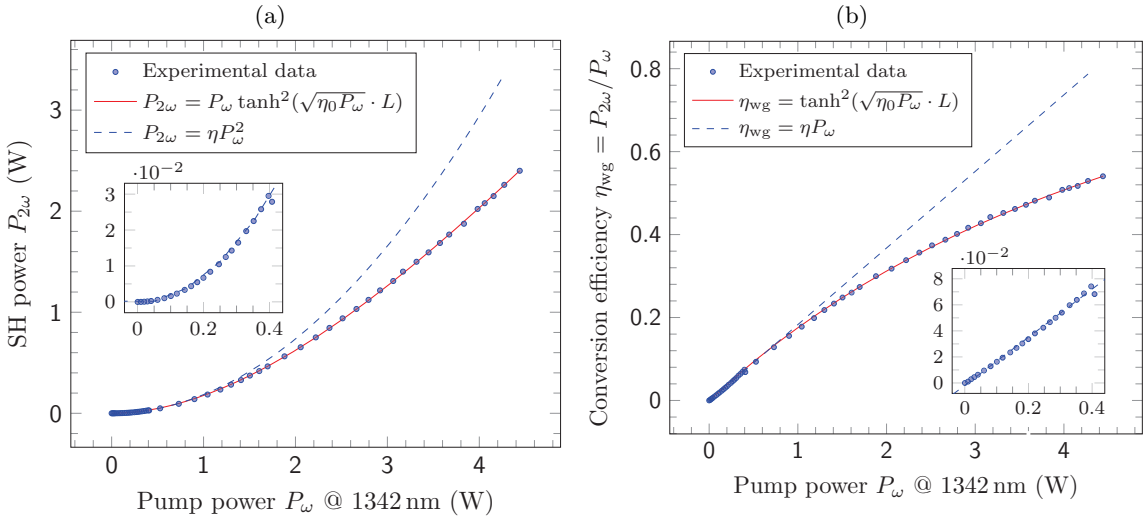

Figure 6.15: SH power output (a) and conversion efficiency (b) versus fundamental IR pump power coupled to the waveguide. The crystal mount temperature is adjusted for every pump power value as presented in Figure 6.14.

$\eta_0 = 19.9\,\%/\mathrm{Wcm}^2$. This underscores the very uncritical behavior of the SHG process we observe at these high powers, requiring only a small readjustment of the phase matching temperature.

A caustic measurement of the SH beam quality parameter yields a value of $M^2 \leq 1.1$ at the output of the ridge waveguide.

6.4.2. Theoretical model

We applied a simplified version of the theoretical model presented in [265] in order to simulate the SHG process and to describe quantitatively the influence of optical absorption on the phase-matching curve. In the following, the subscript index j denotes either the IR light for $j = 1$ or the SH light for $j = 2$.
We define the scalar value of the electric field amplitude according to [266] as

$$A_j = \left(2P_j / S_{\text{eff}} n_j \epsilon_0 c_0\right)^{1/2} , \tag{6.22}$$

where n_j is the refractive index, c_0 is the vacuum light velocity and ϵ_0 is the permittivity of free space. S_{eff} denotes the effective overlap area of the electric field distributions $E_j(y, z)$ of the fundamental TM modes of the waveguide [267]:

$$S_{\text{eff}} = \frac{\left(\iint \mathrm{dxdy}|\mathrm{E_1(y,z)}|^2\right)^2 \left(\iint \mathrm{dxdy}|\mathrm{E_2(y,z)}|^2\right)}{\left|\iint \mathrm{dxdy E_1(y,z)^2 E_2(y,z)^*}\right|^2} , \tag{6.23}$$

which is calculated with an open source mode solver software [268]. The scalar value of the electric field amplitude A_j is calculated by solving a system of coupled wave-equations that was derived in [224] and applied for waveguide simulation in [265]:

$$\frac{\mathrm{dA_0}}{\mathrm{dx}} = \Delta k_{QPM} - \left(2\sigma_1 A_2 - \sigma_2 \frac{A_1^2}{A_2}\right) \cos(\mathrm{A_0}) \tag{6.24}$$

$$\frac{\mathrm{dA_1}}{\mathrm{dx}} = -\sigma_1 A_1 A_2 \sin(\mathrm{A_0}) - \frac{1}{2}\left(\alpha_1 + \delta_{\text{GRIIRA}} \mathrm{A_2^4}\right) \mathrm{A_1} \tag{6.25}$$

$$\frac{\mathrm{dA_2}}{\mathrm{dx}} = \sigma_2 A_1^2 \sin(\mathrm{A_0}) - \frac{1}{2}\left(\alpha_2 + \delta_{\text{2Ph.}} \mathrm{A_2^2}\right) \mathrm{A_2} \tag{6.26}$$

with $A_0 = 2\phi_1 - \phi_2 + \Delta k_{\text{QPM}}$, $\sigma_1 = \omega_1 d_{\text{eff}} / c_0 n_1$, $\sigma_2 = \omega_1 d_{\text{eff}} / c_0 n_2$, where $d_{\text{eff}} = 2/\pi \cdot d_{33}$ is the effective nonlinear coefficient, ω_j is the wave frequency with $\omega_2 = 2\omega_1$, ϕ_j is the electric field phase, α_j is the linear absorption coefficient, $\delta_{\text{GRIIRA}} = \alpha_{\text{GRIIRA}}(n_2 \epsilon_0 c_0/2)^2$ and α_{GRIIRA} is the green induced infrared absorption coefficient [242, 269], $\delta_{\text{2Ph.}} = \beta_{\text{2Ph.}} n_2 \epsilon_0 c_0/2$ and $\beta_{\text{2Ph.}}$ is the two-photon absorption coefficient for the second-harmonic light [270]. Please note that we assume the linear losses in the ridge waveguide to equal the linear optical absorption.
The phase mismatch parameter is defined as

$$\Delta k_{\text{QPM}}(T) = 2\beta_1(T) - \beta_2(T) + \frac{2\pi}{\Lambda(T)} \tag{6.27}$$

with $\Lambda(T)$ the poling period, $\beta_j(T) = N_j(T)\omega_j/c_0$ the waveguide fundamental mode propagation constant and $N_j(T)$ the effective refractive index calculated with the effective index approximation [271]. This calculation uses the temperature dependent Sellmeier equations from [272] for the extraordinary refractive index n_j of 5% MgO-doped congruent PPLN. All of these parameters depend on the temperature T which may vary along the propagation

axis x due to heat generation resulting from optical absorption. Please note that we do not account for any inhomogeneity of the ridge waveguide height z_{R}, which is justified by the observation of a temperature dependent phase matching curve that matches the theoretical sinc^2 distribution very well at low intensities, see Figure 6.13.
The effect of the optical absorption on the temperature distribution along the waveguide axis x is estimated by supposing a one-dimensional, steady-state heat diffusion model [273], represented by a corresponding differential equation for the crystal temperature of the form

$$-k\frac{\partial^2}{\partial z^2}T(z) = \dot{q}(z) \tag{6.28}$$

with boundary conditions corresponding to our waveguide design

$$T(z=0) = T_{\mathrm{mount}} \tag{6.29}$$

$$\frac{\partial}{\partial z}T_(z=z_{\mathrm{H}}) = 0 \tag{6.30}$$

where $k = 5\,\mathrm{W/Km}$ is the heat conductivity of the lithium tantalate substrate [274], z is the vertical coordinate parallel to the crystal optical axis and $z_{\mathrm{H}} = 46.2\,\mu\mathrm{m}$ is the height of the entire waveguide structure.
The heat source density is defined as a boxcar function restricted to the ridge waveguide interval $z_{\mathrm{R}} = 14.2\mu\mathrm{m}$

$$\dot{q}(z) = \begin{cases} \dot{q}_{\mathrm{R}} \text{ for } \mathrm{z_H - z_R < z < z_H} \\ 0 \text{ otherwise.} \end{cases} \tag{6.31}$$

Applying the Green's function ansatz [275], the differential equation (6.28) can be solved for every x position along the propagation axis and the temperature in the center of the ridge waveguide

$$T\left(x, z_{\mathrm{H}} + \frac{z_{\mathrm{R}}}{2}\right) = \frac{\dot{q}_{\mathrm{R}}(x)}{k}\left[z_{\mathrm{H}} z_{\mathrm{R}} - \frac{5}{8}z_{\mathrm{R}}^2\right] + T_{\mathrm{mount}} \tag{6.32}$$

is assumed to be approximately the temperature $T(x)$ of the entire ridge waveguide. This result is applied in the system of coupled equations (6.24)-(6.27). The heat source density depends on the IR and SH intensities and is defined by [270]

$$\dot{q}_{\mathrm{R}}(x) = \left(\alpha_1 + \alpha_{\mathrm{GRIIRA}} I_2^2\right) I_1 + \left(\alpha_2 + \beta_{\mathrm{2Ph.}} I_2\right) I_2\,, \tag{6.33}$$

where $I_j = \left(n_j c_0 \epsilon_0/2\right) A_j^2$ is the light intensity.

In order to reproduce our experimental data concerning the shift of the optimal waveguide mount temperature with increasing fundamental IR pump power, as well as the conversion efficiency of the waveguide, we have to adapt the material dependent optical coefficients of our model. In particular, the values of the nonlinear optical coefficient d_{33} and the poling period Λ need to be set to $12.8\,\mathrm{pm/V}$ and $13.48\,\mu\mathrm{m}$, respectively. The linear optical absorption

coefficients α_1 and α_2, that are assumed to equal for simplification, are found to have a relatively low value of 0.09 l/m, compared to the literature value of 0.2 1/m for 1064 nm [276] and 1.0 1/m for 532 nm [277]. Additionally the two-photon absorption coefficient $\beta_{2\text{Ph.}}$ of 4.5×10^{-11} m/W has to be applied, corresponding well to the literature value of 5×10^{-11} m/W for 532 nm [270, 276]. In our case the intensity dependent GRIIRA coefficient α_{GRIIRA} [269] does not need to be taken into account in order to reproduce the experimental results. We attribute this to the fact that the intensities inside our waveguide remain well below 1 MW/cm^2 even for the highest applied IR pump powers. The results of our simulation, assuming these parameter settings, are presented in Figure 6.13 and Figure 6.14 together with the experimental data points.

6.5. Conclusion

This chapter described the design and the characterization of three different approaches performing efficient frequency doubling of the 1342 nm output beam delivered by the Nd:YVO_4 ring laser presented in Chapter 5. Each of them represents thus a feasible option for creating powerful 671 nm radiation.

After presenting the theoretical concepts necessary to understand second-harmonic generation using periodically-poled nonlinear media, we have described the technical design and the results of the conversion efficiency measurements on a resonant enhancement cavity containing a ppKTP crystal. We have measured a maximum conversion efficiency of 87%, and a maximum of 5.2 W of 671-nm output power. In a similar way we have reported on the setup and results of the intracavity doubled laser, yielding up to 2.1 W of second-harmonic output power. Finally we have detailed the performance and the theoretical description of our third approach for SHG, a wavelength conversion module employing a nonlinear waveguide structure of ppZnO:LN, delivering up to 2.4 W of frequency-double light at 671 nm. In this context, we could also infer information about the absorption processes occurring in the nonlinear medium.

Appendix 6.A Publications

Multiwatt-level second harmonic generation in ppZnO:LN ridge waveguide
N. Kretzschmar, F. Sievers, U. Eismann, F. Chevy and C. Salomon
To be published, see page 149 for a preliminary draft.

Multiwatt-level second harmonic generation in ppZnO:LN ridge waveguide

Norman Kretzschmar[1], Franz Sievers[1] Ulrich Eismann[2], Frédéric Chevy[1] and Christophe Salomon[1]

[1]*Laboratoire Kastler Brossel, ENS, UPMC, CNRS UMR 8552*
24 rue Lhomond, 75231 Paris, France
[2]*LNE-SYRTE, Observatoire de Paris, CNRS, UPMC,*
61 avenue de l'Observatoire, 75014 Paris, France
Norman.Kretzschmar@lkb.ens.fr

OCIS codes: (000.0000) General.

References and links

1. U. Eismann, F. Gerbier, C. Canalias, A. Zukauskas, G. Trénec, J. Vigué, F. Chevy, and C. Salomon, "An all-solid-state laser source at 671 nm for cold-atom experiments with lithium", Appl. Phys. B **106**, 25–36 (2012). 2, 4, 9, 10
2. U. Eismann and A. Bergschneider and F. Sievers and N. Kretzschmar and C. Salomon and F. Chevy, "2.1-watts intracavity-frequency-doubled all-solid-state light source at 671 nm for laser cooling of lithium,", Opt. Express **21**, 9091–9102 (2013). 2, 4
3. Nishida private comm. 2
4. L. McDonagh, R. Wallenstein, R. Knappe, and A. Nebel, "High-efficiency 60 W TEM_{00} Nd:YVO_4 oscillator pumped at 888 nm", Opt. Lett. **31**, 3297–3299 (2006). 4
5. D.S. Sumida, D.A. Rockwell, M.S. Mangir, "Energy storage and heating measurements in flashlamp-pumped Cr:Nd:GSGG and Nd:YAG", IEEE J. Quantum Electron. **24**, 985 (1988) 4
6. F. Lenhardt, M. Nittmann, T. Bauer, J. Bartschke, J.A. Lhuillier, "High-power 888-nm-pumped Nd:YVO_4 1342-nm oscillator operating in the TEM_{00} mode", Appl. Phys. B **96**, 803 (2009). 4
7. G. Trénec, W. Volondat, O. Cugat, and J. Vigué, "Permanent magnets for faraday rotators inspired by the design of the magic sphere," Appl. Opt. **50**, 4788–4797 (2011). 4
8. F. Lenhardt, A. Nebel, R. Knappe, M. Nittmann, J. Bartschke, and J. A. L'huillier, "Efficient single-pass second harmonic generation of a continuous wave Nd:YVO_4- laser at 1342 nm using MgO:ppLN", CLEO **2010**, CThEE5.
9. U. Eismann, "A novel all-solid-state laser source for lithium atoms and three-body recombination in the unitary Bose gas", Ph.D. thesis, Université Pierre et Marie Curie – Paris VI, http://tel.archives-ouvertes.fr/tel-00702865/ (2012).
10. Y. Nishida, H. Miyazawa, M. Asobe, O. Tadanaga, H. Suzuki, "Direct-bonded QPM-LN ridge waveguide with high damage resistance at room temperature", Electron. Lett. **39**(7), 609-610 (2003). 4
11. T. Nishikawa, A. Ozawa, Y. Nishida, M. Asobe, F. Hong, T. W. Hnsch, "Efficient 494 mW sum-frequency generation of sodium resonance radiation at 589 nm by using a periodically poled Zn:$LiNbO_3$ ridge waveguide", Opt. Express **17**, 17792–17800 (2009). 4
12. K. Parameswaran, J. Kurz, R. Roussev, M. Fejer, "Observation of 99% pump depletion in single-pass second-harmonic generation in a periodically poled lithium niobate waveguide", Opt. Lett. **27**, 43–45 (2002). 6
13. D. Jedrzejczyk, R. Güther, K. Paschke, G. Erbert, G. Tränkle, "Diode laser frequency doubling in a ppMgO:LN ridge waveguide: influence of structural imperfection, optical absorption and heat generation", Appl. Phys. B **109**, 33-42 (2012). 7, 8
14. S. Helmfrid, G. Arvidsson, "Influence of randomly varying domain lengths and nonuniform effective index on second-harmonic generation in quasi-phase-matching waveguides", J.Opt. Soc.Am.B **8**(4), 797-804 (1991). 7
15. F. Laurell, G. Arvidsson, "Frequency doubling in Ti:MgO:LiNbO3 channel waveguides", J.Opt. Soc.Am.B **5**(2), 292-299 (1988) 8
16. A. B. Fallahkhair, K. S. Li, T. E. Murphy, "Vector Finite Difference Modesolver for Anisotropic Dielectric Waveguides", J. Lightwave Technol. **26**(11), 1423–1431, (2008). 8
17. J. A. Armstrong, N. Bloembergen, J. Ducuing, P. S. Pershan, "Interactions between Light Waves in a Nonlinear Dielectric", Phys. Rev. **127**(6), 1918–1939 (1962) 8

18. R. G. Batchko, G. D. Miller, A. Alexandrovski, M. M. Fejer, R. L. Byer, “Limitations of high-power visible wavelength periodically poled lithium niobate devices due to green-induced infrared absorption and thermal lensing”, CLEO: Lasers and Electro-Optics, Technical Digest., 75–76 (1998) 8, 9
19. Y. Furukawa, K. Kitamura, A. Alexandrovski, R. K. Route, M. M. Fejer, G. Foulon, “Green-induced infrared absorption in MgO doped LiNbO3”, Appl. Phys. Lett. **78**(14), 1970-1972 (2001) 8
20. O. A. Louchev, N. E. Yu, S. Kurimura, K. Kitamura, “Thermal inhibition of high-power second-harmonic generation in periodically poled LiNbO3 and LiTaO 3 crystals”, Appl. Phys. Lett. **87**(13), 131101 (2005). 8, 9
21. K. Okamoto, “Fundamentals of Optical Waveguides”, Academic Press, San Diego (2000) 8
22. O. Gayer, Z. Sacks, E. Galun, A. Arie, “Temperature and wavelength dependent refractive index equations for MgO-doped congruent and stoichiometric LiNbO3”, Appl. Phys. B **91**, 343–348 (2008). 8
23. J. R. Cannon, “The One-Dimensional Heat Equation”, Cambridge University Press, Cambridge (1984) 8
24. D. Nikogosyan, “Nonlinear Optical Crystals: A Complete Survey”, Springer-Verlag, New York (2005) 8
25. K. D. Cole, J. V. Beck, A. Haji-Sheikh, B. Litkouhi, “Heat Conduction Using Green’s Functions”, 2nd edition, CRC Press (2010) 9
26. V. G. Dmitriev, G .G. Gurzadjan, D. N. Nikogosjan, “Handbook of nonlinear crystals”, 2nd edition, Springer, Berlin (1997) 9
27. J. R. Schwesyg, M. C. C. Kajiyama, M. Falk, D. H. Jundt, K. Buse, M. M. Fejer, “Light absorption in undoped congruent and magnesium-doped lithium niobate crystals in the visible wavelength range”, Appl. Phys. B **100**, 109-115 (2010) 9
28. E. Mimoun, L. De Sarlo, J. Zondy, J. Dalibard, F. Gerbier, “Sum-frequency generation of 589 nmlight with near-unit efficiency”, Opt. Express **16**, 18684–18691 (2008). 9
29. V. Mikhailov, O. Shaunin, I. Shcherbakov, V. Maslov, “Nonlinear absorption in KTP crystals”, Quant. Electr., **27**(4), 356-359 (1997). 9
30. B. Boulanger, I. Rousseau, J. P. Feve, M. Maglione, B. Menaert, G. Marnier, “Optical Studies of Laser-Induced Gray-Tracking in KTP”, IEEE J. Quant. Electr., **35**(3), 281–286 (1999). 10

1. Introduction

For atom cooling applications, simple, yet high-power, single-frequency cw laser sources are required. For addressing the lithium D-line atomic transitions near 671 nm, the choice of laser sources is limited. One reason is the relatively weak performance of semiconductor lasers at shorter wavelengths in the red part of the visible spectrum. Dye lasers, on the other hand, are expensive and difficult to handle. They also display a significant amount of fast frequency noise, requiring advanced frequency locking procedures. An alternative approach followed in our group is frequency doubling of infrared solid-state lasers, which offer high output power and intrinsic stability [1, 2]. However, the necessity of frequency doubling increases the complexity of such setups. Therefore, it is of great practical interest to technically simplify the frequency doubling process.

In contrast to free-propagation schemes, guiding of optical fields has the intrinsic advantage of small mode field diameters along the guiding structure. Such, high-intensity fields can propagate for long distances in a medium without being limited by diffraction. This allows one to increase the effects of interactions between light fields, external fields and fields provided by the medium by a large amount. Therefore, a number of waveguide-based devices have been developed and commercialized, reaching from fiber (Raman) lasers and waveguide EOMs to waveguide-based nonlinear-optics modules, most popular in the form of waveguide frequency doublers. Excellent properties have been demonstrated with the latter, ranging from very high nonlinear conversion efficiencies even at intermediate powers to frequency and phase stability down to state-of-the-art metrology levels. Maximum output powers of 1.6 W at 532 nm have been reported in [3].

In this article, we present a frequency-doubled laser system operating in the vicinity of the lithium D-line resonances. Starting from a record-level single-frequency output power of 6.5 W at 1342 nm, we obtain 2.3 W frequency-doubled light using a custom-made ridge-waveguide PPLN frequency doubling module. While being largely sufficient for running an atom cooling experiment, the light source features a strongly reduced complexity of the locking scheme. This compares favourably to a two-cavity setup similar to the one presented in [1], where the 671 nm

output power is increased to 5.2 W.

2. Fundamental laser setup and characteristics

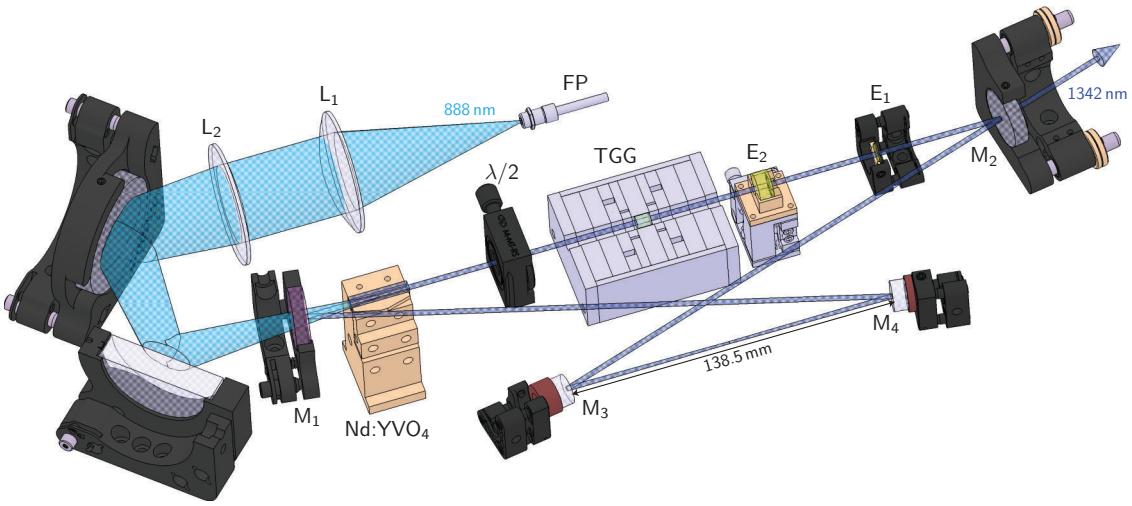

Fig. 1. (Color online) Setup of the 1342 nm laser source. Two lenses, L_1 and L_2, image the output of the pump source, a fiber-coupled diode laser bar (FP), into the Nd:YVO_4 gain medium. The ring resonator consist of four mirrors M_{1-4} in bow-tie configuration, which are all highly reflective at 1342 nm except M_2 serving as partly transmitting output coupling mirror. A Faraday rotator (TGG) in combination with a half-wave plate ($\lambda/2$) enforces unidirectional operation. Insertion of two etalons E_{1-2} allows for single-longitudinal-mode behavior and wavelength tunability.

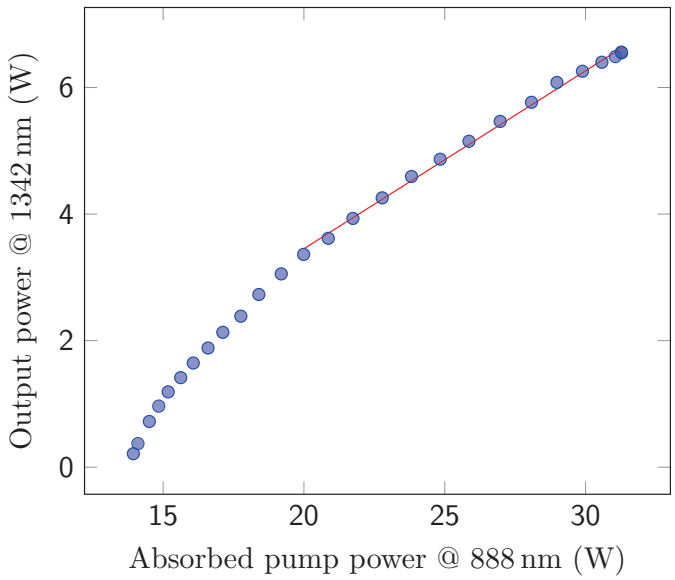

Fig. 2. (Color online) Single-frequency laser output power of the laser (dots) as a function of the absorbed pump power. The setup is optimized for the maximal absorbed pump power $P_{\mathrm{abs,max}} = 31.3\,\mathrm{W}$ resulting in a maximum output power of $P_{\mathrm{out}} = 6.56\,\mathrm{W}$. The oscillation threshold is found at $P_{\mathrm{abs}} = 13.9\,\mathrm{W}$. A linear fit (red line) for $P_{\mathrm{abs}} > 20\,\mathrm{W}$ yields a slope efficiency of $\eta_{\mathrm{sl}} = 28.1\%$ in the high-power regime.

The fundamental light source we use throughout this article is a modified version of the laser presented in [1]. The following improvements have been implemented in order to minimize and compensate for thermal effects inside the laser gain medium:

Firstly, as in [2], we use pump light at 888 nm instead of 808 nm. This lowers the quantum defect per lasing cycle of the active ions by 15%, thus reducing the heat load deposited in the laser crystal [4]. Moreover the lower absorption coefficient at 888 nm allows to spread the thermal load over a longer crystal and a larger pump volume, therefore reducing the heat density and minimizing stress and thermal lensing in the gain medium.

Secondly, the flat pump coupling mirror was replaced by a convex meniscus mirror supposed to compensate for the thermal lens of the Nd:YVO_4 crystal. Its radius of curvature of $r_c = 500$ mm was chosen in accordance with the measured focal length of $f = 170$ mm of the thermal lens under lasing conditions [5, 6].

Figure 1 shows the experimental setup of the optimized oscillator operating at 1342 nm. The 888 nm output of the temperature-stabilized fiber-coupled QPC BrightLase Ultra-50 diode stack (NA = 0.22, 400 µm fiber core diameter), emitting up to 42.6 W at 888 nm (Spectral width (FWHM): 2.2 nm), is focused by two lenses ($f_1 = 75$ mm, $f_2 = 175$ mm) to a top-hat profile of radius $w_{\text{pump}} = 970$ µm inside the laser crystal. The dimensions of the actively cooled Nd:YVO_4 crystal (a-cut, anti-reflection coated for 1342 nm and 888 nm) were chosen to be $4 \times 4 \times 25\,\text{mm}^3$ and the ion doping was accordingly adjusted to 0.5 at. %. The cavity consists of three curved mirrors (M_1, M_3 and M_4) and one flat mirror (M_2), forming a bow-tie cavity. The pump coupling mirror M_1 is, as mentioned above, a convex meniscus mirror with a radius of curvature of $r_c = 500$ whereas M_3 and M_4 are concave mirrors with a radius of curvature of 100 mm and 150 mm, respectively. M_1, M_3 and M_4 are highly reflective coated for 1342 nm, and M_1 is furthermore transmitting at 888 nm. The optimal transmittance of the output coupler M_2 regarding the maximum output power was found to be 7.5%. Unidirectional operation of the ring laser is enforced by a Faraday rotator consisting of a cylindrical terbium-gallium-garnet crystal (TGG) of 6 mm length placed in a strong permanent magnet [7] in combination with a true-zero-order half-wave plate. Two uncoated infrared fused etalons of 500 µm and 4 mm thickness are used in order to assure single frequency behavior and tunability of the wavelength.

Figure 2 shows the output power of the laser as a function of the absorbed pump power for an increasing pump power. The lasing threshold was found at an absorbed pump power $P_{\text{abs}} = 13.9$ W and the power rises linearly above $P_{\text{abs}} = 20$ W with a slope efficiency of $\eta_{\text{sl}} = \mathrm{d}P_{\text{out}}/\mathrm{d}P_{\text{abs}} = 28.1\%$. A maximum output power of $P_{\text{out}} = 6.56$ W was reached for an absorbed pump power of $P_{\text{abs,max}} = 31.3$ W, which is the maximum the pump can deliver. This resulted in an optical-to-optical conversion efficiency of 16.3%. As can be seen in Figure 2, the fundamental output power is not limited by thermal roll-off. Therefore, with more available pump power, we expect to see a further significant increase in single-mode fundamental power.

The beam quality parameter of the IR output beam is determined through a caustic measurement and results in a value of $M^2 \leq 1.2$.

3. Waveguide second-harmonic generation

The nonlinear device applied for second harmonic generation (SHG) in this experiment is a wavelength conversion module from NTT Electronics (WH-0671-000-A-B-C) that is described in detail in [10, 11]. It contains a periodically poled ZnO-doped $LiNbO_3$ (ppZnO:LN) ridge waveguide with a nearly quadratic cross section of $14.8 \times 14.2\,\mu\text{m}^2$ and a length of L = 10 mm. The chosen poling period of 13.2 µm provides quasi-phase-matching (QPM) for SHG at a fundamental wavelength of 1342 nm and at a waveguide temperature of approximately 49°C. It is temperature-stabilized using a built-in NTC thermistor and a thermoelectric cooling element together with a commercial regulator circuit. The entire module is mounted on a passive heat

sink and enclosed in a metal housing. The temperature of the waveguide crystal can therefore be stabilized to within 0.1°C.

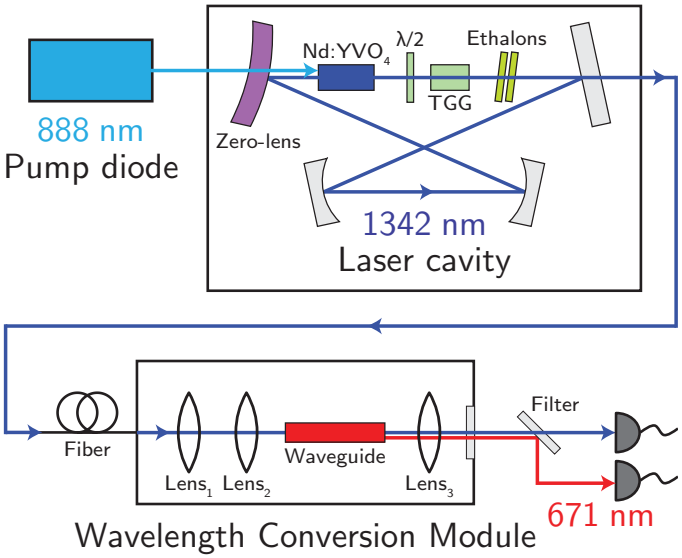

Fig. 3. (Color online) Schematic view of the frequency doubling setup. Shown are the IR laser cavity and the wavelength conversion module. The pump diode output is focused in the Nd:YVO4 laser crystal inside the laser cavity, which also contains a Faraday rotator and a $\lambda/2$-waveplate for unidirectional oscillation and two etalons for frequency selection. The wavelength conversion module includes a ppZnO:LN nonlinear waveguide for second-harmonic generation.

The experimental setup for frequency doubling is schematically presented in Figure 3. The waveguide module is fiber-pigtailed on the input side and includes collimating and focussing lenses ensuring efficient coupling between the fiber and the waveguide. The output light is collimated by a lens and passes through an AR-coated window (Edmund Optics P/N 47837) before exiting the waveguide module. We separate both second-harmonic and residual fundamental radiation using a dichroic beamsplitter set featuring a total transmission of 98.0% and 93.1% for the SH and IR light, respectively.

The coupling efficiency of the fundamental light to the fiber and through the ppZnO:LN crystal waveguide is measured by comparing the IR light power behind and in front of the module without SHG. For this purpose, the crystal mount temperature is set to 20°C which is sufficiently far detuned from the QPM temperature for the SHG process. Alternatively, the transmission at the extraordinary polarization can be directly determined by measuring the transmission at the ordinary polarization since both equal for our particular waveguide design. Taking into account the optical losses for the fundamental wavelength at the optical elements on the output of the waveguide module, the coupling efficiency could be determined to 78%. This value remains constant over the full available input power range.

Subsequently, the phase-matching curve of the waveguide was investigated by tuning the crystal mount temperature and monitoring the variation in SH power. Two tuning curves for different IR pump powers are presented in Figure 4. For a relatively low pump power of 1.07 W, the curve matches the theoretical sinc^2 distribution very well and the maximum SH power of 200 mW is reached at a crystal mount temperature of 48.9°C. The measured curve is symmetric and has an acceptance width (FWHM) of $\Delta T = 5.4$°C. At elevated fundamental power levels, light absorption effects heat the waveguide and modify the phase-matching curve. This results in a shift of the conversion peak down to 46.4°C for the maximum pump power of 4.44 W and

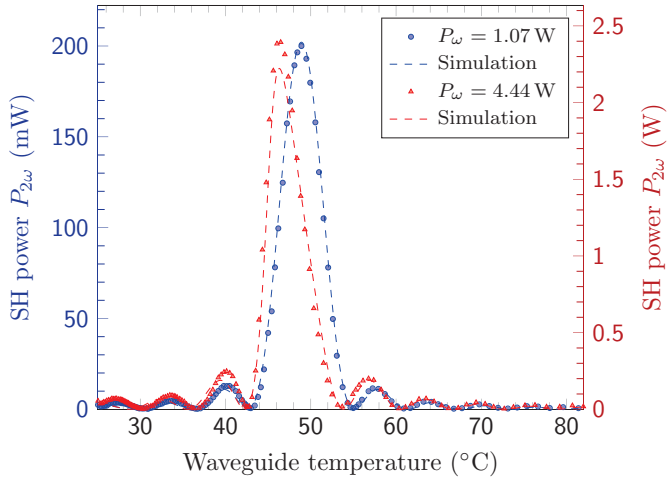

Fig. 4. (Color online) SH power as a function of the waveguide mount temperature T_{mount} at the fundamental IR pump power $P_\omega = 1.07\,\mathrm{W}$ and $P_\omega = 4.44\,\mathrm{W}$ coupled to the waveguide. Shown are the measured data points and the simulation results of our fitted model (dashed lines).

the corresponding SH power of 2.4 W. The shape of the main peak becomes slightly nonsymmetric and its height is lowered with respect to the side-peaks. The acceptance width is in this case only marginally reduced to $\Delta T = 4.8°\mathrm{C}$. Since the shape for low conversion efficiency, and especially the zero-efficiency positions do not change, we attribute the observed thermal effects mainly to absorption of either the second-harmonic light, or to second-harmonic induced fundamental absorption.We note that even at the highest power levels present in the course of this article, thermal effects did not cause power instabilities or other types of output power limitations in our setup.

Figure 5 presents the adjusted crystal mount temperature maximizing the SH output power for a series of different IR pump power values. As we have already stated, the maximum SH power in the limit of low IR pump powers is reached for 48.9°C. While increasing IR pump power, the crystal mount temperature has to be gradually reduced and reaches its minimum value of 46.4°C at the maximum pump power of 4.44 W.

The SH output power characteristics of the waveguide were measured as a function of the coupled fundamental pump power, as shown in Figure 6. At high pump powers, the crystal mount temperature had to be adjusted at each IR pump power value in order to maximize the conversion, as discussed above. For small pump powers up to 400 mW, the experimental results are well fit by a parabola with a conversion efficiency of 18.4 %/W. For elevated fundamental power, pump depletion effects set in and the data points can be very well fit by the coupled waves theory presented in [12]. Fitting the well known lossless solution $\eta_{\mathrm{wg}} = \tanh^2\left[(\eta_0 \mathrm{P}_\omega \mathrm{L}^2)^{1/2}\right]$ to our experimental data yields the normalized efficiency $\eta_0 = 19.9\,\%/\mathrm{Wcm}^2$. This underscores the very uncritical behavior of the SHG process we observe at these high powers, requiring only a small readjustment of the phase matching temperature.

A caustic measurement of the SH beam quality parameter yields a value of $M^2 \leq 1.1$ at the output of the ridge waveguide.

4. Theoretical model

We applied a simplified version of the theoretical model presented in [13] in order to simulate the SHG process and to describe quantitatively the influence of optical absorption on the phase-matching curve. In the following, the subscript index j denotes either the IR light for $j = 1$ or the SH light for $j = 2$.

We define the scalar value of the electric field amplitude according to [14] as $A_j = (2P_j/S_{\text{eff}} n_j \varepsilon_0 c_0)^{1/2}$, where n_j is the refractive index, c_0 is the vacuum light velocity and ε_0

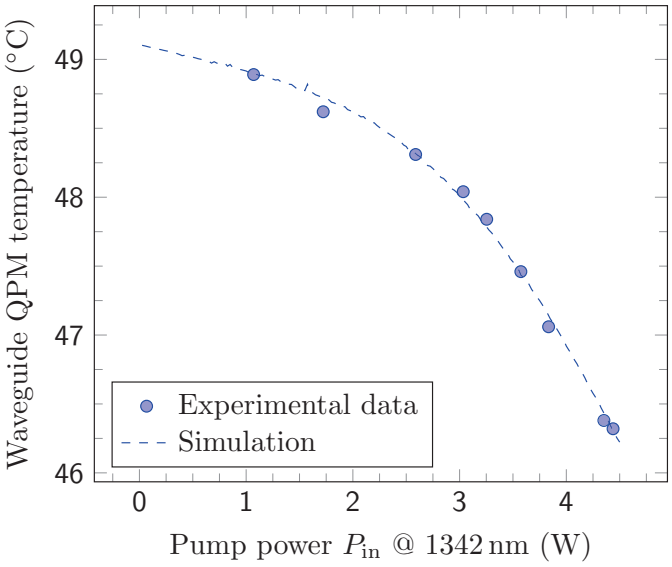

Fig. 5. (Color online) Optimal crystal mount temperature $T_{\text{mount,opt}}$ during SHG process in dependence of the fundamental IR pump power P_ω coupled to the waveguide. The crystal mount temperature is adjusted for every pump power value in order to maximize the corresponding SH power.

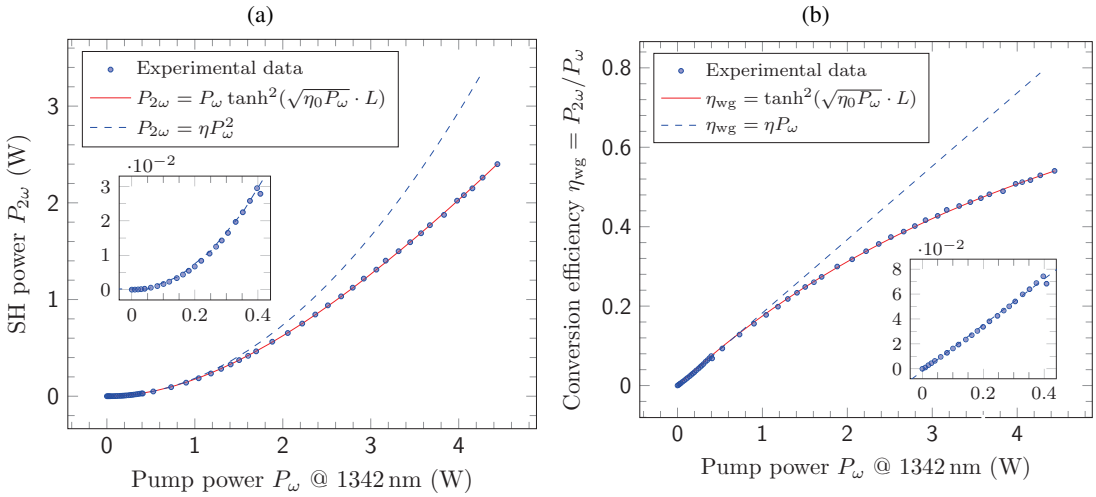

Fig. 6. SH power output (a) and conversion efficiency (b) versus fundamental IR pump power coupled to the waveguide. The crystal mount temperature is adjusted for every pump power value as presented in Figure 5.

is the permittivity of free space. S_{eff} denotes the effective overlap area of the electric field distributions $E_j(y,z)$ of the fundamental TM modes of the waveguide [15]:

$$S_{\text{eff}} = \frac{\left(\iint \mathrm{dxdy}|\mathrm{E_1(y,z)}|^2\right)^2 \left(\iint \mathrm{dxdy}|\mathrm{E_2(y,z)}|^2\right)}{\left|\iint \mathrm{dxdyE_1(y,z)^2E_2(y,z)^*}\right|^2}, \tag{1}$$

which is calculated with an open source mode solver software [16]. The scalar value of the electric field amplitude A_j is calculated by solving a system of coupled wave-equations that was derived in [17] and applied for waveguide simulation in [13]:

$$\frac{\mathrm{dA_0}}{\mathrm{dx}} = \Delta k_{QPM} - \left(2\sigma_1 A_2 - \sigma_2 \frac{A_1^2}{A_2}\right)\cos(\mathrm{A_0}) \tag{2}$$

$$\frac{\mathrm{dA_1}}{\mathrm{dx}} = -\sigma_1 A_1 A_2 \sin(\mathrm{A_0}) - \frac{1}{2}\left(\alpha_1 + \delta_{\text{GRIIRA}}\mathrm{A_2^4}\right)\mathrm{A_1} \tag{3}$$

$$\frac{\mathrm{dA_2}}{\mathrm{dx}} = \sigma_2 A_1^2 \sin(\mathrm{A_0}) - \frac{1}{2}\left(\alpha_2 + \delta_{\text{2Ph.}}\mathrm{A_2^2}\right)\mathrm{A_2} \tag{4}$$

with $A_0 = 2\phi_1 - \phi_2 + \Delta k_{\text{QPM}}$, $\sigma_1 = \omega_1 d_{\text{eff}}/c_0 n_1$, $\sigma_2 = \omega_1 d_{\text{eff}}/c_0 n_2$, where $d_{\text{eff}} = 2/\pi \cdot d_{33}$ is the effective nonlinear coefficient, ω_j is the wave frequency with $\omega_2 = 2\omega_1$, ϕ_j is the electric field phase, α_j is the linear absorption coefficient, $\delta_{\text{GRIIRA}} = \alpha_{\text{GRIIRA}}(n_2\varepsilon_0 c_0/2)^2$ and α_{GRIIRA} is the green induced infrared absorption coefficient [18, 19], $\delta_{\text{2Ph.}} = \beta_{\text{2Ph.}} n_2 \varepsilon_0 c_0/2$ and $\beta_{\text{2Ph.}}$ is the two-photon absorption coefficient for the second-harmonic light [20]. Please note that we assume the linear losses in the ridge waveguide to equal the linear optical absorption.

The phase mismatch parameter is defined as

$$\Delta k_{\text{QPM}}(T) = 2\beta_1(T) - \beta_2(T) + \frac{2\pi}{\Lambda(T)} \tag{5}$$

with $\Lambda(T)$ the poling period, $\beta_j(T) = N_j(T)\omega_j/c_0$ the waveguide fundamental mode propagation constant and $N_j(T)$ the effective refractive index calculated with the effective index approximation [21]. This calculation uses the temperature dependent Sellmeier equations from [22] for the extraordinary refractive index n_j of 5% MgO-doped congruent PPLN. All of these parameters depend on the temperature T which may vary along the propagation axis x due to heat generation resulting from optical absorption. Please note that we do not account for any inhomogeneity of the ridge waveguide height z_{R}, which is justified by the observation of a temperature dependent phase matching curve that matches the theoretical sinc^2 distribution very well at low intensities, see Figure 4.

The effect of the optical absorption on the temperature distribution along the waveguide axis x is estimated by supposing a one-dimensional, steady-state heat diffusion model [23], represented by a corresponding differential equation for the crystal temperature of the form

$$-k\frac{\partial^2}{\partial z^2}T(z) = \dot{q}(z) \tag{6}$$

with boundary conditions corresponding to our waveguide design

$$T(z=0) = T_{\text{mount}} \tag{7}$$

$$\frac{\partial}{\partial z}T_{(}z = z_{\text{H}}) = 0 \tag{8}$$

where $k = 5\,\mathrm{W/Km}$ is the heat conductivity of the lithium tantalate substrate [24], z is the vertical coordinate parallel to the crystal optical axis and $z_{\text{H}} = 46.2\,\mu\mathrm{m}$ is the height of the entire waveguide structure.

The heat source density is defined as a boxcar function restricted to the ridge waveguide interval $z_R = 14.2\mu m$

$$\dot{q}(z) = \begin{cases} \dot{q}_R \text{ for } z_H - z_R < z < z_H \\ 0 \text{ otherwise.} \end{cases} \tag{9}$$

Applying the Green's function ansatz [25], the differential equation (6) can be solved for every x position along the propagation axis and the temperature in the center of the ridge waveguide

$$T\left(x, z_H + \frac{z_R}{2}\right) = \frac{\dot{q}_R(x)}{k}\left[z_H z_R - \frac{5}{8}z_R^2\right] + T_{mount} \tag{10}$$

is assumed to be approximately the temperature $T(x)$ of the entire ridge waveguide. This result is applied in the system of coupled equations (2)-(5). The heat source density depends on the IR and SH intensities and is defined by [20]

$$\dot{q}_R(x) = \left(\alpha_1 + \alpha_{GRIIRA} I_2^2\right) I_1 + \left(\alpha_2 + \beta_{2Ph.} I_2\right) I_2 \,, \tag{11}$$

where $I_j = (n_j c_0 \varepsilon_0/2) A_j^2$ is the light intensity.

In order to reproduce our experimental data concerning the shift of the optimal waveguide mount temperature with increasing fundamental IR pump power, as well as the conversion efficiency of the waveguide, we have to adapt the material dependent optical coefficients of our model. In particular, the values of the nonlinear optical coefficient d_{33} and the poling period Λ need to be set to 12.8 pm/V and 13.48 μm, respectively. The linear optical absorption coefficients α_1 and α_2, that are assumed to equal for simplification, are found to have a relatively low value of 0.09 l/m, compared to the literature value of 0.2 1/m for 1064 nm [26] and 1.0 1/m for 532 nm [27]. Additionally the two-photon absorption coefficient $\beta_{2Ph.}$ of 4.5×10^{-11} m/W has to be applied, corresponding well to the literature value of 5×10^{-11} m/W for 532 nm [20, 26]. In our case the intensity dependent GRIIRA coefficient α_{GRIIRA} [18] does not need to be taken into account in order to reproduce the experimental results. We attribute this to the fact that the intensities inside our waveguide remain well below $1\,MW/cm^2$ even for the highest applied IR pump powers. The results of our simulation, assuming these parameter settings, are presented in Figure 4 and Figure 5 together with the experimental data points.

5. Comparison to SHG in an enhancement cavity

An alternative method for efficient frequency doubling of infrared lasers is to use periodically-poled nonlinear crystals in an external enhancement cavity. Even though this approach is technically more complex than waveguide doubling, due to the requirement of a second cavity, we intended to compare its performance to the results of the waveguide conversion module.

The doubling cavity setup has a similar design as the ones presented in [1, 28] and is illustrated in Figure 7. As for the laser, a four-mirror folded ring-cavity is employed. The fundamental light is coupled through the plane mirror M_1' with reflectivity $R_c = 90\%$ optimizing the cavity impedance matching. All other mirrors are highly reflective at 1342 nm and M_4' is transmitting at 671 nm. M_2' (M_3') is attached to a fast (slow) piezoelectric transducers, allowing to act on the cavity length in the 50 nm (8 μm) range. M_3' and M_4' are concave with a radius of curvature $r_c = 150$ mm and $r_c = 100$ mm, respectively. Their distance M_3'–M_4' is 156 mm. The nonlinear crystal is placed in the corresponding focus with waist $w_0 \simeq 79\,\mu m$. The relatively large waist inside the crystal was chosen in order to reduce intensity-related detrimental effects such as two-photon and second-harmonic-induced absorption [29] and gray-tracking

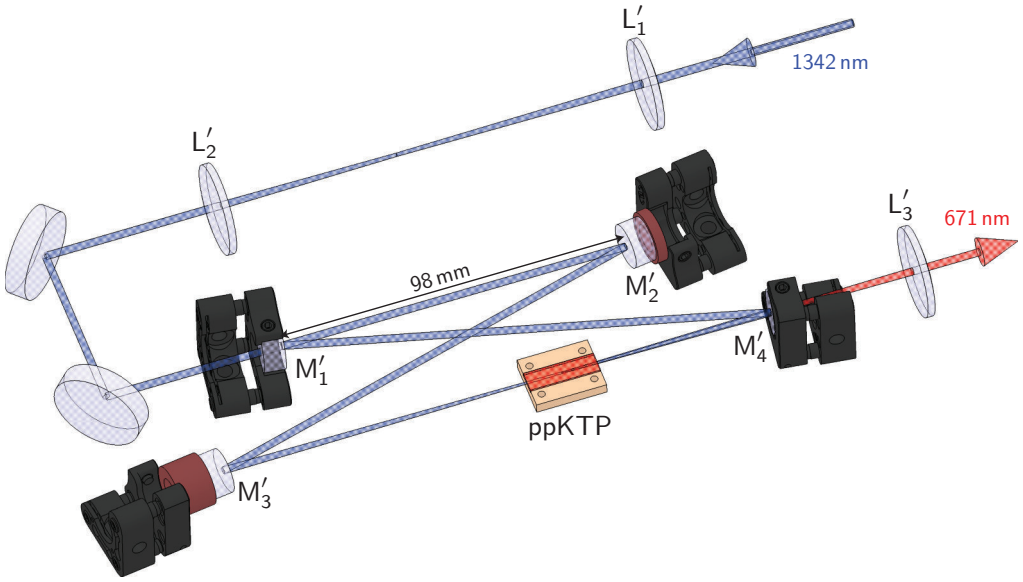

Fig. 7. (Color online) Scheme of the doubling cavity setup comprising the four mirrors M'_{1-4} and the ppKTP nonlinear crystal. The light is coupled to the Gaussian cavity eigenmode using lenses $L'_{1,2}$, whereas L'_3 collimates the SH output. The crystal mount is depicted sectioned to improve visibility and the IR (SH) beam is illustrated in blue (red). The distance M'_3–M'_4 is 156 mm.

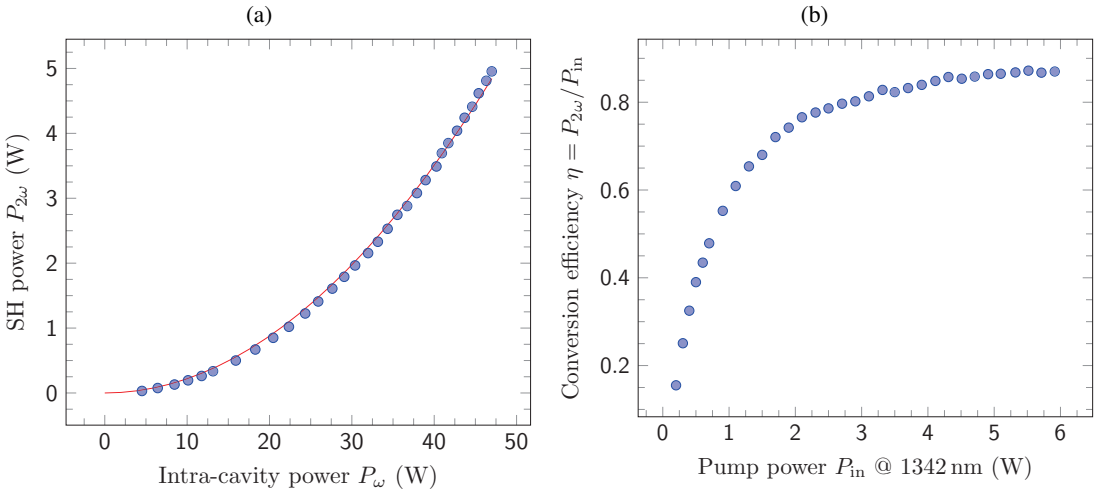

Fig. 8. Measurement of the cavity doubling efficiency, where points are measured data and lines are fits. (a) The second harmonic output power as a function of the fundamental intracavity power. As expected a quadratic function can be fitted to the conversion. (b) The cavity conversion efficiency as a function of the fundamental input power.

[30]. Mode matching between the laser output and the cavity is accomplished using a set of spherical lenses, yielding a mode coupling efficiency of 95%. The frequency doubled light is transmitted through M'_4 and collimated to a $1/e^2$ beam radius of 1.2 mm.

After frequency-locking the cavity to the laser, as described in [1], the SH power $P_{2\omega}$ was measured as a function of the intra-cavity IR power P_ω, see Figure 8(a). As expected, the conversion shows quadratic behavior and fitting yields a single-pass conversion efficiency of

$\eta_{sp} = 0.22\,\%/\mathrm{W}$. The SH output power follows a variation of the intra-cavity fundamental power without observable hysteresis. Moreover, no long-term degradation was observed, indicating the absence of gray-tracking, even for the highest reachable fundamental pump powers in our setup. The maximal SH output power $P_{2\omega} = 5.15\,\mathrm{W}$ is reached for a IR pump power of $P_{in} = 5.91\,\mathrm{W}$, corresponding to a doubling efficiency of $\eta_{conv} = 87\%$, as can be seen in Figure 8(b).

General conclusion and outlook

This thesis presented the development of an experimental apparatus, designed to create degenerate Fermi-Fermi gas mixtures of lithium and potassium. As of this writing, it is already capable to produce a deeply degenerate Fermi gas of ^{40}K with relatively large atom numbers.

At the beginning of my thesis, the Fermix-machine had already been realized to some extent. The dual-species MOT was operational and produced large atomic samples with several 10^9 atoms of both ^{6}Li and ^{40}K at the same time. Moreover, the first magnetic transport sequences were successfully tested. Nevertheless the progress of the experiment was impeded at the time of my arrival, which was mainly due to two problems. First of all, the moderate vacuum quality in the science cell prevented the evaporation dynamics from being efficient enough to reach quantum degeneracy. Secondly, the transport efficiency in terms of atom numbers was still below 50% and the temperatures of the atomic samples in the science cell were too high for initiating an efficient evaporation. A further drawback was the rudimentary control software of the experiment which was not appropriate for operating complex sequences and did not feature automatic parameter list runs.

We started to solve these issues by first replacing the old control software by the Cicero Word Generator software package. This control software particularly designed for atomic physics experiment offers the possibility to handle complicated sequences easily, to scan parameter settings automatically during long list runs and to control the experiment remotely. Being an accurately programmed open source project, the program could easily be adapted to our particular requirements, for example by implementing the control over the magnetic transport power supplies or the RF synthesizers. Experimental data acquisition thus became more efficient and flexible.

Subsequently, we replaced all parts of the vacuum assembly in the transport region by a redesigned setup. Additional ion pumps were installed close to the science cell and the inner walls of the new vacuum parts were coated with an active getter material provided by the CERN. This enhanced the vacuum lifetime in the science-cell from less than 25 s to over 100 s. In order to reach such a long lifetime we had also to take precautions against stray-light from the laser tables.

In order to increase the transport efficiency we were in need for a reduced initial transport temperature. Therefore, we implemented a D_1 sub-Doppler cooling scheme for ^{40}K that was theoretically proposed by Saijun Wu. The D_1 molasses phase cools the ^{40}K atoms in few milliseconds to deep sub-Doppler temperatures, while preserving the large atom numbers of

the MOT. Together with the preceding CMOT phase, which enhances the atomic density by a factor of five, this technique yields a gain in phase space density of about three orders of magnitude.

As a result, the initial and final transport temperatures were reduced considerably and the transport efficiency raised from 50% to 80% for ^{40}K. First, we intended to cool the hot ^{6}Li atoms by letting them thermalize with the cold ^{40}K cloud. However, the large temperature difference between the ^{40}K and ^{6}Li samples after the D_1 molasses phase led to a disadvantageous situation. Due to the small spatial overlap of the two clouds in the magnetic trap both species did not thermalize on reasonable time scales. Therefore, we decided to implement the D_1 molasses cooling scheme also for ^{6}Li.

For the purpose of additional laser cooling of lithium, we developed a novel all-solid state laser source emitting up to 5.2 W of output power close to the lithium D-line transitions at 671 nm. One key ingredient of our new high-power design is an improved heat management in the Nd:YVO_4 gain medium by using the 888 nm pumping transition instead of the common wavelength of 808 nm. Furthermore we tested three different approaches to perform second-harmonic generation, all of them reaching considerably high power outputs: 5.2 W with an enhancement cavity containing a ppKTP crystal, 2.1 W via intracavity doubling, and 2.4 W with a nonlinear waveguide structure, this SHG method being particularly simple to implement. For all three techniques, the laser source has furthermore a transversal mode quality factor of $M^2 \sim 1$, operates longitudinally single-mode and has a narrow linewidth smaller than 200 kHz. Hence, it can serve as a master high-power laser source for cold atoms experiments involving lithium isotopes. Also other applications are imaginable, for example in atom interferometry, for lithium isotope separation, or as pump for Cr:LiSAF lasers featuring low intensity noise.

The simultaneous sub-Doppler cooling for ^{40}K and ^{6}Li proved to yield phase space densities of $\sim 10^{-4}$ for both ^{40}K and ^{6}Li. As a result, the atomic samples in the optically plugged magnetic quadrupole trap were sufficiently dense to provide high elastic collision rates and allowed for efficient evaporative cooling to quantum degeneracy.

Our new sub-Doppler cooling scheme is applicable to all alkali atoms. To date, several other research groups have implemented our D_1 cooling scheme to improve the performance of their experiments working with ^{6}Li [166], ^{7}Li [167] [3] and ^{39}K [168–170]. In addition, this scheme might allow for the implementation of single-atom resolved imaging of fermions in a pinning lattice, as was shown by the group of Stefan Kuhr in Glasgow working with ^{40}K ([171] and private communication). In the case of ^{6}Li, this would enable quantum simulation of lattice fermions in a regime with rapid matter wave dynamics, which is inaccessible by heavy atoms.

In a next step, we constructed and characterized all technical components, necessary for evaporative cooling to quantum degeneracy in the science cell. The forced evaporation is first performed in an optically plugged magnetic quadrupole trap, continues in a single beam optical dipole trap and finishes in a crossed dipole trap. At the moment, we can create a degener-

[3] The D_1 molasses scheme is also applied for ^{7}Li by Ketterle at MIT, Cambridge, United States (private communication)

ate spin mixture of ^{40}K in the spin-states $|F = 9/2, m_F = -9/2\rangle$ and $|F = 9/2, m_F = -7/2\rangle$, with atom numbers of $\sim 1.5 \times 10^5$ in each state, a temperature of 64 nK, and $T/T_F \sim 0.17$. The next challenge for our team will be the optimization of the dual-species evaporation to a quantum degenerate ^{6}Li-^{40}K mixture. Once this major goal achieved, we can study many-body systems in mixed dimensions, meaning that lithium and potassium evolve in different dimensions. For example we could investigate new quantum phases like interlayer superfluidity [113], with ^{6}Li mediating effective interactions between ^{40}K atoms in different layers. In the same context, calculations were performed by our group member Daniel Suchet regarding the transmission of a mechanical perturbation throughout the 2D layers of ^{40}K mediated by the excitation and absorption of phonons in a superfluid of ^{6}Li. Furthermore, we could make an attempt to observe the Efimov-effect in mixed dimensions [105], confinement induced resonances [100–104] or p-wave resonances between ^{6}Li-^{40}K dimers and ^{40}K atoms tunable by the lattice depth [106].

A Publications

The work presented in this thesis has been published in the following peer-reviewed journal articles:

— **Sub-Doppler laser cooling of fermionic ^{40}K atoms in three-dimensional gray optical molasses**
D. R. Fernandes [1], F. Sievers [1], N. Kretzschmar, S. Wu, C. Salomon and F. Chevy
EPL (Europhysics Letters) **100**, 63001 (2012)
See page 47 for print version.

— **2.1-watts intracavity-frequency-doubled all-solid-state light source at 671 nm for laser cooling of lithium**
U. Eismann, A. Bergschneider, F. Sievers, N. Kretzschmar, C. Salomon and F. Chevy
Opt. Express **21**, 9091 (2013)
See page 129 for manuscript version.

— **Simultaneous sub-Doppler laser cooling of fermionic ^{6}Li and ^{40}K on the D_1 line: Theory and experiment**
F. Sievers, N. Kretzschmar, D. R. Fernandes, D. Suchet, M. Rabinovic, S. Wu, C. V. Parker, L. Khaykovich, C. Salomon and F. Chevy
Phys. Rev. A **91**, 023426 (2015)
See page 53 for print version.

— **Multiwatt-level second harmonic generation in ppZnO:LN ridge waveguide**
N. Kretzschmar, F. Sievers, U. Eismann, F. Chevy and C. Salomon
To be published, see page 149 for a preliminary draft.

[1] These authors contributed equally to this work.

Bibliography

[1] M. H. Anderson, J. R. Ensher, M. R. Matthews, C. E. Wieman, and E. A. Cornell, *Observation of bose-einstein condensation in a dilute atomic vapor.*, Science (New York, N.Y.) **269**, 198 (1995). 1

[2] K. Davis, M. Mewes, M. Andrews, N. van Druten, D. Durfee, D. Kurn, and W. Ketterle, *Bose-Einstein Condensation in a Gas of Sodium Atoms*, Physical Review Letters **75**, 3969 (1995). 1, 29

[3] A. Einstein, *Quantentheorie des einatomigen idealen Gases*, Kgl. Preuss. Akad. Wiss (1924). 1

[4] Bose, *Plancks Gesetz und Lichtquantenhypothese*, Zeitschrift für Physik **26**, 178 (1924). 1

[5] C. Bradley, C. Sackett, J. Tollett, and R. Hulet, *Evidence of Bose-Einstein Condensation in an Atomic Gas with Attractive Interactions*, Physical Review Letters **75**, 1687 (1995). 1

[6] K. Madison, F. Chevy, W. Wohlleben, and J. Dalibard, *Vortex formation in a stirred Bose-Einstein condensate*, Physical Review Letters **84**, 806 (2000). 1

[7] J. R. Abo-Shaeer, C. Raman, J. M. Vogels, and W. Ketterle, *Observation of vortex lattices in Bose-Einstein condensates.*, Science (New York, N.Y.) **292**, 476 (2001). 1

[8] B. DeMarco, *Onset of Fermi Degeneracy in a Trapped Atomic Gas*, Science **285**, 1703 (1999). 1, 3, 30

[9] K. Davis, M.-O. Mewes, M. Joffe, M. Andrews, and W. Ketterle, *Evaporative Cooling of Sodium Atoms*, Physical Review Letters **75**, 2909 (1995). 1

[10] W. Ketterle, D. S. Durfee, and D. M. Stamper-Kurn, *Making, probing and understanding Bose-Einstein condensates*, eprint arXiv:cond-mat/9904034 90 (1999). 1, 30, 68

[11] A. Leggett, *Bose-Einstein condensation in the alkali gases: Some fundamental concepts*, Reviews of Modern Physics **73**, 307 (2001). 1

[12] L. Pitaevskii and S. Stringari, *Bose-Einstein Condensation*, Oxford University Press (2003). 1

[13] C. J. Pethick and H. Smith, *Bose–Einstein Condensation in Dilute Gases*, Cambridge University Press, 2nd editio edn. (2008). 1

[14] M. R. Andrews, *Observation of Interference Between Two Bose Condensates*, Science **275**, 637 (1997). 1

[15] A. Matsubara, T. Arai, S. Hotta, J. S. Korhonen, T. Mizusaki, and A. Hirai, *Quest for Kosterlitz–Thouless Transition in Two-Dimensional Atomic Hydrogen*, Cambridge University Press, Cambridge (1995). 2

[16] I. F. Silvera, *The quest for Bose-Einstein condensation in atomic hydrogen*, Journal of Low Temperature Physics **101**, 49 (1995). 2

[17] A. P. Mosk, M. W. Reynolds, T. W. Hijmans, and J. T. M. Walraven, *Optical Observation of Atomic Hydrogen on the Surface of Liquid Helium*, Journal of Low Temperature Physics **113**, 217 (1998). 2

[18] A. Safonov, S. Vasilyev, I. Yasnikov, I. Lukashevich, and S. Jaakkola, *Observation of Quasicondensate in Two-Dimensional Atomic Hydrogen*, Physical Review Letters **81**, 4545 (1998). 2

[19] J. Denschlag, *Generating Solitons by Phase Engineering of a Bose-Einstein Condensate*, Science **287**, 97 (2000). 2

[20] S. Burger, K. Bongs, S. Dettmer, W. Ertmer, and K. Sengstock, *Dark Solitons in Bose-Einstein Condensates*, Physical Review Letters **83**, 5198 (1999). 2

[21] L. Khaykovich, F. Schreck, G. Ferrari, T. Bourdel, J. Cubizolles, L. D. Carr, Y. Castin, and C. Salomon, *Formation of a matter-wave bright soliton.*, Science (New York, N.Y.) **296**, 1290 (2002). 2

[22] K. E. Strecker, G. B. Partridge, A. G. Truscott, and R. G. Hulet, *Formation and propagation of matter-wave soliton trains.*, Nature **417**, 150 (2002). 2

[23] M. Greiner, O. Mandel, T. Esslinger, T. W. Hänsch, and I. Bloch, *Quantum phase transition from a superfluid to a Mott insulator in a gas of ultracold atoms.*, Nature **415**, 39 (2002). 2

[24] J. Weiner and P. S. Julienne, *Experiments and theory in cold and ultracold collisions*, Reviews of Modern Physics **71**, 1 (1999). 2

[25] H. Feshbach, *Unified theory of nuclear reactions*, Annals of Physics **5**, 357 (1958). 2

[26] U. Fano, *Effects of Configuration Interaction on Intensities and Phase Shifts*, Physical Review **124**, 1866 (1961). 2

[27] S. Inouye, M. R. Andrews, J. Stenger, H.-J. Miesner, D. M. Stamper-Kurn, and W. Ketterle, *Observation of Feshbach resonances in a Bose-Einstein condensate*, Nature **392**, 151 (1998). 2, 31

[28] E. Tiesinga, B. J. Verhaar, and H. T. C. Stoof, *Threshold and resonance phenomena in ultracold ground-state collisions*, Physical Review A **47**, 4114 (1993). 2

[29] I. Bloch, J. Dalibard, and W. Zwerger, *Many-body physics with ultracold gases*, Rev. Mod. Phys. **80**, 885 (2008). 2

[30] S. Giorgini and S. Stringari, *Theory of ultracold atomic Fermi gases*, Reviews of Modern Physics **80**, 1215 (2008). 2

[31] L. Radzihovsky and D. E. Sheehy, *Imbalanced Feshbach-resonant Fermi gases*, Reports on Progress in Physics **73**, 076501 (2010). 2

[32] F. Chevy and C. Mora, *Ultra-cold polarized Fermi gases*, Reports on Progress in Physics **73**, 112401 (2010). 2

[33] P. D. Lett, R. N. Watts, C. I. Westbrook, W. D. Phillips, P. L. Gould, and H. J. Metcalf, *Observation of Atoms Laser Cooled below the Doppler Limit*, Phys. Rev. Lett. **61**, 169 (1988). 2

[34] J. Stenger, S. Inouye, A. Chikkatur, D. Stamper-Kurn, D. Pritchard, and W. Ketterle, *Bragg Spectroscopy of a Bose-Einstein Condensate*, Physical Review Letters **82**, 4569 (1999). 2

[35] S. Gupta, Z. Hadzibabic, M. W. Zwierlein, C. A. Stan, K. Dieckmann, C. H. Schunck, E. G. M. Van Kempen, B. J. Verhaar, and W. Ketterle, *Radio-frequency spectroscopy of ultracold fermions.*, Science (New York, N.Y.) **300**, 1723 (2003). 2

[36] Y. Shin, M. Saba, T. Pasquini, W. Ketterle, D. Pritchard, and A. Leanhardt, *Atom Interferometry with Bose-Einstein Condensates in a Double-Well Potential*, Physical Review Letters **92**, 050405 (2004). 2

[37] M. Yasuda and F. Shimizu, *Observation of Two-Atom Correlation of an Ultracold Neon Atomic Beam*, Physical Review Letters **77**, 3090 (1996). 2

[38] E. Burt, R. Ghrist, C. Myatt, M. Holland, E. Cornell, and C. Wieman, *Coherence, Correlations, and Collisions: What One Learns about Bose-Einstein Condensates from Their Decay*, Physical Review Letters **79**, 337 (1997). 2

[39] B. Tolra, K. O'Hara, J. Huckans, W. Phillips, S. Rolston, and J. Porto, *Observation of Reduced Three-Body Recombination in a Correlated 1D Degenerate Bose Gas*, Physical Review Letters **92**, 190401 (2004). 2

[40] S. Fölling, F. Gerbier, A. Widera, O. Mandel, T. Gericke, and I. Bloch, *Spatial quantum noise interferometry in expanding ultracold atom clouds.*, Nature **434**, 481 (2005). 2

[41] W. S. Bakr, J. I. Gillen, A. Peng, S. Fölling, and M. Greiner, *A quantum gas microscope for detecting single atoms in a Hubbard-regime optical lattice.*, Nature **462**, 74 (2009). 2

[42] W. S. Bakr, A. Peng, M. E. Tai, R. Ma, J. Simon, J. I. Gillen, S. Fölling, L. Pollet, and M. Greiner, *Probing the superfluid-to-Mott insulator transition at the single-atom level.*, Science **329**, 547 (2010). 2

[43] J. F. Sherson, C. Weitenberg, M. Endres, M. Cheneau, I. Bloch, and S. Kuhr, *Single-atom-resolved fluorescence imaging of an atomic Mott insulator.*, Nature **467**, 68 (2010). 2

[44] A. G. Truscott, K. E. Strecker, W. I. McAlexander, G. B. Partridge, and R. G. Hulet, *Observation of Fermi pressure in a gas of trapped atoms.*, Science (New York, N.Y.) **291**, 2570 (2001). 3

[45] F. Schreck, L. Khaykovich, K. L. Corwin, G. Ferrari, T. Bourdel, J. Cubizolles, and C. Salomon, *Quasipure Bose-Einstein Condensate Immersed in a Fermi Sea*, Physical Review Letters **87**, 080403 (2001). 3

[46] J. McNamara, T. Jeltes, A. Tychkov, W. Hogervorst, and W. Vassen, *Degenerate Bose-Fermi Mixture of Metastable Atoms*, Physical Review Letters **97**, 080404 (2006). 3

[47] B. J. DeSalvo, M. Yan, P. G. Mickelson, Y. N. Martinez de Escobar, and T. C. Killian, *Degenerate Fermi Gas of ^{87}Sr*, Physical Review Letters **105**, 030402 (2010). 3

[48] M. K. Tey, S. Stellmer, R. Grimm, and F. Schreck, *Double-degenerate Bose-Fermi mixture of strontium*, Physical Review A **82**, 011608 (2010). 3

[49] T. Fukuhara, Y. Takasu, M. Kumakura, and Y. Takahashi, *Degenerate Fermi Gases of Ytterbium*, Physical Review Letters **98**, 030401 (2007). 3

[50] M. Lu, N. Q. Burdick, and B. L. Lev, *Quantum Degenerate Dipolar Fermi Gas*, Physical Review Letters **108**, 215301 (2012). 3

[51] K. Aikawa, A. Frisch, M. Mark, S. Baier, R. Grimm, and F. Ferlaino, *Reaching Fermi Degeneracy via Universal Dipolar Scattering*, Physical Review Letters **112**, 010404 (2014). 3

[52] Z. Hadzibabic, S. Gupta, C. Stan, C. Schunck, M. Zwierlein, K. Dieckmann, and W. Ketterle, *Fiftyfold Improvement in the Number of Quantum Degenerate Fermionic Atoms*, Physical Review Letters **91**, 160401 (2003). 3

[53] S. Nascimbène, N. Navon, K. J. Jiang, F. Chevy, and C. Salomon, *Exploring the thermodynamics of a universal Fermi gas.*, Nature **463**, 1057 (2010). 3, 4

[54] M. Inguscio, W. Ketterle, and C. Salomon (eds.), *Proceedings of the International School of Physics Enrico Fermi on Ultracold Fermi gases, Course CLXIV, Varenna,*, Società Italiana di Fisica (2006). 3

[55] E. Timmermans, *Degenerate Fermion Gas Heating by Hole Creation*, Physical Review Letters **87**, 240403 (2001). 3

[56] L. Carr, T. Bourdel, and Y. Castin, *Limits of sympathetic cooling of fermions by zero-temperature bosons due to particle losses*, Physical Review A **69**, 033603 (2004). 3

[57] S. Granade, M. Gehm, K. O'Hara, and J. Thomas, *All-Optical Production of a Degenerate Fermi Gas*, Physical Review Letters **88**, 120405 (2002). 3

[58] S. Jochim, M. Bartenstein, A. Altmeyer, G. Hendl, C. Chin, J. H. Denschlag, and R. Grimm, *Pure Gas of Optically Trapped Molecules Created from Fermionic Atoms*, Physical Review Letters **91**, 240402 (2003). 3

[59] C. Silber, S. Günther, C. Marzok, B. Deh, P. Courteille, and C. Zimmermann, *Quantum-Degenerate Mixture of Fermionic Lithium and Bosonic Rubidium Gases*, Physical Review Letters **95**, 170408 (2005). 3

[60] M. Taglieber, A.-C. Voigt, T. Aoki, T. Hänsch, and K. Dieckmann, *Quantum Degenerate Two-Species Fermi-Fermi Mixture Coexisting with a Bose-Einstein Condensate*, Physical Review Letters **100**, 010401 (2008). 3, 5

[61] C.-H. Wu, I. Santiago, J. W. Park, P. Ahmadi, and M. W. Zwierlein, *Strongly interacting isotopic Bose-Fermi mixture immersed in a Fermi sea*, Physical Review A **84**, 011601 (2011). 3, 5

[62] G. Roati, F. Riboli, G. Modugno, and M. Inguscio, *Fermi-Bose Quantum Degenerate ^{40}K-^{87}Rb Mixture with Attractive Interaction*, Physical Review Letters **89**, 150403 (2002). 3

[63] S. Inouye, J. Goldwin, M. Olsen, C. Ticknor, J. Bohn, and D. Jin, *Observation of Heteronuclear Feshbach Resonances in a Mixture of Bosons and Fermions*, Physical Review Letters **93**, 183201 (2004). 3

[64] M. Köhl, H. Moritz, T. Stöferle, K. Günter, and T. Esslinger, *Fermionic Atoms in a Three Dimensional Optical Lattice: Observing Fermi Surfaces, Dynamics, and Interactions*, Physical Review Letters **94**, 080403 (2005). 3

[65] T. Rom, T. Best, D. van Oosten, U. Schneider, S. Fölling, B. Paredes, and I. Bloch, *Free fermion antibunching in a degenerate atomic Fermi gas released from an optical lattice.*, Nature **444**, 733 (2006). 3

[66] C. Ospelkaus, S. Ospelkaus, L. Humbert, P. Ernst, K. Sengstock, and K. Bongs, *Ultracold Heteronuclear Molecules in a 3D Optical Lattice*, Physical Review Letters **97**, 120402 (2006). 3

[67] T. Tiecke, *Feshbach resonances in ultracold mixtures of the fermionic quantum gases ^{6}Li and ^{40}K*, Ph.D. thesis, Universiteit van Amsterdam (2009). 3, 5, 30

[68] F. M. Spiegelhalder, A. Trenkwalder, D. Naik, G. Kerner, E. Wille, G. Hendl, F. Schreck, and R. Grimm, *All-optical production of a degenerate mixture of ^{6}Li and ^{40}K and creation of heteronuclear molecules*, Physical Review A **81**, 043637 (2010). 3, 5

[69] B. DeMarco, S. Papp, and D. Jin, *Pauli Blocking of Collisions in a Quantum Degenerate Atomic Fermi Gas*, Physical Review Letters **86**, 5409 (2001). 3

[70] T. Loftus, C. Regal, C. Ticknor, J. Bohn, and D. Jin, *Resonant Control of Elastic Collisions in an Optically Trapped Fermi Gas of Atoms*, Physical Review Letters **88**, 173201 (2002). 4

[71] C. A. Regal and D. S. Jin, *Measurement of Positive and Negative Scattering Lengths in a Fermi Gas of Atoms*, Physical Review Letters **90**, 230404 (2003). 4

[72] C. A. Regal, C. Ticknor, J. L. Bohn, and D. S. Jin, *Tuning p-Wave Interactions in an Ultracold Fermi Gas of Atoms*, Physical Review Letters **90**, 053201 (2003). 4

[73] K. Dieckmann, C. A. Stan, S. Gupta, Z. Hadzibabic, C. H. Schunck, and W. Ketterle, *Decay of an Ultracold Fermionic Lithium Gas near a Feshbach Resonance*, Physical Review Letters **89**, 203201 (2002). 4

[74] K. M. O'Hara, S. L. Hemmer, S. R. Granade, M. E. Gehm, and J. E. Thomas, *Measurement of the zero crossing in a Feshbach resonance of fermionic ^{6}Li*, Physical Review A **66**, 041401 (2002). 4

[75] S. Jochim, M. Bartenstein, G. Hendl, J. Denschlag, R. Grimm, A. Mosk, and M. Weidemüller, *Magnetic Field Control of Elastic Scattering in a Cold Gas of Fermionic Lithium Atoms*, Physical Review Letters **89**, 273202 (2002). 4

[76] D. S. Petrov, C. Salomon, and G. V. Shlyapnikov, *Weakly Bound Dimers of Fermionic Atoms*, Physical Review Letters **93**, 090404 (2004). 4

[77] M. Zwierlein, C. Stan, C. Schunck, S. Raupach, S. Gupta, Z. Hadzibabic, and W. Ketterle, *Observation of Bose-Einstein Condensation of Molecules*, Physical Review Letters **91**, 250401 (2003). 4

[78] S. Jochim, M. Bartenstein, A. Altmeyer, G. Hendl, S. Riedl, C. Chin, J. Hecker Denschlag, and R. Grimm, *Bose-Einstein condensation of molecules.*, Science (New York, N.Y.) **302**, 2101 (2003). 4

[79] M. Greiner, C. A. Regal, and D. S. Jin, *Emergence of a molecular Bose-Einstein condensate from a Fermi gas.*, Nature **426**, 537 (2003). 4

[80] M. Zwierlein, C. Stan, C. Schunck, S. Raupach, A. Kerman, and W. Ketterle, *Condensation of Pairs of Fermionic Atoms near a Feshbach Resonance*, Physical Review Letters **92**, 120403 (2004). 4

[81] C. A. Regal, M. Greiner, and D. S. Jin, *Observation of Resonance Condensation of Fermionic Atom Pairs*, Physical Review Letters **92**, 040403 (2004). 4

[82] M. Bartenstein, A. Altmeyer, S. Riedl, S. Jochim, C. Chin, J. Denschlag, and R. Grimm, *Crossover from a Molecular Bose-Einstein Condensate to a Degenerate Fermi Gas*, Physical Review Letters **92**, 120401 (2004). 4

[83] J. Bardeen, L. N. Cooper, and J. R. Schrieffer, *Theory of Superconductivity*, Physical Review **108**, 1175 (1957). 4

[84] T. Bourdel, L. Khaykovich, J. Cubizolles, J. Zhang, F. Chevy, M. Teichmann, L. Tarruell, S. Kokkelmans, and C. Salomon, *Experimental Study of the BEC-BCS Crossover Region in Lithium 6*, Physical Review Letters **93**, 050401 (2004). 4

[85] M. W. Zwierlein, J. R. Abo-Shaeer, A. Schirotzek, C. H. Schunck, and W. Ketterle, *Vortices and superfluidity in a strongly interacting Fermi gas.*, Nature **435**, 1047 (2005). 4

[86] M. W. Zwierlein, A. Schirotzek, C. H. Schunck, and W. Ketterle, *Fermionic superfluidity with imbalanced spin populations.*, Science (New York, N.Y.) **311**, 492 (2006). 4

[87] G. B. Partridge, W. Li, R. I. Kamar, Y.-A. Liao, and R. G. Hulet, *Pairing and phase separation in a polarized Fermi gas.*, Science (New York, N.Y.) **311**, 503 (2006). 4

[88] J. Joseph, B. Clancy, L. Luo, J. Kinast, A. Turlapov, and J. Thomas, *Measurement of Sound Velocity in a Fermi Gas near a Feshbach Resonance*, Physical Review Letters **98**, 170401 (2007). 4

[89] D. Miller, J. Chin, C. Stan, Y. Liu, W. Setiawan, C. Sanner, and W. Ketterle, *Critical Velocity for Superfluid Flow across the BEC-BCS Crossover*, Physical Review Letters **99**, 070402 (2007). 4

[90] U. Schneider, L. Hackermüller, S. Will, T. Best, I. Bloch, T. A. Costi, R. W. Helmes, D. Rasch, and A. Rosch, *Metallic and insulating phases of repulsively interacting fermions in a 3D optical lattice.*, Science (New York, N.Y.) **322**, 1520 (2008). 4

[91] R. Jördens, N. Strohmaier, K. Günter, H. Moritz, and T. Esslinger, *A Mott insulator of fermionic atoms in an optical lattice.*, Nature **455**, 204 (2008). 4

[92] N. Navon, S. Nascimbène, F. Chevy, and C. Salomon, *The equation of state of a low-temperature Fermi gas with tunable interactions.*, Science (New York, N.Y.) **328**, 729 (2010). 4

[93] M. Horikoshi, S. Nakajima, M. Ueda, and T. Mukaiyama, *Measurement of universal thermodynamic functions for a unitary Fermi gas.*, Science (New York, N.Y.) **327**, 442 (2010). 4

[94] W. Ketterle and M. Zwierlein, *Making, probing and understanding ultracold Fermi gases*, Proc. of the Int. School of Phys. Enrico Fermi **CLXIV**, 247 (2008). 4, 68, 70

[95] M. J. H. Ku, A. T. Sommer, L. W. Cheuk, and M. W. Zwierlein, *Revealing the superfluid lambda transition in the universal thermodynamics of a unitary Fermi gas.*, Science **335**, 563 (2012). 4, 70

[96] Q. Chen, J. Stajic, S. Tan, and K. Levin, *BCS–BEC crossover: From high temperature superconductors to ultracold superfluids*, Physics Reports **412**, 1 (2005). 4

[97] Y. Nishida and S. Tan, *Universal Fermi Gases in Mixed Dimensions*, Phys. Rev. Lett. **101**, 170401 (2008). 4

[98] R. Onofrio and C. Presilla, *Ultracold Atomic Fermi–Bose Mixtures in Bichromatic Optical Dipole Traps: A Novel Route to Study Fermion Superfluidity*, Journal of Statistical Physics **115**, 57 (2004). 4

[99] A. D. Lercher, T. Takekoshi, M. Debatin, B. Schuster, R. Rameshan, F. Ferlaino, R. Grimm, and H. C. Nägerl, *Production of a dual-species Bose-Einstein condensate of Rb and Cs atoms*, The European Physical Journal D **65**, 3 (2011). 4

[100] M. Olshanii, *Atomic Scattering in the Presence of an External Confinement and a Gas of Impenetrable Bosons*, Physical Review Letters **81**, 938 (1998). 4, 163

[101] T. Bergeman, M. Moore, and M. Olshanii, *Atom-Atom Scattering under Cylindrical Harmonic Confinement: Numerical and Analytic Studies of the Confinement Induced Resonance*, Physical Review Letters **91**, 163201 (2003). 4, 163

[102] H. Moritz, T. Stöferle, K. Günter, M. Köhl, and T. Esslinger, *Confinement Induced Molecules in a 1D Fermi Gas*, Physical Review Letters **94**, 210401 (2005). 4, 163

[103] E. Haller, M. J. Mark, R. Hart, J. G. Danzl, L. Reichsöllner, V. Melezhik, P. Schmelcher, and H.-C. Nägerl, *Confinement-Induced Resonances in Low-Dimensional Quantum Systems*, Physical Review Letters **104**, 153203 (2010). 4, 163

[104] G. Lamporesi, J. Catani, G. Barontini, Y. Nishida, M. Inguscio, and F. Minardi, *Scattering in Mixed Dimensions with Ultracold Gases*, Physical Review Letters **104**, 153202 (2010). 4, 163

[105] Y. Nishida and S. Tan, *Confinement-induced Efimov resonances in Fermi-Fermi mixtures*, Physical Review A **79**, 060701 (2009). 4, 163

[106] J. Levinsen, T. Tiecke, J. Walraven, and D. Petrov, *Atom-Dimer Scattering and Long-Lived Trimers in Fermionic Mixtures*, Physical Review Letters **103**, 153202 (2009). 4, 5, 163

[107] P. Anderson, *Localized Magnetic States in Metals*, Physical Review **124**, 41 (1961). 4

[108] J. Kondo, *Resistance Minimum in Dilute Magnetic Alloys*, Progress of Theoretical Physics **32**, 37 (1964). 4

[109] J. Bauer, C. Salomon, and E. Demler, *Realizing a Kondo-Correlated State with Ultracold Atoms*, Physical Review Letters **111**, 215304 (2013). 4

[110] U. Gavish and Y. Castin, *Matter-Wave Localization in Disordered Cold Atom Lattices*, Phys. Rev. Lett. **95**, 20401 (2005). 4

[111] G. Roati, C. D'Errico, L. Fallani, M. Fattori, C. Fort, M. Zaccanti, G. Modugno, M. Modugno, and M. Inguscio, *Anderson localization of a non-interacting Bose-Einstein condensate.*, Nature **453**, 895 (2008). 4

[112] J. Billy, V. Josse, Z. Zuo, A. Bernard, B. Hambrecht, P. Lugan, D. Clément, L. Sanchez-Palencia, P. Bouyer, and A. Aspect, *Direct observation of Anderson localization of matter waves in a controlled disorder.*, Nature **453**, 891 (2008). 4

[113] Y. Nishida, *Phases of a bilayer Fermi gas*, Physical Review A **82**, 011605 (2010). 4, 163

[114] M. Iskin and C. de Melo, *Superfluid and Insulating Phases of Fermion Mixtures in Optical Lattices*, Physical Review Letters **99**, 080403 (2007). 5

[115] P. Fulde and R. A. Ferrell, *Superconductivity in a Strong Spin-Exchange Field*, Phys. Rev. **135**, A550 (1964). 5

[116] A. I. Larkin and Y. N. Ovchinnikov, *Inhomogeneous state of superconductors*, Sov. Phys. JETP **20** (1965). 5

[117] M. Dalmonte, K. Dieckmann, T. Roscilde, C. Hartl, A. E. Feiguin, U. Schollwöck, and F. Heidrich-Meisner, *Dimer, trimer, and Fulde-Ferrell-Larkin-Ovchinnikov liquids in mass- and spin-imbalanced trapped binary mixtures in one dimension*, Physical Review A **85**, 063608 (2012). 5

[118] W. V. Liu and F. Wilczek, *Interior Gap Superfluidity*, Physical Review Letters **90**, 047002 (2003). 5

[119] M. M. Forbes, E. Gubankova, W. V. Liu, and F. Wilczek, *Stability Criteria for Breached-Pair Superfluidity*, Phys. Rev. Lett. **94**, 17001 (2005). 5

[120] D. S. Petrov, G. E. Astrakharchik, D. J. Papoular, C. Salomon, and G. V. Shlyapnikov, *Crystalline Phase of Strongly Interacting Fermi Mixtures*, Phys. Rev. Lett. **99**, 130407 (2007). 5

[121] J. Deiglmayr, A. Grochola, M. Repp, K. Mörtlbauer, C. Glück, J. Lange, O. Dulieu, R. Wester, and M. Weidemüller, *Formation of Ultracold Polar Molecules in the Rovibrational Ground State*, Phys. Rev. Lett. **101**, 133004 (2008). 5

[122] K.-K. Ni, S. Ospelkaus, M. H. G. de Miranda, A. Pe'er, B. Neyenhuis, J. J. Zirbel, S. Kotochigova, P. S. Julienne, D. S. Jin, and J. Ye, *A High Phase-Space-Density Gas of Polar Molecules*, Science **322**, 231 (2008). 5

[123] L. Pollet, M. Troyer, K. Van Houcke, and S. Rombouts, *Phase Diagram of Bose-Fermi Mixtures in One-Dimensional Optical Lattices*, Physical Review Letters **96**, 190402 (2006). 5

[124] A. Zujev, A. Baldwin, R. Scalettar, V. Rousseau, P. Denteneer, and M. Rigol, *Superfluid and Mott-insulator phases of one-dimensional Bose-Fermi mixtures*, Physical Review A **78**, 033619 (2008). 5

[125] I. Ferrier-Barbut, M. Delehaye, S. Laurent, A. T. Grier, M. Pierce, B. S. Rem, F. Chevy, and C. Salomon, *A mixture of Bose and Fermi superfluids*, Science **345**, 1035 (2014). 5

[126] M. Taglieber, A.-C. Voigt, F. Henkel, S. Fray, T. Hänsch, and K. Dieckmann, *Simultaneous magneto-optical trapping of three atomic species*, Physical Review A **73**, 011402 (2006). 5

[127] A. Ridinger, S. Chaudhuri, T. Salez, U. Eismann, D. R. Fernandes, K. Magalhães, D. Wilkowski, C. Salomon, and F. Chevy, *Large atom number dual-species magneto-optical trap for fermionic ^6Li and ^{40}K atoms*, The European Physical Journal D **65**, 223 (2011). 5, 11, 24

[128] E. Wille, F. Spiegelhalder, G. Kerner, D. Naik, A. Trenkwalder, G. Hendl, F. Schreck, R. Grimm, T. Tiecke, J. Walraven, S. Kokkelmans, E. Tiesinga, and P. Julienne, *Exploring an Ultracold Fermi-Fermi Mixture: Interspecies Feshbach Resonances and Scattering Properties of ^6Li and ^{40}K*, Physical Review Letters **100**, 053201 (2008). 5

[129] E. Tiemann, H. Knöckel, P. Kowalczyk, W. Jastrzebski, A. Pashov, H. Salami, and A. Ross, *Coupled system a $\Sigma 3+$ and X $\Sigma 1+$ of KLi: Feshbach resonances and corrections to the Born-Oppenheimer approximation*, Physical Review A **79**, 042716 (2009). 5, 30

[130] T. G. Tiecke, M. R. Goosen, J. T. M. Walraven, and S. J. J. M. F. Kokkelmans, *Asymptotic-bound-state model for Feshbach resonances*, Physical Review A **82**, 042712 (2010). 5

[131] T. G. Tiecke, M. R. Goosen, A. Ludewig, S. D. Gensemer, S. Kraft, S. J. J. M. F. Kokkelmans, and J. T. M. Walraven, *Broad Feshbach resonance in the ^6Li-^{40}K mixture*, Physical Review Letters **104**, 053202 (2010). 5

[132] D. Naik, A. Trenkwalder, C. Kohstall, F. M. Spiegelhalder, M. Zaccanti, G. Hendl, F. Schreck, R. Grimm, T. M. Hanna, and P. S. Julienne, *Feshbach resonances in the ^{6}Li-^{40}K Fermi-Fermi mixture: elastic versus inelastic interactions*, The European Physical Journal D **65**, 55 (2011). 5

[133] A.-C. Voigt, M. Taglieber, L. Costa, T. Aoki, W. Wieser, T. W. Hänsch, and K. Dieckmann, *Ultracold Heteronuclear Fermi-Fermi Molecules*, Physical Review Letters **102**, 020405 (2009). 5

[134] A. Trenkwalder, C. Kohstall, M. Zaccanti, D. Naik, A. I. Sidorov, F. Schreck, and R. Grimm, *Hydrodynamic Expansion of a Strongly Interacting Fermi-Fermi Mixture*, Physical Review Letters **106**, 115304 (2011). 5

[135] C. Kohstall, M. Zaccanti, M. Jag, A. Trenkwalder, P. Massignan, G. M. Bruun, F. Schreck, and R. Grimm, *Metastability and coherence of repulsive polarons in a strongly interacting Fermi mixture.*, Nature **485**, 615 (2012). 5

[136] M. Jag, M. Zaccanti, M. Cetina, R. S. Lous, F. Schreck, R. Grimm, D. S. Petrov, and J. Levinsen, *Observation of a Strong Atom-Dimer Attraction in a Mass-Imbalanced Fermi-Fermi Mixture*, Physical Review Letters **112**, 075302 (2014). 5

[137] K. M. O'Hara, S. L. Hemmer, M. E. Gehm, S. R. Granade, and J. E. Thomas, *Observation of a strongly interacting degenerate Fermi gas of atoms.*, Science (New York, N.Y.) **298**, 2179 (2002). 5

[138] J. T. Stewart, J. P. Gaebler, C. A. Regal, and D. S. Jin, *Potential energy of a ^{40}K Fermi gas in the BCS-BEC crossover*, Physical Review Letters **97**, 220406 (2006). 5

[139] D. R. Fernandes, F. Sievers, N. Kretzschmar, S. Wu, C. Salomon, and F. Chevy, *Sub-Doppler laser cooling of fermionic ^{40}K atoms in three-dimensional gray optical molasses*, EPL (Europhysics Letters) **100**, 63001 (2012). 6, 41

[140] F. Sievers, N. Kretzschmar, D. R. Fernandes, D. Suchet, M. Rabinovic, S. Wu, C. V. Parker, L. Khaykovich, C. Salomon, and F. Chevy, *Simultaneous sub-Doppler laser cooling of fermionic ^{6}Li and ^{40}K on the D_1 line: Theory and experiment*, Phys. Rev. A **91**, 023426 (2015). 6, 41, 78

[141] A. Ridinger, *Towards quantum degenerate Fermi mixtures : Photoassociation of weakly bound ^{6}Li-^{40}K molecules*, Ph.D. thesis, Université Pierre et Marie Curie - Paris VI (2011). 11, 12, 15, 16, 18, 19, 21, 22

[142] T. Salez, *Towards quantum degenerate atomic Fermi mixtures*, Ph.D. thesis, Université Pierre et Marie Curie - Paris VI (2011). 11

[143] K. L. Moore, T. P. Purdy, K. W. Murch, S. Leslie, S. Gupta, and D. M. Stamper-Kurn, *Collimated, single-pass atom source from a pulsed alkali metal dispenser for laser-cooling experiments*, Review of Scientific Instruments **76**, 023106 (2005). 11

[144] A. Gozzini, F. Mango, J. H. Xu, G. Alzetta, F. Maccarrone, and R. A. Bernheim, *Light-induced ejection of alkali atoms in polysiloxane coated cells*, Il Nuovo Cimento D **15**, 709 (1993). 11

[145] C. Klempt, T. van Zoest, T. Henninger, O. Topic, E. Rasel, W. Ertmer, and J. Arlt, *Ultraviolet light-induced atom desorption for large rubidium and potassium magneto-optical traps*, Physical Review A **73**, 013410 (2006). 11

[146] M. Greiner, I. Bloch, T. W. Hänsch, and T. Esslinger, *Magnetic transport of trapped cold atoms over a large distance*, Phys. Rev. A **63**, 31401 (2001). 12, 28

[147] G. Ferrari, M.-O. Mewes, F. Schreck, and C. Salomon, *High-power multiple-frequency narrow-linewidth laser source based on a semiconductor tapered amplifier*, Optics Letters **24**, 151 (1999). 16

[148] F. Sievers, *Ultracold Fermi mixtures and simultaneous sub-Doppler laser cooling of fermionic ^{6}Li and ^{40}K*, Ph.d. thesis, Université Pierre et Marie Curie - Paris VI (2014). 17, 18, 27, 29, 33, 37, 126

[149] W. Phillips and H. Metcalf, *Laser Deceleration of an Atomic Beam*, Physical Review Letters **48**, 596 (1982). 18

[150] H. J. Metcalf and P. van der Straten, *Laser cooling and trapping of atoms*, Journal of the Optical Society of America B **20**, 887 (2003). 18, 24

[151] K. Dieckmann, R. Spreeuw, M. Weidemüller, and J. Walraven, *Two-dimensional magneto-optical trap as a source of slow atoms*, Physical Review A **58**, 3891 (1998). 19

[152] J. Schoser, A. Batär, R. Löw, V. Schweikhard, A. Grabowski, Y. Ovchinnikov, and T. Pfau, *Intense source of cold Rb atoms from a pure two-dimensional magneto-optical trap*, Physical Review A **66**, 023410 (2002). 19

[153] S. Chaudhuri, S. Roy, and C. Unnikrishnan, *Realization of an intense cold Rb atomic beam based on a two-dimensional magneto-optical trap: Experiments and comparison with simulations*, Physical Review A **74**, 023406 (2006). 19

[154] J. Catani, P. Maioli, L. De Sarlo, F. Minardi, and M. Inguscio, *Intense slow beams of bosonic potassium isotopes*, Physical Review A **73**, 033415 (2006). 19

[155] N. Castagna, J. Guéna, M. D. Plimmer, and P. Thomann, *A novel simplified two-dimensional magneto-optical trap as an intense source of slow cesium atoms*, The European Physical Journal Applied Physics **34**, 21 (2006). 19

[156] T. Tiecke, S. Gensemer, A. Ludewig, and J. Walraven, *High-flux two-dimensional magneto-optical-trap source for cold lithium atoms*, Physical Review A **80**, 013409 (2009). 19

[157] B. DeMarco, J. Bohn, J. Burke, M. Holland, and D. Jin, *Measurement of p-Wave Threshold Law Using Evaporatively Cooled Fermionic Atoms*, Physical Review Letters **82**, 4208 (1999). 30, 67

[158] F. Schreck, *Mixtures of ultracold gases: Fermi sea and Bose-Einstein condensate of Lithium isotopes*, Ph.D. thesis, Université Pierre et Marie Curie - Paris VI (2002). 30

[159] S. Falke, H. Knöckel, J. Friebe, M. Riedmann, E. Tiemann, and C. Lisdat, *Potassium ground-state scattering parameters and Born-Oppenheimer potentials from molecular spectroscopy*, Physical Review A **78**, 012503 (2008). 30

[160] B. DeMarco, *Quantum behavior of an atomic Fermi gas*, Ph.D. thesis, University of Colorado (2001). 31, 70

[161] R. Grimm, M. Weidemüller, and Y. B. Ovchinnikov, *Optical dipole traps for neutral atoms* 39 (1999). 31, 68

[162] A. Keshet, *Cicero Word Generator Technical and User Manual* (2008). 36

[163] M. Teichmann, *Ultracold 6Li Atoms in the BEC-BCS Crossover: Experiments and the Construction of a New Apparatus*, Ph.D. thesis, Université Pierre et Marie Curie - Paris VI (2007). 38

[164] D. Boiron, A. Michaud, P. Lemonde, Y. Castin, C. Salomon, S. Weyers, K. Szymaniec, L. Cognet, and A. Clairon, *Laser cooling of cesium atoms in gray optical molasses down to 1.1 μK*, Physical Review A **53**, R3734 (1996). 41

[165] G. Grynberg and J.-Y. Courtois, *Proposal for a Magneto-Optical Lattice for Trapping Atoms in Nearly-Dark States*, EPL (Europhysics Letters) **27**, 41 (1994). 41

[166] A. Burchianti, G. Valtolina, J. A. Seman, E. Pace, M. De Pas, M. Inguscio, M. Zaccanti, and G. Roati, *Efficient all-optical production of large ^{6}Li quantum gases using D_1 gray-molasses cooling*, Phys. Rev. A **90**, 043408 (2014). 42, 162

[167] A. T. Grier, I. Ferrier-Barbut, B. S. Rem, M. Delehaye, L. Khaykovich, F. Chevy, and C. Salomon, *Λ-enhanced sub-Doppler cooling of lithium atoms in D_1 gray molasses*, Physical Review A **87**, 063411 (2013). 42, 162

[168] D. Nath, R. K. Easwaran, G. Rajalakshmi, and C. S. Unnikrishnan, *Quantum-interference-enhanced deep sub-Doppler cooling of ^{39}K atoms in gray molasses*, Physical Review A **88**, 053407 (2013). 42, 162

[169] G. Salomon, L. Fouché, P. Wang, A. Aspect, P. Bouyer, and T. Bourdel, *Gray-molasses cooling of ^{39}K to a high phase-space density*, EPL (Europhysics Letters) **104**, 63002 (2013). 42, 43, 162

[170] G. Salomon, L. Fouché, S. Lepoutre, A. Aspect, and T. Bourdel, *All-optical cooling of ^{39}K to Bose-Einstein condensation*, Phys. Rev. A **90**, 033405 (2014). 42, 162

[171] E. Haller, J. Hudson, A. Kelly, D. A. Cotta, B. Peaudecerf, G. D. Bruce, and S. Kuhr, *Single-atom imaging of fermions in a quantum-gas microscope*, ArXiv e-prints (2015). 42, 162

[172] J. Walraven and T. Hijmans, *Atomic hydrogen in magnetostatic traps*, Physica B: Condensed Matter **197**, 417 (1994). 65

[173] W. Ketterle and N. J. V. Druten, *Evaporative Cooling of Trapped Atoms*, Advances in Atomic, Molecular and Optical Physics **37**, 181 (1996). 65

[174] H. Hess, *Evaporative cooling of magnetically trapped and compressed spin-polarized hydrogen*, Physical Review B **34**, 3476 (1986). 65

[175] O. Luiten, M. Reynolds, and J. Walraven, *Kinetic theory of the evaporative cooling of a trapped gas*, Physical Review A **53**, 381 (1996). 65

[176] Y.-J. Lin, A. Perry, R. Compton, I. Spielman, and J. Porto, *Rapid production of ^{87}Rb Bose-Einstein condensates in a combined magnetic and optical potential*, Physical Review A **79**, 063631 (2009). 67

[177] A. Ludewig, *Feshbach Resonances in ^{40}K.*, Ph.D. thesis, University of Amsterdam (2012). 68

[178] C. A. Regal, M. Greiner, and D. S. Jin, *Lifetime of Molecule-Atom Mixtures near a Feshbach Resonance in* ^{40}K, Phys. Rev. Lett. **92**, 083201 (2004). 68

[179] D. Rio Fernandes, *Trapping and cooling of fermionic alkali atoms to quantum degeneracy. Sub-Doppler cooling of Potassium-40 and Lithium-6 in gray molasses*, Theses, Université Pierre et Marie Curie (2014). 69, 70

[180] W. Gerlach and O. Stern, *Das magnetische Moment des Silberatoms*, Zeitschrift für Physik **9**, 353 (1922). 69

[181] E. A. Hinds and I. G. Hughes, *Magnetic atom optics: mirrors, guides, traps, and chips for atoms*, Journal of Physics D: Applied Physics **32**, R119 (1999). 69

[182] F. Y. Hou, L. Yu, X. J. Jia, Y. H. Zheng, C. D. Xie, and K. C. Peng, *Experimental generation of optical non-classical states of light with 1.34 μm wavelength*, The European Physical Journal D **62**, 433 (2011). 75

[183] F. A. Camargo, T. Zanon-Willette, T. Badr, N. U. Wetter, and J.-J. Zondy, *Tunable Single-Frequency Nd:YVO_4 BiB_3O_6 Ring Laser at 671 nm*, Quantum Electronics, IEEE Journal of **46**, 804 (2010). 75, 135

[184] U. Eismann, F. Gerbier, C. Canalias, A. Zukauskas, G. Trénec, J. Vigué, F. Chevy, and C. Salomon, *An all-solid-state laser source at 671 nm for cold-atom experiments with lithium*, Applied Physics B **106**, 25 (2011). 75, 83, 96, 98, 120, 130, 131, 132, 133, 134, 135, 136, 137, 138

[185] A. Miffre, M. Jacquey, M. Büchner, G. Trénec, and J. Vigué, *Atom interferometry measurement of the electric polarizability of lithium*, The European Physical Journal D - Atomic, Molecular, Optical and Plasma Physics **38**, 353 (2006). 75

[186] H. Müller, S.-w. Chiow, Q. Long, S. Herrmann, and S. Chu, *Atom Interferometry with up to 24-Photon-Momentum-Transfer Beam Splitters*, Phys. Rev. Lett. **100**, 180405 (2008). 75

[187] I. E. Olivares, A. E. Duarte, E. A. Saravia, and F. J. Duarte, *Lithium Isotope Separation With Tunable Diode Lasers*, Appl. Opt. **41**, 2973 (2002). 75

[188] S. A. Payne, L. K. Smith, R. J. Beach, B. H. T. Chai, J. H. Tassano, L. D. DeLoach, W. L. Kway, R. W. Solarz, and W. F. Krupke, *Properties of Cr:$LiSrAlF_6$ crystals for laser operation*, Appl. Opt. **33**, 5526 (1994). 75

[189] L. Mcdonagh, *888 nm pumping of Nd:YVO_4 for high-power TEM_{00} lasers*, Ph.D. thesis, Technische Universität Kaiserslautern (2008). 79, 86

[190] H. Rast, H. Caspers, and S. Miller, *Infrared Spectral Emittance and Optical Properties of Yttrium Vanadate*, Physical Review **169**, 705 (1968). 80

[191] CASTECH, INC., *Manufacturer's website* (2015). 81

[192] M. Bass, C. DeCusatis, J. Enoch, V. Lakshminarayanan, G. Li, C. MacDonald, V. Mahajan, and E. Van Stryland, *Handbook of Optics, Third Edition Volume IV: Optical Properties of Materials, Nonlinear Optics, Quantum Optics*, Handbook of Optics, McGraw-Hill Education (2009). 81

[193] L. McDonagh, R. Wallenstein, R. Knappe, and A. Nebel, *High-efficiency 60 W TEM_{00} Nd:YVO_4 oscillator pumped at 888 nm*, Opt. Lett. **31**, 3297 (2006). 81, 83, 84, 85, 130

[194] A. W. Tucker, M. Birnbaum, C. L. Fincher, and J. W. Erler, *Stimulated-emission cross section at 1064 and 1342 nm in Nd:YVO_4* (1977). 81

[195] J. Doualan, P. Camy, and R. Moncorgé, *Measurement of the stimulated emission cross section minus excited state absorption cross-section of Nd:YVO_4 crystal* (2008), private communication. 81, 83, 104, 105

[196] M. Okida, M. Itoh, T. Yatagai, H. Ogilvy, J. Piper, and T. Omatsu, *Heat generation in Nd doped vanadate crystals with 1.34 mum laser action.*, Optics express **13**, 4909 (2005). 81, 83, 92

[197] X. Peng, A. Asundi, Y. Chen, and Z. Xiong, *Study of the mechanical properties of Nd:YVO4 crystal by use of laser interferometry and finite-element analysis.*, Applied optics **40**, 1396 (2001). 81

[198] Y. F. Chen, *Design Criteria for Concentration Optimization in Scaling Diode End-Pumped Lasers to High Powers: Influence of Thermal Fracture*, IEEE Journal of Quantum Electronics **35**, 234 (1999). 81, 91

[199] L. Fornasiero, S. Kuck, T. Jensen, G. Huber, and B. H. T. Chai, *Excited state absorption and stimulated emission of Nd^{3+} in crystals. Part 2: YVO_4, $GdVO_4$, and $Sr_5(PO_4)_3F$*, Applied Physics B-Lasers and Optics **67**, 549 (1998). 81, 82

[200] A. E. Siegman, *Lasers*, University Science Books, Mill Valley, California (1986). 87, 88, 89, 102, 103

[201] B. E. A. Saleh and M. C. Teich, *Fundamentals of photonics*, Wiley, New York, NY (1991). 88

[202] S. Chénais, F. Druon, S. Forget, F. Balembois, and P. Georges, *On thermal effects in solid-state lasers: The case of ytterbium-doped materials*, Progress in Quantum Electronics **30**, 89 (2006). 90

[203] F. Lenhardt, M. Nittmann, T. Bauer, J. Bartschke, and J. A. L'huillier, *High-power 888-nm-pumped Nd:YVO4 1342-nm oscillator operating in the TEM_{00} mode*, Applied Physics B **96**, 803 (2009). 90, 93, 132, 138, 139

[204] B. Neuenschwander, R. Weber, and H. Weber, *Determination of the thermal lens in solid-state lasers with stable cavities*, IEEE Journal of Quantum Electronics **31** (1995). 93

[205] B. Ozygus and Q. Zhang, *Thermal lens determination of end-pumped solid-state lasers using primary degeneration modes*, Applied Physics Letters **71**, 2590 (1997). 93

[206] B. Ozygus and J. Erhard, *Thermal lens determination of end-pumped solid-state lasers with transverse beat frequencies*, Applied Physics Letters **67**, 1361 (1995). 93

[207] J. L. Blows, J. M. Dawes, and T. Omatsu, *Thermal lensing measurements in line-focus end-pumped neodymium yttrium aluminium garnet using holographic lateral shearing interferometry*, Journal of Applied Physics **83**, 2901 (1998). 93

[208] D. Sumida, D. Rockwell, and M. Mangir, *Energy storage and heating measurements in flashlamp-pumped Cr:Nd:GSGG and Nd:YAG*, Quantum Electronics, IEEE Journal of **24**, 985 (1988). 93

[209] U. Eismann, *A novel all-solid-state laser source for lithium atoms and three-body recombination in the unitary Bose gas*, Ph.D. thesis, Université Pierre et Marie Curie - Paris VI (2012). 96, 98, 105, 123, 135

[210] U. Eismann, A. Bergschneider, F. Sievers, N. Kretzschmar, C. Salomon, and F. Chevy, *2.1-watts intracavity-frequency-doubled all-solid-state light source at 671 nm for laser cooling of lithium*, Opt. Express **21**, 9091 (2013). 99, 109, 110, 129

[211] Y. Chen, T. Huang, C. Kao, C. Wang, and S. Wang, *Optimization in scaling fiber-coupled laser-diode end-pumped lasers to higher power: influence of thermal effect*, IEEE Journal of Quantum Electronics **33**, 1424 (1997). 100, 131

[212] V. Evtuhov and A. E. Siegman, *A "Twisted-Mode" Technique for Obtaining Axially Uniform Energy Density in a Laser Cavity*, Appl. Opt. **4**, 142 (1965). 102

[213] F. Biraben, *Efficacite des systemes unidirectionnels utilisables dans les lasers en anneau*, Optics Communications **29**, 353 (1979). 102

[214] D. Hutchings, F. Tooley, and D. Russell, *Unidirectional operation of a ring laser using an absorbing Fabry-Pérot filter*, Optics letters **12**, 322 (1987). 102

[215] S. Dinev, I. Koprinkov, K. Stamenov, and K. Stankov, *A narrowband unidirectional pulsed ring dye laser*, Optics Communications **35**, 403 (1980). 102

[216] G. Trénec, W. Volondat, O. Cugat, and J. Vigué, *Permanent magnets for Faraday rotators inspired by the design of the magic sphere*, Appl. Opt. **50**, 4788 (2011). 102, 130

[217] R. Sarrouf, T. Badr, and J. J. Zondy, *Intracavity second-harmonic generation of diode-pumped continuous-wave, single-frequency 1.3μm Nd:YLiF$_4$ lasers*, Journal of Optics A: Pure and Applied Optics **10**, 104011 (2008). 102

[218] W. Leeb, *Losses introduced by tilting intracavity etalons*, Applied physics **6**, 267 (1975). 104, 135

[219] Y. Chen, T. Huang, C. Wang, L. Lee, and S. Wang, *Theoretical and experimental studies of single-mode operation in diode pumped Nd: YVO4/KTP green laser: influence of KTP length*, Optics communications **152**, 319 (1998). 106

[220] T. Toyoda and M. Yabe, *The temperature dependence of the refractive indices of fused silica and crystal quartz* (2000). 106

[221] W. Haynes, *CRC handbook of chemistry and physics*, CRC Press. (2010). 106

[222] L. S. Rothman, I. E. Gordon, A. Barbe, D. Benner, P. F. Bernath, M. Birk, V. Boudon, L. R. Brown, A. Campargue, J.-P. Champion, K. Chance, L. H. Coudert, V. Dana, V. M. Devi, S. Fally, J.-M. Flaud, R. R. Gamache, A. Goldman, D. Jacquemart, I. Kleiner, N. Lacome, W. J. Lafferty, J.-Y. Mandin, S. T. Massie, S. N. Mikhailenko, C. E. Miller, N. Moazzen-Ahmadi, O. V. Naumenko, A. V. Nikitin, J. Orphal, V. I. Perevalov, A. Perrin, A. Predoi-Cross, C. P. Rinsland, M. Rotger, M. Simeckova, M. A. H. Smith, K. Sung, S. A. Tashkun, J. Tennyson, R. A. Toth, A. C. Vandaele, and J. V. Auwera, *The HITRAN 2008 molecular spectroscopic database*, Journal of Quantitative Spectroscopy and Radiative Transfer **110**, 533 (2009). 110, 136

[223] R. W. Boyd, *Nonlinear optics*, Academic Press, 3rd editio edn. (2008). 116, 117, 118

[224] J. A. Armstrong, N. Bloembergen, J. Ducuing, and P. S. Pershan, *Interactions between Light Waves in a Nonlinear Dielectric*, Phys. Rev. **127**, 1918 (1962). 116, 118, 143

[225] D. A. Kleinman, A. Ashkin, and G. D. Boyd, *Second-Harmonic Generation of Light by Focused Laser Beams*, Phys. Rev. **145**, 338 (1966). 117

[226] G. D. Boyd and D. A. Kleinman, *Parametric Interaction of Focused Gaussian Light Beams*, Journal of Applied Physics **39**, 3597 (1968). 117, 133

[227] P. A. Franken and J. F. Ward, *Optical harmonics and nonlinear phenomena*, Reviews of Modern Physics **35**, 23 (1963). 118

[228] M. Yamada, N. Nada, M. Saitoh, and K. Watanabe, *First-order quasi-phase matched LiNbO3 waveguide periodically poled by applying an external field for efficient blue second-harmonic generation*, Applied Physics Letters **62**, 435 (1993). 118

[229] L. E. Myers, R. C. Eckardt, M. M. Fejer, R. L. Byer, W. R. Bosenberg, and J. W. Pierce, *Quasi-phase-matched optical parametric oscillators in bulk periodically poled LiNbO3*, J. Opt. Soc. Am. B **12**, 2102 (1995). 118

[230] M. Peltz, U. Bäder, A. Borsutzky, R. Wallenstein, J. Hellström, H. Karlsson, V. Pasiskevicius, and F. Laurell, *Optical parametric oscillators for high pulse energy and high average power operation based on large aperture periodically poled KTP and RTA*, Applied Physics B **73**, 663 (2001). 118, 119, 123, 124, 127, 134

[231] R. Schiek and T. Pertsch, *Absolute measurement of the quadratic nonlinear susceptibility of lithium niobate in waveguides*, Opt. Mater. Express **2**, 126 (2012). 119

[232] S. Emanueli and A. Arie, *Temperature-Dependent Dispersion Equations for $KTiOPO_4$ and $KTiOAsO_4$*, Appl. Opt. **42**, 6661 (2003). 119, 121, 134, 135, 137

[233] K. Fradkin, A. Arie, A. Skliar, and G. Rosenman, *Tunable midinfrared source by difference frequency generation in bulk periodically poled $KTiOPO_4$*, Applied Physics Letters **74**, 914 (1999). 119, 121, 134, 135, 137

[234] D. H. Jundt, *Temperature-dependent Sellmeier equation for the index of refraction, ne, in congruent lithium niobate*, Opt. Lett. **22**, 1553 (1997). 119

[235] G. Hansson, H. Karlsson, S. Wang, and F. Laurell, *Transmission Measurements in KTP and Isomorphic Compounds*, Appl. Opt. **39**, 5058 (2000). 119

[236] J. Hirohashi, *Characterization of domain switching and optical damage properties in ferroelectrics*, Ph.D. thesis, Department of Applied Physics, Royal Institute of Technology, Stockholm, Sweden (2006). 119

[237] A. Arie, G. Rosenman, A. Korenfeld, A. Skliar, M. Oron, M. Katz, and D. Eger, *Efficient resonant frequency doubling of a cw Nd:YAG laser in bulk periodically poled KTiOPO4*, Opt. Lett. **23**, 28 (1998). 119

[238] Photonik-Zentrum Kaiserslautern (PZKL), *Periodisch gepolte Materialien*, Ph.D. thesis (2010). 119

[239] J. D. Bierlein and H. Vanherzeele, *Potassium titanyl phosphate: properties and new applications*, J. Opt. Soc. Am. B **6**, 622 (1989). 119

[240] S. Manivannan, S. Dhanuskodi, S. Tiwari, and J. Philip, *Laser induced surface damage, thermal transport and microhardness studies on certain organic and semiorganic nonlinear optical crystals*, Applied Physics B **90**, 489 (2008), 10.1007/s00340-007-2911-4. 119

[241] S. V. Tovstonog, S. Kurimura, and K. Kitamura, *High power continuous-wave green light generation by quasiphase matching in Mg stoichiometric lithium tantalate*, Applied Physics Letters **90**, 051115 (2007). 119

[242] Y. Furukawa, K. Kitamura, A. Alexandrovski, R. K. Route, M. M. Fejer, and G. Foulon, *Green-induced infrared absorption in MgO doped $LiNbO_3$*, Applied Physics Letters **78**, 1970 (2001). 119, 143

[243] C. Canalias, S. Wang, V. Pasiskevicius, and F. Laurell, *Nucleation and growth of periodic domains during electric field poling in flux-grown KTiOPO[sub 4] observed by atomic force microscopy*, Applied Physics Letters **88**, 032905 (2006). 120

[244] E. Mimoun, L. D. Sarlo, J.-J. Zondy, J. Dalibard, and F. Gerbier, *Sum-frequency generation of 589 nm light with near-unit efficiency*, Opt. Express **16**, 18684 (2008). 120

[245] V. A. Maslov, V. A. Mikhailov, O. P. Shaunin, and I. A. Shcherbakov, *Nonlinear absorption in KTP crystals*, Quantum Electronics **27**, 356 (1997). 123

[246] B. Boulanger, I. Rousseau, J. P. Feve, M. Maglione, B. Menaert, and G. Marnier, *Optical studies of laser-induced gray-tracking in KTP*, IEEE Journal of Quantum Electronics **35**, 281 (1999). 123

[247] G. C. Bjorklund, *Frequency-modulation spectroscopy: a new method for measuring weak absorptions and dispersions*, Optics Letters **5**, 15 (1980). 126

[248] I. Dolev, A. Ganany-Padowicz, O. Gayer, A. Arie, J. Mangin, and G. Gadret, *Linear and nonlinear optical properties of MgO:LiTaO3*, Applied Physics B **96**, 423 (2009). 129

[249] P. Laporta and M. Brussard, *Design criteria for mode size optimization in diode-pumped solid-state lasers*, IEEE Journal of Quantum Electronics **27**, 2319 (1991). 131

[250] W. W. Rigrod, *Gain Saturation and Output Power of Optical Masers*, Journal of Applied Physics **34**, 2602 (1963). 131

[251] E. Khazanov, N. Andreev, A. Mal'shakov, O. Palashov, A. Poteomkin, A. Sergeev, A. Shaykin, V. Zelenogorsky, I. Ivanov, R. Amin, G. Mueller, D. Tanner, and D. Reitze, *Compensation of thermally induced modal distortions in Faraday isolators*, IEEE Journal of Quantum Electronics **40**, 1500 (2004). 132

[252] R. Polloni and O. Svelto, *Optimum coupling for intracavity second harmonic generation*, IEEE Journal of Quantum Electronics **4**, 528 (1968). 133

[253] R. Smith, *Theory of intracavity optical second-harmonic generation*, IEEE Journal of Quantum Electronics **6**, 215 (1970). 133

[254] J.-J. Zondy, F. A. Camargo, T. Zanon, V. Petrov, and N. U. Wetter, *Observation of strong cascaded Kerr-lens dynamics in an optimally-coupled cw intracavity frequency-doubled Nd:YLF ring laser*, Opt. Express **18**, 4796 (2010). 133, 137

[255] K. I. Martin, W. A. Clarkson, and D. C. Hanna, *Self-suppression of axial mode hopping by intracavity second-harmonic generation*, Opt. Lett. **22**, 375 (1997). 135, 137

[256] S. Helmfrid and K. Tatsuno, *Stable single-mode operation of intracavity-doubled diode-pumped Nd:YVO_4 lasers: theoretical study*, J. Opt. Soc. Am. B **11**, 436 (1994). 135, 137

[257] R. DeSalvo, H. Vanherzeele, D. J. Hagan, M. Sheik-Bahae, G. Stegeman, and E. W. V. Stryland, *Self-focusing and self-defocusing by cascaded second-order effects in KTP*, Opt. Lett. **17**, 28 (1992). 136

[258] S. Holmgren, V. Pasiskevicius, and F. Laurell, *Generation of 2.8 ps pulses by mode-locking a Nd:$GdVO_4$ laser with defocusing cascaded Kerr lensing in periodically poled KTP*, Opt. Express **13**, 5270 (2005). 136

[259] C. Schäfer, C. Fries, C. Theobald, and J. A. L'huillier, *Parametric Kerr lens mode-locked, 888 nm pumped Nd:YVO_4 laser*, Opt. Lett. **36**, 2674 (2011). 136

[260] J. E. Hastie, S. Calvez, M. D. Dawson, T. Leinonen, A. Laakso, J. Lyytikäinen, and M. Pessa, *High power CW red VECSEL with linearly polarized TEM_{00} output beam*, Opt. Express **13**, 77 (2005). 138

[261] F. Lenhardt, A. Nebel, R. Knappe, M. Nittmann, J. Bartschke, and J. A. L'huillier, *Efficient Single-Pass Second Harmonic Generation of a Continuous Wave Nd:YVO_4-Laser at 1342 nm Using MgO:PPLN*, in *Conference on Lasers and Electro-Optics 2010*, CThEE5, Optical Society of America (2010). 139

[262] Y. Nishida, H. Miyazawa, M. Asobe, O. Tadanaga, and H. Suzuki, *Direct-bonded QPM-LN ridge waveguide with high damage resistance at room temperature*, Electronics Letters **39**, 609 (2003). 139

[263] T. Nishikawa, A. Ozawa, Y. Nishida, M. Asobe, F.-L. Hong, and T. W. Hänsch, *Efficient 494 mW sum-frequency generation of sodium resonance radiation at 589 nm by using a periodically poled Zn:LiNbO3 ridge waveguide*, Opt. Express **17**, 17792 (2009). 139

[264] K. R. Parameswaran, J. R. Kurz, R. V. Roussev, and M. M. Fejer, *Observation of 99% pump depletion in single-pass second-harmonic generation in a periodically poled lithium niobate waveguide*, Opt. Lett. **27**, 43 (2002). 141

[265] D. Jedrzejczyk, R. Güther, K. Paschke, G. Erbert, and G. Tränkle, *Diode laser frequency doubling in a ppMgO:LN ridge waveguide: influence of structural imperfection, optical absorption and heat generation*, Applied Physics B **109**, 33 (2012). 143

[266] S. Helmfrid and G. Arvidsson, *Influence of randomly varying domain lengths and nonuniform effective index on second-harmonic generation in quasi-phase-matching waveguides*, J. Opt. Soc. Am. B **8**, 797 (1991). 143

[267] F. Laurell and G. Arvidsson, *Frequency doubling in Ti:MgO:LiNbO3 channel waveguides*, J. Opt. Soc. Am. B **5**, 292 (1988). 143

[268] A. B. Fallahkhair, K. S. Li, and T. E. Murphy, *Vector Finite Difference Modesolver for Anisotropic Dielectric Waveguides*, J. Lightw. Technol. **26**, 1423 (2008). 143

[269] R. G. Batchko, G. D. Miller, A. Alexandrovski, M. M. Fejer, and R. L. Byer, *Limitations of high-power visible wavelength periodically poled lithium niobate devices due to green-induced infrared absorption and thermal lensing*, in *Conference on Lasers and Electro-Optics*, CTuD6, Optical Society of America (1998). 143, 145

[270] O. A. Louchev, N. E. Yu, S. Kurimura, and K. Kitamura, *Thermal inhibition of high-power second-harmonic generation in periodically poled LiNbO3 and LiTaO3 crystals*, Applied Physics Letters **87**, 131101 (2005). 143, 144, 145

[271] K. Okamoto, *Fundamentals of Optical Waveguides*, Electronics & Electrical, Elsevier (2000). 143

[272] O. Gayer, Z. Sacks, E. Galun, and A. Arie, *Temperature and wavelength dependent refractive index equations for MgO-doped congruent and stoichiometric LiNbO3*, Applied Physics B **91**, 343 (2008). 143

[273] J. Cannon, *The One-Dimensional Heat Equation*, Cambridge University Press (1984). 144

[274] D. Nikogosyan, *Nonlinear Optical Crystals: A Complete Survey*, Springer (2005). 144

[275] K. Cole, J. Beck, A. Haji-Sheikh, and B. Litkouh, *Heat Conduction Using Green's Functions, 2nd edition*, CRC Press (2010). 144

[276] V. Dmitriev, G. Gurzadyan, , and D. Nikogosyan, *Handbook of nonlinear optical crystals*, Springer series in optical sciences, Springer (1997). 145

[277] J. Schwesyg, M. Kajiyama, M. Falk, D. Jundt, K. Buse, and M. Fejer, *Light absorption in undoped congruent and magnesium-doped lithium niobate crystals in the visible wavelength range*, Applied Physics B **100**, 109 (2010). 145